Australian Government
Geoscience Australia

INTEGRATED EXPLORATION IN A CHANGING WORLD
ASEG-PESA
SYDNEY 2004

Airborne Gravity 2004

Abstracts from the ASEG-PESA Airborne Gravity 2004 Workshop

Edited by Richard Lane

Record
2004/18

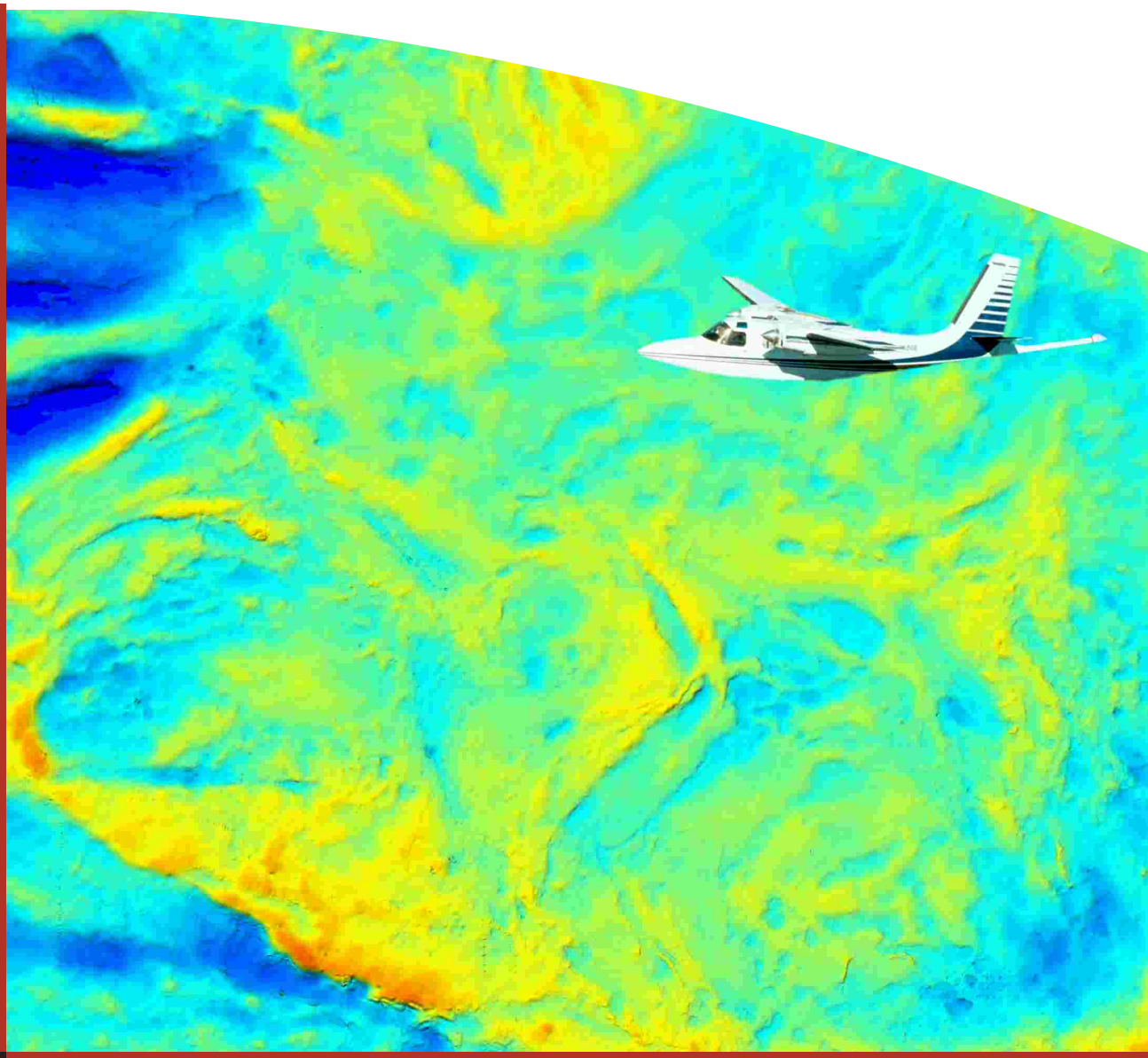

Geoscience Australia Record 2004/18

Airborne Gravity 2004

Abstracts from the ASEG-PESA Airborne Gravity 2004 Workshop

Edited by Richard Lane

Department of Industry, Tourism & Resources

Minister for Industry, Tourism & Resources: The Hon. Ian Macfarlane, MP
Parliamentary Secretary: The Hon. Warren Entsch, MP
Secretary: Mark Paterson

Geoscience Australia

Chief Executive Officer: Neil Williams

ISSN: 1448-2177
ISBN: 1 920871 13 6

GeoCat no. 61129

Bibliographic Reference:

a) For the entire publication

Lane, R.J.L., editor, 2004, Airborne Gravity 2004 – Abstracts from the ASEG-PESA Airborne Gravity 2004 Workshop: *Geoscience Australia Record* 2004/18.

b) For an individual paper

van Kann, F., 2004, Requirements and general principles of airborne gravity gradiometers for mineral exploration, in R.J.L. Lane, editor, Airborne Gravity 2004 - Abstracts from the ASEG-PESA Airborne Gravity 2004 Workshop: *Geoscience Australia Record* 2004/18, 1-5.

Contents

“Airborne Gravity 2004 Workshop” Record

Richard Lane
Geoscience Australia
richard.lane@ga.gov.au

Mark Dransfield
BHP Billiton
Mark.H.Dransfield@bhpbilliton.com

David Robson
NSW Department of Primary Industries, Mineral Resources
robsond@minerals.nsw.gov.au

Robert Smith
Greenfields Geophysics
greengeo@bigpond.net.au

Greg Walker
BHP Billiton
Greg.B.Walker@BHPBilliton.com

Preface

The "Airborne Gravity 2004 Workshop" was held in Sydney on August 15, in conjunction with ASEG-PESA Sydney 2004 (the ASEG's 17th Geophysical Conference and Exhibition). The aims of the workshop were to provide participants with a review of the current state of the art in airborne gravity instrumentation, to present case histories of the use of these methods in minerals and petroleum applications, and to distribute sample data sets. "Airborne gravity" is used in this context to include both airborne gravimeter and airborne gravity gradiometer methods.

The program was split into 2 sessions. The morning session provided a review of the systems, with presentations covering a number of systems currently in operation as well as some that are still under development. The focus shifted in the afternoon session to case histories, with examples from surveys spanning the globe; from Antarctica to the tropics of Papua New Guinea, from Africa through Australia to Canada.

To capture the essence of the day and to promote the ongoing development of airborne geophysical methods, speakers were invited to submit papers for inclusion in a workshop volume. The papers were reviewed prior to publication in this Geoscience Australia Record. Participants received a copy at the workshop, and additional copies of the Record are available on an ongoing basis from Geoscience Australia (www.ga.gov.au).

Units

Physical quantities should be expressed in SI units. The Bureau International des Poids et Mesures (BIPM) is the custodian of this system. To quote from their website (www.bipm.fr): “Its mandate is to provide the basis for a single, coherent system of measurements throughout the world, traceable to the International System of Units (SI)”.

The SI unit for acceleration is “metre per second squared” (m/s^2). The signals encountered in gravity surveys for exploration are small, and the prefix “micro” is commonly used (micrometre per second squared, $\mu m/s^2$). The gal (or Gal), equal to 1 cm/s^2, is a derived unit for acceleration in the CGS system of units. A prefix of “milli” is commonly used (milligal, mGal). In rare cases in the literature, a “gravity unit” (gu) may be encountered. In this publication, the $\mu m/s^2$ has been the preferred unit for gravity measurements, but mGal has been accepted.

1 $\mu m/s^2 = 10^{-6}$ m/s^2
1 mGal = 10 $\mu m/s^2$
1 gu = 1 $\mu m/s^2$

The gravity gradient is a gradient of acceleration and so the appropriate units are acceleration units divided by distance units. Thus, “per second squared” (s^{-2}) is appropriate in the SI system. Typical gravity gradients measured in exploration are extremely small, and the prefix “nano” is appropriate in most circumstances (per

nanosecond squared, ns^{-2}). The eotvos unit (Eo), although not recognised in either the SI or CGS systems, is used almost universally in geophysics as the unit for gravity gradient measurements. It is equal to 1 ns^{-2}. In this publication, the ns^{-2} and Eo have both been accepted as units for gravity gradient measurements.

$1\ ns^{-2} = 10^{-9}\ s^{-2}$
1 Eo= 1 ns^{-2}

Acknowledgments

The Airborne Gravity 2004 Workshop Organising Committee would like to acknowledge the support of the ASEG-PESA 2004 Conference Organizing Committee and the Conference Secretariat. Support from Geoscience Australia, BHP Billiton and the NSW Department of Primary Industries - Mineral Resources helped to make the workshop a success. The diligence of Mario Bacchin, Katharine Hagan, Angie Jaensch, Jim Mason, Peter Milligan, Ian Hone and Roger Clifton enabled this Record to be produced in time for the Workshop, despite a tight deadline. Finally, a vote of thanks goes to the speakers who committed their time and energy to deliver presentations on the day and to compose this permanent record of the event.

Requirements and general principles of airborne gravity gradiometers for mineral exploration

Frank van Kann
University of Western Australia
frank@physics.uwa.edu.au

Introduction

The quest for airborne gravity is as old as airborne exploration itself. In contrast to magnetic methods, where airborne and ground based methods are of almost equal precision, it has not yet been possible to replicate the high precision of ground based gravity exploration methods in the airborne environment.

One of the fundamental reasons behind the enormous challenge of airborne gravity is the "equivalence principle" which underpins the fact that no inertial sensor can distinguish between (desired) spatial variations in the gravity field and the (undesired) variations in the acceleration of the aircraft.

There are two distinct kinds of airborne gravity methods, namely gravity and gravity gradiometry.

Airborne gravity for detailed mineral exploration

Airborne gravity requires an additional non-inertial sensor, such as GPS, to separate the platform acceleration from the gravity measurement. Limitations in GPS measurements mean that it is unlikely that airborne gravity will have sufficient accuracy for detailed mineral exploration in the foreseeable future. This does not, however, preclude a role for airborne gravity in petroleum, regional geological and geodetic applications.

To date, one of the best airborne gravity systems is the AIRGrav system (Sander et al., 2004), which uses aerospace accelerometers in place of the more conventional gravimeter adapted for airborne operation. The performance of the Sander system appears to be limited by the GPS correction (Bruton, 2000), as shown below.

Based on an analysis by Torge (1989), but with updated parameters, it is assumed that the spectrum of the GPS position noise is approximately

$$S_X(f) = S_{o2}\left(1+\left(\frac{f_c}{f}\right)^n\right) ,$$

where S_{o2} is 0.01m, f_c is 0.015Hz and the exponent n is 3. This function reflects the fact that the spectrum is approximately flat down to about 0.01Hz, rising rapidly below that. The exponent n greater than 1 represents this rapid rise.

The GPS signal is passed through a low pass filter with cut-off frequency f_f. This sets a minimum wavelength that will be present in the GPS data

$$\lambda = \frac{v}{f_f} ,$$

where v is the speed of the aircraft.

Thus the GPS limited error correction is

$$a_{rms} = \sqrt{\langle a^2 \rangle} = (2\pi)^2 \sqrt{S_{o2}} \left(\frac{v^5}{5\lambda^5} + \frac{f_c^n v^{5-n}}{(5-n)\lambda^{5-n}} \right)^{1/2} .$$

This function is plotted for v equal to 180 km/h as the thick dashed line in Figure 1, labelled "Limit at 1σ". Using the stated parameters, it fits well to the Sander data, plotted as crosses and this indicates that the Sander instrument is limited by the GPS correction. The Carson (Carson Services Inc., 1995; W. Gumert, personal communication, 1996) and LCT data (LCT Inc., 1995) have noise that falls above the line, showing that these systems are not limited by GPS but by instrumental errors in the gravimeters.

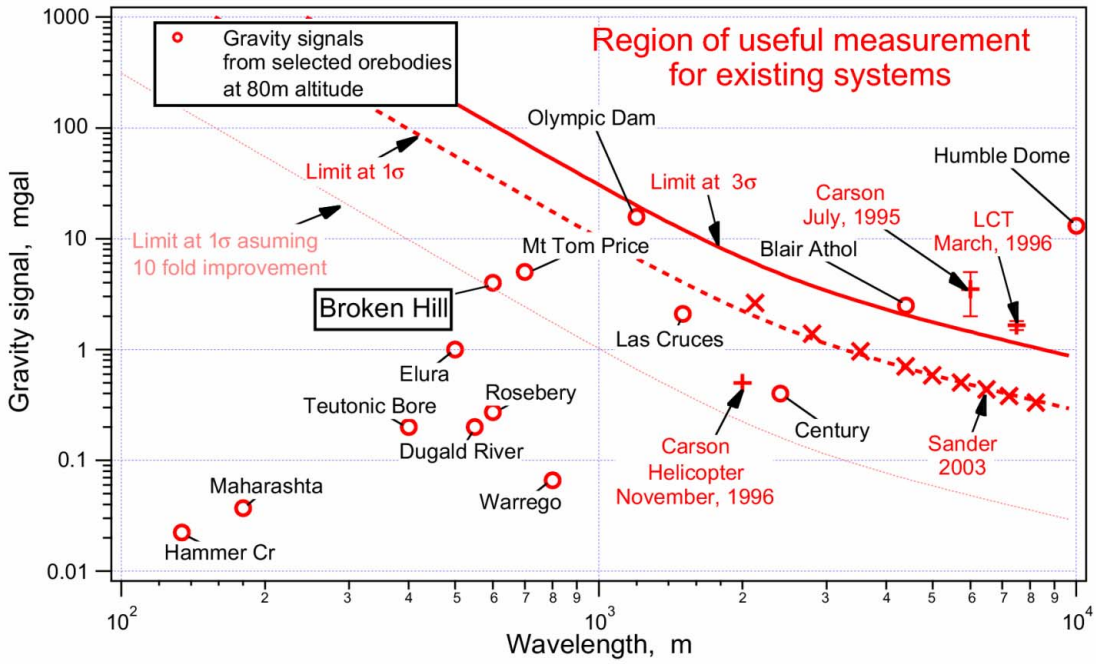

Figure 1. Plot of vertical gravity response against wavelength showing signals for selected orebodies. The noise levels for various airborne systems are shown (i.e., Carson helicopter system in November 1996, Carson fixed-wing system in July 1995, LCT fixed-wing system in March 1996, Sander fixed-wing system in 2003). Also shown are lines corresponding to GPS-related acceleration noise ("Limit at 1σ", "Limit at 3σ", and "Limit at 1σ assuming 10-fold improvement").

Also plotted in Figure 1 are points representing various orebodies (Dransfield, 1994; Matthews, 2002). For this analysis, it is sufficient to represent the modelled orebody in terms of the strength and wavelength of its gravity signal. Also shown are a coal resource, Blair Athol, and an oil field associated with a salt dome, Humble Dome.

The thick solid line (labelled "Limit at 3σ") separates the regions on this diagram for which present-day airborne gravimetry systems are useful and not useful. The 3σ criterion is used as it is necessary to resolve some detail in the anomaly, rather than just detect it. This demonstrates that while the Humble Dome field Blair Athol coal resource are resolved, none of the mineral deposit anomalies would be resolved.

This situation is unlikely to change in the foreseeable future. The line labelled "Limit at 1σ assuming 10 fold improvement" shows that at least an order of magnitude would be required to be useful. Such an improvement, which corresponds to an accuracy of 1 mm, is not expected to be achievable according to experts in the industry (staff of Trimble Navigation Australia Pty Ltd, personal communication).

Airborne gravity gradiometry for detailed mineral exploration

The prospects for successful airborne gravity gradiometry in mineral exploration are much better.

For detailed mineral exploration, the instrumental noise should be about 1 Eö rms in a 50 to 100 m wavelength. This is illustrated in Figure 2, which shows the same anomalies represented in terms of the vertical gravity gradient component Γ_{zz} of their gravity gradient signal. Other components, such as Γ_{xy}, would have smaller signals and different wavelengths.

Superimposed on the figure are lines depicting the instrumental limits for systems with different noise levels and airspeeds.

The solid line labelled "Limit at 3σ of 12Eö/√Hz system..." corresponds to a system with a noise level of 12 Eö/√Hz (Dransfield et al., 2001). This again assumes the 3σ criterion for useful characterisation of the anomaly, although it will be shown below that this could be somewhat optimistic. Only about half of the orebodies fall above the line.

All of the orebodies lie above the line corresponding to a 1 Eö/√Hz system, which is about an order of magnitude better than achieved to date by any airborne system. Some of the systems under development are targeted to achieve this level of performance (Chan and Paik, 1987; Matthews, 2002).

The anomalies plotted in Figures 1 and 2 serve to illustrate the fundamental concepts involved in a comparison of airborne gravimetry and gravity gradiometry. However, the representation of an orebody by the magnitude and wavelength of its signal is a simplification and a more realistic example discussed below illustrates this.

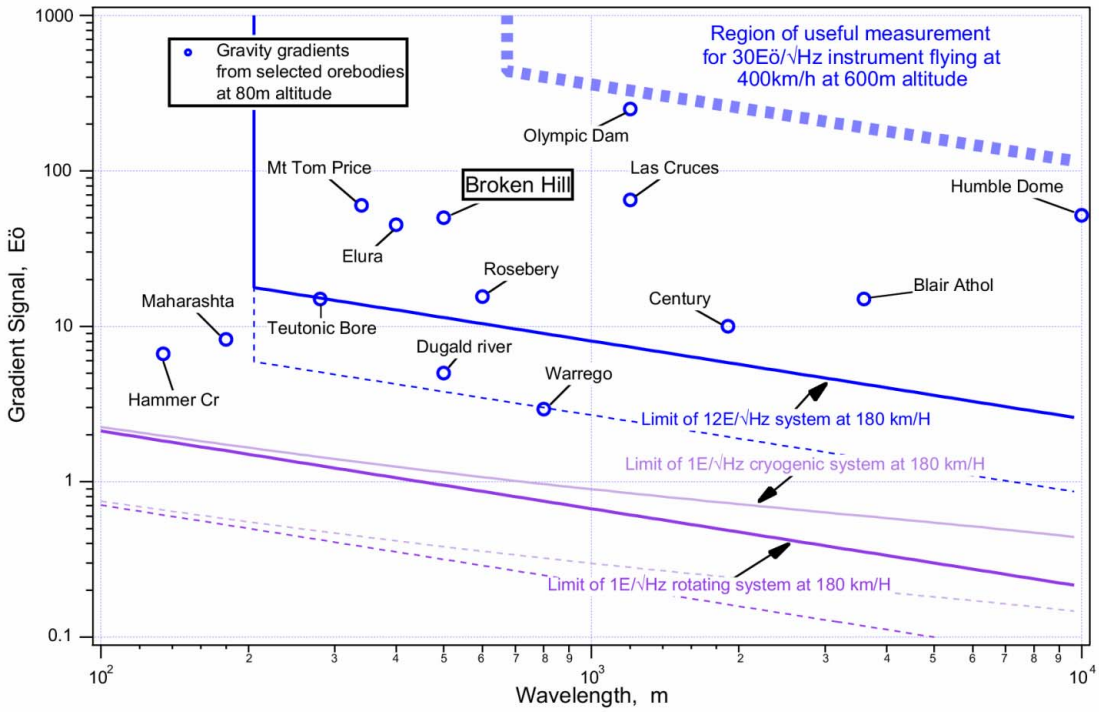

Figure 2. Plot of vertical gravity gradient response against wavelength showing signals for selected orebodies. Also shown are lines corresponding to systems with different noise levels.

Simulated airborne gravity gradiometer response for Broken Hill

The geology of the Broken Hill orebody and surrounding area in western NSW, Australia, has been extensively studied and is shown in Figure 3. Simulated airborne gravimeter and gravity gradiometer survey data have been generated from a density model of this area (Dransfield, 1994). These data can be used to determine the noise level that must be achieved to map details of the anomaly related to a large base metal deposit using an airborne gravity gradiometer.

The simulated Γ_{zz} gravity gradient at an altitude of 80 m above the ground over Broken Hill prior to mining is shown as a false colour image in Figure 4. Note that some additional Banded Iron Formation and cover units are included in the density model but are not shown in the geological map. The calculations were performed on a 50 m square grid and no noise apart from numerical rounding is present. This ideal vertical gravity gradient map resembles the geology map in Figure 3, and the response of the orebody and its immediate host is recognisable as a sinuous yellow to orange feature at approximately 4000-9000mE 5000mN.

To simulate an actual airborne survey, the characteristics of the instrument, including noise and wavelength response, must be included and a realistic flight line direction and spacing chosen. A simulated fixed-wing aircraft survey conducted at an altitude of 80 m and a line spacing of 250 m is shown in Figure 5. The modelled instrument measures the component Γ_{xy} and the combination $(\Gamma_{xx} - \Gamma_{yy})/2$, and this is used to obtain the component Γ_{zz} by standard spatial filtering techniques. The instrumental noise corresponds to 12 Eö/√Hz and a filter with a cut-off wavelength of 500 m has been used. With an instrument having this performance, some details of the geology are lost. The response of the orebody is not resolved and only the broader features of the geological structures are visible.

Figure 6 is similar to Figure 5, except the modelled noise is reduced to 1 Eö/√Hz and a 100 m filter is used. Although the map in Figure 6 has lost some of the detail found in the ideal map of Figure 4, it does reproduce significant geological detail and the anomaly related to the orebody and its immediate host is clearly resolved. This sets the target performance for an instrument capable of detailed mineral exploration.

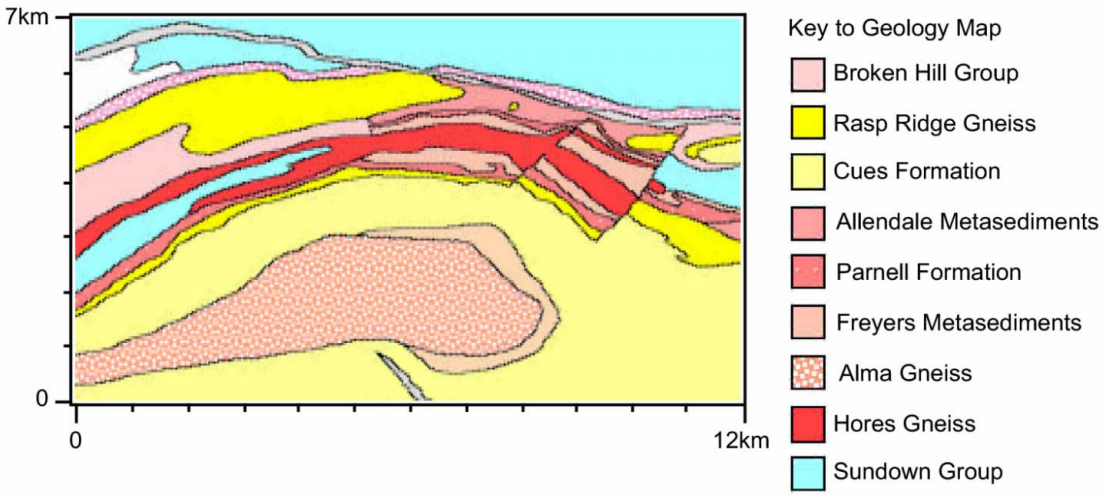

Figure 3. Surface geology of the Broken Hill model. Grid north for the model is 44° west of true north. Dips are generally steep.

Progress towards achieving the target specifications

The target of 1 Eö rms in a 50 to 100 m wavelength is a challenging one and the problems of sensor noise, sensor drift and errors produced by aircraft motion (both translation and rotation) are common to every instrument (whether operating or under development). Each design solves these problems in a different way.

The difficulties are rather awe-inspiring: it is required to measure displacements on the order of 10^{-13} m (i.e., the regime of nuclear dimensions) in the presence of disturbances some 10^{10} times greater than the signal being measured.

To achieve the desired sensitivity is difficult enough but has been achieved in the laboratory by at least two of the instruments under development (Matthews, 2000).

The real challenge is to translate this performance into the environment of a light aircraft and some of the strategies designed to achieve this will be compared. With sound technical and commercial management, the goal is now within reach.

References

Bruton, A.M., 2000, Improving the Accuracy and Resolution of SINS/DGPS Airborne Gravimetry: Ph.D Thesis, The Department of Geomatics Engineering, University of Calgary, UCGE Report No. 20145. (http://www.geomatics.ucalgary.ca/Papers/Thesis/KPS/00.20145.AMBruton.pdf)

Carson Services Inc., 1995, Brochure: Carson Services Inc., 32-H Blooming Glen Road, Perkasie, PA 18944.

Chan, H.A. and Paik, H.J., 19897, Superconducting Gravity Gradiometer for Sensitive Gravity Measurements. I. Theory: Phys. Rev. D **35**, 3551-3571.

Dransfield, M.H., 1994, Airborne Gravity Gradiometry: PhD Thesis, Department of Physics, University of Western Australia. (http://internal.physics.uwa.edu.au/~Frank/GGWebPage/thesis.html)

Dransfield, M. H., Christensen, A. N., Diorio, P. P., Rose, M. M. and Stone, P. M., 2001, FALCON test results from the Bathurst Mining camp: Exploration Geophysics, 32, 243-246.

Jekeli, C., 1988, The Gravity Gradiometer Survey System (GGSS): EOS, **69**, 105 and 115-116.

LCT Inc., 1995, Airborne Gravity & Magnetics Surveys: Brochure, LCT Inc., 1155 Dairy Ashford, Suite 500, Houston, TX 77079.

Matthews, R., 2002, Mobile Gravity Gradiometry: PhD Thesis, University of Western Australia. (http://internal.physics.uwa.edu.au/~frank/GGTheses/Rob_Matthews.html)

Sander, S., Argyle, M., Elieff, S., Ferguson, S., Lavoie V., and Sander, L., 2004, The AIRGrav airborne gravity system: This volume.

Torge, W., 1989, Gravimetry: deGruyter, Berlin.

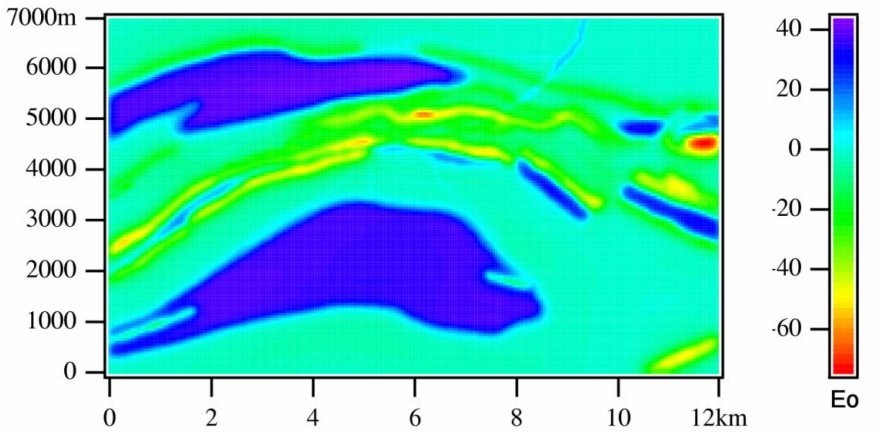

Figure 4. Noise-free image of simulated Γ_{zz} gravity gradient at a terrain clearance of 80 m over Broken Hill prior to mining. The response was calculated at 50 m centres. The response of the orebody and its immediate host is recognisable as a sinuous yellow to orange feature at approximately 5000-9000mE 5000mN.

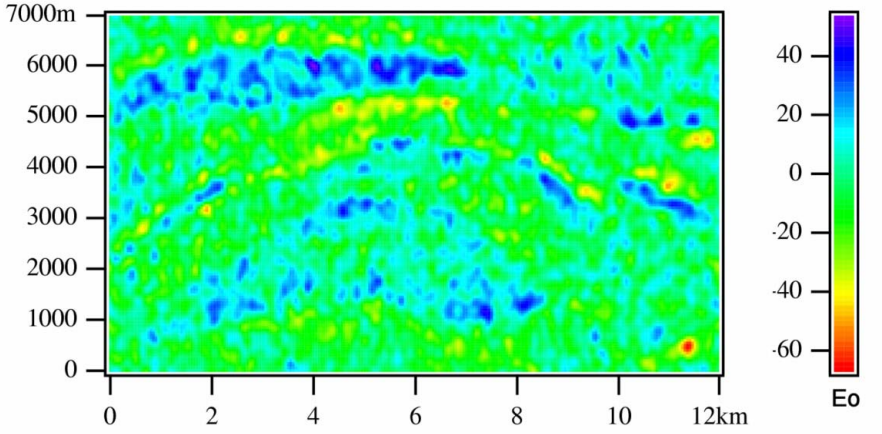

Figure 5. Image of simulated Γ_{zz} gravity gradient at a terrain clearance of 80 m and line spacing of 250 m. The modelled instrument measures the component Γ_{xy} and the combination $(\Gamma_{xx} - \Gamma_{yy})/2$, and this is used to obtain the component Γ_{zz} by standard spatial filtering techniques. The instrumental noise corresponds to 12 Eö/√Hz and a filter with a cut-off wavelength of 500 m has been used.

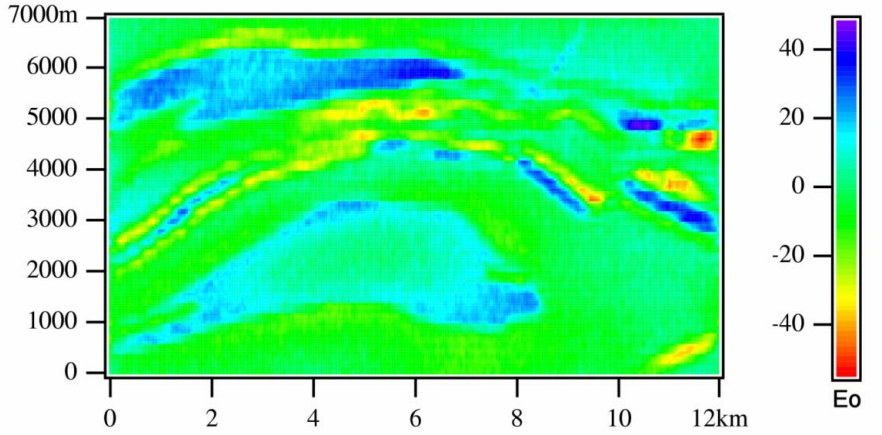

Figure 6. Image of simulated Γ_{zz} gravity gradient at a terrain clearance of 80 m and line spacing of 250 m. The modelled instrument measures the component Γ_{xy} and the combination $(\Gamma_{xx} - \Gamma_{yy})/2$, and this is used to obtain the component Γ_{zz} by standard spatial filtering techniques. The instrumental noise corresponds to 1 Eö/√Hz and a filter with a cut-off wavelength of 100 m has been used.

The Air-FTG™ airborne gravity gradiometer system

Colm A. Murphy
Bell Geospace
cmurphy@bellgeo.com

Abstract

Air-FTG™ is a multiple accelerometer moving platform technology that measures the full gravity gradient tensor. Full tensor gradient measurements provide more information about the gravity field from each measurement location than partial tensor gradient or single vector field measurements. This facilitates interpretation of sub-surface features exhibiting a lateral density contrast to their surrounds.

Surveys are flown for both detailed and regional applications; with line spacings from 50 to 2000 m. Processing and interpretation techniques utilise all components of the data to enhance signal to noise ratios. The standard deviation of noise in the vertical gravity gradient component is typically 5 to 6 Eo after low-pass filtering to remove wavelengths less than 400 to 600 m.

Introduction

The gradiometer instrument at the heart of the Air-FTG™ system was developed by Bell Aerospace (now Lockheed Martin) during the 1970's and 80's for the US Navy (Brzezowski and Heller, 1988; Jekeli, 1993). The full tensor gradiometer (FTG) instrument represents a significant advance in gradiometer instrumentation and is the only operational moving platform full tensor gravity gradiometer.

Gravity gradiometers measure the spatial rate of change in the gravity field. This form of measurement captures the high frequency signal associated with near-surface lateral density variations more clearly than conventional vertical gravity field instruments. This is possible because the gradiometer signal strength falls off with the cube of the distance to the target (Hammond and Murphy, 2003), in contrast to the conventional vertical gravity signal which decays with the square of the distance. Given typical accuracy levels for gravity gradiometer and vertical gravity measurements, the gradiometer enjoys an advantage for identification and mapping of certain near-surface mineral or hydrocarbon occurrences (Li, 2001).

Air-FTG™ was launched in 2002 on the strength of its marine counterpart's success. Two marine FTG instruments were previously deployed; one each in the Gulf of Mexico and offshore NW Europe from 1998 to 2002. These instruments were then modified for use on an aircraft and are currently operational in North America and Africa. More than 60 000 line km of data have been acquired to date. Both systems can be deployed on either marine or airborne platforms, thus offering a flexible service to the exploration industry.

In this paper, the nature of the Air-FTG™ measurements will be described, an analysis of the accuracy of these measurements will be provided, and then the key parameters that need to be considered for successful application of the technology in exploration programmes will be discussed.

Air-FTG™

Air-FTG™ accurately measures small changes in the gravity field caused by subsurface densities at prospect level resolution. The system works by taking ultra sensitive real-time measurements of the differences in the gravity gradient field in all directions. Gradient data can be directly related to geological structures and discrete bodies that have a density contrast relative to their surroundings, such as kimberlites or massive sulphides.

What is measured?

Gravitational potential is a scalar quantity that represents the energy associated with a unit mass in a gravitational or 'gravity' field. The gravity field is a vector field that describes the spatial variations in potential (i.e., the potential gradients). It can be decomposed into three mutually perpendicular components, shown schematically in Figure 1. In this paper, a coordinate system with the x-axis aligned east-west, the y-axis aligned north-south, and the z-axis aligned vertically is used. Conventional ground or marine gravity methods entail measurements of the vertical component of gravity (Gz). Gravity gradiometry involves measurement of the spatial variations (gradients) of the gravity field. Each of the three vector components of the gravity field has a gradient parallel to each of the three mutually perpendicular coordinate axes. Thus, a FTG instrument

must measure or derive nine components of the gravity gradient tensor, T_{ij}, where i and j are one of x, y or z (Figure 1).

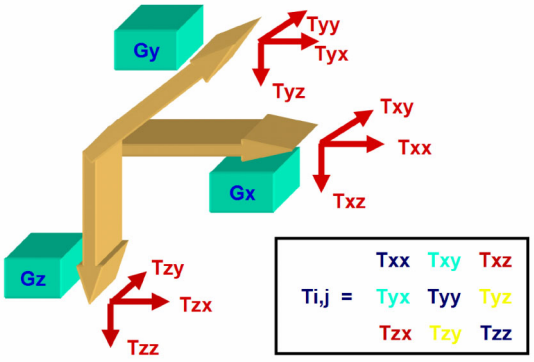

Figure 1. Schematic diagram showing the gravity field vector elements in gold and the tensor components in red. The nine tensor components, $T_{i,j}$, are summarised in matrix form, with colours used to identify the five independent tensor components. Any two of Txx, Tyy and Tzz are independent.

Although the full tensor consists of nine components, only five are truly independent. Gravity is a conservative field, which means that the amount of work required to move from A to B is independent of the path taken between the two points. From this, it can be shown (e.g., Blakely, 1995) that the gravity gradient tensor is symmetric about the leading diagonal (i.e., T_{ij} equals T_{ji}) (Figure 1). For measurements made above the surface of the Earth and ignoring the mass of the atmosphere, gravitational potential obeys the Laplace Equation and the diagonal element Tzz equals the negative sum of the other two elements of the leading diagonal, Txx and Tyy (e.g., Blakely, 1995). Therefore, the five independent components of the full gradient tensor are Txy, Txz, Tyz, and any two of Txx, Tyy and Tzz. In practice, the vertical gravity gradient or Tzz term is given even if Txx and Tyy are also given because Tzz is the gradient that is most easily related to subsurface geology.

Gradients are measured in units of eotvos, with 1 Eo equal to 0.1 mGal/km.

Spatial images of the individual tensor components reflect different attributes of target geology. Figure 2a shows a tensor component display for an Air-FTG™ survey acquired onshore Louisiana, USA. The target was a salt cap rock which yielded the prominent positive anomaly in the centre of the Tzz image. The location of this feature is highlighted in white in all of the data images. The salt cap rock response can be compared with the synthetic tensor component display for a buried discrete positive density feature shown in Figure 2b. Images of the individual tensor components provide information about geological setting. Txx and Txz identify the north-south edges of the target, revealing in this example those lineaments relevant to the body's emplacement. Similarly, Tyy and Tyz map the east-west trending lineaments and east-west edges of the target. The Txy cap rock anomaly has the characteristic quadrupole anomaly form with 2 highs and 2 lows that is associated with a discrete target. Txx and Tyy anomaly magnitudes can be used to investigate body thickness.

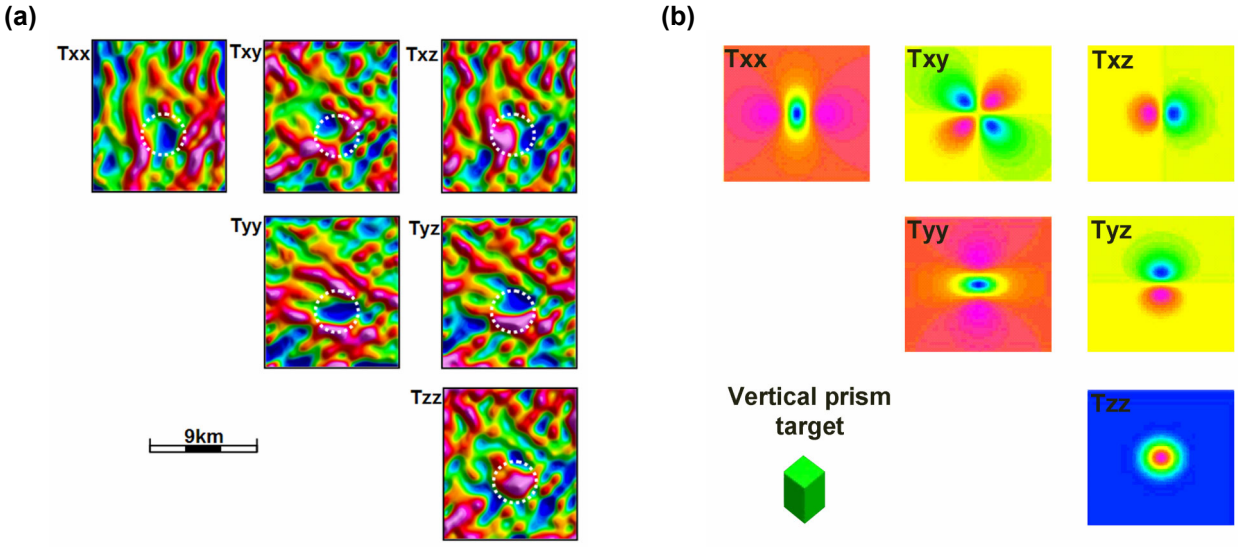

Figure 2. Tensor display for (a) an Air-FTG™ survey acquired over a known salt caprock feature onshore USA, and (b) a theoretical response for an idealised target. The white polygon helps to locate the response of the caprock in each component.

How do we measure the tensor components?

The instrument contains three Gravity Gradient Instruments (GGIs) each consisting of two opposing pairs of accelerometers arranged on a disc (Figure 3). The gradient of the gravity field is measured as the difference in readings between the opposing pairs of accelerometers on each disc. The three GGIs are mounted such that their axes are mutually perpendicular and each make the same angle with the vertical. Viewed from above, the projections of the three axes are 120 degrees apart. To minimise any bias related to the orientation or movement direction of the instrument, the assembly of GGIs is rotated at constant speed about a vertical axis. Brett (2000) gives a more detailed account on the workings of the system.

The measurements from each GGI can be resolved into two gradients in the plane of the rotating disc by taking into account the distance between each accelerometer and the frequency of spin of the disc. The tensor components measured in the external coordinate axis directions are obtained by forming the appropriate linear combination of the six GGI outputs. A three-GGI configuration is required to obtain the five independent tensor components that constitute the basis of the full tensor.

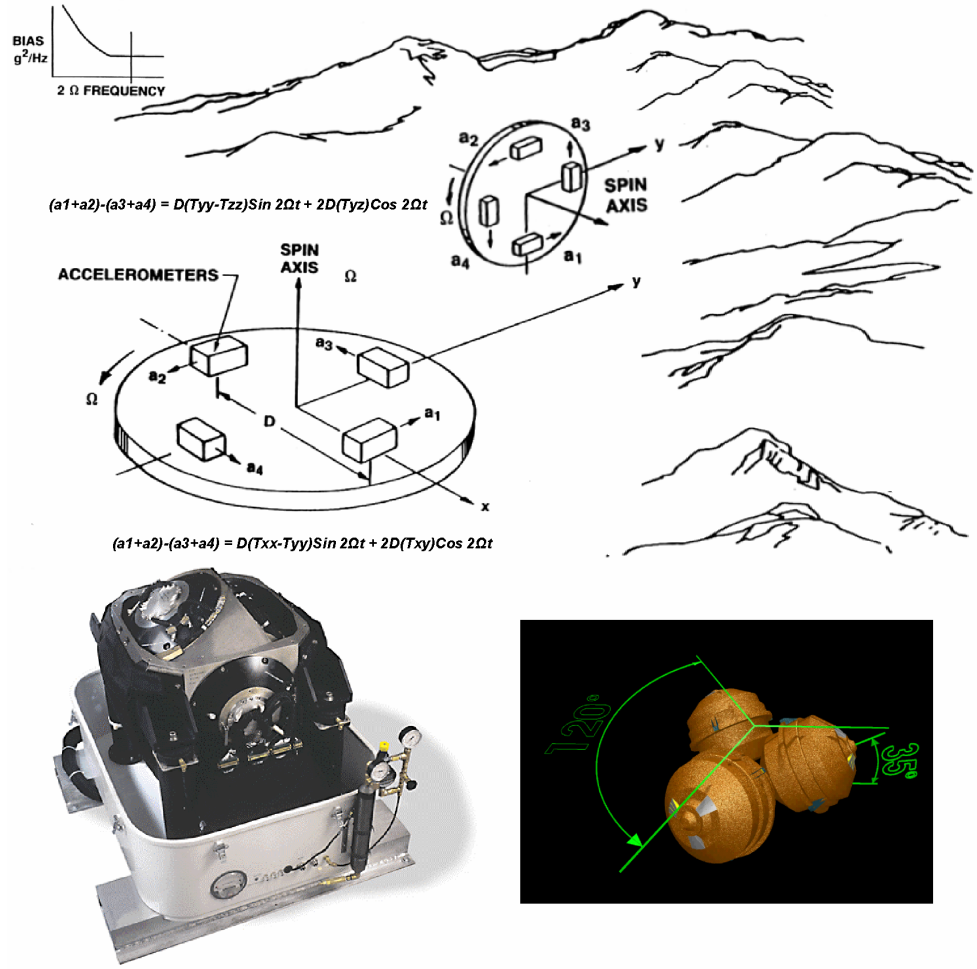

Figure 3. Photograph of the Air-FTG™ instrument with schematic diagram of accelerometer arrangement within each GGI. The darkened inset illustrates the umbrella configuration of the GGIs within the instrument.

Accuracy

The most effective means of evaluating Air-FTG™ data is via comparison with ground gravity data. This can be done by either spatial integration of Air-FTG™ tensor component data to estimate vertical gravity data or spatial transformation of the ground vertical gravity data to estimate a tensor quantity. The rms value for the difference between ground and airborne datasets provides an estimate of the combined errors in the ground and airborne data. This procedure does not allow these errors to be separated, nor does it account for errors that arise because the airborne datasets are acquired over survey areas of finite extent. Provided the ground data are adequately sampled and sufficiently accurate, the contribution of the ground data errors to the differences can be assumed to be small. The rms value can then be taken as an estimate of the upper bound for the noise in the airborne data.

An Air-FTG™ survey was carried out in the Ventersdorp region, South Africa, to assist in the identification and mapping of diamondiferous palaeochannel sequences. A total of 7500 line km of data were acquired with an in-line spacing of 400 m oriented east-west and tie-line spacing of 1600 m oriented north-south. A smaller orientation survey was flown prior to the main survey at 200 m in-line spacing and was merged with the larger data set. The survey was flown on a gentle drape surface at 80 m terrain clearance. The data indicate the presence of a series of north-south and east-north-east trending low density features. These follow the known palaeochannels in the area and confirmed the interpretation based on a series of gravity lows outlined with previously acquired ground gravity measurements. The ground gravity data were acquired at 50 m station spacing along north-east oriented lines spaced at 100 m intervals. A subset covering the same area was extracted from the airborne and ground datasets (Figure 4). The area of the subset lies within the boundary of the orientation survey where data were acquired at 200 m line spacing.

The ground gravity data were first upward continued to a mean height of 1649 m above sea level to align these data with the airborne drape surface (i.e., an 80 m drape above ground) and then a Tzz response was computed by taking the first vertical derivative of the vertical gravity data (Figure 4c). The consistency between the airborne and ground datasets can be judged qualitatively using the three prominent Tzz lows for reference. Quantitatively, the difference between the Tzz data derived from airborne and ground measurements (Figure 4d) has a standard deviation of approximately 5.5 Eo. The yellow-green areas in Figure 4d indicate where both data sets are closely in agreement and testify to the accuracy of the Air-FTG™ system. Many of the areas shown in red, where the differences are larger in magnitude, are where the ground data indicate rapid spatial changes in value. The airborne data are low-pass filtered to remove wavelengths less than 400 m, and this limits the accuracy in areas of rapid spatial changes.

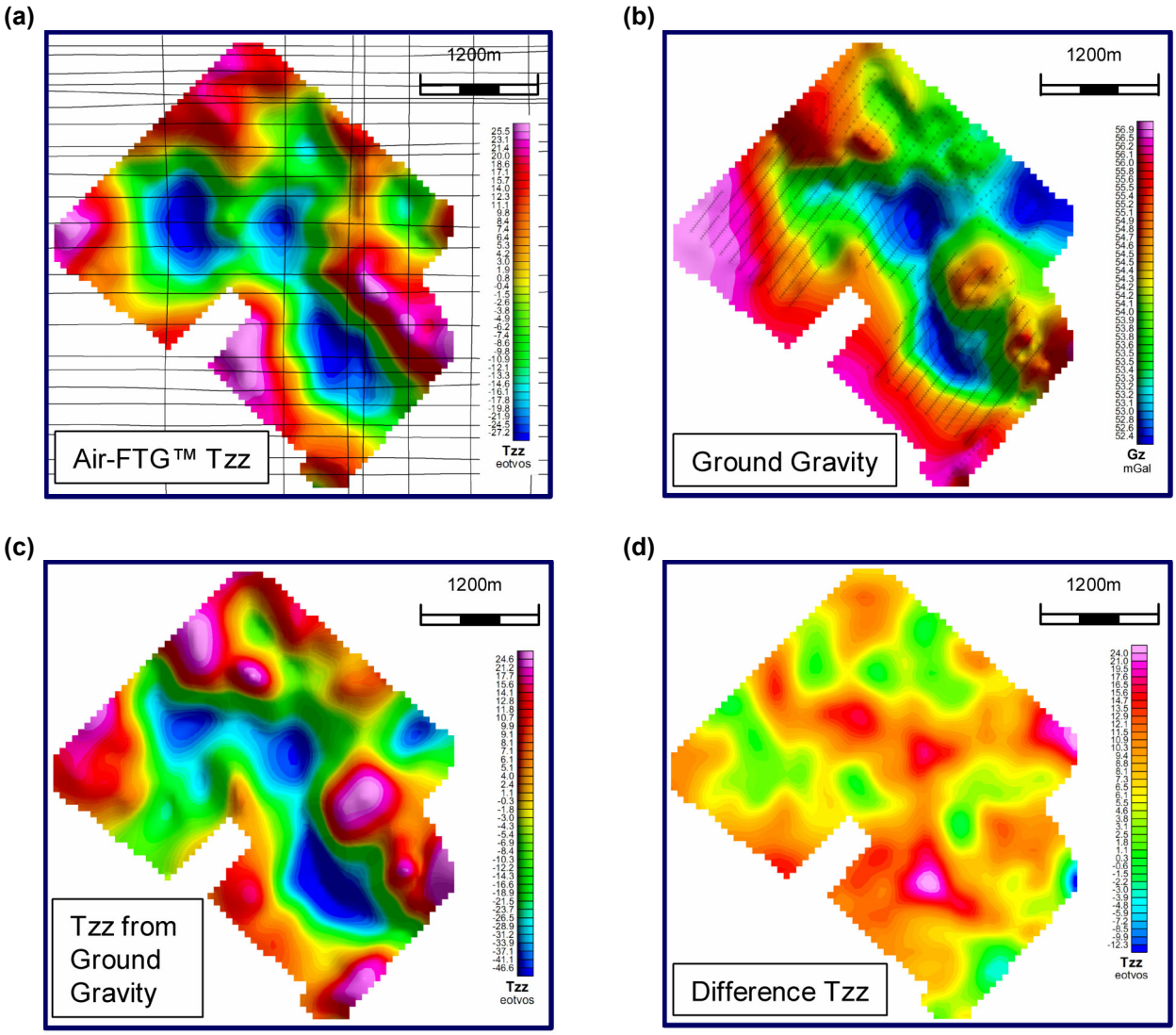

Figure 4. Comparison of Air-FTG™ Tzz data with ground gravity data from the Ventersdorp area, South Africa. Both data sets are terrain corrected. (a) Air-FTG™ Tzz response with flight lines shown as an overlay. (b) Ground gravity Gz image with stations shown as an overlay. (c) Tzz image derived from upward continued ground gravity data. (d) A difference image for the Tzz values derived from Air-FTG™ and the ground gravity data.

Acquisition issues

The two key issues affecting FTG surveys are choice of platform (i.e., aircraft in the case of Air-FTG™) and survey design.

Platform

Air-FTG™ is a highly sensitive instrument requiring a noise free and stable environment to operate to maximum efficiency. This is clearly not possible in the real world, so that issues such as engine activity and propeller speeds that contribute to platform vibrations must be managed. Furthermore, it must be possible for the instrument to be installed close to the centre of gravity of the vessel. This last point, together with the fact that the instrument and data acquisition system together have a mass in excess of 450 kg limits the choice of airborne platform. A Cessna Grand Caravan is currently the preferred platform as it can adequately meet the above requirements. The aircraft is of sufficient size to host the technology and its single engine induces a manageable vibration noise level on the system. The propeller speeds, engine noise and vibrations acting on the system are monitored throughout each flight and the data are compensated for residual noise effects using these auxiliary measurements.

Since the strength of signal in an Air-FTG™ survey falls off with the cube of the distance to the target, it is important to fly at low terrain clearance to capture the small amplitudes associated with subtle targets. Air-FTG™ surveys are typically flown using drape methods at 80 m above ground. This is the lowest flying height that is considered safe given the aircraft performance levels.

Survey design optimising signal

As with any geophysical technique, the choice of line spacing, orientation and survey size for an Air-FTG™ survey is critical to effective surveying. Target size, orientation, density contrast and depth of burial are key factors in determining survey parameters. These issues are always analysed prior to a survey.

As an example, a subset of Air-FTG™ Tzz data from a recent survey acquired in Africa is shown in Figure 5. An anomaly that is a 350 m in length is present in the centre of the image. This feature is well defined when surveyed with 50 m line spacing (Figure 5a). By selecting groups of lines in the database, it is possible to simulate surveys flown with 150 or 250 m line spacing (Figure 5b and c). The results indicate that 150 m line spacing would allow the feature to be mapped with adequate detail. The optimum line orientation in this particular case would be east-west, perpendicular to the long axis of the anomaly.

Air-FTG™ surveys are typically flown with line spacings from 50 to 2000 m. Tight line spacings are required for small scale geological targets such as kimberlites, whilst wider line spacings can be used for regional mapping applications on large surveys. Such wide line spaced surveys are possible with Air-FTG™ because the system measures the horizontal components Txz and Tyz in addition to Txx, Tyy and Txy, thus increasing confidence when interpolating from line to line. This is a well-known benefit of gradient measurements (Schmidt and Clark, 2000).

Geographic coverage

The technology, although declassified, is still governed by the US State Department's International Trade in Arms Regulatory (ITAR) Licensing Restrictions (22.CFR121.1). This in effect means that there are a number of embargoed countries where it would be difficult to obtain a license to perform a survey. Fortunately, the number of embargoed countries is small. Air-FTG™ surveys have been acquired in the USA, Canada, South Africa, Botswana, Zambia, and Mali.

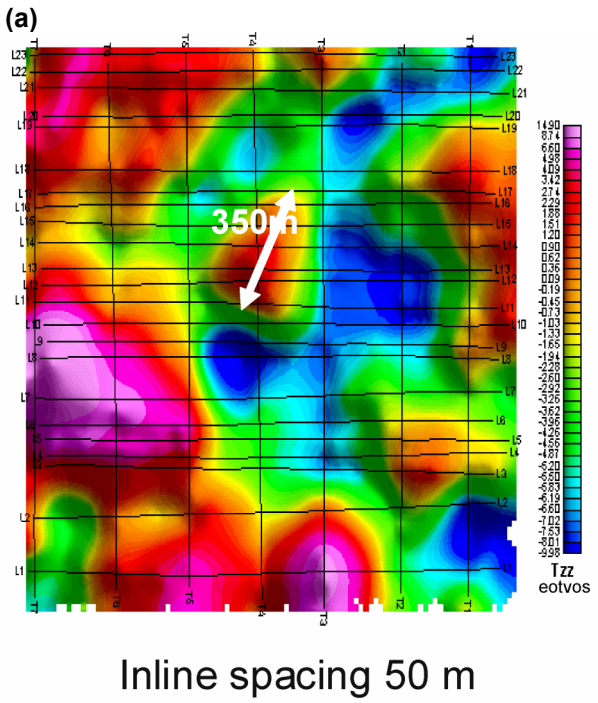

Figure 5. Images illustrating line spacing issues. A survey flown with 50 m lines spacing shown in (a) was reprocessed for line spacing of 150 m (b) and 250 m (c). The central 350 m wide target is resolved best with 50 to 150 m line spacings.

Products

Processing

There are 2 stages in processing Air-FTG™ data: “High Rate” and “Post-mission Processing”. During the High Rate stage, the accelerometer output is compensated for the effects of external forces. This initial stage uses Lockheed Martin proprietary software to correct for centripetal forces resulting from spinning of discs, to apply a self-gradient correction relating to aircraft motion and drainage of fuel, and to correct for accelerations acting on the instrument. At the end of the stage, the data are demodulated in preparation for input to the second stage. During demodulation, the data are re-sampled to 0.5 Hz (2 second intervals), and individual tensor components are extracted and transformed from an internal coordinate system to an external real-world coordinate system.

Post-mission Processing employs a combination of Bell Geospace proprietary and industry-standard techniques. The first is a “Line Correction” procedure that accounts for GGI drift and uses both differentially-

corrected GPS and inertial navigation data to correct for heading errors. Industry-standard techniques such as levelling and micro-levelling are then applied.

The final phase of Post-mission Processing is the application of a “Denoising” routine. This proprietary technique makes use of the properties of full tensor measurements to identify and remove residual noise in the data. A subsurface body with a density contrast will yield characteristic responses in each tensor component such as those shown in Figure 2. The Denoising routine works by identifying an anomaly in one of the components and then looking systematically for the corresponding response in each of the other components. It uses multiple lines and makes no assumptions about density and source geometry in its computations. If the expected response is not found, then the anomaly is considered to arise from noise and is eliminated from the dataset.

Topography represents the single largest density contrast encountered with airborne gravity gradient data. A detailed Digital Terrain Model is required to calculate terrain corrections that remove the effect of this interface prior to interpretation. Terrain corrections are routinely applied to Air-FTG™ data during the processing sequence.

The processing steps described here are continuously refined and upgraded and have lead to improvements in Air-FTG™ noise levels from 12-15 Eo to 5 Eo in the past 18 months.

Interpretation

Interpreting Air-FTG™ data is a challenge to the uninitiated! The volume of information often makes it difficult to find a starting point. However, it is useful to start with the Tzz component as this is the tensor component that best images the subsurface geology. The individual tensor components may then be used to help resolve particular attributes of the target, i.e., locating edges and assisting to estimate thickness and / or density contrast of specific geological features. As with many other geophysical data types, anomalies from different sources overlap, and the different anomalies must be separated before target signatures can be identified.

A number of techniques are routinely applied to interpret gradient data such as Fourier filtering (i.e., separating signals according to wavelength), lineament analysis (i.e., using the horizontal component data to identify geological structure and target boundaries), use of 3D display techniques to allow the interpreter to view the dataset from all angles thus aiding identification of targets, and 3D density modelling to investigate the geometry and density contrasts of geological features.

An enabling technology

Air-FTG™ is generally considered as an enabling technology. It can be used to advantage when identifying or screening targets, or when making a quick assessment of acreage at the early stages in an exploration program. It can also be used to ease land access issues by enabling surveying to be carried out in terrain that would be difficult to access on the ground due to cultural sensitivities, rugged topography, desert conditions or vegetation. This allows key areas for detailed follow up to be identified before direct ground access is required.

In summary, Air-FTG™ is a tool that can be used to enhance an exploration portfolio and reduce risk when making exploration decisions.

Summary

The following points summarise the key issues addressed in this paper:

- Air-FTG™ is a multiple accelerometer moving platform technology acquiring the full gravity gradient tensor;
- Full tensor measurements provide more information than partial tensor measurements, and this increases confidence when interpreting lateral density contrasts in the subsurface;
- The system currently achieves resolution of approximately 5 Eo when low-pass filtered to remove wavelengths less than 400 to 600 m;
- The preferred platform is currently a Cessna Grand Caravan, a single engine fixed wing aircraft;
- Surveys for smaller targets are flown in drape mode at 80 m terrain clearance;
- Line spacings from 50 to 2000 m can be used
    - i.e., both local and regional surveying techniques are possible;

- The processing sequence includes an innovative noise reduction routine that makes use of all five independent tensor components;
- Additional interpretation techniques are available for use with the multi-component output
  - Fourier filtering, 3D display techniques and 3D modelling; and
- Air-FTG™ is an enabling technology facilitating rapid decision-making and reducing risk in exploration programmes.

Acknowledgements

Etruscan Resources Inc. are greatly thanked for releasing the ground gravity data and for granting permission to publish the Air-FTG™ data in the comparison analysis. Bell Geospace are acknowledged for granting permission to publish examples of airborne data and their constructive review of this paper at all stages. Richard Lane of Geoscience Australia is also thanked greatly for his critical review and in making this a better paper.

References

Blakely, R.J., 1995, Potential Theory in Gravity and Magnetic Applications: Cambridge University Press.

Brett, J., 2000, Theory of FTG measurements: www.bellgeo.com/

Brzezowski, S.J. and Heller, W.G., 1988, Gravity gradiometer survey errors: Geophysics, 53, 1355-1361.

Hammond, S. and Murphy, C.A., 2003, Air-FTG™: Bell Geospace's gravity gradiometer – a description and case study: ASEG Preview, 105, 24-26.

Jekeli, C., 1993, A review of gravity gradiometer survey system data analyses: Geophysics, 58, 508-514.

Li, X., 2001, Vertical resolution: gravity versus vertical gravity gradient: The Leading Edge, 20, 901-904.

Schmidt, P.W. and Clark, D.A, 2000, Advantages of measuring the magnetic gradient tensor: ASEG Preview, April 2000, 26-30.

The FALCON® airborne gravity gradiometer survey systems

Mark H. Dransfield
BHP Billiton
Mark.H.Dransfield@bhpbilliton.com

James B. Lee
BHP Billiton
Jim.B.Lee@bhpbilliton.com

Introduction

It is almost five years since BHP Billiton performed the first airborne gravity gradiometer (AGG) survey over a mining province: the FALCON® AGG system survey of the Bathurst Camp, New Brunswick (Dransfield et al., 2001).

Since that survey, three FALCON® AGG systems have been introduced into operational use; “Einstein” in October 1999, “Newton” in April 2000 and “Galileo” in June 2002. These systems acquire airborne gravity data with the sensitivity and spatial resolution necessary for minerals exploration (Christensen et al., 2001; Mahanta et al., 2001; Liu et al., 2001), and by doing so have raised the interest of the geophysics community in airborne gravity.

The systems are operated by Sander Geophysics (Newton and Einstein) and by Fugro Airborne Surveys, Perth (Galileo).

The FALCON® AGG systems are based on gravity gradient instrument (GGI) and inertial platforms developed by Bell Aerospace (now Lockheed Martin). However the design used in the FALCON® systems is unique. This design was determined on the basis of extensive feasibility studies to optimise performance for the airborne application.

In 2003, Bell Geospace began operations with another airborne gravity gradiometer system, the FTG (full tensor gradiometer) system. The FTG system has the original Bell Aerospace design used in US Navy submarines, and which was used in early feasibility studies. Its introduction to airborne operation has broadened the options for acquisition of airborne gravity gradient data and raised questions of the comparative performance of FALCON® and FTG systems.

In almost five years of operations with the FALCON® systems, we have continued to make incremental improvements in system performance, reliability and productivity. The basic and operational parameters of the FALCON® systems will be discussed below, including discussion of factors which limit their performance.

Instrumentation

The FALCON® AGG technology has been described previously (Lee, 2001). The key technology is a GGI sensor mounted in an inertial platform. The GGI uses a set of four low-noise inertial-grade accelerometers (called an accelerometer complement) mounted orthogonally on a rotating block. The summed output of these accelerometers provides the gravity gradient signal. The precision of matching the sensitivity of these accelerometers is critical to achieving satisfactory rejection of the common mode accelerations, and is maintained by active compensation feedback circuits. The inertial platform reduces angular rotations to which the GGI is inherently sensitive in addition to maintaining the orientation of the GGI.

Significant differences of the FALCON® design from the original GGI design used in US Navy and USAF programs are an increase in the spacing of the accelerometers by a factor of approximately two, the inclusion of a second independent accelerometer complement on the GGI rotor, and the almost vertical alignment of the rotor axis. In these respects it is closer in design to the Lockheed Martin 4-D system (DiFrancesco and Talwani, 2002).

The AGG monitors the dynamic environment of the GGI (principally accelerations and rotations) and uses this information in post-processing compensation to remove any noise contributions, which can be modelled from this information. These models include residual sensitivity, and non-linearity of sensitivity, to acceleration and rotation, and corrections for the gravity self-gradient of the AGG and the aircraft (Lee, 2001).

Each FALCON® system includes a laser scanner (Riegl LMS-Q140i-80) for measurement of the terrain below the aircraft. Range measurements from this scanner are used to construct a digital elevation model (DEM) of the terrain and from this the topographic contribution to the gravity gradient is calculated for

correction of the measured gradients (Stone and Simsky, 2001). GPS is an integral part of the FALCON® survey systems for generation of the DEM, positioning of the gravity gradient (and other measurements) and for time synchronisation between the various data streams.

Other instrumentation supporting and complementing the gravity gradiometer includes a stinger mounted caesium-vapour magnetometer, and optional scintillation spectrometer. There is also a capability for vector magnetometry (Christensen and Dransfield, 2002; Dransfield et al., 2003).

Survey Operations

Survey operation with the FALCON® AGG systems is only slightly more involved than other airborne geophysics surveys such as magnetometry. The principal differences are the need to keep the systems continuously powered to maintain the necessary high degree of thermal control of the GGI, and the need to re-acquire the state of the navigation algorithm for the inertial platform on a daily basis prior to flight. The temperature of the FALCON® system in the aircraft cabin is maintained whilst on the ground, requiring a ground support heating or cooling system.

Survey parameters

In general the parameters for FALCON® surveys are dictated by operational safety, rather than any requirement of the survey instrumentation. Cessna Grand Caravan aircraft were selected, in preference (at the time) to de Havilland Twin Otter aircraft after a risk analysis indicated that the apparent safety advantage of a twin-engine aircraft is not valid for low level survey flight. It was essential that the aircraft have an engine with superlative reliability.

Other measures taken to improve safety of the air crew include the use of full-face cover helmets for protection in case of direct bird strike, continuous tracking of the aircraft location from the base of survey operations (“flight-following”) and carriage of appropriate survival equipment.

A principal safety issue is always the selection of the nominal clearance for the flight. Clearance as low as 80 m has been possible in terrain with low relief and vegetation (i.e., Canadian arctic) while a clearance of 120 m is usually possible. A drape surface is pre-planned by our survey contractor for each survey, based on the climb and descent rates the aircraft can achieve, but inevitably leading to a greater clearance in some parts of the survey.

We set a minimum line length of 10 km, and a minimum 4 km survey width. While these could be reduced, any survey for which this was necessary would be unrealistically small. There is no restriction on line spacing, however most surveys have a line spacing of between 100 m and 400 m depending on target size. Although the directly measured horizontal curvature components of the gravity gradient, G_{NE} and G_{UV}, where the subscripts refer to a north, east, and down right-handed coordinate system and G_{UV} is equal to $(G_{NN}-G_{EE})/2$, are unaffected by line spacing, the transformation to vertical gravity (g_D) and its vertical gradient (G_{DD}) does impose requirements on sampling. In practice, we find that we can recover good quality g_D and G_{DD} data from surveys at line spacings of up to 1 km but that the quality deteriorates for greater line spacings. Control lines perpendicular to the survey line direction, are usually flown at 2 – 5 km spacing. There is a short lead-in required before the start of each line, but this is provided by the end-of-line turn manoeuvre without loss of survey efficiency.

In the normal survey configuration (i.e., no radiometrics), the aircraft flight endurance can be up to 6 hours. This does reduce at higher temperatures and altitudes, and can also be reduced by runway length and surface. Time available for surveying is reduced by ferry time, end of line manoeuvres, and a short calibration procedure carried out on some flights prior to the first survey line. We have achieved over 1000 line-km in a single flight, but the average is usually around 500 line-km. Average production rate is approximately 3000 line-km per week, with 7500 line-km having been achieved under optimal conditions when two flights per day were possible.

The gravity gradient noise is, to an extent, dependent on the turbulence experienced, as there is some residual un-modelled sensitivity to the acceleration environment. For this reason we set a threshold limit on the turbulence experienced during the survey. This is monitored continuously during the survey flight and the flight is curtailed if the threshold is reached. Take-off time is varied in many locations to take advantage of the variation in turbulence through the day. Often this means take-off at sunrise, but in some areas it is late in the day that gives the smoothest flying conditions.

Pre-flight procedures are largely automated and include the required navigation update, plus calibration and noise measurements for verification of gravity gradiometer performance. Flight procedures for operation of

the AGG are likewise automated to ensure reliable system operation, and the system output is monitored for anomalies throughout the survey. Automation has improved system reliability very considerably, by eliminating scope for incorrect instrument setting interfering with system performance, and ensuring that pre-checks of important parameters are made. In-flight automation extends to first pass processing of the gravity gradient and laser scanner data to produce a reduced data set suitable for further processing to the final gravity gradient products.

Data processing

Survey data is assessed in the field after each flight against quality criteria. These criteria include the estimated noise level of the gravity gradient and magnetometer data, positional accuracy of the GPS data, navigation performance of the inertial platform, and completeness of laser scanner terrain data. Both raw and post-compensation gravity gradient noise is assessed. Failure on any criterion will require a re-flight of affected lines.

Data are also processed in the field to the stage of compensated line gradient data. A standard set of compensations is applied for the residual sensitivities of the GGI. These data are exported to a database and transferred electronically to the Falcon Operations centre in Melbourne for final processing. In some cases, final processing may be done in the field. Final processing involves more sophisticated compensation, terrain correction and transformation to g_D (vertical gravity) and G_{DD} (vertical gravity gradient) data.

Boggs and Dransfield (2003) report on the long wavelengths in transformed g_D data. The transformation to g_D and G_{DD} is performed by integration techniques (both in the spatial and wave-number domains) and by equivalent source techniques. Each method differs in boundary conditions and in approach to provide numerical stability. We improve our confidence in results by comparing them across all methods. We find the largest differences occur at the longest wavelengths.

As indicated by Boggs and Dransfield (2003), a gravity gradiometer has a limited ability to recover the gravity field at wavelengths larger than the smallest dimension of the survey area. They go on to demonstrate a typical error in g_D of 0.1 mGal/√km for wavelengths less than this dimension and describe a method for merging Falcon® system data with surface gravity data to provide a product with complete long wavelength information.

A reporting schedule and delivered data formats are agreed with the customer for each survey. Typically, final reports are delivered within 3 months of completion of the survey.

Commercial Availability

The FALCON® AGG system is restricted in its use by the US State Department. It may only be used in countries approved in the applicable export license approvals. The list of approved countries does change, as countries are added through an amendment process, and countries can be removed by the US State Department at any time. To date FALCON® AGG surveys have been carried out in Australia, Botswana, Canada, Chile, Mexico, Papua New Guinea, Peru, South Africa, USA, and Zambia. Currently, the Newton system is in North America, and services North and South America, Einstein is in southern Africa, and Galileo is being mobilised from Australia to join Einstein in southern Africa.

Further restrictions apply under the export license. There are strict limits on access to unprocessed data and to detailed information concerning the instrumentation and its performance.

BHP Billiton makes the FALCON® technology available to the mineral exploration community through its partnership program. In general this is through alliances, joint ventures and participation opportunities, rather than a fee-for-service basis. BHP Billiton will fly on a fee-for-service basis for mineral commodities that it regards as not being of strategic interest and for oil and gas. This policy maximises system utilisation, helping to defray fixed costs.

Performance

The performance of the FALCON® systems is assessed in a variety of ways.

Measurements of the total signal level (called “quiescent noise”) whilst the aircraft is stationary before survey flying serve as an indicator that the system is functioning normally. These measurements are automatically performed before every flight. At high altitude, there is an insignificant amount of gravity data in the short wavelength part of the total signal. At the start of each survey, a high altitude line is flown and the short

wavelength signal band (called “raw noise”) is recorded and used to check that the compensation feedback systems of the AGG are properly adjusted.

Post-flight, we apply compensations and then examine each survey line separately to check for residual noise. As the survey lines usually contain significant signal (from topography and self gradients, if not from geology), it is necessary to account for this signal in making a valid noise estimate. We are fortunate to have essentially two instruments in one, so that the signal component can be separated, and un-correlated noise estimated, by differencing the two horizontal curvature gradient signals. Comparison of this noise estimate with high altitude raw noise shows that more than 80% of the noise is un-correlated so that this difference provides a good estimate of noise.

Difference noise is our prime measure of AGG data quality.

The difference noise is calculated as the standard deviation of half the difference and presented as an RMS error over a DC to 0.18 Hz bandwidth. At survey speed, 0.18 Hz corresponds to about 300 m. The noise level varies with turbulence, which we calculate as the RMS vertical acceleration in the frequency band 0.3 to 10 Hz. Typical difference noise in the horizontal curvature gradients is between 4 and 7 Eö as turbulence increases to 1 m/s^2. Occasionally we obtain noise down below 3.5 Eö. Lines with a difference noise above 7 Eö are re-flown. Expressed as a noise density, the typical difference noise is 13 Eö/√Hz.

A further assessment can be made after generation of the final product g_D and G_{DD} data.

Separate processing of the two complements of data to yield a difference noise estimate in g_D and G_{DD} is only done on occasional surveys. A typical recent survey had a difference noise in g_D of 0.3 mGal and in G_{DD} of 6 Eö (the horizontal curvature difference noise on this survey was 4.4 Eö). The bandwidth is difficult to estimate due to the complexities of the processing but was about 0.18 Hz for this survey. This puts the noise density for G_{DD} at 17 Eö/√Hz. The g_D difference noise is not white so that a noise density is misleading.

We have done several studies using the difference between ground gravimeter survey data and Falcon data. Typically, we find G_{DD} error predicted from these comparisons to be in the range 20 to 28 Eö/√Hz (corresponding to 8 to 12 Eö RMS in a 0.18 Hz bandwidth). The g_D predicted error from these studies is found to increase from about 0.15 mGal at 500 m wavelength to 0.5 mGal at 10 km wavelength. Boggs and Dransfield (2003) demonstrate a typical error in g_D of 0.1 mGal/√km for wavelengths less than the smallest survey dimension. These results are higher than the difference noise estimates but often there are clear shortcomings in the quality of the ground gravity data used in the comparison so that these results represent an upper limit on FALCON® noise.

We are not in a position to make a direct comparison of the performance of the FALCON® systems with that of the Bell Geospace FTG systems, as we do not have access to data from the latter system. The paper by Hinks et al. at this workshop is expected to provide a direct comparison (Hinks et al., 2004). While there are known differences in the gradiometer designs, which we believe provide the FALCON® systems with a significant performance advantage, this cannot be quantified without knowing the performance of the FTG systems. We also believe that the performance as measured by the accuracy of the product gradient maps is dependent on the performance of the algorithms used for transformation of the measured gradients. BHP Billiton has invested a significant effort in development of the algorithms we use, and make use of redundancy in this process to improve our understanding of the reliability of the results.

We regard our ability to make an accurate topographic correction, based on reliable and accurate terrain data that is collected concurrent with the gradiometer data, to be one factor, which improves our ability to deliver accurate results.

The FTG systems do measure additional components of the gravity gradient tensor, and this has been claimed as an advantage. Undoubtedly there is additional information available from the three additional components of the tensor that the FTG systems measure. For a single (stationary) measurement this information resolves some of the ambiguities in source location, remembering that as a potential field measurement, some ambiguity will always remain. However these ambiguities are also resolved by measurements at different locations, so that any practical survey flown to cover a contiguous survey area, will also serve to achieve the same outcome. Our success in providing reliable g_D and G_{DD} maps from the FALCON® system surveys is confirmation of this. On client request, we also deliver full tensor data calculated in the same way as the G_{DD} data i.e., by transformation from the measured horizontal curvature data.

Beyond resolution of ambiguities, the additional gradient component measurements can be expected to contribute an improvement in noise performance, in the same way that the second accelerometer complement of the FALCON® instrument makes a contribution.

References

Boggs, D.B., and Dransfield, M.H., 2003, Analysis of errors in gravity derived from the FALCON Airborne Gravity Gradiometer: Submitted for inclusion in M. Talwani and E. Biegert (eds), Gravity Gradiometry – Instrumentation, Processing and Case Studies, Society of Exploration Geophysicists. (Reproduced as a paper in this volume).

Christensen, A. N., Mahanta, A. M., Boggs, D. H. and Dransfield, M. H., 2001, FALCON gravity gradiometer survey results over the Cannington Ag-Pb-Zn deposit: Extended Abstract, ASEG 15th Geophysical Conference and Exhibition, August 2001, Brisbane.

Christensen, A. and Dransfield, M., 2002, Airborne vector magnetometry over banded iron-formations: 72nd Ann. Internat. Mtg: Soc. of Expl. Geophys., 13-16.

DiFrancesco, D. and Talwani, M., 2002, Time-lapse gravity gradiometry for reservoir monitoring, 72nd Ann. Internat. Mtg: Soc. of Expl. Geophys., 787-790.

Dransfield, M. H., Christensen, A. N., Diorio, P. P., Rose, M. M. and Stone, P. M., 2001, FALCON test results from the Bathurst Mining camp: Exploration Geophysics, 32, 243-246.

Dransfield, M. H., Christensen, A. N. and Liu, G., 2003, Airborne vector magnetics mapping of remanently magnetised banded iron-formations at Rocklea, Western Australia: Exploration Geophysics, 34, 93-96.

Hinks, D., McIntosh, S., and Lane, R., 2004, A comparison of the Falcon® and Air-FTG™ airborne gravity gradiometer systems at the Kokong Test Block, Botswana: This volume.

Lee, J. B., 2001, FALCON gravity gradiometer technology: Exploration Geophysics, 32, 247-250.

Liu, G., Diorio, P. A., Stone, P. M., Lockhart, G., Christensen, A. N., Fitton, N. C. and Dransfield, M. H., 2001, Detecting kimberlite pipes at Ekati with airborne gravity gradiometry: Extended Abstract, ASEG 15th Geophysical Conference and Exhibition, August 2001, Brisbane.

Mahanta, A. M., Boggs, D. B., Dransfield, M. H., Whittal, M., Liu, G. and Scott, R. L., 2001, King George: Measured and modelled AGG response over an IOCG terrain: Extended Abstract, ASEG 15th Geophysical Conference and Exhibition, August 2001, Brisbane.

Stone, P.M. and Simsky, A., 2001, Constructing high resolution DEMs from Airborne Laser Scanner Data: Extended Abstract, ASEG 15th Geophysical Conference and Exhibition, August 2001, Brisbane.

A superconducting gravity gradiometer tool for exploration

J. M. Lumley, J. P. White and G. Barnes
Oxford Instruments Superconductivity Ltd

D Huang
ARK Geophysics Limited

H. J. Paik
University of Maryland

Summary

Superconducting gravity gradiometry with no moving parts has long been recognised as a technique offering key advantages over competitive techniques with respect to obtaining gravity or gravity gradient data. Superconductivity and low temperatures confer low noise, negligible scale factor drift and mechanical stability. Additionally, a Superconducting Gravity Gradiometer (SGG) incorporates superconducting circuits which can be balanced such that its responses to gravity gradients are largely independent of all linear and angular accelerations applied to the instrument. This "balance" relies on the ability to set and maintain persistent currents in the various superconducting loops. What makes the SGG so attractive an instrument for both satellite and airborne operation is the complete absence of drift in these currents once they have been set. This means that the scale factors remain perfectly stable in time and can thus be balanced precisely, with excellent null stability.

The European Space Agency (ESA) recognised these advantages of the SGG and have continually supported the development of a satellite version of an SGG with Oxford Instruments. We shall report both numerical analysis and experimental results of our work on the ESA SGG. We shall also report on the design and analysis of the SGG we are proposing as an exploration tool. Our analysis indicates that it will be possible to build and operate an SGG in an airborne environment to achieve the accuracy required. This device will measure all linear and angular accelerations to which the SGG is subjected, as is the case for our spaceborne SGG. These outputs are to be used to correct the measured gravity gradient data. When used in conjunction with accurate GPS data, the acceleration outputs will be useful in their own right to directly measure the long-wavelength components of the gravity field over the region of interest.

1. Introduction

The principle that gravity gradiometry is potentially extremely useful for exploration has been established since the beginning of the 20th century when von Eotvos developed the first practical instrument (Domenico, 1994). Although his torsion balance instrument was extremely sensitive, it was very slow, so the technique was largely abandoned even though it contributed to finding billions of barrels of oil. It is clear that an airborne gravity gradiometer with similar sensitivity to the original von Eotvos tool would be extremely powerful for exploration purposes.

This paper describes the superconducting gravity gradiometer tool proposed for airborne operation. First the paper summarises some basic gravity theory followed by a brief resume of the theory of 2-D Fourier transformations. The errors present in any measurement of gravity gradient are then discussed, which include alignment and scale factor errors inherent in any in-line gravity gradiometer and tilt and centrifugal acceleration errors. Sections 6-12 then discuss the Exploration Superconducting Gravity Gradiometer tool (SGG) proposed for airborne surveys - its basic principles, its alignment circuitry, its intrinsic noise, its mathematical analysis and its basic design.

2. Theory – gravity and gravity gradiometry

The gravity field from an extended body is most easily understood in terms of its gravity scalar potential $\Phi(r)$ at r,

$$\Phi(r) = G\int \frac{\rho(r')}{|r'-r|} d^3r' \qquad (2.1)$$

where $\rho(r')$ is the density of material at position r' and $G = 6.668\times10^{-11} Nm^2kg^{-2}$ is the gravitational constant. Gravity and gravity gradients are easily calculated from the scalar potential and in Cartesian coordinates

$$g(r) = \nabla\Phi(r) = \frac{\partial\Phi}{\partial x}\hat{i} + \frac{\partial\Phi}{\partial y}\hat{j} + \frac{\partial\Phi}{\partial z}\hat{k} \qquad (2.2)$$

Gravity gradient is used to describe how a particular component of gravity varies with position, e.g.,

$$g_x(r+\delta r) = g_x(r) + \frac{\partial^2\Phi}{\partial x^2}\delta x + \frac{\partial^2\Phi}{\partial y\,\partial x}\delta y + \frac{\partial^2\Phi}{\partial z\,\partial x}\delta z \qquad (2.3)$$
$$= g_x(r) + \Gamma_{xx}\delta x + \Gamma_{xy}\delta y + \Gamma_{xz}\delta z$$

The gravity gradient tensor, Γ, is as follows

$$\Gamma = \begin{vmatrix} \Gamma_{xx} & \Gamma_{xy} & \Gamma_{xz} \\ \Gamma_{yx} & \Gamma_{yy} & \Gamma_{yz} \\ \Gamma_{zx} & \Gamma_{zy} & \Gamma_{zz} \end{vmatrix} = \begin{vmatrix} \frac{\partial^2\Phi}{\partial x^2} & \frac{\partial^2\Phi}{\partial y\,\partial x} & \frac{\partial^2\Phi}{\partial z\,\partial x} \\ \frac{\partial^2\Phi}{\partial x\,\partial y} & \frac{\partial^2\Phi}{\partial y^2} & \frac{\partial^2\Phi}{\partial z\,\partial y} \\ \frac{\partial^2\Phi}{\partial x\,\partial z} & \frac{\partial^2\Phi}{\partial y\,\partial z} & \frac{\partial^2\Phi}{\partial z^2} \end{vmatrix} \qquad (2.4)$$

It is a symmetric tensor, since the order of differentiation of a scalar quantity is irrelevant and, because gravity is a central force obeying Laplace's equation in free space, the sum of the diagonal components is zero for an inertial frame of reference. Thus there are only five independent components of the gravity gradient tensor.

For a spherical body of mass M whose density is a function of radius only, along the radial direction, in spherical polar coordinates,

$$\Phi(r) = \frac{GM}{r},\ g_r = -\frac{GM}{r^2},\ \Gamma_{rr} = \frac{2GM}{r^3} \qquad (2.5)$$

where r refers to distance from centre of object. Other components can easily be calculated and other co-ordinate systems can be used; the main point to note here is that gravity gradient has a more rapid variation with position than does gravity so it falls away quicker from its maximum value near a mass anomaly. This ultimately translates to gravity gradient providing better estimation of edge location than does gravity.

3. Theory – Fourier transforms and gravity surveys

The gravitational scalar potential is the primary quantity and, once determined, all gravitational quantities follow. Below it is shown how, using 2-D Fourier transformations, it is possible to deduce the scalar potential at all positions outside the surface of the earth by measuring any derivative of the scalar potential over a large surface above the earth. Once this is done, all quantities can be forward calculated and this removes the difficulty of not being able to transform gravity gradients between frames of reference if all components are not known. In the following, all quantities are deduced/measured over an $x-y$ plane at height z_0.

The 2-D Fourier transform of the scalar potential $\Phi(x, y, z_0)$ is

$$\Im_{k_x,k_y}(\Phi) = \int_{-\infty}^{\infty}\int_{-\infty}^{\infty}\Phi(x,y,z_0)e^{-ik_x x}e^{-ik_y y}dxdy \qquad (3.1)$$

The inverse transform of (3.1) recovers the scalar potential

$$\Phi(x,y,z_0) = \int_{-\infty}^{\infty}\int_{-\infty}^{\infty}\Im_{k_x,k_y}(\Phi)e^{ik_x x}e^{ik_y y}dk_x dk_y \qquad (3.2)$$

Thus, once the Fourier transform of the scalar potential is known over this plane, the scalar potential can be deduced.

Next consider the Fourier transformation of $g_x = \frac{\partial\Phi}{\partial x}$

$$\Im_{k_x,k_y}\left(\frac{\partial\Phi}{\partial x}\right) = \int_{-\infty}^{\infty}\int_{-\infty}^{\infty}\frac{\partial\Phi(x,y,z_0)}{\partial x}e^{-ik_x x}e^{-ik_y y}dxdy \qquad (3.3)$$

Fourier transform manipulations or integration by parts yields

$$\Im_{k_x,k_y}\left(\frac{\partial\Phi}{\partial x}\right)=ik_x\int_{-\infty}^{\infty}\int_{-\infty}^{\infty}\Phi\left(x,y,z_0\right)e^{-ik_x x}e^{-ik_y y}\,dxdy \qquad (3.4)$$

Inspection of (3.4) and (3.1) reveals

$$\Im_{k_x,k_y}\left(\frac{\partial\Phi}{\partial x}\right)=ik_x\Im_{k_x,k_y}\left(\Phi\right) \qquad (3.5)$$

Thus a particular component of the Fourier transform of the gravity field is simply related to the same component of the Fourier transform of the scalar potential. Once this is known, it is then straightforward to invert this transformation to recover the scalar potential as follows.

$$\begin{aligned}\Phi\left(x,y,z_0\right)&=\Im_{x,y}^{-1}\left[\frac{1}{ik_x}\Im_{k_x,k_y}\left(\frac{\partial\Phi}{\partial x}\right)\right]\\&=\int_{-\infty}^{\infty}\int_{-\infty}^{\infty}\frac{1}{ik_x}\Im_{k_x,k_y}\left(\frac{\partial\Phi}{\partial x}\right)e^{ik_x x}e^{ik_y y}\,dk_x dk_y\end{aligned} \qquad (3.6)$$

The interpretation of (3.6) is that it is possible to deduce the scalar potential over a particular surface from a measurement of one of the horizontal components of gravity over the surface.

Next consider $\Gamma_{xy}=\frac{\partial}{\partial y}\frac{\partial\Phi}{\partial x}$ whose Fourier transform is

$$\Im_{k_x,k_y}\left(\frac{\partial^2\Phi}{\partial y\,\partial x}\right)=\int_{-\infty}^{\infty}\int_{-\infty}^{\infty}\frac{\partial^2\Phi\left(x,y,z_0\right)}{\partial y\partial x}e^{-ik_x x}e^{-ik_y y}\,dxdy \qquad (3.7)$$

As above, manipulation yields

$$\begin{aligned}\Im_{k_x,k_y}\left(\frac{\partial^2\Phi}{\partial y\,\partial x}\right)&=\left(i\right)^2k_xk_y\int_{-\infty}^{\infty}\int_{-\infty}^{\infty}\Phi\left(x,y,z_0\right)e^{-ik_x x}e^{-ik_y y}\,dxdy\\&=-k_xk_y\Im_{k_x,k_y}\left(\Phi\right)\end{aligned} \qquad (3.8)$$

The scalar potential can be derived by inversion as before

$$\begin{aligned}\Phi\left(x,y,z_0\right)&=\Im_{x,y}^{-1}\left[-\frac{1}{k_xk_y}\Im_{k_x,k_y}\left(\frac{\partial}{\partial y}\frac{\partial\Phi}{\partial x}\right)\right]\\&=\int_{-\infty}^{\infty}\int_{-\infty}^{\infty}\frac{-1}{k_xk_y}\Im_{k_x,k_y}\left(\frac{\partial}{\partial y}\frac{\partial\Phi}{\partial x}\right)e^{ik_x x}e^{ik_y y}\,dk_x dk_y\end{aligned} \qquad (3.9)$$

These deceptively simple relations, (3.6) and (3.9), indicate that, if any of $g_x, g_y, \Gamma_{xx}, \Gamma_{xy}, \Gamma_{yy}$ is measured over a plane, the scalar potential can be deduced over that plane and hence all its derivatives with respect to *x* and *y* can be forward calculated.

The treatment can be continued for any *x,y* derivative of the scalar potential and in general, (3.5) and (3.8) become

$$\Im_{k_x,k_y}\left(\frac{\partial^n}{\partial y^n}\frac{\partial^m\Phi}{\partial x^m}\right)=\left(ik_x\right)^m\left(ik_y\right)^n\Im_{k_x,k_y}\left(\Phi\right) \qquad (3.10)$$

Thus, any of the *x,y* derivatives on the survey plane can be used to calculate $\Phi\left(x,y,z_0\right)$. Of course, once the scalar potential is known over the z_0 plane, any of its spatial derivatives can be forward calculated directly.

In order to use any of the *z* derivatives of the scalar potential, further analysis is needed. In the case of gravity gradients, the Fourier transform of Laplace's equation requires

$$\Im(\Gamma_{xx}) + \Im(\Gamma_{yy}) + \Im(\Gamma_{zz}) = 0 \qquad (3.11)$$

which, following similar treatment to that above yields

$$\begin{aligned}\Phi(x,y,z_0) &= \Im^{-1}_{x,y}\left[\frac{1}{k_x^{\,2}+k_y^{\,2}}\Im_{k_x,k_y}\left(\frac{\partial^2\Phi}{\partial z^2}\right)\right] \\ &= \Im^{-1}_{x,y}\left[\frac{1}{|k|^2}\Im_{k_x,k_y}(\Gamma_{zz})\right]\end{aligned} \qquad (3.12)$$

The other z derivatives are a little more difficult to deduce and the treatment is beyond the scope of this paper (Bracewell, 1986). However, the final result is similar to (3.10), viz.

$$\Im_{k_x,k_y}\left(\frac{\partial^1\Phi(x,y,z_0)}{\partial z^1}\right) = (-|k|)^1\,\Im_{k_x,k_y}(\Phi(x,y,z_0)) \qquad (3.13)$$

The completely general expression combines (3.10) & (3.13)

$$\Im_{k_x,k_y}\left(\frac{\partial^m}{\partial x^m}\frac{\partial^n}{\partial y^n}\frac{\partial^1}{\partial z^1}\Phi\right) = (ik_x)^m(ik_y)^n(-|k|)^1\,\Im_{k_x,k_y}(\Phi) \qquad (3.14)$$

Thus, any derivative of the scalar potential can be measured over the z_0 plane and its 2-D Fourier transform is simply related to the Fourier transform of the scalar potential. By inverse transformation the scalar potential can be deduced.

$$\frac{\partial^m}{\partial x^m}\frac{\partial^n}{\partial y^n}\frac{\partial^1}{\partial z^1}\Phi = \Im^{-1}_{x,y}\left[(ik_x)^m(ik_y)^n(-|k|)^1\,\Im_{k_x,k_y}(\Phi)\right] \qquad (3.15)$$

That is, all derivatives of the scalar potential on the x,y,z_0 plane can be obtained from the Fourier transformation of the scalar potential or of any of its derivatives.

With this, it is clearly possible to deduce the scalar potential at any point outside the surface of the earth (where Laplace's equation is valid) by a Taylor series expansion. This is called upward continuation. There is indeed a Green's identity which highlights this directly (Blakely, 1995).

$$\Phi(r) = \frac{1}{4\pi}\int_{S_0}\left(\frac{1}{|r-r'|}\frac{\partial\Phi}{\partial n} - \Phi\frac{\partial}{\partial n}\frac{1}{|r-r'|}\right)dS' \qquad (3.16)$$

where *S'* is the surface on which the scalar potential and its derivative with respect to the outward normal is known.

In the following sections, gravity gradiometers are described in general terms and the proposed exploration SGG is described in detail. For a fuller treatment of the issues relating to the SGG the reader is referred to Chan and Paik (1987).

4. In-line gravity gradiometer, basic theory, errors

The general schematic for an in-line gravity gradiometer is shown in Figure 1 where the two proof masses, m_1, m_2 have sensitive axes for detection $\hat{n}_1, \hat{n}_2$. The displacement of the proof mass centres of gravity is represented by $\ell, \hat{\ell}, |\ell|$ which are the vector, the unit vector and the base line of the instrument.

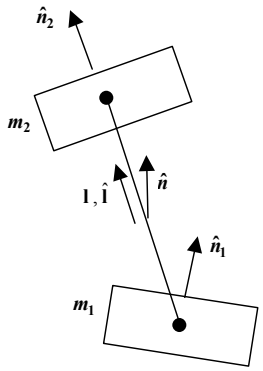

Figure 1. Schematic of in-line gravity gradiometer.

In general, such a gravity gradiometer measures Γ_{xx} as

$$\Gamma_{xx} = \frac{1}{\mathbf{l}}\left(\sigma_2 f_2 . \hat{n}_2 - \sigma_1 f_1 . \hat{n}_1\right) \qquad (4.1)$$

where $f_1, f_2, \sigma_1, \sigma_2$ represent the specific force at and the scale factors of each accelerometer. The specific force is

$$f = g_{dc} + g(t) + a_{dc} + a(t) = f_{dc} + f(t) \qquad (4.2)$$

In order to discuss alignment and scale factor errors in the system the following notation is used.

$$\begin{aligned} \hat{n} &= \tfrac{1}{2}\left(\hat{n}_1 + \hat{n}_2\right) \\ \delta\hat{n} &= \hat{n}_2 - \hat{n}_1 \perp \hat{n}, \hat{\mathbf{l}} \\ \delta\hat{\mathbf{l}} &= \hat{\mathbf{l}} - \hat{n} \perp \hat{n}, \hat{\mathbf{l}} \\ \delta\sigma &= \sigma_2 - \sigma_1 \end{aligned} \qquad (4.3)$$

For the pair of accelerometers, these represent the average orientation of their sensitive axes, the non parallelism of their sensitive axes, the offset in their centres of gravity and the difference in their scale factors. In general, these will all be time dependent.

In the event that the gravity gradiometer is placed in an environment where there is zero gravity gradient, i.e., $g_1 = g_2$, the apparent gravity gradient "measured" by the instrument is

$$\delta\Gamma_{xx} = \frac{\delta\sigma(t)}{\mathbf{l}} f . \hat{n} + \frac{1}{\mathbf{l}} \delta\hat{n} . f(t) + \left(\delta\hat{\mathbf{l}} \times \hat{n}\right) . \alpha(t) \qquad (4.4)$$

where $f, f(t), \alpha(t)$ are respectively, the average total acceleration (including platform motion), the time dependent part of the total acceleration, and the angular accelerations.

Inspection of (4.4) shows that the total acceleration vector in the direction of the sense axis (static plus platform) couples into the measured gravity gradient via scale factor errors (noise, drift and difference). Further, the linear and angular accelerations about orthogonal degrees of freedom couple in via the alignment errors. For a gravity gradiometer to work in a hostile airborne environment, these errors have to be either eliminated by design/setup or measured and removed in software, and usually a combination of both.

5. Centrifugal acceleration and tilt errors

The above treatment did not consider the non inertial nature of the measurement frame of reference of the gravity gradiometer. For an instrument moving with an instantaneous angular rate $\Omega(t)$ and total linear acceleration $a(t)$, both with respect to an inertial frame of reference, the equation of motion for each proof mass with respect to the platform is given by Chan and Paik, (1987) and Symon (1961).

$$\left.\frac{\partial^2 r}{\partial t^2}\right|^* = \nabla\Phi - \Omega\times(\Omega\times r) - 2\Omega\times\left.\frac{\partial r}{\partial t}\right|^* - \left.\frac{\partial\Omega}{\partial t}\right|^*\times r - a(t) \qquad (5.1)$$

where starred quantities are evaluated in the platform frame of reference. In order to obtain the desired derivative of the scalar potential, the correction terms are difficult to obtain with the desired accuracy. The best that can be obtained, including use of state of the art stabilised platform and GPS/INS systems to deduce platform accelerations, $a(t)$, is to deduce gravity to an accuracy ≈5mGal/Hz$^{1/2}$ (≈0.5 mGal over approximately 100 s period, i.e., approximately 5-10 km wavelength).

Gravity gradient in the platform frame of reference is obtained by differentiating (5.1) to yield

$$\Gamma_{ij}^{\ *} = \Gamma_{ij} - \left(\Omega_i\Omega_j - \Omega^2\delta_{ij}\right) + \sum_k \varepsilon_{ijk}\alpha_k(t) - 2\Omega_i\left(\delta\Omega_j\right) \qquad (5.2)$$

where Γ_{ij} is the true gravity gradient signal from the earth, $\alpha_k(t) = \dfrac{\partial\Omega_k^{\ *}}{\partial t}$ is the angular acceleration of the platform with respect to an inertial frame, $\delta\Omega_j$ is the relative angular acceleration between platform and SGG sensor and ε_{ijk} is the Levi-Civita symbol which is zero if any two indices are the same, 1 if order is $xyz\ (yzx, zxy)$ or –1 if order is $xzy\ (zyx, yxz)$.

Equation (5.2) indicates a number of important points. First, the last term is usually very small and can be deduced from knowledge of measured angular acceleration, this being obtained either from the stabilised platform or from the instrument itself, as discussed later in this paper. Second, the angular acceleration is usually much larger than any off diagonal gravity gradient term so $\Gamma_{ij}^{\ *}$ as measured is almost pure angular acceleration. Third, any diagonal component of gravity gradient, $\Gamma_{ii}^{\ *}$, does not explicitly contain an angular acceleration term. Finally, any single off diagonal component explicitly contains angular accelerations but these can be removed by adding $\Gamma_{ij}^{\ *}, \Gamma_{ji}^{\ *}$ to yield

$$\begin{aligned}\Gamma_{ij}(sym)^* &= \frac{1}{2}\left(\Gamma_{ij}^{\ *} + \Gamma_{ji}^{\ *}\right) \\ &= \Gamma_{ij} - \left(\Omega_i\Omega_j - \Omega^2\delta_{ij}\right) - \left(\Omega_i\delta\Omega_j + \Omega_j\delta\Omega_i\right)\end{aligned} \qquad (5.3)$$

By subtracting the two components rather than adding them, it is possible to measure the angular acceleration and remove any small corruption due to off diagonal gravity gradient

$$\begin{aligned}\Gamma_{ij}(asym)^* &= \frac{1}{2}\left(\Gamma_{ij}^{\ *} - \Gamma_{ji}^{\ *}\right) \\ &= \sum_k \varepsilon_{ijk}\alpha_k(t) - \left(\Omega_i\delta\Omega_j - \Omega_j\delta\Omega_i\right)\end{aligned} \qquad (5.4)$$

The full tensor gradiometer version of our proposed exploration tool performs such a measurement.

To correct for the terms shown in (5.3) the angular rate has to be measured, either by integration of the output of an angular acceleration superconducting circuit or by use of the GPS/INS system. In general it is also desirable to stabilise the platform since the biggest angular rate terms in (5.3) relate to the angular motions of the aircraft.

The other major angular error term is due to tilt of gradiometer from its nominally aligned axes. This gives rise to a measured gravity gradient in the “wrong” orientation. The true and measured gravity gradients are related via rotation matrices

$$\Gamma_{meas} = R\cdot\Gamma_{true}\cdot R^{-1} \qquad (5.5)$$

where R is the rotation matrix from what is believed to be the true frame to the actual measurement frame of reference. Again, the terms involved in this can be measured or estimated and used to correct the gravity gradient.

All the terms in this section will benefit from the use of a stabilised platform. Indeed, if the requirement is for the errors these terms introduce to be below system noise, then this sets stringent requirements on the stabilised platform and indeed upon the aircraft's own control and stabilisation scheme.

All other major errors relate to the operation of the gravity gradiometer, how it is set up, how it works and the cryogenic environment in which it needs to work.

There has been much debate over the relative merit of measuring gravity or gravity gradient. Section 3 on Fourier analysis proves that it does not matter which is chosen so the issue is always about the instrument which delivers the best signal to noise for the parameter to be measured. Because of the different spatial dependences of gravity and gravity gradient, a measure of gravity gradient will always be superior to one of gravity for short wavelength features or shallow objects. In fact, (2.5) gives a convenient way of looking at this because it shows that there will be a unique distance/depth at which a spherically symmetric source can give nominated values of gravity and gravity gradient.

By choosing 1 Eo as the target sensitivity for gravity gradient and 5 mGal as the target sensitivity of the best airborne gravity tool (both per root Hz), we find that the distance/depth, d_0 of such a source is given simply as

$$\frac{g_z}{\Gamma_{zz}} = \frac{GM}{{d_0}^2} \cdot \frac{{d_0}^3}{2GM} = \frac{d_0}{2} \qquad (5.6)$$

Simple substitution shows that the proposed SGG tool will always provide cleaner data than will a state of the art airborne gravity tool for sources with depths less than d_0 = 100 km.

6. The superconducting accelerometer - principles

The principles of the superconducting accelerometer and the SGG have already been established by Chan and Paik (1987) so only the most important concepts will be presented here.

The main superconducting features utilised in the SGG are the Meissner effect and flux quantisation, the latter giving the low Tc SGG its inherent phenomenal stability. The SGG requires magnetic flux in all superconducting loops to be absolutely stable and the ability to pass large currents (>10 A) through coils, wires and joints. Failure to be able to do this renders the SGG noisy at best or inoperable at worst. This is the reason for using low temperature superconductors and wires. High temperature superconductors are just not suited for this application as none of the required technologies are mature enough. In any event, the higher temperature of operation will make the system intrinsically noisier.

Low temperatures also confer mechanical stability of all construction materials used in the SGG. At 4.2 K the thermal expansion coefficient is reduced to approximately 10^{-9} of its room temperature value. Cryogenic environments are also extremely stable with 50 μK/Hz$^{1/2}$ being easily achieved. Analysis readily shows that thermal noise generates changes in the length of the gradiometer and this looks like a gravity gradient noise. However, for the low temperatures of operation and for the temperature stability proposed for the exploration SGG, this noise can be shown to be less than the intrinsic SGG noise.

The principle of the superconducting accelerometer is best described by first considering the inductance of a coil placed close to a superconductor. Meissner first demonstrated that a superconductor expels all magnetic field up to a material dependent critical field. If current is passed through a coil outside a superconductor, a superconducting surface current is generated which, at every point inside the superconductor, produces a field equal and opposite to that produced by the external coil. This surface current interacts with the current in the coil producing a repulsive force between the coil and the superconductor. For simple geometries, it is easy to show that both the field outside the superconductor and the force between the superconductor and coil are as if there is an image coil within the superconductor. This image coil is exactly the same distance behind the superconducting surface as the real coil is in front of it and this image coil carries exactly the same current but with opposite sign. This is illustrated in Figure 2 for a flat spiral "pancake" coil.

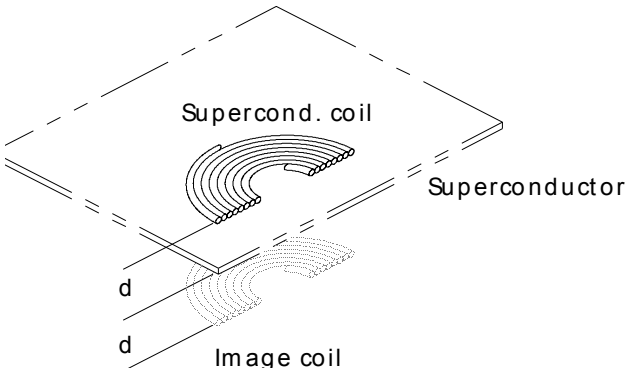

Figure 2. Superconducting "image" coil construction.

It is also straightforward to calculate the inductance of this image coil which is, in fact, the mutual inductance between the coil and the surface current or the coil and its image. Note first that, for a flat pancake coil in this geometry, the coil-image coil model proves that the magnetic field is confined to the region between the coil and the superconductor (note that there is no field in a superconductor). This field is simply

$$B = \mu_0 ni \qquad (6.1)$$

where $n =$ turns/m and i is the current in the coil. The total energy in this system is simply the field energy per unit volume times the volume between coil and superconductor.

$$E = \frac{B^2}{2\mu_0} Ax = \frac{1}{2}\mu_0 n^2 Axi^2 \qquad (6.2)$$

from which it is clear that the inductance of the coil is

$$L = \mu_0 n^2 Ax + O\left(x^2\right) \qquad (6.3)$$

This is the first crucial result and shows that, to first order, the inductance of the pancake coil is proportional to its separation from the superconductor. If the coil moves relative to the superconductor, its inductance will change. The first non-linear term is easily understood since the field will start falling off from its maximum value at a distance : x from the edges of the coil. Thus the effective coil area is reduced from its purely geometric value by an area proportional to the perimeter of the coil multiplied by its separation from the superconductor.

Above it was demonstrated that there is a repulsive force on a "proof mass" when a current is passed through a coil in its vicinity and this force is always present when the current flows. This force follows from the energy (6.3)

$$F = \frac{1}{2}\frac{\partial L}{\partial x} i^2 = \frac{1}{2}\mu_0 n^2 Ai^2 + O(x) \qquad (6.4)$$

The stiffness of this magnetic spring is determined by coil non-linearities. Note also that the sign of the current is irrelevant; it is its magnitude which determines the force.

The next step in understanding the SGG is to consider what happens when the pancake coil-proof mass system is placed within a closed superconducting loop as illustrated in Figure 3.

It is a truly remarkable property of superconductors that the magnetic flux in a superconducting loop, once set, is impossible to change. The flux "set" in the loop is that flux which was in the loop as the superconductor passed through its transition temperature. The "set" flux is absolutely stable and has no noise on it. This is the crucial issue for operation of the superconducting accelerometer. In reality this flux is

quantised but the unit, $\Phi_0 = 2.07 \times 10^{-15} Wb$, is so small that in practical terms it doesn't affect operation of the SGG – in operation, the SGG there contains; $10^{11}\Phi_0$ in many loops.

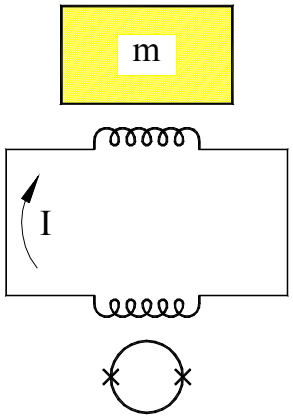

Figure 3. Superconducting accelerometer schematic.

Whenever the proof mass moves, in response to an acceleration or change in gravity, the coil inductance changes and the circulating current must change to preserve the original flux in the loop. This new current exerts a different force, given by (6.4) and the system stiffness is now dominated by this effect. The change in current is detected by a SQUID, a highly sensitive superconducting magnetic flux detector with resolution $\approx 3 \times 10^{-6} \Phi_0 / Hz^{1/2}$. The SQUID is a null detector and will only respond to changes in flux which are transformer coupled from the loop.

This is the superconducting accelerometer. From the simple description given above, it is immediately obvious how important it is that flux quantisation works and that the SQUID is a null detector of unparallelled sensitivity. When the flux transfer calculation is done properly, it transpires that the noise level of the SGG effectively detects flux/current changes of : 10^{-13} of their dc values.

7. The Superconducting Gravity Gradiometer

The schematic for a superconducting gravity gradiometer is shown in Figure 4 below where the SGG is assumed to be sensitive to gravity changes in the vertical direction. To understand the operation of the SGG requires understanding of the principles of the superconducting accelerometer with additional ingredients determined by the fact that there are two masses and two loops.

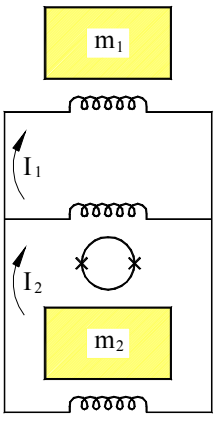

Figure 4. Superconducting accelerometer schematic.

First, consider that the SGG is subjected to a common gravity or acceleration such that both proof masses move the same distance in the same direction, assumed downwards. This causes the inductances of both pancake coils to decrease. Flux quantisation for each superconducting loop therefore requires both I_1, I_2 to increase. Since these two currents flow in opposite directions through the inductor coupling to the SQUID, the changes tend to cancel one another. The system is "balanced" when the changes cancel one another completely. The SQUID does not then see a common mode gravity signal.

Note that the current through the outer loop is the average of I_1, I_2 so, with both currents increasing, there is a measurable current change around this loop. This current can be measured by coupling to another SQUID loop using the additional transformer as indicated in Figure 5 below.

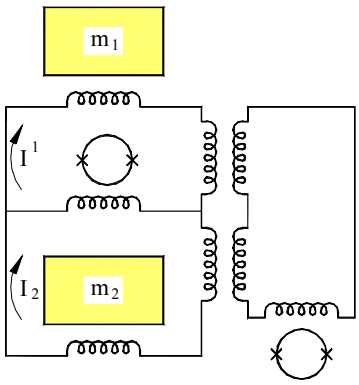

Figure 5. SGG with additional coupling inductor for outer loop.

Next, consider what happens if there is a differential gravity applied to the SGG with the top proof mass moving upwards and the bottom proof mass moving down. This causes I_1 to decrease and I_2 to increase. There is therefore a net current flowing through the central arm of the SGG. When the SGG is balanced, the two current changes are equal in magnitude. This circuit therefore detects gravity gradient through its central arm. In the outer loop these current changes flow in different directions so there is no change in the average of I_1, I_2, so such changes would not couple to a SQUID detecting common mode motion as in Figure 5.

All circuits in the SGG are generically identical to those presented in Figure 4 and Figure 5 and have the same general properties related to flux quantisation and balance. The other property they have relates to current flow through central and outer arms of the SGG. These are always related to orthogonal degrees of freedom, either, differential mode and common mode, as described here, or angular acceleration and transverse linear acceleration and so on.

It has been shown above, that the stability conferred on all SGG circuits by flux quantisation means that the scale factors between applied acceleration and current output remains absolutely constant. Because the gravity gradient function is performed within such circuits in this “current-differencing” SGG, the balance remains stable absolutely stable and the DM output is a true measure of the gravity gradient.

Of course, it is essential that mechanical stability of components through temperature fluctuations does not cause apparent gravity gradients. Fortunately this is an extremely small effect at low temperatures and, by choosing the right materials and a quiet cryogenic environment, the errors produced by this process will be smaller than the intrinsic noise of the SGG.

8. An SGG exploration tool

The basic concepts of an SGG have been elaborated above. The general circuit used in the proposed exploration tool is of the type shown in Figure 6, which is the differential mode detection circuit. Here coils interact with opposite faces of the proof masses and in most circuits the currents in the outer loops are coupled to additional SQUIDs as shown in Figure 5.

In general, the explanation of the workings of these circuits is similar is all cases. All that is needed is knowledge of the coil parameters and on what proof mass faces the coils interact. In this system there are no mechanical springs interacting with the proof mass, only magnetic ones. The proof masses are levitated against gravity by passing large currents through the necessary coils and the magnetic springs are formed by the use of closed superconducting loops with large circulating currents. Large currents are needed because, for operation in the airborne environment, it is necessary to stiffen the SGG as much as possible against all accelerations applied through the platform. Other coils interact with virtually all surfaces of the proof masses and these coils are integrated into circuits to perform the required functions.

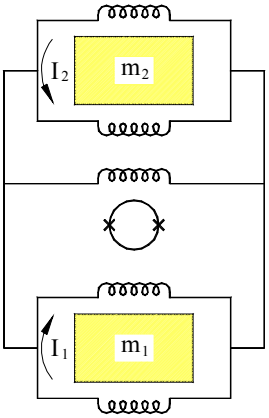

Figure 6. Differential mode circuit for exploration SGG.

The exploration SGG tool proposed here is designed to utilise the differential mode circuit to measure the gravity gradient signal but additionally to measure all linear and angular accelerations. These are needed, as seen in the simple error analysis above, because all major motion induced errors are related to these accelerations including the angular terms which can be obtained by integration of the angular acceleration outputs of the instrument. In general, even with the alignment technique discussed next, there will be residual errors which cannot be balanced out in hardware, so it is necessary to measure the motions and use software analysis to correct the data to the final required precision.

9. Alignment circuit for the SGG

It was noted earlier that a perfectly aligned gradiometer will not couple to linear or angular accelerations in orthogonal degrees of freedom. In order to achieve this, the proposed tool includes patented alignment circuits to align the sensitive axes of the proof masses as illustrated in Figure 7. Without loss of generality, consider the x, y, z orientations as being out of the page, to the right in the plane of the page and up. The origin is at the centre of gravity of the SGG.

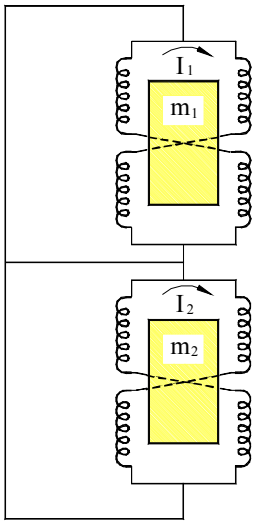

Figure 7. Alignment circuit for exploration SGG.

The alignment circuit of Figure 7 is used to rotate each proof mass about its centre of gravity. First, biasing currents, $I_1 \cong I_2$ are "set" in the loops around each proof mass. These biasing currents thus flow "down" past top right and bottom left sides of each proof mass and "up" past the bottom right and top left of each proof mass.

The proof masses and coils are drawn in the approximate geometric position which they will occupy. That is, for each proof mass the coils act in pairs, one pair acting on top right and bottom left of the proof mass and the other pair acting on the top left and bottom right. If the currents are unequal through the two pairs, there will be a net torque on the proof mass and it will rotate about a line though its centre of gravity parallel to the x axis.

Consider the result of a clockwise current injected into the outer loop. At the junction indicated at the top of proof mass 1, this current will divide, approximately equally. One half will add to the current going “down” past top right and bottom left of proof mass 1 and the other half will subtract from the current coming “up” past the bottom right and top left of proof mass 1. Proof mass 1 will thereby experience a net torque which will cause it to rotate counter-clockwise. This clockwise outer loop current will clearly have the same effect for proof mass 2.

That is, a current through the outer loop of this circuit causes each proof mass to rotate about its own centre of gravity about a line parallel with the x axis and with the same sense. So, if the proof mass axes are offset but parallel, a current through the outer loop will bring them into co-linearity with respect to the $x-z$ plane.

A current injected into the central arm of the circuit divides equally and returns through the arms of the outer loop. An argument similar to that given above shows that such a current causes each proof mass to rotate about its centre of gravity, as before, but this time they rotate in opposite senses. Thus, if the proof masses are non parallel, then a current set through the inner loop returning via the two arms of the outer loop will cause the proof mass axes to become parallel.

Thus by setting the currents in the alignment circuit of Figure 7 as described, the proof mass sensitive axes can be made co-linear in the $x-z$ plane.

A similar circuit to that of Figure 7 allows the two sense axes to be brought into co-linearity in the $y-z$ plane.

This scheme, therefore, has the ability to actively align the two proof mass sense axes and make them completely co-linear.

This alignment scheme is based around the same generic superconducting circuitry used for the detection circuits so has the same flux quantisation benefits. The alignment errors are stable for this instrument and the above description indicates how they can be minimised. It is anticipated that this scheme will allow “hardware” set rejection for linear accelerations to be improved from a mechanical assembly alignment of 10^{-3} to 10^{-7} radians, leaving software to reject another two to three orders of magnitude to achieve the required rejection. For angular accelerations, the total rejection required is a couple of orders of magnitude less.

Initial results from such a scheme are shown in Figure 8 which shows the variation of the proof mass alignment with the current stored in one of the alignment circuits. It can clearly be seen that the alignment scheme works.

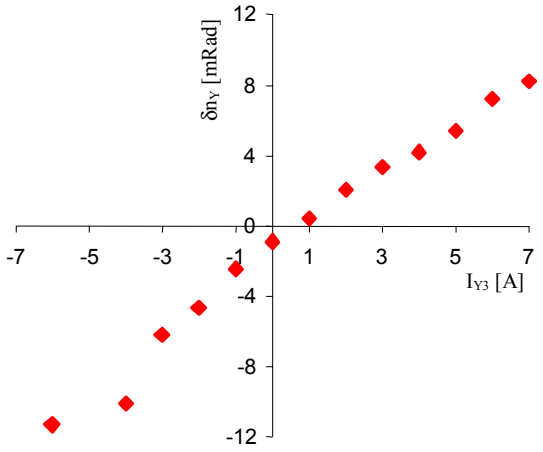

Figure 8. Alignment result for prototype gradiometer (ESA). A known horizontal acceleration is applied to the instrument and the error signal is measured. The misalignment, δn_Y is deduced from (4.4). In the above case, the proof masses become aligned with an alignment current near to 1.0 A.

10. Mathematics of the SGG

The theory of the SGG is relatively straightforward in principle but becomes extremely complicated when carried through to second and third order terms in the equations. The ultimate goal of the mathematics is to show that it is indeed possible to set the instrument up so that, irrespective of the accelerations to which it might be subjected, these accelerations do not couple into the differential mode. A simple linear theory has been developed by Chan and Paik (1987). Here the basic mathematical procedure is described indicating how all non linear terms can be handled. It is straightforward to show that the SGG can always be perfectly balanced to first order but it is the second and third order terms which give rise to problems.

There are two fundamental equations to consider to deduce the dynamic behaviour of the proof masses, the flux equations and the force equations.

Flux conservation requires that, once a magnetic flux is set in a superconducting loop, it cannot change no matter where or how the proof mass moves. Thus as long as the inductance of each coil is known as a function of position and orientation then the currents in all the loops can be calculated with certainty. This current will, in general, be a non linear function of position and orientation. Assembly, orientation and manufacturing errors are straightforward to include but the complexity of the detail rapidly becomes difficult to handle.

Once the current as a function of proof mass position and orientation is known, the dynamic force equations can be used to calculate how the proof mass(es) respond to forces, gravity gradients and angular accelerations. For the analytical solution, these calculations are much better handled in the frequency domain. The result of this is that the steady state solutions for the motion of the proof masses are known, including all the non linear terms.

Once the acceleration to position is determined, as above, by the force equations, this is used in the flux conservation equations to calculate the steady state currents as a function of frequency of applied acceleration.

For the gradiometer, the procedure is as follows. First, a set of currents in all the loops is chosen which corresponds self consistently to a starting position/orientation for the proof masses. The gradiometer response to an applied acceleration is then calculated for all SGG circuits. The set up is changed slightly and the response to external accelerations is calculated again. The aim is to look for a starting set up which achieves perfect balance over the range of external accelerations which the instrument will encounter in flight. Each circuit in the SGG is needed to calculate the response of the SGG to a given external acceleration but the currents in each circuit are determined only by the position/orientation of the proof masses and the initial currents in that circuit.

The mathematical procedure is illustrated for the single sided accelerometer in Figure 6. The flux conservation equation is,

$$\left(L_p + L_{SQ}\right)\cdot i_{circ} = \Phi_1 \qquad (10.1)$$

The following notation shall be used

$$\begin{aligned} &x(t) = x(0) + x, \\ &i_{circ}(t) = i(0) + i \\ &L_p(x(t)) = L_p(x) = L(x_0) + \Lambda x + bx^2 + \ldots \\ &\qquad\qquad = L_p(x_0) + \Delta L_p(x) \end{aligned} \qquad (10.2)$$

Substitution of (10.2) into (10.1) yields

$$i = -i(0)\frac{\Delta L(x)}{L_{SQ} + L(x)} \qquad (10.3)$$

Note that this equation is analytically correct, it is not an approximation and this is because the inductance used in the denominator is that at the displaced position, not the inductance at the starting position. This simple modification of standard treatment allows the full analytical solution to be calculated to arbitrary order.

This same technique is valid for all loops in the SGG. Note also that (6.3) and (10.3) indicate that i is a polynomial function of position due to terms in both the numerator and the denominator.

Next, consider the force equation which can be written as

$$m\ddot{x} = -mg(x(t))\cdot\hat{n} - \gamma\dot{x}(t) + F_R(x(t)) + \frac{1}{2}\frac{\partial L_p}{\partial x}(i_{circ}(t))^2 \quad (10.4)$$

where $g.\hat{n}, F_R, \gamma$ is the gravity resolved along sensitive axis at the proof mass position, other forces on the proof mass (from other circuits), and a conventional damping term. The equilibrium position is assumed to be at $x(0)$ where (10.4) becomes a self consistency condition for the currents and forces

$$0 = -mg(x(0))\cos\theta + F_R(x(0)) + \frac{1}{2}\frac{\partial L_p(x(0))}{\partial x}i^2(0) \quad (10.5)$$

where $g(x(0))$ is assumed to be the gravity at time zero when the proof mass is at position $x(0)$. With nomenclature

$$\begin{aligned} &g(t).\hat{n} = g(x(0))\cos\theta + \delta g(t) \\ &\frac{\partial L_p}{\partial x}(x(0)+x) = \frac{\partial \bar{L}_p}{\partial x} \\ &\frac{\partial \bar{L}_p}{\partial x} - \frac{\partial L_p}{\partial x}(x(0)) = \Delta\left(\frac{\partial L_p}{\partial x}\right) \end{aligned} \quad (10.6)$$

the dynamic equations become

$$m\ddot{x} = -m\delta g(t) - \gamma\dot{x} + (F_R(x(0)+x) - F(x(0))) + \Delta\left(\frac{\partial L_p}{\partial x}\right)i(0)^2 + \frac{\partial \overline{L_p}}{\partial x}(2i(0)\cdot i + i^2) \quad (10.7)$$

From inspection of (10.2) and (10.3) it is clear that the last two terms in (10.7) are polynomial functions of x. The force from the other circuits is clearly of the same form as these last two terms of (10.7) so it will also be a polynomial function of x. Without evaluating the terms explicitly, (10.7) will therefore be of the form,

$$m\ddot{x} = -m\delta g(t) - \gamma\dot{x} - A_1 x + A_2 x^2 + A_3 x^3 \quad (10.8)$$

The first term in this expansion is

$$A_1 = -\left.\frac{\partial F_R}{\partial x}\right|_{x(0)} + i(0)^2\left(-\frac{1}{2}\frac{\partial^2 L_p}{\partial x_1^{\,2}} + \frac{\Lambda^2}{L_{SQ} + L_p(x(0))}\right) \quad (10.9)$$

This clearly is the “Hooke’s Law” stiffness of the magnetic spring. The treatment to this point has been completely general without having to choose a form for $\delta g(t)$. Exactly the same type of analysis is followed for all of the more complex SGG circuits and the route from this point on is the same as well. Progress is made by assuming a particular frequency for the applied acceleration – the analytical treatment cannot be continued in the time domain. Assuming

$$\delta g(t) = g(\omega)e^{jwt} \quad (10.10)$$

it is sensible to look for a steady state solution of the form

$$x = x_1(\omega)e^{jwt} + x_2(\omega)e^{2jwt} + x_3(\omega)e^{3jwt} + \ldots \quad (10.11)$$

where the expressions for the coefficients of the frequency components will be expressed in terms of A_1, A_2, A_3. The first two terms are

$$x_1(\omega) = \frac{g(\omega)}{\left(\omega_0{}^2 - \omega^2 + j\frac{\omega\omega_0}{Q}\right)} \qquad (10.12)$$

and

$$x_2(\omega) = \frac{A_2\left(x_1(\omega)\right)^2}{\left(\omega_0{}^2 - 4\omega^2 + j\frac{2\omega\omega_0}{Q}\right)} \qquad (10.13)$$

where $\omega_0{}^2 = \frac{A_1}{m}$ is the resonance frequency of the system and $Q = \frac{\omega_0 m}{\gamma}$ is the quality factor of the resonance.

It is clear that when the accuracy is taken to higher order, the lower order terms are not affected so the treatment is always accurate to the order considered – this treatment can be carried to arbitrary accuracy. Each component, $x_n(\omega)$ includes all A_i components up to and including A_n.

The final step in the analysis is to calculate the current as a function of applied acceleration. For this, (10.11) is substituted into (10.3) to deduce the components, $i_n(\omega)$, in (10.14) below

$$i(\omega,t) = i_1(\omega)e^{j\omega t} + i_2(\omega)e^{2j\omega t} + i_3(\omega)e^{3j\omega t} + \ldots \qquad (10.14)$$

The coefficients, $i_n(\omega)$ come simply from the analysis and

$$i_1(\omega) = -\frac{i(0)}{L_{SQ} + L_p}\left\{\frac{\partial L_p}{\partial x}x_1(\omega)\right\} \qquad (10.15)$$

$$i_2(\omega) = -\frac{i(0)}{L_{SQ} + L_p}\left\{\begin{array}{l}\frac{\partial L_p}{\partial x}x_2(\omega) \\ +\left[\frac{1}{2}\frac{\partial^2 L_p}{\partial x^2} - \frac{1}{L_{SQ} + L_p}\left(\frac{\partial L_p}{\partial x}\right)^2\right]\left(x_1(\omega)\right)^2\end{array}\right\} \qquad (10.16)$$

The change in current response at the frequency of this gravity or acceleration excitation, $g(\omega)$, is obtained by substituting for $x_1(\omega)$ from (10.12) into (10.15)

$$i_1(\omega) = -\frac{i(0)}{L_{SQ} + L_p}\frac{\partial L_p}{\partial x}\frac{g(\omega)}{\left(\omega_0{}^2 - \omega^2 + j\frac{\omega\omega_0}{Q}\right)} \qquad (10.17)$$

Inspection of (10.9) and (10.12) reveals that the first order solution is just a classic “mass on a spring” problem with the spring constants due to the accelerometer circuit being given by two terms as discussed earlier. One of these is due to the non linearity of the pancake coil inductance and contains only terms relevant to this coil. The other term is due to the closing of the loop and includes the total loop inductance, SQUID coupling plus pancake coil and the linear coefficient of the pancake coil inductance.

The current at the fundamental frequency is also resonant and all variants of these circuits have this form. The ratio between the applied acceleration, $g(\omega)$ and the induced current $i(\omega)$ is the scale factor for the accelerometer and is denoted as H_{gi}.

For the gradiometer circuit shown in Figure 6, exactly the same treatment can be executed but now, as there are two proof masses, there are two degrees of freedom. The time dependent accelerations applied to each proof mass can either be in phase, i.e., common acceleration or $g_c(\omega)$, or they can be out of phase, i.e., differential acceleration or $g_d(\omega)$. The current flowing around the outer loop at balance is proportional to common mode acceleration and the current flowing through the central arm is proportional to differential mode acceleration. If the current in the central arm is labelled $i_d(\omega)$ then, in the linear approximation

$$i_d(\omega) = H_{gi}^{dc} g_c(\omega) + H_{gi}^{dd} g_d(\omega) \qquad (10.18)$$

Each of the H_{ij}^{kl} terms will be the sum or difference of terms which look very similar to those in (10.17).

The goal of the balance procedure is to make $H_{gi}^{dc} = 0$. For a real situation with real assembly/component tolerance errors, it is easy to achieve a first order balance at a particular frequency merely by adjusting one of the major currents around one of the proof masses. In general, however, this does not give a balance at a different frequency so the balance procedure needs to first balance at one frequency, then change the frequency of excitation acceleration, adjust a different current to achieve balance and continue until the instrument is balanced at both frequencies. This procedure gives a wide band balance. What we are balancing in this procedure are the scale factors of the two halves of the SGG. It is possible to "prove" the existence of a perfect first order balance, i.e., one at the frequency of the applied acceleration.

In general, this wide band balance does not simultaneously balance out the higher order non-linear terms (10.16) which will be large in an airborne environment. The SGG dynamics must therefore be linearised by the use of forced feedback. This works by controlling the proof mass displacements thus ensuring that the non-linear terms are negligible.

Once the balance has been achieved, flux quantisation ensures that it is maintained. The SGG is complex to set up, but once this is done, the balance is "set". The use of the alignment scheme is incorporated into this procedure so that the final set up of the instrument rejects common mode accelerations in sense direction (primarily by adjusting currents in the differential mode circuit) and rejects accelerations in orthogonal directions by the use of the alignment scheme.

The use of (4.4) together with typical accelerations as seen in an aircraft shows that the alignment issues and scale factor match issues must be treated together and that the instrument balance will not improve unless all errors, scale factor and alignment, are improved in rotation. An extremely high scale factor balance in hardware does not necessarily give a low noise if an alignment error is causing noise injection from another degree of freedom.

It is possible to perform a real time numerical analysis of the system but it is much more time consuming to run the software. Using this scheme, the ESA design with known typical assembly and manufacturing errors has been shown to be able to achieve a wide band balance for common mode accelerations with rejection in excess of one in 10^8. Extrapolating this analysis for the parameters of the exploration SGG suggests that a wide band balance to a level greater than one in 10^6 is possible for the accelerations expected.

11. Fundamental noise/resolution of the SGG

Paik and Chan (1987) and Vitale (1999) have both analysed the fundamental noise limit of a superconducting gravity gradiometer. There are two major sources of noise viz. the noise of the SQUID readout and the Brownian motion noise of the proof masses interacting with their magnetic springs. For each of these fundamental noise sources, the noise is represented as the gravity gradient signal which would yield the same result. The full expression of noise in terms of its power spectral density (PSD) is

$$S_\Gamma = \frac{8}{ml^2}\left(\frac{k_B T}{Q}\omega_0 + \omega_0^2 \cdot \frac{E_A(f)}{2\beta\eta}\right) \qquad (11.1)$$

where Q is the quality factor of the differential mode resonance which has a resonance frequency ω_0, k_B is Boltzmann's constant, T is the temperature of the SGG, $E_A(f)$ is the coupled energy sensitivity of the SQUID (one of the standard specifications for a SQUID), β is the ratio of the differential mode energy in the differential mode circuit divided by the total energy in the differential mode resonance and η is a coupling factor from the pancake coil inductance to the SQUID (basically the ratio of SQUID inductance to total inductance in circuit).

The units of S_Γ are $s^{-4}Hz^{-1}$.

A detailed design of the exploration SGG has been carried out and the above treatment indicates that, for an airborne instrument, absolute sensitivity, although important, is not the major concern. It is quite possible to design an SGG with resolution at the 10^{-3} Eo/$Hz^{1/2}$ level but such an instrument would be impossible to use

in a hostile airborne environment with virtually all outputs being saturated. For the exploration SGG it is necessary to stiffen all modes as much as is possible by use of large coils and large currents which generate both large forces and large stiffness.

With the designs chosen for this instrument, which include the proof masses and all the coils and circuits which interact with them, all parameter values for the modelling are fully calculable. The result for the exploration SGG is as shown in Figure 9 below. Note that the instrument will really only be useful at low frequencies because of the speed of the plane and its distance above the ground. This means that typical "best" spatial resolutions will be of the order of a few hundred metres (~flying height) which will take several seconds to fly.

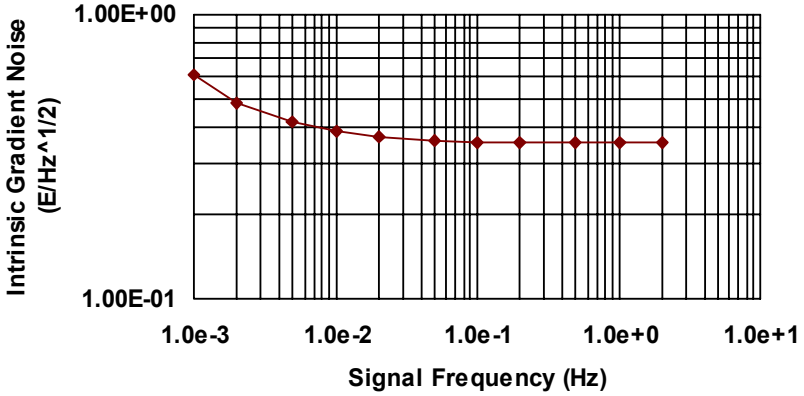

Figure 9. Fundamental resolution of exploration SGG.

12. Design of the exploration SGG

The design of the exploration SGG utilises similar designs to those used for the European Space Agency prototype tool developed under ESA contract 10393/93/NL/PB. The circuits are similar in design and in principle to those used to describe the basic concepts above and the SGG utilises proof masses which are as indicated in Figure 10 below. These proof masses are made from pure Niobium, weigh 100 g and are 50 mm in both length and diameter. The sensitive axis for gravity gradient measurement is axial and the sense coils for both gravity gradient and axial common mode motion sense interact with the flange perpendicular to this axis inside the proof mass. Coils acting on all the other surfaces, inside and out, are used for the alignment function and to sense all other motions when utilised in circuits as above.

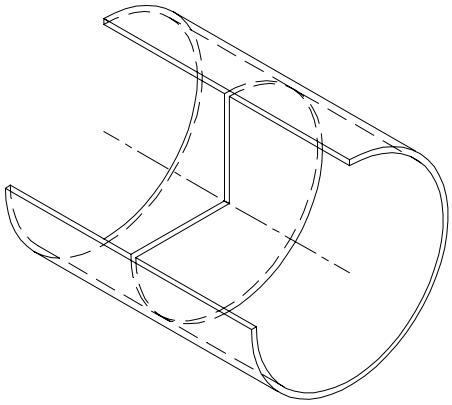

Figure 10. Exploration SGG proof mass.

There are two versions of the exploration tool, the first of which will measure Γ_{zz} and which will be made, flown and tested first, and the other a full tensor gradiometer. The Γ_{zz} tool shall measure

a_x, a_y, a_z,	i.e., all linear accelerations
α_x, α_y	i.e., all measurable angular accelerations
Γ_{zz}	the vertical diagonal gravity gradient

From these measurements and the use of a sophisticated GPS/INS system, all quantities needed to correct the data for all platform motions will be acquired or calculated. Analysis demonstrates that the Γ_{zz} component is less susceptible to platform motion and better performance is therefore obtainable than for Γ_{xx} and Γ_{yy} for the same level of rejection of common accelerations for all directions of flying.

The mechanical layout of the exploration SGG is shown in Figure 11. This design can take six accelerometer modules to perform the full tensor gradiometer function but just two will be used in the first instrument, the Γ_{zz} SGG.

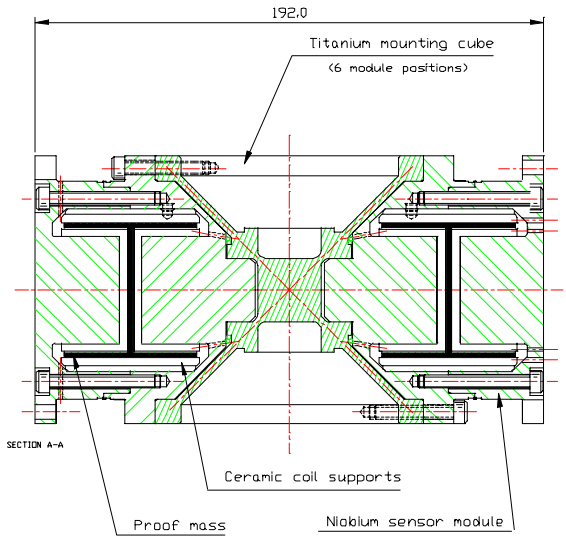

Figure 11. Cross section construction drawing of one SGG axis.

Finally, it is necessary to make some comment about a stabilised platform. It is clearly desirable to remove as much noise as possible from the aeroplane. However, because of the physical amplitude of the linear motions, it is impractical to consider anything other than angular stabilisation together with passive or active isolation of low amplitude high frequency linear accelerations. Whatever is left in the way of angular and linear accelerations must be handled by the SGG itself.

Analysis shows that, if the following angular stability could be achieved, then with the exception of the centrifugal error, which cannot be rejected, angular motions will not cause errors in excess of the fundamental noise limit presented above.

$$\begin{aligned} &10^{-2}\,rad && \text{- Absolute pointing} \\ &10^{-4}\,rad/\sqrt{Hz} && \text{- Pointing stability} \\ &1.3\times10^{-6}\,rad/s/\sqrt{Hz} && \text{- Angular velocity} \\ &10^{-4}\,rad/s^2/\sqrt{Hz} && \text{- Angular acceleration} \end{aligned} \qquad (11.2)$$

The hardest of these is the angular rate error. Of course, signals above these are not death to the SGG, all that is then required is more software correction of the induced errors or, in the case of angular acceleration motion, a better intrinsic rejection.

13. Conclusion

The theory for the analysis and use of a superconducting gravity gradiometer has been presented. It has been shown that this tool will achieve better results than any other gravity gradiometer available today and any airborne gravity tool. The phenomenal stability of this tool is afforded by flux quantisation and the Meissner effect, fundamental quantum mechanical properties of superconductors. The design proposed for the exploration SGG has been discussed briefly and it has been demonstrated that there are parameters which allow it to achieve 1 Eo/Hz$^{1/2}$ in difficult airborne environments.

14. References

Blakely, R.J., 1995, Potential Theory in Gravity and Magnetic Applications: Cambridge University Press.
Bracewell, R.N., 1999, The Fourier Transform and Its Applications: McGraw-Hill, 3rd edition.
Chan, H.A. and Paik, H.J., 1987, Superconducting Gravity Gradiometer for Sensitive Gravity Measurements. I. Theory: Phys. Rev. D 35, 3551-3571.
Domenico, N., 1994, The SEG Museum's torsion balance: The Leading Edge, 13, 683-686.
Symon, K.R., 1961, Mechanics: Addison-Wesley, 2nd edition.
Vitale, S., 1999, GOCE Phase A study: European Space Agency.

A high resolution airborne gravimeter and airborne gravity gradiometer

Bjarni Tryggvason
Gedex Inc.
bjarni.tryggvason@gedex.ca

Brian Main
Gedex Inc.
Brian.Main@Gedex.ca

Barry French
Gedex Inc.
barry.french@gedex.ca

Introduction

For airborne gravity gradiometry to significantly impact geophysical exploration by permitting detection of ore bodies in the presence of variability in host geology, a target resolution has been set at 1 eotvos (Eo) at 1 sample per second. This has not yet been demonstrated by any airborne system and remains a design target for many systems now under development.

While the first order response of a gravity gradiometer can be designed to be relatively insensitive to accelerations, isolating and compensating the complete response of an airborne gradiometer to accelerations of an aircraft remains a significant challenge. Dynamic modes of the gradiometer and aircraft vibrations interact to produce sensor noise and limit the achievable signal to noise ratio. Somewhat analogous to the processing of airborne gravity data, one approach is to measure and compensate for aircraft accelerations. Significant noise is accepted as part of the primary signal and then removed through processing. However, as with airborne gravity, the errors induced by aircraft accelerations can be dramatically larger than the gravity gradient signal of interest. In the case of a gravity gradiometer designed to detect a gradient change of 1 Eo, errors induced by the accelerations of a moving platform can range from tens to thousands of Eo. Quantifying and correcting for these errors to obtain a resolution of 1 Eo at one sample per second is a considerable challenge.

Recognizing this challenge, a total systems approach has been adopted, with equal emphasis on the gravity gradiometer instrument, the isolation system, the aircraft, and data processing. This systems approach also provides the basis for an airborne gravimeter system with a target performance of sub-milligal at one sample per second.

The Orthogonal Quadrupole Responder (OQR), developed and demonstrated under the leadership of Dr. Frank van Kann at the University of Western Australia (Matthews, 2000), is the gravity gradiometer chosen for the Gedex Airborne Gravity Gradiometer (AGG) system. The design is based on micro-flexures supporting pairs of balance beams, which directly measure gravity gradients with a design resolution of 1 Eo at one sample per second. The sensing elements are designed to be first order insensitive to linear and rotational accelerations of the airborne platform. To achieve this resolution while operating from an aircraft, an advanced isolation platform that significantly protects the OQR sensing element from both rotational and translational aircraft accelerations will be utilized. This will significantly reduce the level of corrections and signal processing required to extract the desired gravity gradient signal. For a platform translating at 100 knots (~50 m/s), the isolation system will be instrumental in achieving the target spatial resolution of 1 eotvos every 50 m for the gravity gradiometer, and sub-milliGal for the gravimeter. This paper summarizes progress made to date and the fundamental principles behind the system.

Principle of the AGG

The OQR is based on two precision balance beams supported on flexural pivots as illustrated schematically in Figure 1. The pivots are designed to have a fairly low natural frequency for the sensing mode, which is a rotation of the beams about the pivot, while having very high frequencies for dynamic modes that involve shearing, stretching or other distortion of the pivot. The stiffness of the pivot for the sensing mode needs to be minimized in order to provide high sensing resolution, but must still be high enough such that the sensor will respond to the frequencies of interest. For the AGG the sense mode frequency is set somewhat higher than the desired sampling rate of 1 sample/s. At the same time, the pivot must be designed such that distortion of the pivot under acceleration loads will not produce excessive errors. This required that the natural frequencies for these error-generating modes must be set quite high.

Extensive analysis of the error terms has been done for the OQR, and each error term has been defined quantitatively through analytic expressions. By combining these models with acceleration spectra as measured in flight, the errors to be expected can be evaluated. This analysis has been performed to define the performance that must be achieved on the platform isolation system.

The fundamental requirement for the sensor design is to achieve an acceptable signal to noise (SNR) ratio against the Brownian motion noise of the sensor. The SNR is given by an expression of the form:

$$SNR = \frac{\Gamma}{\omega}\sqrt{\frac{I}{k_B T}}$$

where Γ is the gravity gradient at a fixed place, ω is the natural frequency of the sensor in its sensing mode, I is the mass moment of inertia of the sensor, k_B is Boltzmann's constant and T is the absolute temperature. Note that this equation applies for a quasi-static case, i.e., where time variations in the gravity gradient being sensed are slow compared to the response time of the sensor. The equation for the SNR is written in this form to highlight the effect of the sensor frequency for the sensing mode as well as that of the effective mass and damping for this mode. This expression can be taken as quite general, as a comparable expression will hold for any sensor. In order to achieve a sample rate of 1 sample/s, the natural frequency for the sense mode must be set higher than 1 Hz. However, as this sense mode frequency is increased the signal to noise ratio decreases. Hence this expression provides the means for optimising the design of the sensor. In the case of the OQR, which is designed to operate at liquid helium temperatures, a beam mass of approximately 0.5 kg gives a SNR that allows detection of a 1 Eo gravity gradient signal. The above represents a fundamental limit to the resolution of the sensor.

The SNR for the complete system will be degraded by the impact of the supporting hardware. For the sensor itself this includes the noise levels in whatever transducer and electronics are used to sense the beam rotation. The OQR uses superconducting quantum interference devices (SQUID) to achieve the resolution and low noise required to maintain the SNR.

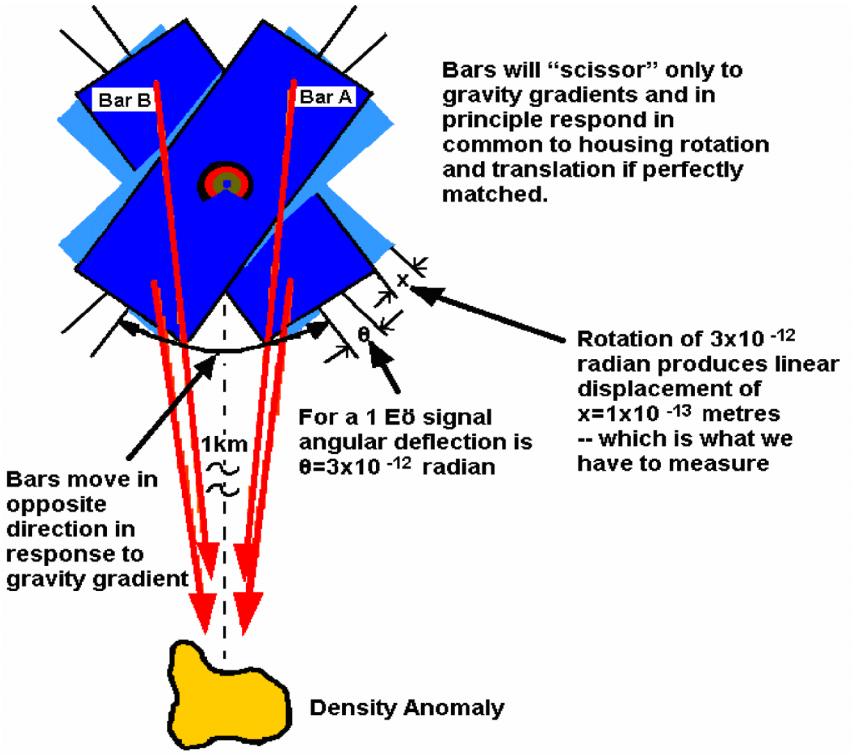

Figure 1. Conceptual view of the two-beam OQR gravity gradiometer.

Noise terms in the AGG

The OQR uses two balance beams perpendicular to one another with parallel pivot axes. The centre of mass of each beam is set to coincide with the centre of rotation of the beam about the pivot. To first order this makes the sensor insensitive to linear accelerations. Under rotational accelerations, the beams rotate with respect to the housing in a common direction, whereas under gravity gradient loads, the beams rotate in opposite directions. The electronic sensing is configured to amplify the differential mode signal, while cancelling the common mode signal, again making the sensor to first order insensitive to rotational accelerations. An essential element of the sensor design is to achieve very high mechanical matching for the common mode response. This is refined through electronic tuning.

The dominant remaining error terms in the OQR are associated with distortion in the beam flexures and with response to rotations of the sensor support platform. The rotational effects are common to any gravity gradiometer and require rotational stabilization of the sensor platform. For the OQR the pivot flexural modes can be excited by second order terms driven by linear accelerations. All gravity gradiometers will have comparable error terms. An advantage of the QOR design is that it is possible to push these modes to quite high frequencies, of the order of 2000 Hz for the current OQR configuration. While we will not discuss all of the error terms in this short note as they are presented in detail in Matthews (2002), an example is provided that relates to acceleration products. The form of this error is given by:

$$E_{acc=prod} = \frac{6a_x a_y}{\omega_{S-bend}{}^2 (l^2 - b^2)}$$

where a_x and a_y are the linear accelerations in two orthogonal directions, ω_{S-bend} is the frequency for pivot shear mode, and l and b are the length and width of the beam respectively. The form of this error term is similar to others in the sense that the errors are typically dependent on design aspects of the sensor, in the above case the S-bend frequency, and the disturbance levels from the environment, in the above case the products of cross-accelerations. This interaction between sensor properties and the environment has prompted a complete systems approach to be applied.

For a pivot shear mode frequency of 1000 Hz (6283 rad/s) and linear accelerations of 1 m/s^2 the error is 20000 Eo. To limit this error term to be less than 1 Eo requires limiting the linear accelerations to slightly less than 0.01 m/s^2, or compensating for the linear accelerations either through force feedback compensation or by correcting the total signal post-flight for the measured accelerations. While such correction procedures can in principle be developed and applied, the AGG is mounted on a motion isolation platform, the GeoMIM, that is able to reduce the linear accelerations of the sensor to limit this error term to be less than 1 Eo. The effect of other error terms will be limited to not exceed 1 Eo through use of the isolation system combined with corrections for residual accelerations if necessary.

Aircraft accelerations

As part of the full system design, the acceleration environment has been studied for several aircraft. Figure 2 shows the power spectral densities for accelerations measured on a light twin-engine aircraft flown in moderate turbulence at approximately 400m above fairly level ground. Note that the energy is overestimated somewhat in the low frequencies, as these spectra have not been corrected for aircraft attitude variation. The cumulative RMS acceleration curves associated with these acceleration spectra are shown in Figure 3. When the accelerations are combined with the model for the sensor error term, the power spectral density for that error term can be obtained. This is given for the above error term in Figure 4. This figure shows the power spectral density for the gravity gradient error for a sensor that is affected directly by the aircraft accelerations, and the reduction in the gradient error when optimal control is used to limit the aircraft motion at low frequencies and when the sensor is isolated from the residual aircraft motions with a motion isolation system. Figure 5 shows the growth in the rms gravity gradient error as the frequency bandwidth is increased. Without the isolation system, the error is of the order of 150 Eo rms up to 1 Hz. With the isolation system, the error is reduced to less than 1 Eo rms.

Isolation system

The isolation system acts as a low pass filter that isolates the sensor platform from aircraft motions. The motion range available for the isolation system limits the lowest frequency above which isolation can be effective. The intention is to limit the motion of the aircraft at frequencies below 0.1 Hz by optimising the 'altitude hold' function on the autopilot to limit departures to less than 1 m from the ideal flight path. Above 0.1 Hz, this will allow the isolation system to limit the acceleration that the instrument experiences to well below 0.01 m/s^2.

Application to gravimetry

Given the exacting performance requirement for the isolation system demanded by the OQR gradiometer, the system also provides an excellent platform for a gravimeter. This application has been explored and will in fact be the initial use for the isolation system. The isolation system provides significant reduction in the noise in the measured acceleration signal, leaving much simpler data analysis for removing the aircraft (inertial) acceleration from the measured total acceleration.

Gravimeter

The gravimeter that will be installed on the prototype GeoMIM uses the Honeywell Q-Flex accelerometers. These have demonstrated resolution of the order of 1 μm/s^2 based on experience in long-term operation on the Russian Mir space station and on the space shuttle. The challenge in the airborne gravimetry application is to measure the total signal with better than 10 μm/s^2 resolution. The electronics that will be used to achieve this is based on the high resolution signal conditioning and digitising module developed by the Canadian Space Agency and licensed to Gedex. Figure 6 shows the power spectral density for this module and Figure 7 shows the cumulative rms noise growth with frequency for this module. The noise floor in the module is 10^{-12} m^2/s^4/Hz from DC to 250 Hz. Above 250 Hz, the anti-aliasing filter reduces the noise energy by three orders of magnitude. The cumulative growth is only 0.8 μm/s^2 rms by 1 Hz, and only 10 μm/s^2 rms by 250 Hz. The noise level for the gravimeter will be limited only by the noise in the accelerometers, which as stated above is below 10 μm/s^2 up to 1 Hz. The main limitation will come from the ability to correct for the aircraft accelerations.

Conclusions

Work on the airborne gravity systems is progressing well. The detailed designs for the first three stages of the five-stage GeoMIM are complete and the first two stages have been manufactured. The detailed design of the complete system will be complete by the end of August 2004, with flight tests of the full system starting in September. The partially completed GeoMIM will go through initial flight tests in August.

In parallel, the high resolution electronics for the GeoMIM and gravimeter are being manufactured and are scheduled for completion by the end August, with ground testing of the gravimeter planned for September and initial flight tests expected by October.

Work on the gradiometer is progressing. A room temperature test version of the gradiometer should be completed in the second half of 2004. This will provide a cost-effective means of validating the three dimensional (3D) finite element model (FEM) of the gradiometer and how it reacts to accelerations (i.e., what the errors will be as a consequence of the beams flexing) before the detailed design of the cryogenic sensor is finalized.

References

Matthews, R., 2002, Mobile Gravity Gradiometer: PhD Thesis, Department of Physics, University of Western Australia.

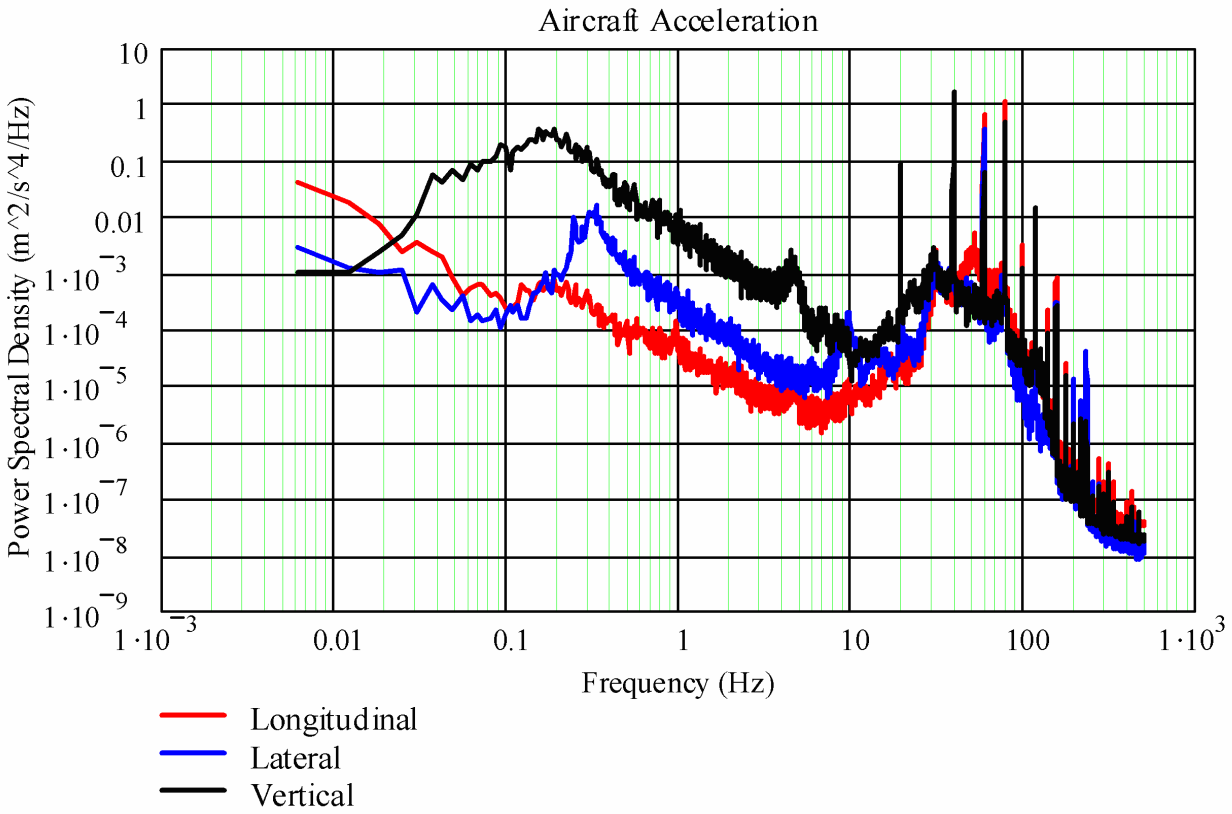

Figure 2. Power spectral density for acceleration measured on a twin-engine light aircraft in moderate turbulence.

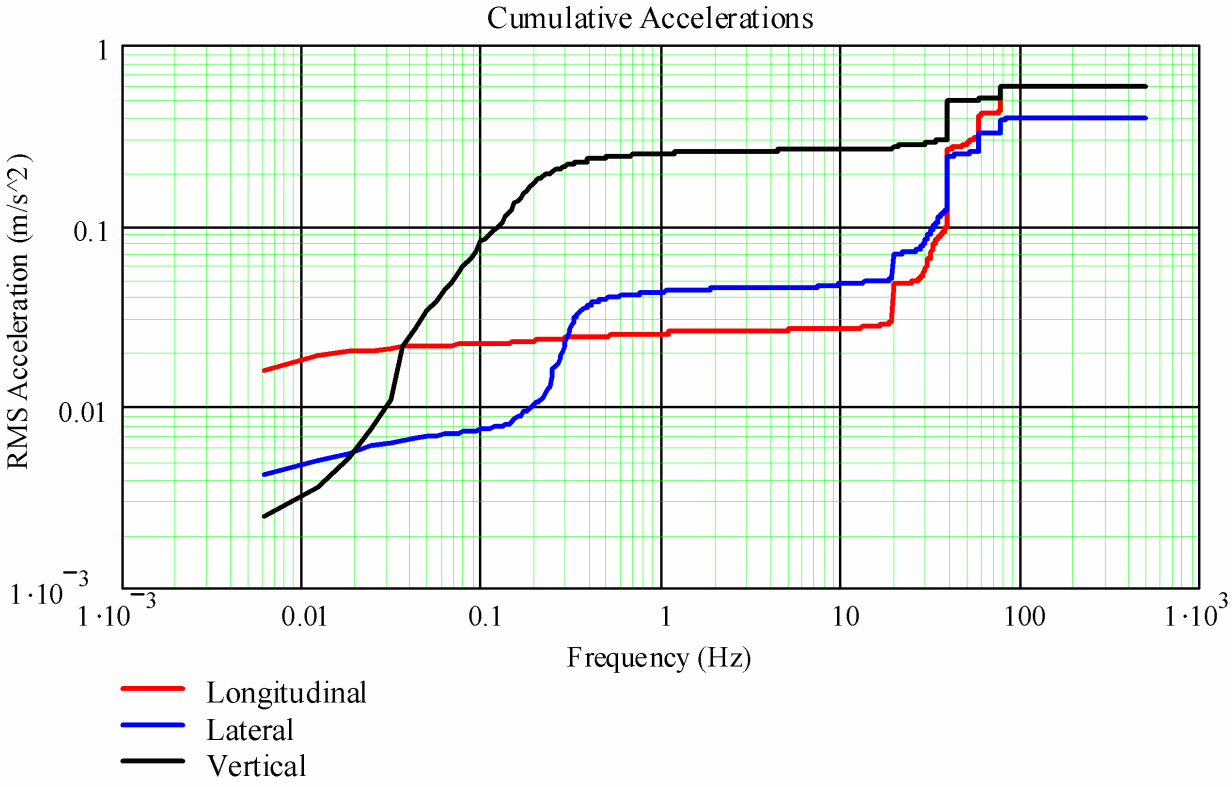

Figure 3. Cumulative rms accelerations for a twin-engine light aircraft in moderate turbulence.

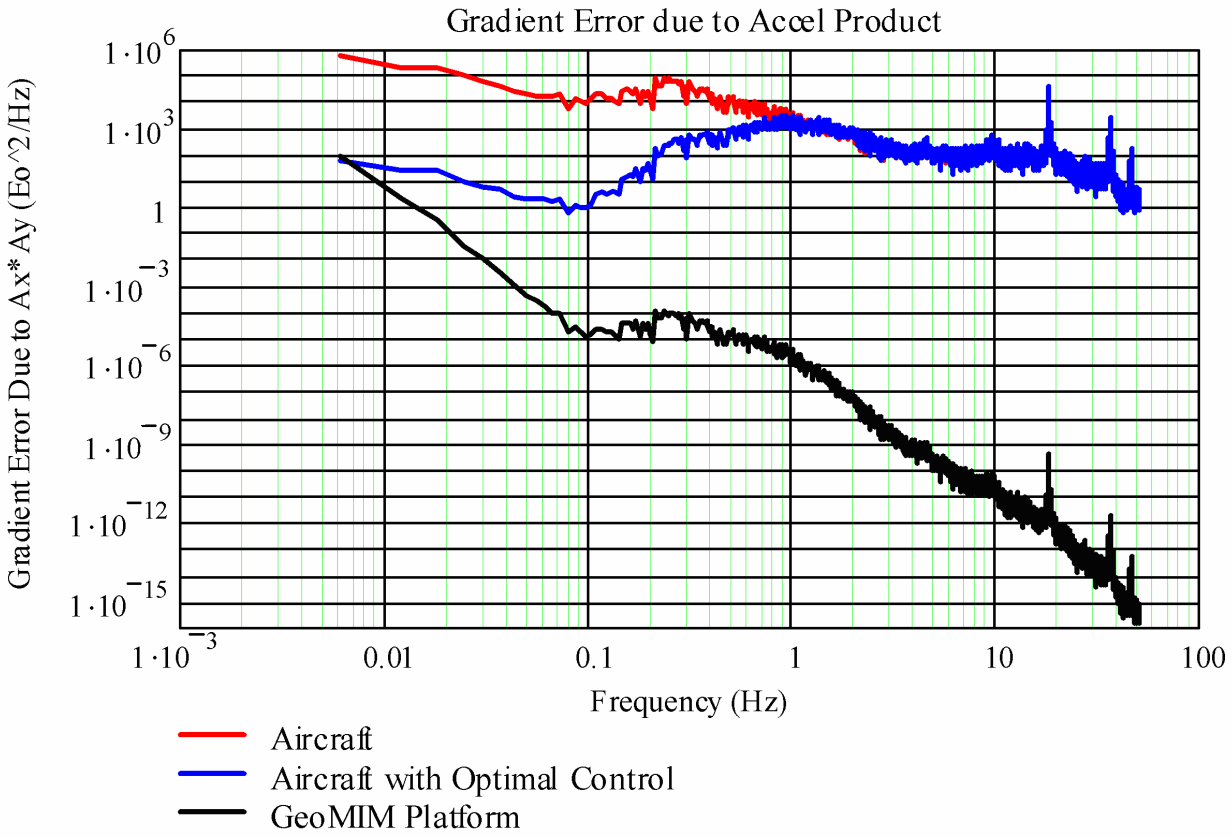

Figure 4. Power spectral density for the gradient response of the OQR to acceleration products.

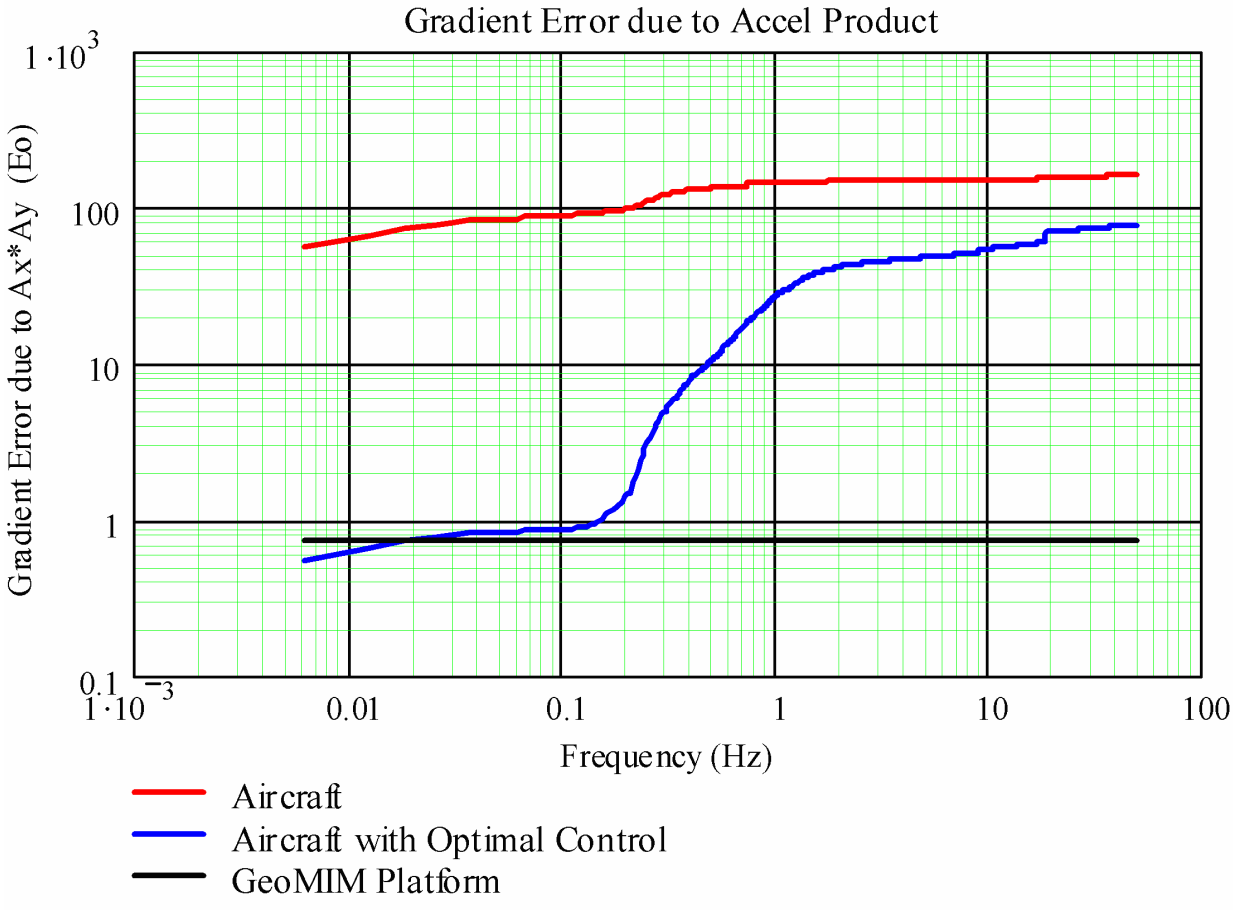

*Figure 5. Cumulative gradient error for acceleration product a_x*a_y.*

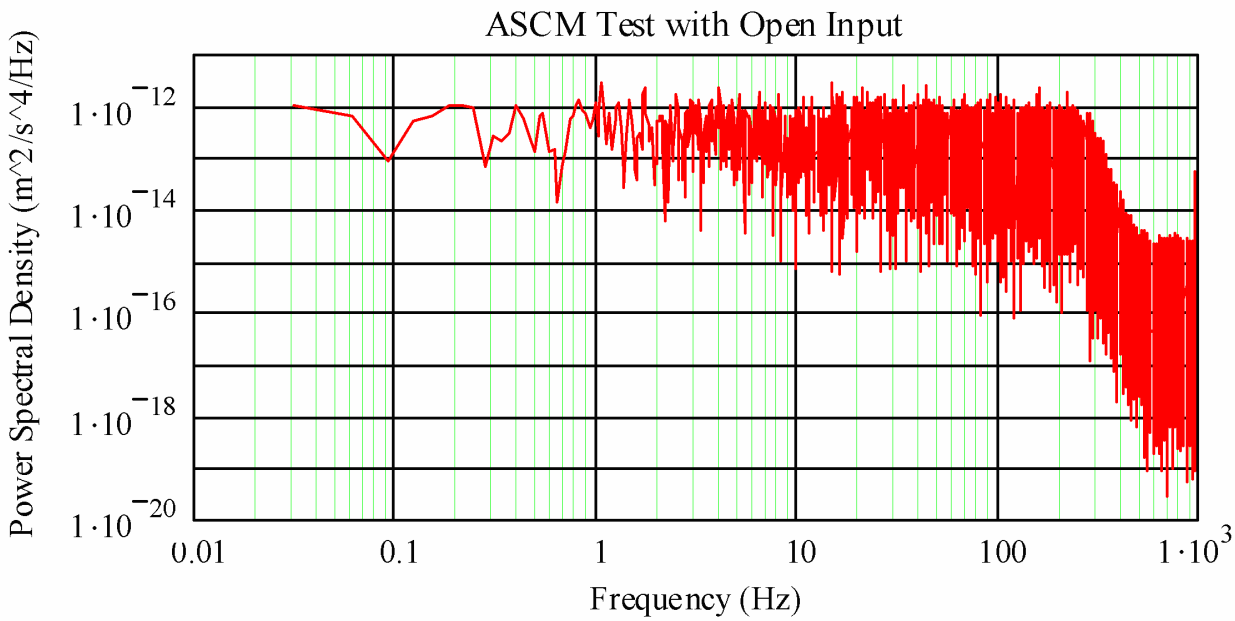

Figure 6. Power spectral density for the gravimeter signal conditioning module.

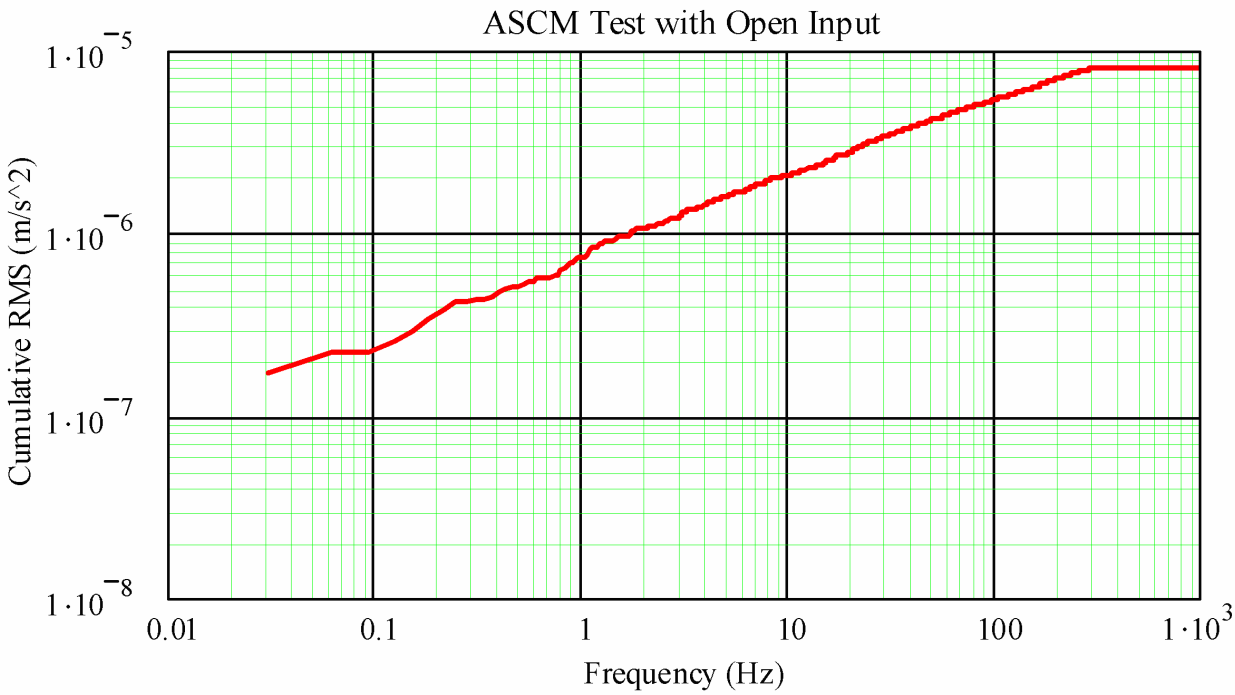

Figure 7. Cumulative rms noise in the gravimeter signal conditioning module.

The AIRGrav airborne gravity system

Stephan Sander, Malcolm Argyle, Stefan Elieff, Stephen Ferguson, Veronique Lavoie and Luise Sander
Sander Geophysics Ltd.
stephan@sgl.com

Abstract

An overview of the AIRGrav system (Airborne Inertially Referenced Gravimeter) is presented. Several design features and their positive effect on survey operations and system accuracy are discussed. These attributes are demonstrated in a case study of an AIRGrav survey of the Turner Valley gas and oil production field in Alberta, Canada.

Introduction

In 1992, Sander Geophysics Limited undertook a project to design an airborne gravimeter that would be well suited to the dynamic environment of an aircraft. The five year research and development project resulted in the AIRGrav system, which has been used for airborne surveying since 1997. The majority of these surveys have been conducted for the petroleum industry, as well as some applications to mining exploration. At present, four AIRGrav systems are employed in worldwide survey operations.

The AIRGRav system

The AIRGrav system consists of a three-axis gyro stabilized inertial platform with three orthogonal accelerometers. Unlike gravimeters used in traditional airborne surveys, the AIRGrav system does not use any spring-type apparatus. The accelerometer is held within 10 arc seconds (0.0028 degrees) of level by a Schuler tuned inertial platform, monitored through the complex interaction of gyroscopes and accelerometers. This arrangement ensures that the gravimeter remains oriented vertically, independent of the manoeuvres of the aircraft.

The three-axis stabilized platform used in AIRGrav is controlled in a fundamentally different way to the platforms used with the Lacoste and Romberg (L&R) or Bell gravimeters. The L&R and Bell two-axis platforms rely on a control loop which attempts to null the horizontal accelerometers on the platform with a settable time constant. The setting of this time constant is a trade-off between averaging out the disturbing effects of horizontal accelerations and still being able to correct for the drift of the gyros. The control loop used in AIRGrav relies on the very low drift of its high-accuracy gyros, and the platform can be Schuler tuned to the period of 84 minutes so that is does not tilt when accelerated (Lawrence, 1992). This allows draped surveys to be flown and allows surveying in turbulence similar to what is practical for high resolution magnetometer surveys. This is demonstrated in Figure 1, which shows there is little correlation between noise level and turbulence.

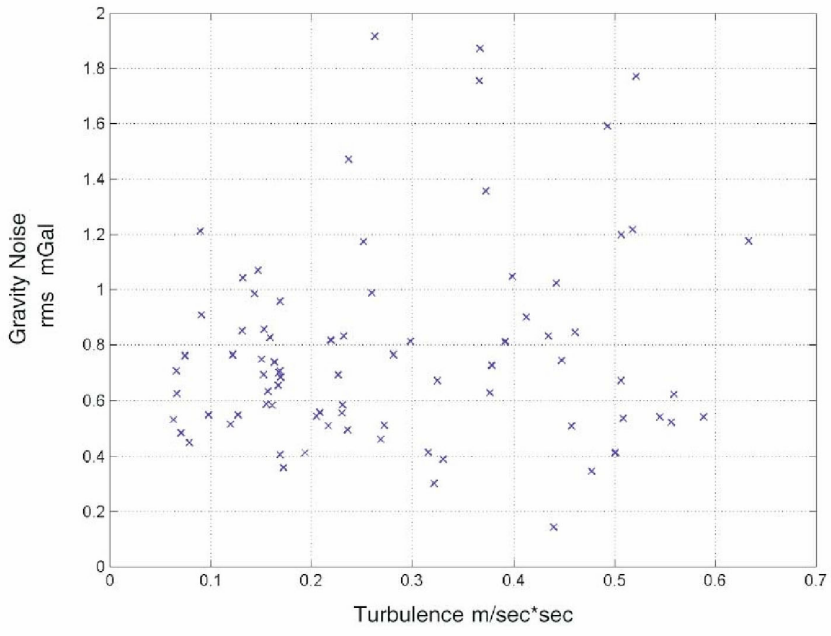

Figure 1. A comparison of the standard deviation of the vertical accelerations on the gravimeter to the gravity noise, determined from a comparison to ground gravity, for five-minute periods on the same test lines. The turbulence levels experienced have no noticeable effect on the gravity data. The slope of a line fitted to these points is almost zero, and some of the segments flown under the most turbulent conditions have the least gravity noise. These lines were flown under normal daytime conditions over three weeks. The turbulence ranged from calm to moderate. Figure reproduced from Argyle et al., (2000).

The gravity sensor used in AIRGrav is a very accurate three-axis accelerometer with a wide dynamic range. This avoids the saturation that occurs with spring-type sensors during strong vertical motion of the aircraft. Testing has shown the accuracy of gravity recovery to be almost completely unaffected by aircraft dynamics up to what is considered “moderate” turbulence. The wide dynamic range also allows draped surveys to be flown, something which is nearly impossible with other gravimeters. The AIRGrav sensor has extremely low cross-coupling (i.e., errors introduced by deformation of the sensor and conversion of horizontal acceleration into vertical acceleration) due to the very tight servo control of its proof mass, and needs no corrections for this effect. The sensor is extremely linear and does not need a test range to be calibrated. The design of the platform is such that the sensor can be “tumbled” in the gravity field at a calibrated point to set the scale factor and offset.

AIRGRav operations

The AIRGrav system itself is lightweight, with an installed weight of less than 100 kg. This allows it to be installed in survey aircraft in conjunction with other geophysical equipment, including that necessary for magnetic surveys. The gravimeter has been flown in a range of aircraft; twin engine Cessna 404 and Britten-Norman Islanders, single turbine engine Cessna 208B Grand Caravans, as well as in a Eurocopter AS 350 helicopter. The resolution and accuracy of the final gravity data is primarily dependent on flying speed and line spacing rather than the type of aircraft.

There are no additional restrictions on flight parameters beyond those typically used for aeromagnetic surveys in terms of operating altitude, ground clearance, and turbulence. Level flight is not required; a draped surface can be used to follow the terrain. A short lead-in of 3-5 km is typically flown to minimize on-line effects from aircraft turns. In practice, a large portion of this extension data can be included in the final data set because turn effects are minimal. The system has been used successfully offshore, in mountainous terrain, in deserts in Africa and the Middle East, and in the Canadian high arctic in winter conditions.

During field operations, the accelerometer scale factors and offsets can be calibrated at the survey base to correct for slow time variations in these parameters by rotating the platform through 180 degrees to measure the strength of the gravity of the Earth with positive and negative polarity. A test calibration range is not needed. The value used for gravity during calibration is ideally from a ground instrument or a known local gravity point, although it is possible to determine a local gravity value with sufficient accuracy using only the AIRGrav instrument. The system also automatically aligns and calibrates its gyros on start up before each flight, by determining the gyro drifts and XY bias.

Before and after each flight, the accuracy of the local gravity reading computed by the system is verified and instrument drift monitored by measuring gravity on the ground for 15 minutes or more. This period can also be used as an initialization period when the differential GPS data processing is performed, resulting in better accuracy. Daily before-flight and after-flight average readings are plotted and monitored for signs of instrument drift. Linear drift corrections have proved unnecessary and are not applied. Pre- and post-flight readings typically match within +/- 1 mGal, and variations over the course of a survey are only a few mGal. Gravity data can be tied to the local gravity system by comparing the measured gravity to existing gravity data where available, but this is not necessary. In many remote locations where the AIRGrav system has operated, the self calibrated AIRGrav measurements are potentially more accurate than the pre-existing gravity data.

Data processing

Whilst flying a survey, accelerations in an aircraft can reach 1 m/s, equivalent to 100 000 mGal. Data processing must extract gravity data from this very dynamic environment. This is achieved by modelling the movements of the aircraft in flight by extremely accurate GPS measurements. Dual frequency GPS receivers are employed on the aircraft and in ground reference stations used for differential GPS processing. Extensive research at SGL has resulted in high quality differential GPS processing techniques which are critical to achieving high resolution and high accuracy gravity data. In addition to providing the lowest possible noise levels, these techniques allow surveys to be completed successfully despite poor satellite geometry and high ionospheric activity, an essential requirement for surveys in far northern and southern latitudes.

Gravimeter data are recorded at 128 Hz. Accelerations are filtered and decimated to match the GPS, recorded at 10 Hz, using specially designed filters to avoid biasing the data. Gravity is calculated by subtracting the GPS derived accelerations from the measured accelerations. The calculated gravity is corrected for the Eötvös effect and normal gravity, and the sample interval is reduced to 2 Hz.

The following standard corrections are then applied to the gravity data to calculate the Bouguer anomaly.

a) Free air correction, g_{fa} in mGal given by

$$g_{fa} = -0.3086 \cdot z$$

where z is height of the aircraft in metres above the geoid.

b) Bouguer, g_{sb} given by

$$g_{sb} = -2\pi\gamma\rho h$$

where γ is the Universal Gravity constant, ρ is a density appropriate for the area, and h is height of the ground above the geoid.

c) Curvature correction, g_{ec} in mGal given by

$$g_{ec} = (1.464e-3)h - (0.3533e-6)h^2 + (0.000045e-9)h^3$$

where h is height of the ground above the geoid in metres.

d) Terrain, g_t, computed using 2D FFT methods with a density appropriate for the area. Since the accuracy of the terrain correction is limited by the accuracy of the input terrain model, an on-board laser altimeter or LIDAR is employed which, in conjunction with differential GPS processing, enables the calculation of a digital terrain model in the survey area. As in ground surveys, poorly modelled terrain data could cause a significant error in the processed gravity data.

e) Level Correction, g_{lc} , based on averages of intersection differences between primary and tie lines after low-pass filtering. Individual lines are levelled by applying a constant level shift to the entire line to minimise the differences between line and tie line intersections. In recent airborne gravity surveys only very minor constant per-line levelling corrections have been needed.

Applying these corrections, the complete Bouguer anomaly, g_{cba} is given by

$$g_{cba} = g_{En} - g_{sb} - g_{ec} + g_t - g_{lc}$$

where g_{En} is the calculated gravity adjusted for Eötvös effect and normal gravity.

The gravity data are filtered to remove noise using a low pass FFT filter prior to free air correction. Different filter settings are used depending on the application. After the standard corrections have been applied, the gravity data are gridded using the same minimum curvature gridding algorithm that is used for aeromagnetic data. A 2D spatial filter is then applied to the gridded data to maximize the resolution of the data by allowing noise cancellation between adjacent lines.

Turner Valley case study

In 2001, SGL flew a large AIRGrav survey in Western Canada over the Turner Valley area, an oil and gas producing region south of Calgary, Alberta (Pierce et al., 2002a, b; Sander et al., 2002). The survey area covered the foothills of the Rocky Mountains. The general trend of the geology in the area is north-north-west / south-south-east. A total of 12 500 line km of AIRGrav and magnetometer data were acquired simultaneously using a fixed-wing aircraft. The survey was completed in less than five weeks over very mountainous terrain, ranging from approximately 1000 m ASL to approximately 2000 m ASL. East-west traverse lines were spaced at 250 m and north-south tie lines at 1000 m.

Figure 2 shows the AIRGrav and aeromagnetic data acquired during the Turner Valley Survey. The colour image displays the first vertical derivative of Bouguer gravity, with the warm colours representing vertical gravity gradient highs. The grey shades are the shadow of the first vertical derivative of the aeromagnetic data.

The western side of the survey area is dominated by north-south trending faults associated with the foothills region. The eastern side of the area consists of flat lying sediments. Gas and oil producing areas are outlined by solid and dotted lines respectively. The long north-south trending field in the centre of the area is the Turner Valley Field, discovered in 1914. The Turner Valley and Quirk Creek Fields (in the north-west of the area) are generally associated with gravity highs. East-west trending lineaments, marked with dashed lines, were defined by joining terminations seen in the aeromagnetic data. The same lineaments also mark changes in the gravity signal, and offset the Turner Valley Field.

Existing ground gravity readings were compared with the AIRGrav data. Figure 3 shows the very good agreement between the two data sets. The uniform sampling provided by the airborne survey, however, brings out additional detail in areas that are sparsely sampled by ground data. Creating a grid of airborne gravity using only points where ground gravity exists improves the apparent correlation with the ground data, an indication that differences are due to improved airborne sampling (Pierce, 2002). The ability to provide uniform sampling over difficult terrain that is often inaccessible to ground surveys is one of the advantages of an airborne survey. The AIRGrav system is particularly well suited to this task it has low sensitivity to aircraft motion. The survey area is subject to frequent periods of turbulence caused by winds blowing down from the Rocky Mountains, and the climb into the foothills required a draped flying surface.

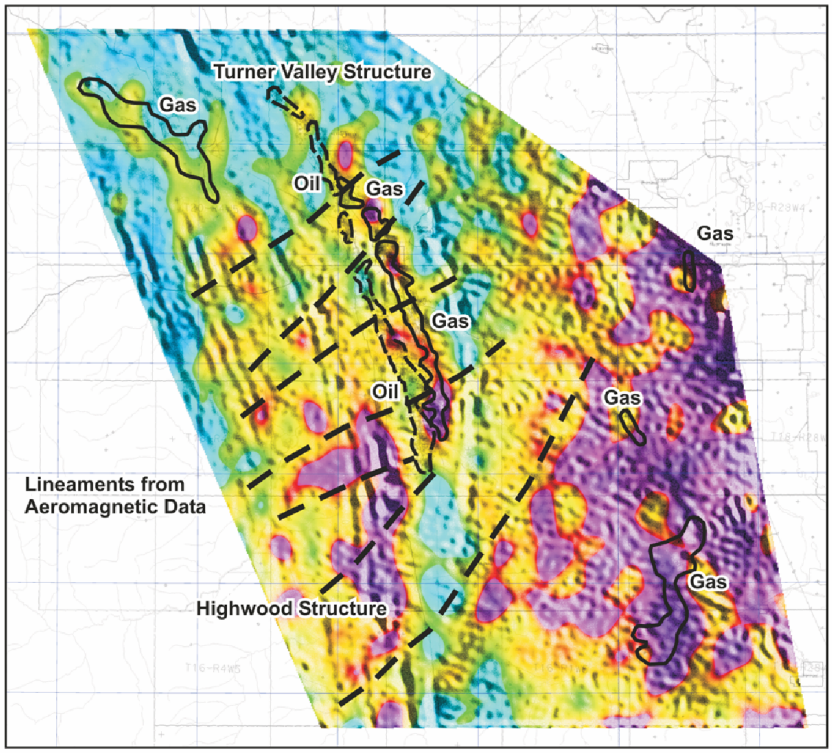

Figure 2. First vertical derivative of AIRGrav data from the Turner Valley Survey with a shadow of the first vertical derivative of the magnetic data. The known oil and gas fields are shown. The survey area is 60 km from south to north. Figure reproduced from Sander et al. (2002).

Estimate of noise

Noise levels and system resolution require careful specification. Survey parameters, along with the instrument itself, are important factors in the resolution and accuracy of the final data products delivered to a client. A survey flown with tight line spacing, for example, takes advantage of over-sampling to reduce noise levels (Sander et al., 2003). Flying speed plays a role in determining AIRGrav resolution since the primary source of noise is from the GPS signal, which is time dependant. It is possible to increase the resolution to a degree simply by flying slower.

AIRGrav typically delivers gravity data which have been low-pass filtered using a filter of half-length 40 s. Converted to wavelength, this equals a half-width of 2.0 km in a Cessna Grand Caravan or Britten-Norman Islander flown at 100 knots, 2.9 km in a Cessna 404 flown at 140 knots, and 1.0 km in a Eurocopter AS350 helicopter flown at 50 knots. These numbers are based on the repeatability of 40 test lines flown near Ottawa using different aircraft.

Once the objectives of the survey are established, line spacing and flying speed are tailored towards meeting those objectives. In a recent petroleum survey flown in the Middle East, for example, 500 m line spacing was used. The final grid had real anomalies as small as 0.4 mGal and 2.0 km in size that were independently verified in a blind test using detailed ground measurements. Noise levels on the final grid data

were 0.2 mGal, based on a measurement of internal consistency made using independent grids formed from alternate lines.

This method of comparing independent grids of airborne data to estimate the precision of the measurements was applied in the Turner Valley example (Sander et al., 2002). The line spacing of 250 m over-sampled the data given the application of a low-pass filter with 4 km cut-off. Two independent grids were produced by separating the data into two subsets (i.e., odd and even line number grids with 500 m line spacing). The rms value of the differences between these grids indicated a precision of 0.3 mGal for the complete dataset.

A case study for a survey in Timmins (Ontario, Canada) (Elieff, 2003; Elieff et al., 2004) quantified noise levels using a number of internal and external measures. This survey was flown with 500 m line spacing, and the gridded data were low-pass filtered with a cut-off wavelength of 2.85 km. The standard deviation of differences at flight and tie line crossovers indicated a precision of 0.45 mGal for the filtered line data. Differences between odd and even flight line number grids had a standard deviation that indicated a precision of 0.15 mGal in the final grid after spatial filtering. The standard deviation of differences between the airborne data and upward continued ground data was 0.62 mGal. This provides an upper bound estimate of the external accuracy of the system since it also includes errors present in the ground data and differences resulting from application of filtering to the airborne dataset but not to the ground dataset.

Conclusions

AIRGrav has been used to acquire airborne gravity data for both on-shore and off-shore surveys. The system allows drape surveys to be flown, resulting in better signal levels in surveys areas with significant topographic relief. Final grids created with low-pass filters in the 2 – 4 km range have noise standard deviations between 0.15 and 0.3 mGal. This number is dependant upon survey parameters, such as line spacing and aircraft speed, as well as the details of the specific filter used.

References

Argyle, M., Ferguson, S., Sander, L., and Sander, S., 2000, AIRGrav results: a comparison of airborne gravity data with GSC test site data: The Leading Edge, October 2000, 19, 1134-1138.

Elieff, S., 2003, Project report for an airborne gravity evaluation survey, Timmins, Ontario: Report produced for the Timmins Economic Development Corporation on behalf of the Discover Abitibi Initiative. (http://www.discoverabitibi.com/technical-projects.htm)

Elieff, S., and Sander, S., 2004, AIRGrav Airborne Gravity Survey in Timmins, Ontario: This volume.

Lawrence, A., 1993, Modern inertial technology: navigation, guidance, and control: Springer-Verlag, New York.

Pierce, J.W., Sander, S., Charters, R. A., and Lavoie, V., 2002a, Turner Valley, Canada – A Case History in Contemporary Airborne Gravity: Presented at EAGE 64th Conference & Technical Exhibition – Florence, Italy, 27-30 May 2002.

Pierce, J.W., Sander, S., Charters, R. A., and Lavoie, V., 2002b, Turner Valley, Canada – A Case History in Contemporary Airborne Gravity: 72nd Ann. Internat. Mtg: Soc. of Expl. Geophys., 783-786..

Sander, S., Ferguson, S., Sander, L., Lavoie, V., and Charters, R.A., 2002, Measurement of noise in airborne gravity data using even and odd grids: First Break, August 2002, 20, 524-527.

Sander, S., Lavoie, V., and Peirce, J., 2003, Advantages of close line spacing in airborne gravimetric surveys: The Leading Edge, February 2003, 22, 136–137.

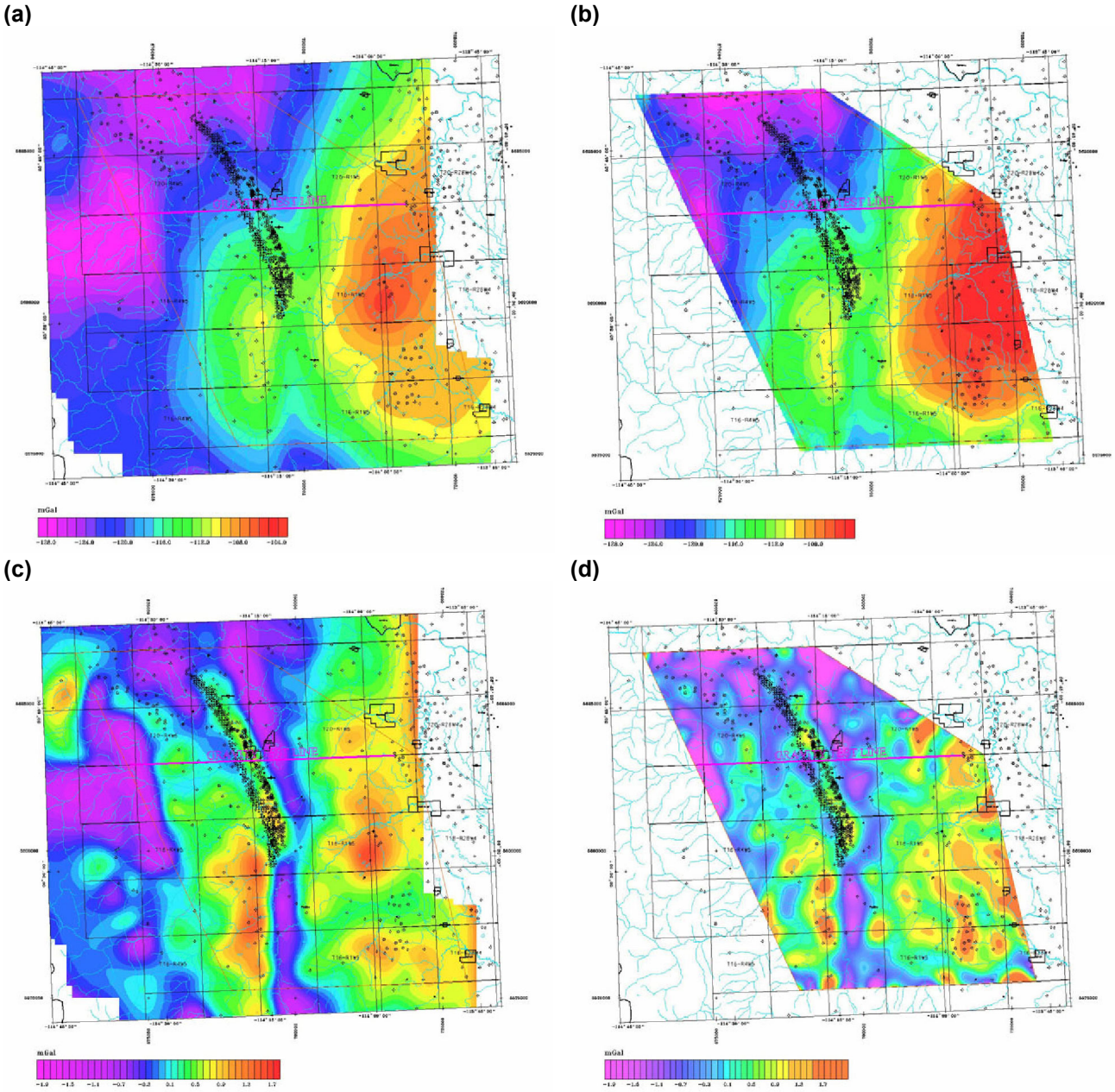

Figure 3. Complete Bouguer Gravity data from the Turner Valley area. The images in (a) and (c) are based on older ground gravity data. These data have been upward continued 500 m and filtered with a 5300 m low-pass filter to match the airborne parameters as closely as possible. The images in (b) and (d) are from the Turner Valley Airborne Survey. The images in (a) and (b) show complete Bouguer gravity data, whilst (c) and (d) show the first vertical derivative of complete Bouguer gravity data. The regional slope reflects the isostatic effect of the Rocky Mountains, just west of the survey area. Figure reproduced from Pierce et al. (2002b).

The GT-1A mobile gravimeter

Andrew Gabell
Canadian Micro Gravity Pty Ltd
andy@canadianmicrogravity.com

Helen Tuckett
Canadian Micro Gravity Pty Ltd
helen@canadianmicrogravity.com

Daniel Olson
Canadian Micro Gravity Pty Ltd
dan@canadianmicrogravity.com

Abstract

The GT-1A is a small, lightweight, low-power GPS-INS gravimeter suitable for use in a wide range of vehicles. To date, it has been used mainly in fixed wing aircraft to acquire in excess of 30 000 line km of data. Given an acquisition speed of 50 to 70 m/s and filter length of around 100 s, resolution (standard deviation) is 0.6 mGal or better for a half-wavelength of 2.0 to 3.5 km. Limited, but promising testing of the instrument has been carried out in a small helicopter, and it is expected that a half-wavelength spatial resolution of 0.8 km or better should be achievable.

Introduction

Since being commissioned in April 2003, the GT-1A mobile gravimeter has been used to acquire in excess of 30 000 line km of data outside of the Russian Federation and a similar quantity of data within Russia. The gravimeter was developed by Joint Stock Company Gravimetric Technologies in the Russian Federation as a "dual purpose technology" – designed for both military and civilian applications. The post-processing software was developed by the Lomonosov Moscow State University's Department of Mechanics and Mathematics. The GT-1A is made available for commercial use for non-military applications outside the Russian Federation by Canadian Micro Gravity Pty Ltd.

Description

The GT-1A is an airborne, single sensor, vertical scalar, GPS-INS gravimeter with a Schuler-tuned three-axis inertial platform. The gravimeter, shown in Figure 1 installed in a Cessna 404, weighs 50 kg. It sits on a turntable (the brass-coloured unit in the centre of the photograph) that provides the platform's azimuth axis control. Together, the gravimeter and turntable measure 40 x 40 cm by 70 cm high. In turn, they are installed on a shock-mount that is partially obscured towards the bottom of Figure 1, an arrangement of 4 main springs and 8 dampers having a cut-off frequency of 5 Hz. The shock-mount is 60 cm in diameter and 22 cm high, and weighs 60 kg, giving an overall height to the gravimeter of 92 cm, and an overall weight of 110 kg. The top third of the main unit houses most of the electronics (Figure 2), while the gravity sensor is held in vertical alignment by the inertial platform, located in the bottom of the main unit (Figure 3).

Figure 1. Photograph of the GT-1A gravimeter installed in a Cessna 404. The gravimeter sits on a brass-coloured rotating table, which in turn sits on the shock mount. In the left foreground is the uninterruptible power supply (UPS), and to its right is a small blue Z-Surveyor dual frequency GPS receiver.

Figure 2. Photograph of the GT-1A gravimeter from above, with cover removed showing the electronics bay.

Figure 3. Photograph of the GT-1A gravimeter from the side, with cover removed showing the gyro-stabilized platform contained in a double-axis gimbal suspension.

Connections to the gravimeter are a 27 V DC power source drawing approximately 5 A, an RS-232 serial link through which GPS velocity and co-ordinate data are transmitted to assist in aligning the platform vertical, and a second serial connection to a field data acquisition computer. This computer acts as the control and display unit for the gravimeter, as well as collecting and storing data.

The gravity sensor and inertially-stabilized platform

The vertical accelerometer, or gravity sensing element (GSE), has an axial design with a reference mass on a spring suspension, a photoelectric position pickup and a moving-coil force feedback transducer. The GSE suspension design minimizes the effect of cross-coupling, an undesirable effect which contaminates gravity measurements with components of horizontal accelerations induced by aircraft motion. This feature allows the GT-1A to collect data in the presence of large horizontal accelerations, such as during aircraft turns or during periods of high turbulence. The GSE, with a bandwidth of 100 Hz, is installed on the gyro-stabilized platform contained in a double-axis gimbal suspension.

In addition to the GSE, the platform also holds two horizontal accelerometers, a dynamically tuned gyro, a fibre optic gyro (FOG) for azimuth control, and two gravimeter calibration devices (GCD's). The GCD's are designed to calibrate the gravimeter by means of inclination without dismounting the GSE The gravimeter also contains a microprocessor, input/output interfaces, and secondary power supplies, all within the electronics bay at the top of the main unit. The GSE is placed in a double-loop constant-temperature environment on the inertial platform. The other elements installed on the platform, plus the current regulator of a code-to-current converter within the gyro control circuit, are individually temperature controlled.

Internal software

The internal microprocessor carries out a large number of measurement and control functions. Measurements of platform orientation, rotation rates and accelerometer outputs are taken at 300 Hz, the same rate at which critical platform control and other internal functions are carried out. The high sampling rate minimises aliasing of the high frequency vibrations encountered in an aircraft. These data are passed through an anti-aliasing filter and are subsequently processed at a rate of 18.75 Hz. The main control loop also runs at this frequency, and the output data files are recorded at either this rate or at 3.125 Hz, depending on the channels recorded.

Velocity and latitude information are fed through to a Kalman filter from the GPS receiver to provide GPS-aided platform levelling.

Operating software

The gravimeter is operated by programs running on an external control and display computer, which can be any robust data acquisition computer with a serial port. The Windows-based program includes calibration and diagnostic functions. The calibration program has two modes for carrying out automatic GSE calibration. A 3-hour measurement period provides GSE calibration coefficients, while over a period of 5.5 hours; the program determines the above coefficients plus the non-perpendicularity of angles between the GSE and the platform surface. The calibration program is normally run once before each survey project and does not need to be run at the completion of the project.

The diagnostic program maintains a running check on the serviceability of all gravimeter sub-systems. Warnings regarding data quality are presented to the pilot through an indicator light: solid green means all

systems are okay; flashing red means turbulence is approaching upper limits for the acquisition of high quality data; and solid red means a system failure has occurred.

Operation

The gravimeter is fully automated – no operator is required on board the aircraft while collecting data on survey lines. All systems including stabilization servo systems, temperature control systems and gyroscopic correction systems are controlled by the in-built microprocessor. The computer also takes control of actuation, reference measurements, balancing, and measurements in survey mode. A vertical gyro correction system using GPS-derived information on heading, latitude and aircraft speed provides vertical gyro stability. A Kalman filter is implemented in control algorithms for both the stabilization servo system and the vertical gyro correction system.

The calibration sequence is also fully automated, and is initiated by selection of an item from a drop-down menu.

The normal data acquisition procedure requires that the aircraft be located at the same reference position at the airfield before and after each flight. The location of the aircraft GPS antenna, and that of the GPS base station antenna, needs to be known accurately. With the GPS base station operating, a 20 minute pre-flight reference measurement is undertaken, and the gravimeter is then configured for data recording “in motion”. The instrument records continuously in flight, including during turns. This results in very short (typically 4 km) “lead-ins” and “lead-outs” from survey lines. Following each flight, the aircraft is parked at the same reference location, and the gravimeter is configured for the post-flight reference measurement, which normally has a duration of 1 hour.

The main operational drawback of the GT-1A, as is the case for most gravimeters, is the requirement for the system to remain powered continuously. Aircraft manoeuvres are restricted to 12° in pitch and roll. Some experimental flights have been undertaken at low altitude, using terrain following (draping) rather than constant altitude. Preliminary results from these flights indicate that noise levels are higher, but that satisfactory data can still be collected.

System performance

Dynamic range

Two dynamic ranges are measured and recorded simultaneously: +/- 250 Gals (2.5 m/s) and +/- 500 Gals (5 m/s). The smaller range data has a finer resolution, and is used to process data collected during periods of calm to moderate flying conditions, while the coarse range allows processing of measurements made in more turbulent conditions. Data are acquired through short periods of accelerometer saturation in extreme turbulence by the automatic application of a reduced-order Kalman filter, enabling platform misalignment to be computed and hence controlled. These design elements together provide a high tolerance to turbulence.

Spatial Resolution

The spatial resolution can be calculated by multiplying the filter length by the aircraft speed in m/sec, and dividing by 2 to obtain the half-wavelength resolution in metres. The filter response is shown in Figure 4. The filter length is specified as the period at which the output response is attenuated by half. The GT-1A is capable of providing a range of spatial resolutions through the choice of aircraft, and the application of filters with varying cut-off frequencies. Filters are chosen on the basis of aircraft ground speed, survey line spacing, and target dimensions.

Filters typically vary from 80 to 110 s, which provides half-wavelength resolutions of 2.0 and 2.75 km respectively with an aircraft ground speed of 50 m/s.

A helicopter flying at 20 m/s would provide half-wavelength resolutions of 800 m and 1.1 km with 80 and 110 s filters respectively.

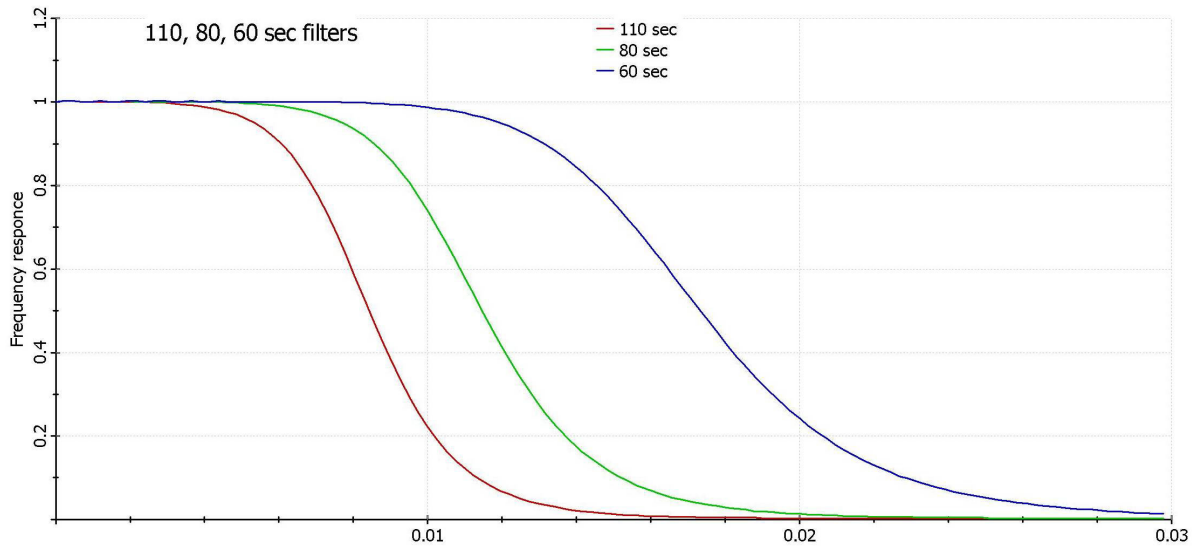

Figure 4. Plot of the filter response used in processing GT-1A data. The filter length is specified as the period at which the output response is attenuated by half.

Sensitivity

Two methods for estimation of noise levels will be discussed. The first method entails analysis of data acquired along a 90 km long repeat line at Vredefort Dome, near Johannesburg in South Africa. Figure 5 shows the results obtained with two different gravimeters; GT-1A serial numbers 1 and 2. Figures 5a and 5b each show five profiles of free-air gravity values acquired on separate passes along the repeat line with GT-1A serial numbers 1 and 2 respectively. The five profiles, plotted in different colours, are virtually indistinguishable at this plotting scale. The method of Green and Lane (2003) was used to estimate noise levels for each data set independently. The overall results were standard deviations of 0.54 mGal for serial number 1 and 0.47 mGal for serial number 2. A filter of length 107 s was applied to these data, which corresponds to a wavelength of 7.3 km at an average speed of 68 m/s. It is interesting to note that the corresponding standard deviation of repeat line data from serial number 2 using an 80 second filter was 0.36 mGal.

The five lines from each instrument were then averaged, and one average was subtracted from the other. The result is shown in the Figure 5c. The standard deviation of this "difference profile" is 0.29 mGal.

The second method used to estimate noise entailed comparison of airborne data with upward-continued ground data from the Kalgoorlie region of Western Australia. Figures 6a and 6b show the ground and airborne free-air gravity data respectively. The northern two thirds of the ground data were acquired along east-west traverses with 50 m station spacing and 200 m traverse spacing. The station spacing was 200 m in the southern third of the area. Two sets of airborne data were acquired. The airborne data shown in Figure 6b ("Area 1") were acquired on north-south traverses with 250 m line spacing, at a constant barometric altitude averaging 378 m above the mean terrain height. After trimming the "lead-ins" and lead-outs" these lines were 20 km long. A second set of lines, also at 250 m spacing, was acquired at constant barometric altitude averaging 500 m above mean terrain height, with traverses oriented east-west ("Area 2"). These lines were acquired over the central half of the area covered by the north-south survey lines.

A standard deviation was calculated for each of a series of "difference grids", as follows:

- Ground data (upward continued by 328 m) minus Area 1 grid – 0.41 mGal;
- Ground data (upward continued by 500 m) minus Area 2 grid – 0.42 mGal
- Area 1 grid (upward continued by 172 m) minus Area 2 grid – 0.44 mGal

Of interest, a series of repeat lines acquired while the GT-1A was mounted in a Toyota Land Cruiser 4WD vehicle driven at 5 m/s resulted in noise estimates of the order of 0.3 mGal (Gabell and Tuckett, 2003).

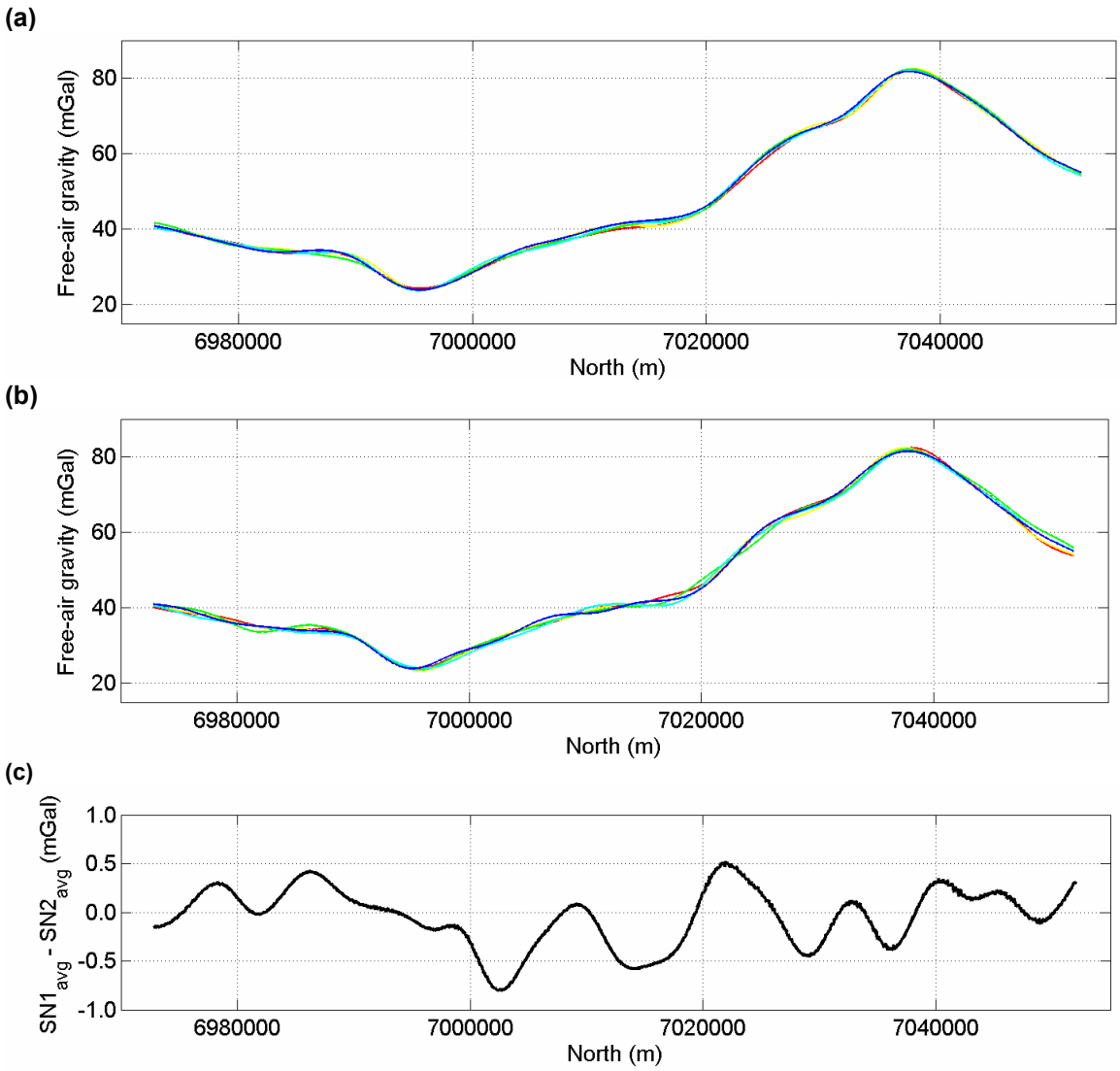

Figure 5. Profiles of data for a 90 km long repeat line from Vredefort Dome, near Johannesburg, South Africa. (a) Free-air gravity values for 5 lines acquired in March 2004 with GT-1A serial number 1. The noise estimate standard deviation using the method of Green and Lane (2003) is 0.54 mGal.
(b) Free-air gravity values for 5 lines acquired in May 2004 with GT-1A serial number 2. The noise estimate standard deviation is 0.47 mGal.
(c) Profile of the difference between the average values of the 5 lines of data from each gravimeter – the standard deviation of this difference profile is 0.29 mGal.

Productivity

Productivity is highly dependent on survey design, the distance from the base of operations to the survey area, and flying conditions. In particular, the onset of thermal turbulence when surveying over land usually determines the length of the flight. In extreme conditions, such as those encountered in Arnhem Land (Northern Territory, Australia) in September 2003 where temperatures were typically between 30 and 40°C and a large part of the survey area was over bare rock, as little as 3 hours was available for data acquisition. This reduced daily production to approximately 350 line km.

In more benign conditions, such as those encountered in Africa in 2004, daily production exceeded 1000 line km on a number of occasions, and 800 line km was often achieved for a full-length flight.

Off-shore thermal turbulence is not an issue, and productivity is primarily determined by the aircraft's endurance, and the ferry distance to the survey area.

Drift

The GT-1A's GSE design provides for a slow and highly linear drift which is easily compensated by recording 20 minutes of reference data at the same location immediately prior to each flight, and 1 hour of reference data at the same location following each flight. Total drift for flights of up to 6 hours has always been less than 1.0 mGal. The reference measurements are used to correct for instrument drift using linear interpolation.

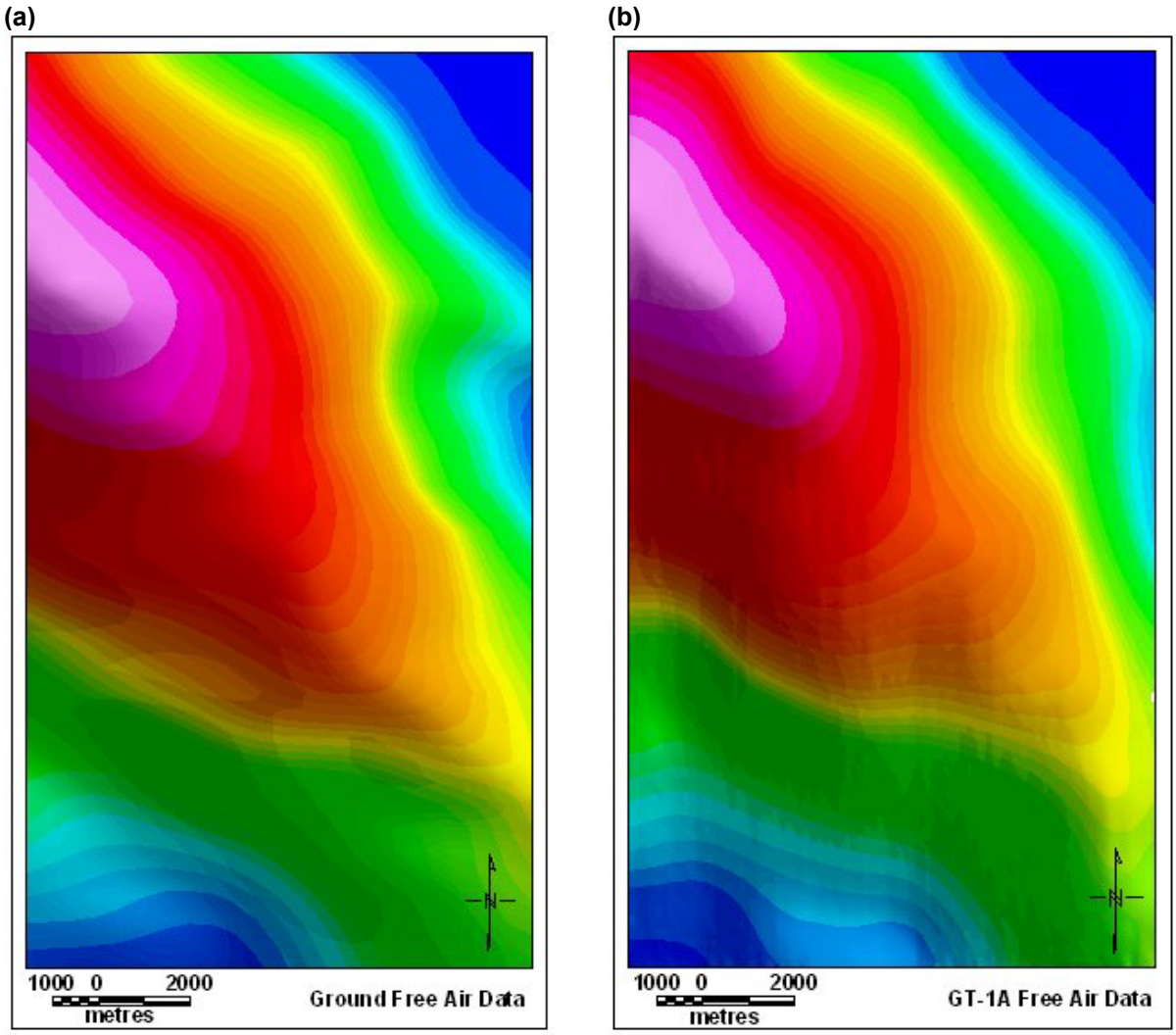

Figure 6. Free-air data from the Kalgoorlie region, Western Australia. (a) Ground data upward continued by 328 m. (b) Airborne data acquired at constant altitude 328 m above the mean terrain altitude. The standard deviation of the difference between these grids is 0.41 mGal.

Data post-processing

Proprietary programs developed by Moscow State University (MSU) are used in conjunction with commercially-available software to post-process GPS and gravimeter data.

Waypoint's GrafNav is first used to generate a position file (a "C-file") from base and rover GPS data. The C-file is input, along with binary GPS files and "S-files" (INS platform data recorded by the gravimeter) to "GTNAV", an MSU program. The output files are loaded into Geosoft and critical parameters examined for QC purposes. GTQC20, another MSU program, is then used to QC "S-files" and "G-files" (acceleration data recorded by the gravimeter).

The files produced by the previous programs are loaded into GTGRAV, the final MSU program. GTGRAV calculates the free-air gravity anomaly using a user-defined filter length and several other parameters that are used to tune a Kalman filter. The free-air anomaly can be produced using a variety of latitude and free air correction formulae, and, if an absolute reading is available for the reference position, absolute free air anomalies are output.

The resultant data are then loaded into Geosoft for production of grids and levelling. Grids are produced on a daily basis, and are usually available 4 to 6 hours after data is loaded onto the laptop computer used for field processing, depending on the amount of data collected. In some cases a 2D noise reduction filter is applied to the gridded data.

If required, simple and complete Bouguer corrections can be generated. As the free-air anomaly output from GTGRAV is filtered, the Bouguer and terrain corrections also need to be filtered using the same 1D and/or 2D filters. This ensures that the frequency content of the corrections matches that of the free-air anomaly data. The Bouguer correction is usually supplied as a filtered, "normalized" correction (i.e. using a density of 1.0 g/cm^3) to allow the end-user to generate Bouguer corrections using different densities without having to filter the resultant correction.

Final data are typically available 2 to 4 weeks after completion of the survey.

Conclusions

The GT-1A is suitable for use in a wide range of vehicles due to its small size, light weight and low power consumption. This results in the ability to acquire data with a wide range of spatial resolutions. On a fixed wing aircraft, at acquisition speeds of 50 to 70 m/s, the resultant half-wavelengths vary from 2.0 to 3.5 km when a filter of 100 s is applied. On a helicopter, a spatial resolution of 0.8 km or better should be achievable at acquisition speeds of 20 m/s.

The instrument is fully automated, collects data continuously, and does not require an operator during acquisition flights. Productivity is good, due to a high tolerance of turbulent flying conditions, and the need for only short lead-ins and lead-outs.

The sensitivity specification is a standard deviation of 0.6 mGal using a 107 s filter. Results from analysis of repeat lines as well as comparison of airborne and upward-continued ground data grids, demonstrates that this sensitivity is usually relatively easily achieved. Data processing is relatively fast, with grids being produced on a daily basis in the field.

Acknowledgements

The contribution of colleagues who developed the GT-1A and associated processing software deserves acknowledgement. From JSC STC Gravimetric Technologies, Valentin Ilyin, Sam Yurist, Yuri Smoller, and Vladimir Berzhitzky have all worked for a number of years on technology that culminated in the GT-1A. In addition, colleagues from Lomonosov Moscow State University – Professors Nicolai Parusnikov, Andrey Golovan and Yuri Bolotin have also contributed significantly through their development of GPS and gravimeter post-processing software. We would also like to thank Martin Frere and Ollie Wright from Fugro Airborne Surveys Central Region for kind permission to publish the comparison of repeat line data collected with GT-1A serial numbers 1 and 2.

References

Berzhitzky, V. N., Bolotin, Y. V., Golovan, A. A., Ilyin, V. N., Parusnikov, N. V., Smoller, Y. L., and Yurist, S. S., 2002, GT-1A Inertial Gravimeter System - Results of Flight Tests: Unpublished report, available from CMG.

Gabell, A. R. and Tuckett, H.J., 2003, The GT-1A Demonstration Project: Unpublished report for Project Sponsors, available from CMG.

Green, A. A., and Lane, R., 2003, Estimating Noise Levels in AEM Data: Extended Abstracts, ASEG 16th Geophysical Conference and Exhibition, February 2003, Adelaide.

A synopsis of airborne gravity data presentation, modelling, interpretation and inversion software

Greg Walker
BHP Billiton Ltd
Greg.B.Walker@BHPBilliton.com

Abstract

A non-exhaustive attempt was made to list and summarise currently available presentation, modelling, interpretation and inversion software relevant to airborne gravity data. In the workshop presentation, the functionality of major commercial software packages was described where applicable to airborne gravity and gradiometry data, and representative output from these packages was shown. Interpretation tools used or provided by operators of airborne gravity and gradiometry systems were also discussed. In addition, inversion research projects currently being carried out by academic institutions and selected consortia and agencies were described with examples.

The following pieces of software and/or research were included in the presentation:

Commercial software:	GM-SYS Profile Analyst ModelVision INTREPID EMIGMA Potent Fugro-LCT
Contractors/operators software:	Bell Geospace FALCON® Mira Geoscience
Research software:	University of British Columbia Geophysical Inversion Facility University of Utah/CEMI Consortium Colorado School of Mines Gravity and Magnetics Research Consortium Rice University University of Leeds/GETECH

Software providers were invited to make CD-ROMs containing demonstration versions of software and sample data available at the workshop.

Acquisition and preliminary impressions of airborne gravity gradient and aeromagnetic data in the Eastern Papuan Basin, Papua New Guinea

Andrew Nelson
InterOil
andrew.nelson@interoil.com

Abstract

Hydrocarbons are being sought by InterOil in southern Papua New Guinea within sandstone, volcanoclastic and limestone reservoirs, with both structural (e.g., thrust induced anticlines) and stratigraphic (e.g., reefs) traps anticipated.

Mapping of the area by airborne gravity and magnetic techniques was considered due to the limited availability of base geological information from other methods. Density contrasts suitable for mapping using gravity methods were inferred to be present at shallow depth between limestone slabs and surrounding mudstones. Magnetic methods were anticipated to help map volcanic units, since these rocks have elevated magnetic susceptibility whilst the remainder of the sequence is non-magnetic. Sufficient seismic, ground gravity and outcrop information are available to enable an assessment of the airborne data to be carried out and to guide interpretation of these data over other parts of the survey area.

In 2002 and 2003, a Falcon™ Airborne Gravity Gradiometer system was used to acquire 6167 line km of airborne gravity gradiometer and magnetic data Interpretation of these data is currently in progress, but preliminary work has indicated that the airborne data will indeed prove valuable. Correlation of features in the aeromagnetic and gravity data with mapped outcrop and seismic observations has provided the confidence to use the airborne data to interpolate between and extrapolate away from these observations. This has led to improvements in the mapping of the area. This in turn may lead to siting of a well or planning for additional seismic data when the interpretation is completed.

Introduction

In Papua New Guinea, airborne geophysical exploration methods are preferred for exploration due to the high cost and slow progress of most ground based operations. This presupposes that they can provide the required target definition. Ground geophysical and geological work is hampered by rugged terrain, jungle cover and lack of roads. Airborne gravity gradiometer (AGG) and aeromagnetic methods have been used in InterOil Petroleum Prospecting Licences (PPLs) both to assist in detailing known leads and to extend existing interpretations from seismic, ground- and landsat-geological mapping, and wells. Due to the relative novelty of the AGG method, data were acquired in areas which already had seismic and ground gravity coverage. Not only did this help in the assessment of the airborne data, but enabled features in the airborne data to be tied to independent geological observations. We have been sufficiently encouraged at an early stage in the interpretation process to further assess the airborne data, and consider it possible that more extensive use of airborne methods could be carried out in the future should the interpretation show that these data can assist in the location and definition of exploration targets.

Geology

InterOil PPLs (Figure 1) are located in the Eastern Papuan Basin. Exploration targets are mainly within the Late Cretaceous and Tertiary interval, though hydrocarbon source rocks include sections as old as the Jurassic. The Papuan Basin represents the northeastern margin of the Australian continental plate. The Papuan Peninsula is a sliver of the plate which broke away with the opening of the Coral Sea, starting around Late Early Cretaceous time. It has since rejoined in its current position. The Aure Trough is a mobile zone at the edge of the Australian plate which received a Miocene section measuring several kilometres thick and has since partly inverted. St John (1990), on the basis of gravity data interpretation assisted by limited well and surface mapping information, estimated the preserved combined Miocene-Pliocene thickness to be up to six kilometres.

An outline of the stratigraphy of the licence area is shown in Figure 2. The lithology of the Aure Group in the Aure Trough section is predominantly fine clastics with occasional sands and greywackes/turbidites. This suggests a deep marine environment (Carman, 1993), but in areas of higher relief, reefal limestones, sandier units and pebble conglomerates are present suggesting a near-shore or sub-aerial environment in part. Prior

to the development of the Aure Trough, limestone deposition was extensive (e.g., Eocene Limestone), and limestone deposition continued around and within the trough where environmental conditions permitted. Some limestone units are porous and/or fractured and act as reservoirs. On the Papuan Peninsula, a more stable environment largely persisted, but volcanoclastics and basalt flows (Talama Volcanics) also feature in the section. The volcanoclastics have significant porosity and permeability where tested in offshore wells Maiva-1 and Lokea-1.

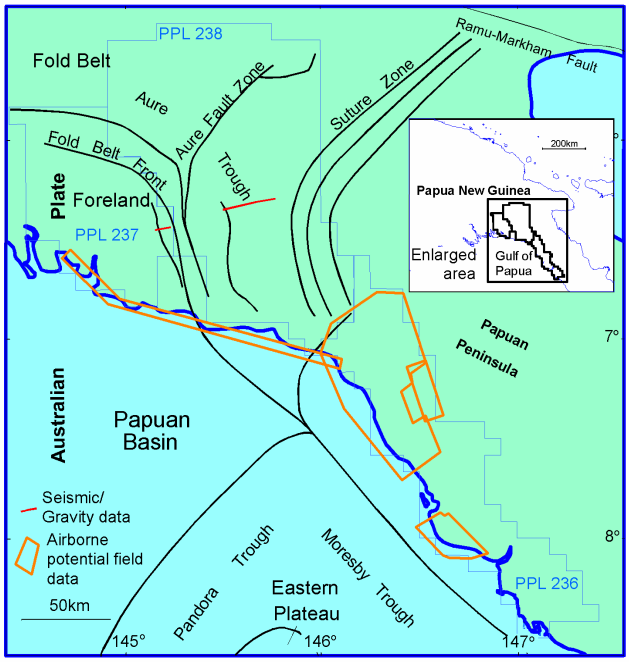

Figure 1. Location and tectonic elements map, InterOil licences, Papua New Guinea.

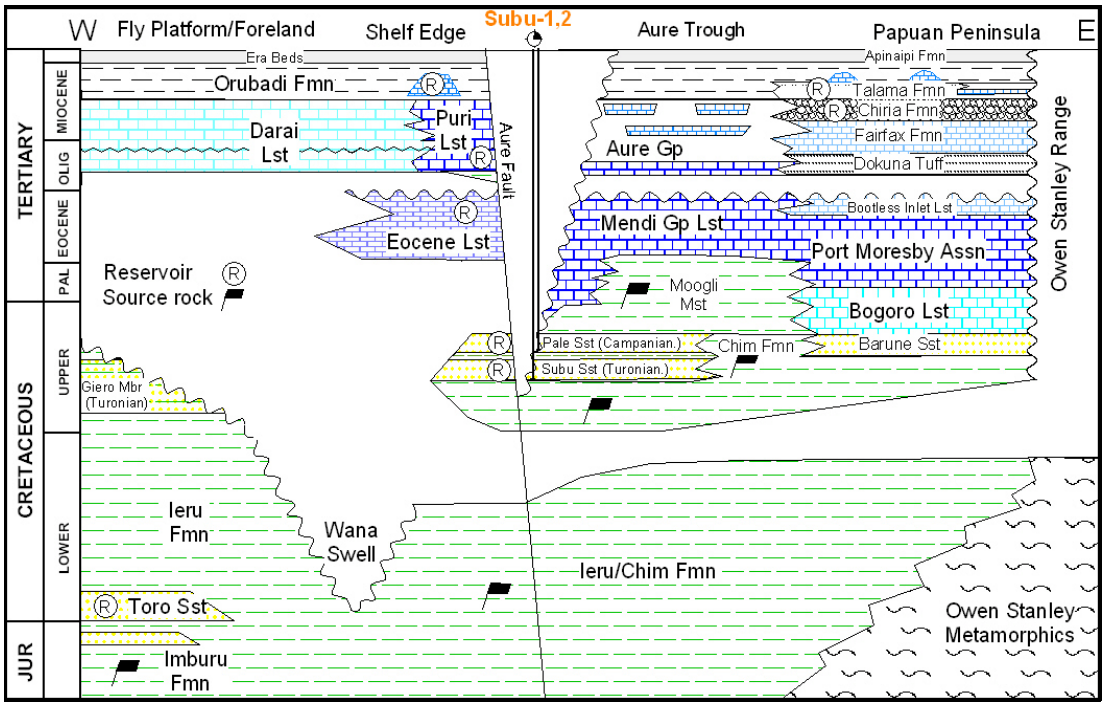

Figure 2. Stratigraphic chart, Eastern Papuan Basin and Papuan Peninsula. Note that source rocks are indicated with flag symbols whilst potential reservoirs intervals are shown with an ® symbol.

Basin inversion began as early as the end of the Early Miocene (Home et al., 1990) and is likely continuing today. The Orubadi Formation (mainly marine mudstone) represents redeposition of material eroded from the uplifted foldbelt. As deposition infilled and exceeded subsidence in the foreland area, conditions changed to nonmarine (Era Beds/Apinaipi Formation) and included occasional fluvial sands, coals and conglomerates.

GPS observations of plate movements (Tregoning, 2003) show that the Papuan Peninsula is currently moving in a westerly direction relative to the Australian Plate.

Pre-acquisition

Prior to acquisition, geological models of drilled and undrilled structures, including reef and buried faulted/folded limestone sheets, were used to determine the suitability of AGG methods to explore for this style of target. Forward modelling (BHP Billiton, 2002) suggested that reef targets could be resolved using a flight line spacing of 250 m. Due to a considerable range in terrain conditions from flat foreland areas less than 40 m above sea level to mountainous thrust belt areas, significant effort was applied to planning of a drape surface that would enable lines and tie lines to be flown as closely as possible to the nominal minimum terrain clearance of 120 m.

Acquisition

A total of 7500 line km was originally planned for acquisition in November and December 2002. It transpired that 6167 line km of airborne data were acquired in two phases in 2002 and 2003 (Figures 1 and 3). The original acquisition areas were modified to avoid areas where jungle cover would not allow an emergency landing to be carried out. This restricted acquisition to coastal areas where clearing or swamps reduced the extent of vegetation cover, and precluded acquisition in the jungle-covered areas with greater topographic relief.

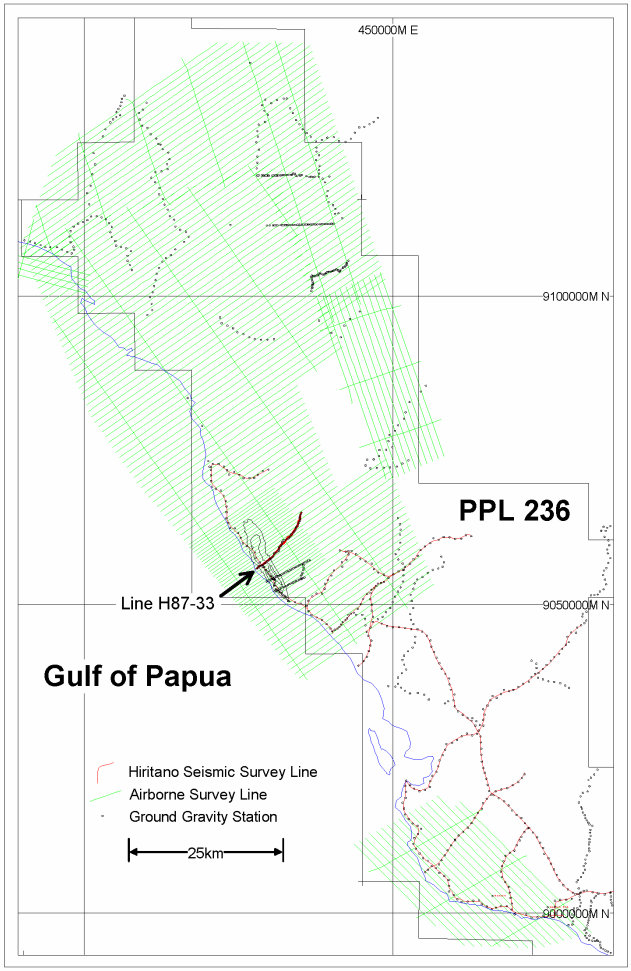

Figure 3. Airborne data from PPL 236, showing the location of existing seismic and ground gravity data. Seismic line H87-33 (arrowed) in the Oiapu area is shown in Figures 4 and 5.

Data were acquired with a Falcon™ airborne gravity gradiometer system. Aeromagnetic data were acquired at the same time. Although earlier studies had suggested a line spacing of 250 m, other constraints dictated that this spacing be increased to 1 km, with 500 m line spacing in an area where greater detail was required (Figure 3). Although individual reef targets might have required the closer line spacing, existing information suggested that strike continuity would allow general mapping objectives to still be achieved with 1 km line

spacing. A line spacing of 1 km would also still allow appropriate noise reduction measures, requiring linkages and assumptions to be set up for data on adjacent lines, to be applied during data processing.

The rate of data acquisition varied between approximately 250 and 650 km/day. Occasional delays were caused by the presence of cloud and, on one occasion, by magnetic storms.

Existing data

Part of the area in which AGG data were acquired was covered by a 1987 reconnaissance-style vibroseis seismic survey (Figure 3). These data were reprocessed in 2000 and data quality was assessed as fair to good. Ground gravity data with a station interval of 250 m had also been acquired along the seismic lines in 1987. Spot gravity stations were available in other parts of the survey area.

Results

Quantitative interpretation is still at a preliminary stage and discussion will be limited to qualitative results. Figure 4 shows airborne data in profile form in combination with the seismic section for H87-033, whilst Figure 5 shows airborne data in plan view together with interpreted outlines of the surface-extent of geological units.

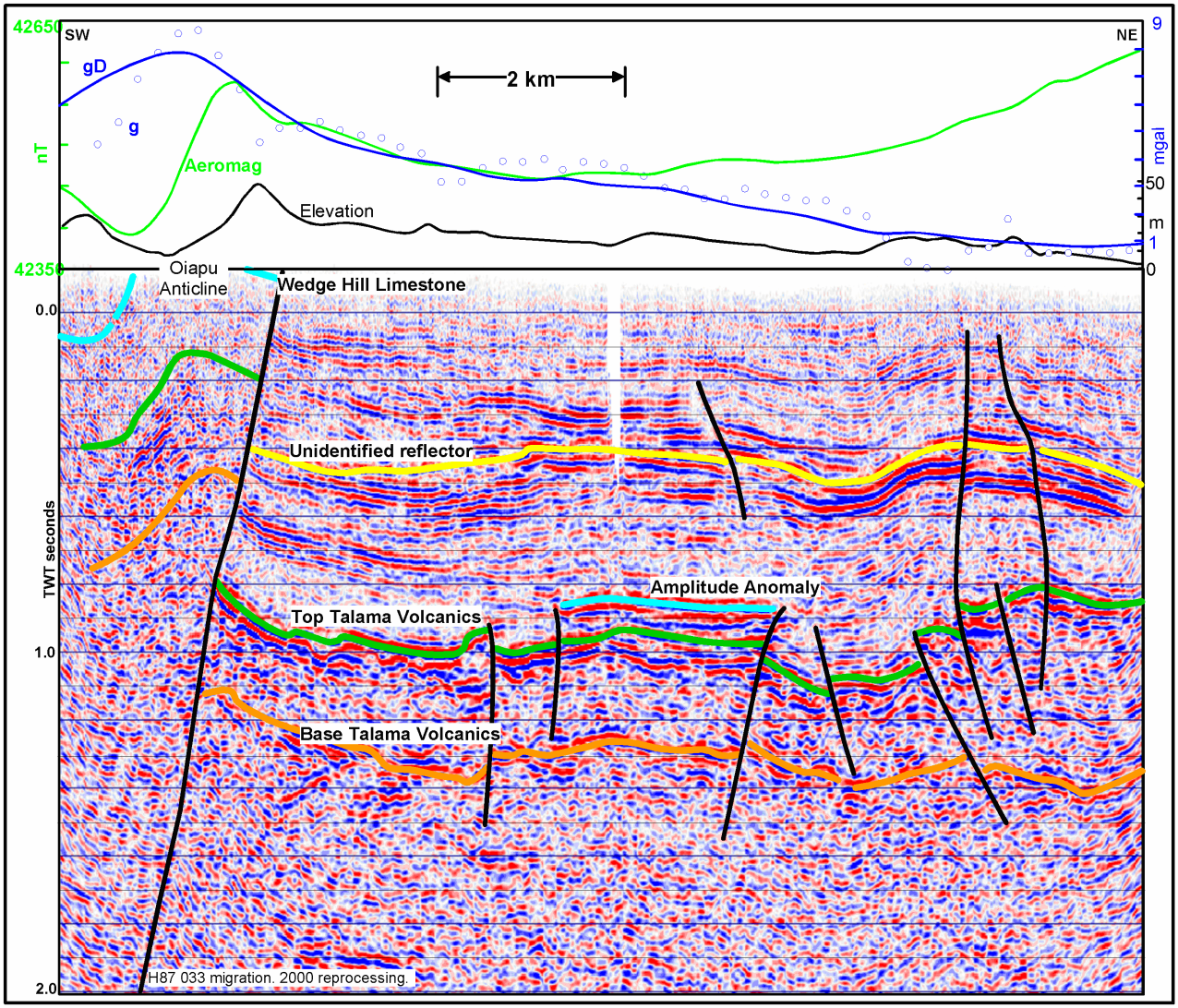

Figure 4. Seismic section H87-33 with profiles of ground vertical gravity (g), vertical gravity (gD), and aeromagnetic data plotted above. The horizon labelled "Aplitude Anomaly" is estimated to be at 840 m below surface.

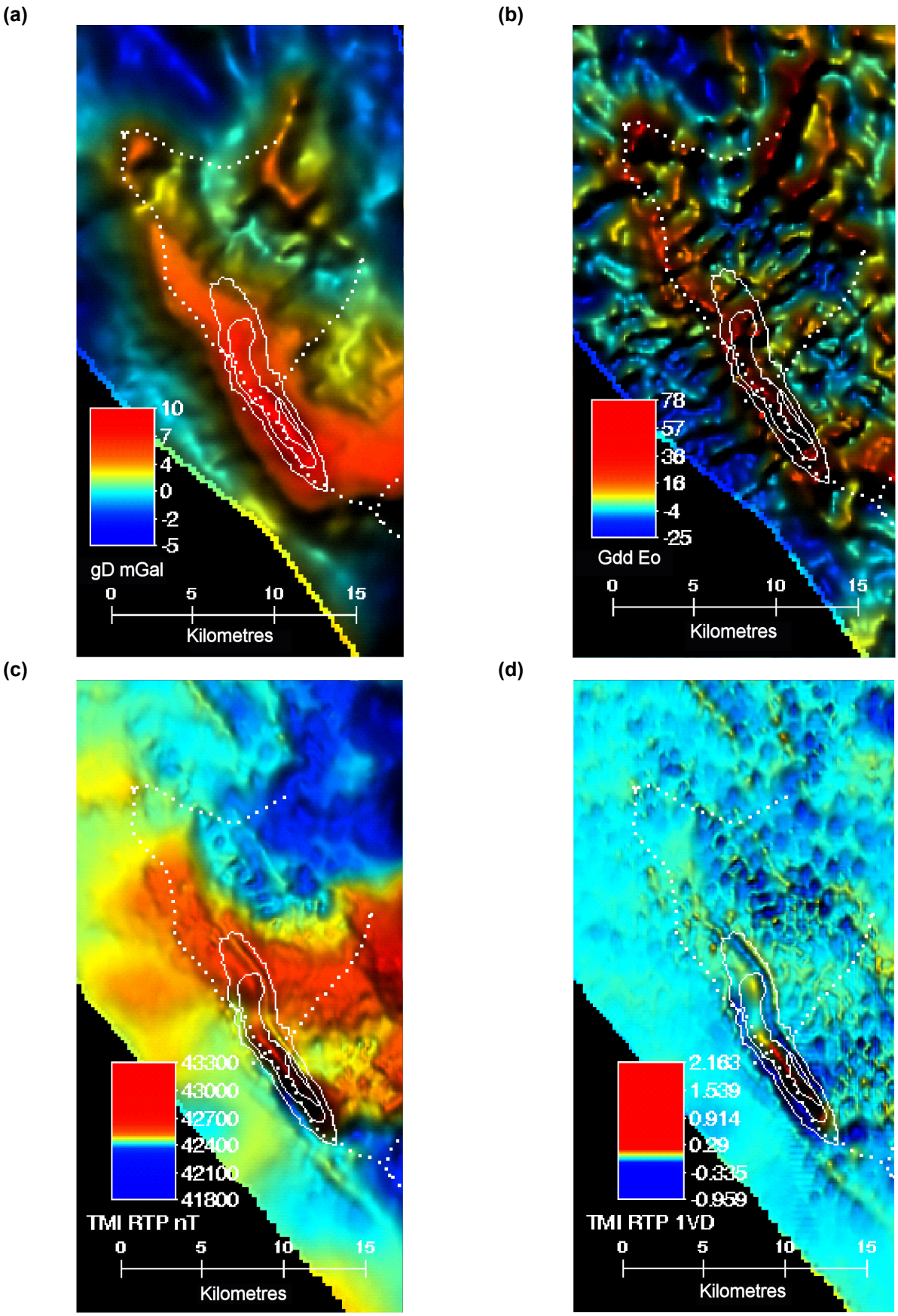

Figure 5. Sunshaded images of AGG and magnetic data from the Oiapu area. Seismic line locations are shown dotted, including H87-033 (Figure 4), together with mapped outcrop boundaries on the Oiapu Anticline. (a) Vertical gravity, gD. (b) Vertical gravity gradient, Gdd. (c) Total magnetic intensity reduced to the pole, TMI RTP. (d) First vertical derivative of total magnetic intensity reduced to the pole, TMI RTP 1VD.

These data demonstrate some of the spatial relationships between features in the airborne data and existing geological and seismic observations. For example, there is a TMI high where the Oiapu Anticline brings the volcanics close to the surface before a fault displaces them lower down into the section. More subtle features in the TMI appear to correlate with the interpreted surface extent of the Wedge Hill Limestone (Figure 5). It is anticipated that the available geological and seismic observations will help to constrain gravity and magnetic modelling such that the values of magnetic susceptibility and density might be reasonably determined for the various units where these are not available from sample data. This information might then be used for extrapolation of the interpretation into areas where mapping based on seismic data is less definitive or simply not available.

Nelson et al. (2004) show an example from Area 5 (southernmost acquisition area, Figure 1) of this survey where the AGG data are used to support and extend the correlation of a fault through three widely spaced seismic line intersections, thereby increasing the area of a lead.

Figure 4 provides a comparison of ground vertical gravity data (blue dots) with vertical gravity values (gD, blue line) derived from AGG data. As is expected from the terrain clearance and filtering of the airborne survey, the short wavelength resolution and dynamic range of the airborne data is less than the comparable quantities in the ground data. However, the comparison provides confidence that the gD values can be used as a proxy for ground gravity in this environment with only minor regard for the limitations in the former.

Our experience with ground gravity data shows that it can be difficult to obtain proper terrain corrections for readings on razorback ridges even when accurate elevation data are available (Nelson et al., 2004). Elevation control for the airborne survey is provided by GPS and laser scanner measurements made during AGG acquisition (Stone and Simsky, 2001). This information is used to calculate terrain corrections, but the accuracy of the results depends on the line spacing. In the case of 1 km or 500 m spaced lines, the elevation coverage is incomplete and Shuttle Radar Topography Mission data of lower accuracy were used to fill the gaps. The effect of thick jungle canopy, which limits the ability of the laser scanner to obtain reflections from the ground, has yet to be assessed in terms of reduced accuracy in the derived Digital Elevation Model and hence in the accuracy of the terrain corrections for the AGG data.

Analysis of the airborne magnetic data indicated that beds within the shallowest widespread interval in PPL 236, the Apinaipi Formation, show susceptibility contrasts that are presumed to be due to the presence of varying amounts of volcanic material. On larger structures where uplift and erosion exposes these beds, this observation can assist in correlating beds, estimating their dip, and locating faults which may segment structures.

The line spacing of 1 km appears to have been appropriate for the AGG data in PPL 236, given the strike extent of most of the structures. It is less apparent what extra resolution and additional information might have been obtained with a line spacing of 250 m. The original survey proposal called for 250 m spaced lines to directly detect reef bodies at depths of 1.5 km or more. Analysis of data where flight lines were extended along the coast in a narrow swath to cover a known buried reef in PPL 237 (Figure 1) suggests that the reef was not detected. Since adjacent lines are used for noise reduction during processing, the resolution of the AGG method is in part a function of line spacing. It might be concluded that the line spacing should have been reduced to the recommended 250 m in this area in order to properly test the method. It is also possible that the actual density contrasts present in the vicinity of the reef were significantly different from those used in the pre-survey analysis and that the resultant anomaly from the reef was too small to measure with the AGG system.

Conclusions

Preliminary analysis of airborne potential field data acquired in 2002 and 2003 for petroleum exploration purpose in PNG suggests that such data can significantly assist with mapping and hence decreasing exploration costs. Within the survey area, the density and magnetic susceptibility contrasts of the stratigraphy and the presence of shallow faulted and folded structures were favourable for the use of these techniques. A correlation of density and susceptibility values with stratigraphic units has been established using limited amounts of seismic and ground gravity data, together with outcrop mapping. This allows the potential field data to be used to extend mapping between and away from the existing observations and interpretations.

Acknowledgments

The airborne survey was funded by InterOil. The assistance of BHP Billiton during planning, acquisition and interpretation is acknowledged. The survey was flown by Fugro Airborne Surveys.

References

BHP Billiton, 2002, Falcon Airborne Gravity Gradiometer Proposal PPL 220 and 230, PNG: Unpublished report.

Carman, G.J., 1993, Palaeogeography of the Coral Sea, Darai and Foreland Megasequences in the eastern Papuan Basin: In Carman, G.J. & Z. (eds) Petroleum Exploration & Development in Papua New Guinea, - Proceedings of the 2nd PNG Petroleum Convention, Port Moresby, Papua New Guinea, 31st May-2nd June, 291-309.

Home, P.C., Dalton, D.G., and Brannan, J., 1990, Geological Evolution of the Western Papuan Basin: In Carman, G.J. & Z. (eds) Petroleum Exploration in Papua New Guinea, - Proceedings of the First PNG Petroleum Convention, Port Moresby, Papua New Guinea, 12th to 14th February, 1990, 107-117.

Nelson, A., Holland, D., Yogi, O., Heidorn, R., Leech, D., 2004, Integrated use of seismic, ground and airborne gravity/gravity gradiometer, and ground geological mapping methods in the eastern Papuan Basin, PNG: Extended Abstract, ASEG-PESA Conference, Sydney, Australia, 2004.

St John, V.P., 1990, Regional Gravity and the Structure of the Eastern Papuan Fold Belt: In Carman, G.J. & Z. (eds) Petroleum Exploration in Papua New Guinea, - Proceedings of the First PNG Petroleum Convention, Port Moresby, Papua New Guinea, 12th to 14th February, 1990, 311-318

Stone, P.M., and Simsky, A., 2001, Constructing high resolution DEMs from airborne laser scanner data: Extended Abstract, ASEG Conference, Brisbane, 2001.

Tregoning, P., 2003, Is the Australian Plate deforming? A space geodetic perspective: Geological Society of Australia Special Publication, 22 *and* Geological Society of America Special Publication, 372, 41-48.

Evaluation of a full tensor gravity gradiometer for kimberlite exploration

David Hatch
De Beers Consolidated Mines Limited
Dave.Hatch@debeersgroup.com

Abstract

Test surveys of a full tensor gravity gradiometer (FTG) operated as the "Air-FTG™" system, were carried out over three sites in Botswana. The main purpose of this program was to evaluate the resolution of the system as well as the amplitude and spectral character of the noise. This information can be utilized to determine the effectiveness of the system for kimberlite exploration in other environments.

High resolution ground gravity data had previously been collected over all three of the FTG test blocks. These data were upward-continued to the level of the airborne drape surface before a first vertical derivative transformation was applied. After re-sampling at the locations of the airborne survey observations, the resultant data were subtracted from the airborne vertical gravity gradient data. Assuming that the ground gravity data are accurate and measured with sufficient sampling density, the residual provides a post-processing estimate of the noise of the airborne system data. The rms noise values obtained from the three separate tests carried out over a 10-month period progressively decreased from 15.4 Eo to 5.4 Eo as acquisition and processing methods were improved by the contractor. The airborne FTG data contain information for wavelengths down to approximately 400 m, which corresponds to a bandwidth of zero to 0.15 Hz given an average airspeed of 60 m/s. There is a significant amount of residual noise in the wavelength range of 300 m to 900 m, with longer wavelength noise also present which is thought to be due to mis-leveling of traverse lines.

The noise characteristics that were derived from the test surveys were used in a forward modeling exercise to determine the effectiveness of this system for kimberlite exploration. The results from modeling a range of kimberlite bodies of different sizes and depths of burial indicated that larger kimberlite bodies would be readily detected, but noise would limit the detection of smaller and more deeply buried bodies. The specifics of this result were, of course, contingent on the density contrasts assigned to the bodies and would need to be adjusted from one geological environment to another. The results of the modeling could be used as an input, along with line-km costs and a definition of the acceptable level of risk, to determine the optimal line spacing.

A number of products were calculated from the tensor components in an attempt to enhance the signals due to kimberlites. The most useful operator was found to be the determinant (I_2) of the gravity gradient tensor which incorporates information from all of the tensor components. This quantity tends to highlight kimberlite anomalies, but at the expense of a decrease in the overall signal-to-noise ratio.

Introduction

The ground gravity technique has been used successfully by De Beers in the discovery and delineation of kimberlites in a variety of geological settings around the world. However, due to the length of time required to collect ground data over large areas and the inadequate resolution and sensitivity of airborne systems in the past, the gravity technique has not been commonly used as a reconnaissance exploration tool by De Beers.

With the advent of airborne systems based on the Lockheed-Martin airborne gravity gradiometer technology (e.g., Falcon®, Air-FTG™), it appeared that the latest airborne systems might have noise levels and resolution that are suitable for reconnaissance kimberlite exploration (Liu et al., 2001). When the Air-FTG™ system was deployed on a fully commercial basis in 2003 (Hammond and Murphy, 2003), a series of test surveys were carried out to ascertain the noise levels and resolution of the system. This paper describes the results of these tests and provides modeling that demonstrates the effectiveness of the system for the detection of kimberlite bodies. The results of evaluating a number of enhanced products that can be derived from the full tensor measurements are also discussed from the perspective of improving the detection of kimberlite anomalies.

System evaluation

Typically, new geophysical systems are evaluated via a case study approach by flying test surveys over a number of economic bodies. Although such case studies are useful, economic kimberlites can have a very wide range of surface extents, shapes, depths of burial and density contrasts. Potentially economic

kimberlites can range from sub-hectare bodies to over 100 Ha in size and can be intruded in Archaean basement through to Palaeozoic and Mesozoic aged sediments. The flying of orientation surveys over a small number of deposits may not provide adequate information to allow the effectiveness of a system to be predicted for a wide range of exploration scenarios.

In the role of a client, it is not always possible to obtain all of the information concerning operational noise levels and processing steps that are required to define the performance of the system without recourse to independent comparisons. By comparing airborne data from a new system with adequately sampled and accurate ground data, the character of the final data from the acquisition and processing system can be ascertained. The performance levels determined in this manner can be combined with information provided by the exploration team about the local geological environment, emplacement model, erosion level and weathering characteristics to develop a survey plan which sets out the limits of detection and balances the risks of missing an economic target balanced the survey costs.

Survey description

Three Air-FTG™ surveys were flown over blocks in Botswana during 2003 (Table 1). The surveys were carried out in different seasons; January (summer), July (winter) and November (spring). All of the surveys were within the Kalahari Desert where extreme daytime temperatures and turbulence are common in the summer months. The maximum temperature is rarely above 25 ^{o}C in winter, and the resultant lower levels of turbulence allow greater survey productivity.

Each of the Air-FTG™ test surveys covered an area approximately 25 km^2. Traverse line spacing was 200 m whilst the tie-line spacing was 2000 m. In-fill lines were occasionally flown. The flying height was a constant 80 m above ground which was controlled from radar altimeter readings. The aircraft was not equipped with a laser scanner for these surveys.

The data used to construct the digital terrain model for the test areas were acquired during the ground gravity surveys with a dual channel, differential GPS system. Since the survey areas generally possess only first order topographic variation, and given centimeter-scale accuracy from the DGPS measurement, the DTM based on these measurements more than met the 1 m accuracy required to produce a terrain correction with insignificant errors (Stone and Simsky, 2001). The terrain-corrected vertical gravity gradient (Gzz) data from the FTG survey over Test Area 3 are shown in Figure 1a.

The ground gravity data had been previously acquired for exploration purposes but their availability provided an ideal opportunity to compare these data with the output from the Air-FTG™ system. The ground measurements have a traverse line spacing of 100 m and station spacing of 50 m, and there are 13 600 ground stations in total. The data were collected with a CG-3 gravimeter, which has an observation error of less than 0.05 mGal. The vertical gravity gradient data derived from the ground gravity data had very little visible noise after being upward-continued to the 80 m flying height of the airborne survey (Figure 1b).

Noise and resolution analysis

In order to analyze the noise of the Air-FTG™ system, the Gzz data from the Air-FTG™ system were compared with the equivalent vertical gravity gradient data calculated from the ground gravity observations. The ground data were first upward-continued to the drape surface of the airborne survey. A first vertical derivative transformation was applied to produce vertical gravity gradient data. This response was then re-sampled at the same positions as the airborne data. The rms error between the ground and Air-FTG™ Gzz datasets was then calculated for each of the three areas (Table 1).

The improvement in rms error over time was thought to be largely due to the reduction of system noise and improvements in processing techniques. To some extent the poor result of the first survey can be attributed to the turbulent weather conditions at the time of this survey.

The results from the final test are thought to provide a reasonable estimate of what can currently be achieved on a production survey with good quality-control measures in place. A comparison of the ground and airborne data over Test Area 3 with the same sampling parameters is shown in Figure 1. The Air-FTG™ data were leveled and filtered by the contractor using proprietary algorithms without prior knowledge of the ground gravity response.

Table 1. Noise statistics for the Air-FTG™ test blocks.

	Survey Date	rms error	Maximum absolute error	Line-kms for the test block
Test area 1	January 2003	15.5 Eo	50 Eo	220 km
Test area 2	July 2003	8.5 Eo	31 Eo	410 km
Test area 3	October 2003	5.4 Eo	16 Eo	140 km

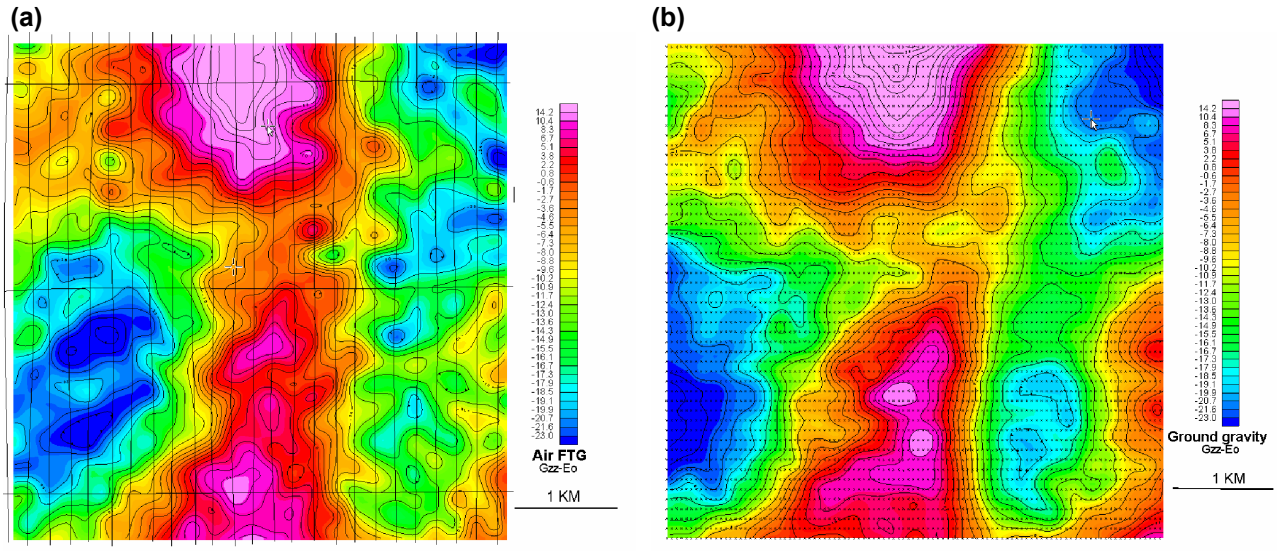

Figure 1. (a) (a) The Gzz component from the Air-FTG survey of Test Area 3, and (b) the equivalent Gzz response calculated from the upward continued ground gravity data. The flight-path of the airborne survey and locations for the ground stations are superimposed on the appropriate plots.

On visual inspection, the long wavelength features of the two data sets are similar including those that are of relatively low amplitude. However, there are a number of shorter wavelength anomalies, mainly present in the FTG data, which do not correlate between the two datasets. This is more easily seen by subtracting the ground response from the airborne data (Figure 2). Assuming that the ground data are accurate and adequately define the geologic signal, the difference grid represents the residual noise that is left after processing of the Air-FTG™ data. In addition to the expected single-line anomalies that would be due to short-period turbulence effects, there are several coherent trends and larger anomalies that are visible across several lines.

Average spectra of the differences between the processed FTG and ground gravity data calculated in the east-west and north-south directions are shown in Figure 3. A curve of scaled white noise that has been upward-continued to survey altitude has also been plotted for reference. The difference grid has spectral response similar to that of white noise at longer wavelengths (i.e., wavelengths greater than 700 m). The spectra show rapid attenuation, however, for wavelengths less than 400 m. Several factors combine to ensure that the upward continued ground data have very low spectral amplitude at short wavelengths; low noise levels in these data, the presence of relatively homogenous flat-lying geological cover units across the test area, and upward continuation (i.e., low-pass filtering) of these data to a terrain clearance of 80 m. To suppress noise in the raw FTG data, the contractor applies several proprietary processing algorithms. Although this low-pass filtering has been restricted to preserve kimberlite signatures, it is felt that there is little signal remaining following processing for wavelengths less than 400 m. The absence of response in either the ground or airborne data for wavelengths less than 400 m ensures that the difference grid between these two datasets also shows very low amplitude and these wavelengths.

Another feature of the difference grid is the presence of relatively long-wavelength anomalies (i.e., greater than 2000 m) that are elongated in the north-south direction. Variations in aircraft altitude and topography were eliminated as possible causes of these long wavelength anomalies. As proper tide, drift and loop procedures were employed during acquisition of the ground gravity data, the regional component of these data was thought to be accurately defined and unlikely to contribute to the difference grid. Some of the long wavelength variations are elongated parallel to the flight-direction, suggesting errors in the line leveling as

being a possible cause. The anisotropy in the difference grid is also apparent in the amplitude spectra, which shows that amplitude variations in the east-west (i.e., across-line) direction are twice as large as those in the north-south (i.e., along-line direction.

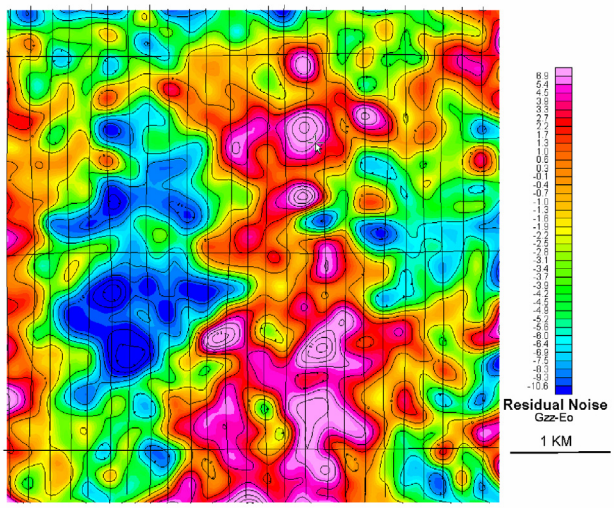

Figure 2. Image of the residual noise grid for Test Area 3 calculated by subtracting the Gzz derived from ground data from the Air-FTG Gzz data.

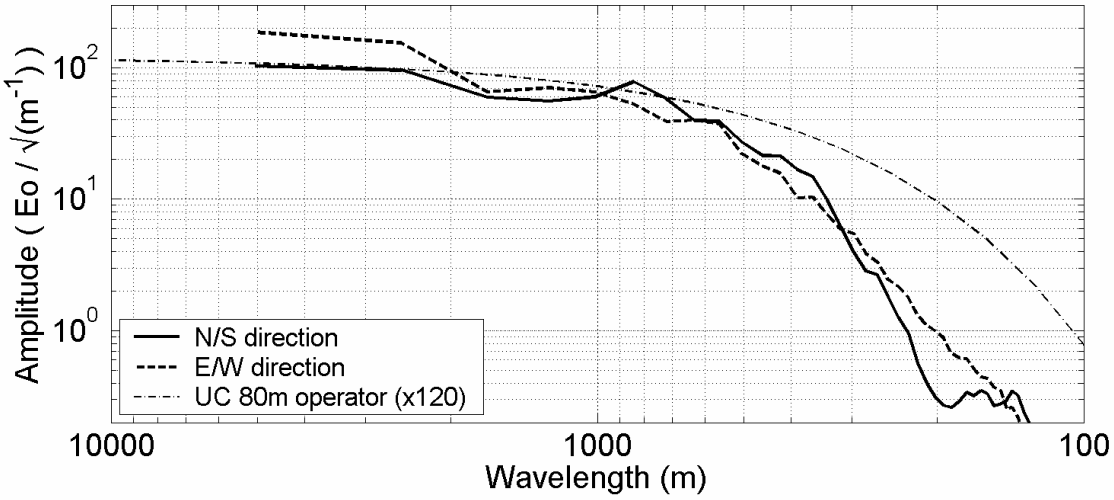

Figure 3. Averaged spectra for E/W and N/S directions from the residual noise grid calculated by subtracting the Gzz derived from the ground data from the Air-FTG™ Gzz data. A curve corresponding to scaled white noise that has been subject to an 80 m upward continuation operator has been plotted for comparison.

Assuming that virtually the entire signal has been eliminated for wavelengths shorter than 400 m and that the airspeed was roughly 60 m/s, the bandwidth of the measurements is zero to 0.15 Hz. The rms noise of 5.4 Eo is thus equivalent to a spectral density of 14 Eo/√Hz.

Of importance for kimberlite exploration, the difference grid and associated spectra show that the noise has relatively high energy for features with wavelengths of 300 m to 900 m. Noise in this bandwidth will have an impact on the detection of smaller kimberlites.

Detection of kimberlites

With an understanding of the noise that is present in the processed data from the Air-FTG system, it is possible to investigate the effectiveness of kimberlite detection in different environments with various survey parameters. Figure 4a shows the Gzz response calculated with ModelVision over a number of kimberlites with a range of surface areas (2 Ha, 6 Ha and 10 Ha) and depths of burial (20 m, 60 m and 100 m) sampled with a line spacing of 50 m. For this example, the model used was a simple disk with a density contrast of -0.3 g/cm^3 and a thickness of 100 m, representing the weathered cap and crater facies component of a kimberlite intrusion. To provide a realistic scenario, noise with an amplitude and spectral content as determined from the Air-FTG test has been added (Figure 4b). To test the effect of varying the line spacing, the data were re-sampled to simulate surveys with line spacing of 100 and 200 m (Figures 4c and 4d).

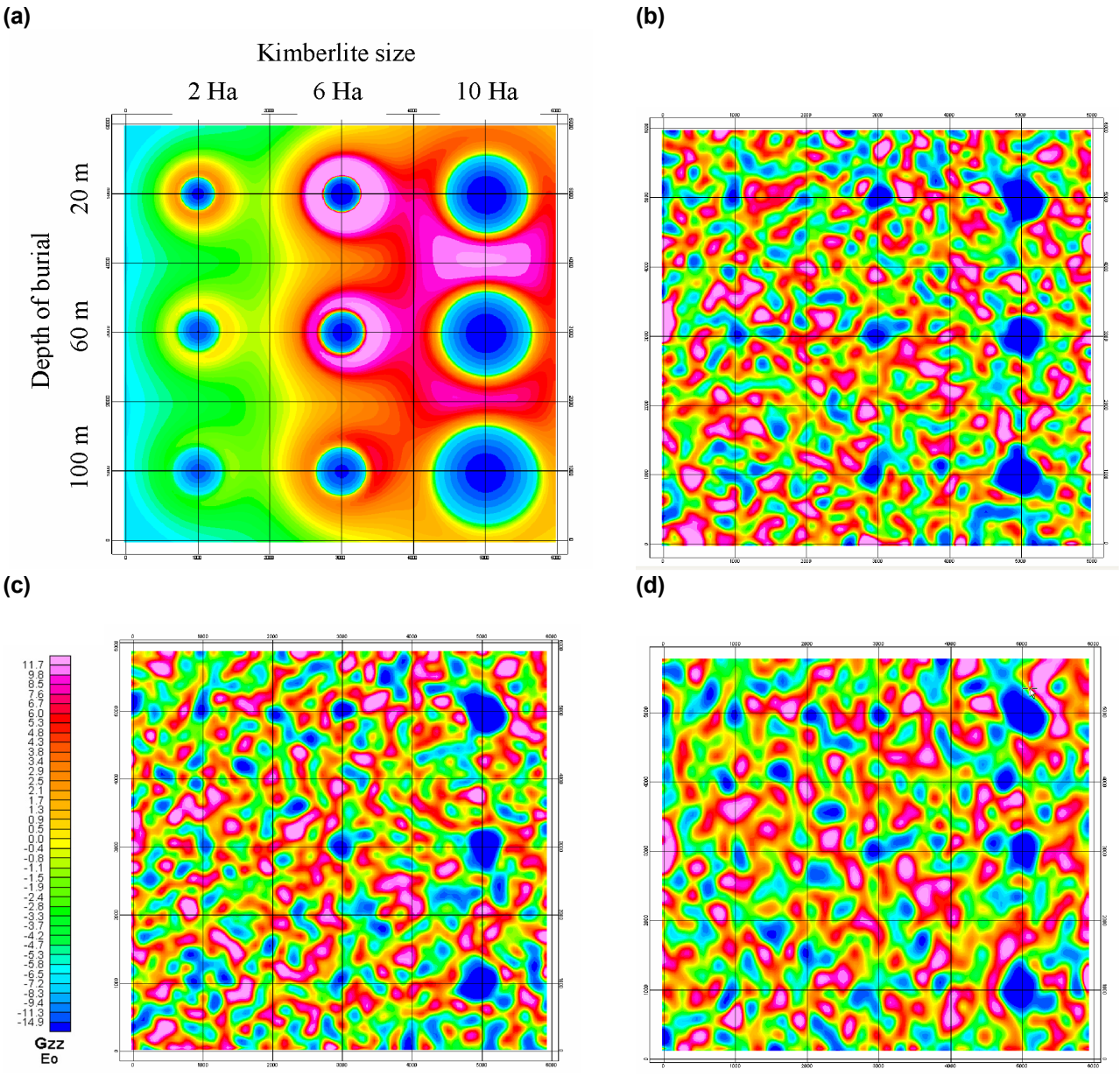

Figure 4. (a) Noise-free forward model response for kimberlites of different sizes at various levels of burial sampled with a line spacing of 50m. (b) Noise with an amplitude and bandwidth representative of the Air-FTG™ system has been added to the response shown in (a). The line spacing has been broadened to 100 m in (c) and 200 m in (d). A 1 km graticule is used with each image.

With 50 m line spacing, all of the modeled kimberlites can be seen but the amplitude of the response from the smaller and more deeply buried bodies is close to the noise level. It would be unlikely that an interpreter would be able to distinguish some of these anomalies from the residual noise, particularly with a geological background signal also present. Increasing the line spacing to 100 m and 200 m reduces the number of kimberlites that can be reliably interpreted, with only the 10 Ha bodies being readily visible at 200 m line spacing. Further modeling runs could be carried out to examine the effect of a more complex kimberlite model and changes to other variables such as the density contrast.

The selection of line spacing in a particular area is a balance between close line spacing to detect anomalies from economically viable targets and cost constraints. Given noise levels for the Air-FTG system, density models for the target body and host, survey costs per line km and a profile of the acceptable exploration risk, modeling can be used to select an appropriate line spacing that will provide an optimal cost-benefit. In areas where the density contrast is not well known or where higher levels of geologic noise are likely, the survey line spacing can be reduced (with a cost penalty) to mitigate the risk of missing potentially economic bodies.

Interpretation techniques for kimberlite exploration

Schmidt and Clark (2000) provide an overview of the advantages of utilizing the magnetic gradient tensor for interpretation, many of which are also applicable to gravity gradients. One of the main advantages of FTG data is that it can be used to highlight directional features and edges which are useful for geologic and structural mapping. Of paramount importance in kimberlite exploration is the identification of discrete anomalies thought to be derived from intrusive bodies. In practice, only the Gzz component can be used to visually select kimberlite targets because the other tensor elements have complex anomaly forms such as quadrupoles.

A number of products were derived from the tensor measurements to evaluate whether these products could enhance the Gzz component or bring components other than Gzz into the visual interpretation process. Higher-order derivatives, upward continuation and band pass filtering of Gzz data were all trialed, with the results confirming the well-understood advantages and disadvantages of these transformations.

The measurement of the full tensor allows the direct calculation of a number of scalar operators on a point-by-point basis. Pedersen and Rasmussen (1990) describe rotational invariants that do not change under coordinate transformation. Of particular interest is the invariant that they term "I_2" (Equation 10c in Pederson and Rasmussen, 1990) which is simply the determinant of the gravity gradient tensor. This quantity has the properties of increasing the resolution of anomalies over shallow sources while preserving the correct sign of the anomalies. An analysis of the rotational invariants was made by Dransfield (1994) and he found that these operators can reveal different and useful information contained within the gravity gradient tensor while avoiding the complex, and possibly misleading response of the individual tensor components. Dransfield demonstrated that the I_2 quantity responds best to point sources; this is a desirable characteristic in the context of exploration for kimberlites.

As anticipated, the invariant I_2 (Figure 5) increases the amplitude of the high frequency anomalies compared to longer wavelength features. There are some features that are more clearly visible in the I_2 plot which correlate with anomalies in the ground gravity data. However, there are a large number of high amplitude anomalies in the I_2 map which do not correlate with ground gravity responses. These features are suspected to be due to noise in the airborne data. Some of these noise anomalies are not visible in the Gzz plot and are therefore thought to originate from other tensor components. Although the I_2 operator appears to show some promise, it has a lower signal-to-noise ratio than the Gzz component and could draw attention to anomalies that are not of a geological origin.

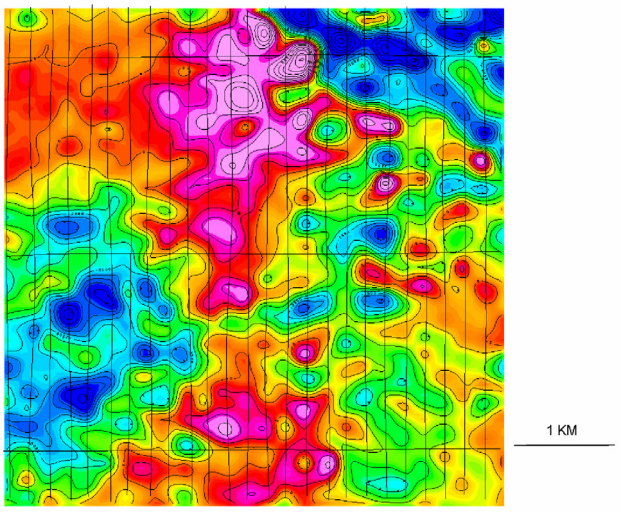

Figure 5. Image of the rotational invariant I_2, which is the determinant of the gravity gradient tensor measured by the Air-FTG system.

Conclusions

The Air-FTG system was trialed over three areas in Botswana. The FTG data were compared with ground gravity data which allowed noise levels for the final processed data to be estimated. The lowest rms error observed for the Gzz component was 5.4 Eo and this is thought to be a reasonable estimate for the noise in this component for the current implementation of the system. Filtering applied by the contractor to improve the signal-to-noise ratio removes most of the wavelengths less than 400 m, so this noise level is equivalent to a noise spectral density of 14 Eo/√Hz, assuming airspeed of 60 m/s.

A significant amount of the residual noise that remains after processing is in the range of 300 m to 900 m, which would impact on the detection of anomalies associated with kimberlites.
A long wavelength component was observed in the residual noise data and this was thought to be associated with errors in line leveling.

When integrated into a forward modeling exercise so that both signal and noise levels are considered, the noise estimated for the Air-FTG system would appear to significantly limit the detection of smaller and more deeply buried kimberlites. This could be mitigated somewhat by decreasing the flight line spacing. Larger kimberlites should be easily detected. Due to variability in host and target densities and depth of burial, forward modeling would be required in new exploration environments to derive an optimal cost-benefit for a planned survey.

For all practical purpose, the Gzz component was found to be the only single tensor component that was suitable for visual selection of anomalies thought to be associated with kimberlites. The rotation invariant I_2, the determinant of the gravity gradient tensor, was investigated and found to highlight some anomalies of geologic origin but overall reduced the signal to noise ratio of the data.

Acknowledgements

I am grateful for the permission of De Beers Consolidated Mines Limited to publish this paper. I would like to thank the staff of Bell Geospace (Colm Murphy, Gary Mumaw and James Brewster) and also Phill Houghton of Arkex for their time to help me understand the Lockheed-Martin FTG system. I would also like to thank Richard Lane for his review and for his insightful comments which greatly improved this paper.

The Air-FTG surveys were carried out by Bell Geospace using a Cessna Grand Caravan aircraft operated by Fugro Airborne Surveys. ModelVision software is produced by Encom Technology Pty. Ltd.

References

Dransfield, M.H., 1994, Airborne Gravity Gradiometry: PhD. Thesis, Department of Physics, University of Western Australia. (http://internal.physics.uwa.edu.au/frank/GGwebpage/thesis.html)

Hammond, S. & Murphy, C.A., 2003, Air-FTG™: Bell Geospace's Airborne Gravity Gradiometer - a description and case study: ASEG Preview, 105, 24-26.

Liu, G., Diorio, P., Stone, P., Lockhart, G., Christensen, A., Fitton, N., Dransfield, M., 2001, Detecting Kimberlite Pipes at Ekati with Airborne Gravity Gradiometry: Proceeding of ASEG 15th Geophysical Conference and Exhibition, August 2001.

Pedersen, L.B., Rasmussen, T.M., 1990, The Gradient Tensor of Potential Field Anomalies: Some Implications on Data Collection and Data Processing of Maps: Geophysics, 55, 1558-1566.

Schmidt, P.W. & Clark, D.A, 2000, Advantages of Measuring the Magnetic Gradient Tensor: ASEG Preview, April 2000, 26-30.

Stone, P. M., Simsky, A, 2001, Constructing High Resolution DEMs from Airborne Laser Scanner Data: Proceeding of ASEG 15th Geophysical Conference and Exhibition, August 2001.

Integrating ground and airborne data into regional gravity compilations

Richard Lane
Geoscience Australia
richard.lane@ga.gov.au

Abstract

A procedure for taking vertical gravity data from an airborne gravity (AG) or airborne gravity gradiometry (AGG) survey and combining it with vertical gravity data from ground measurements to produce a regional compilation is described. The method is illustrated using examples of AG data from West Arnhem Land (Northern Territory, Australia) and AGG data from Broken Hill (New South Wales, Australia). Despite significant differences in the acquisition and processing methods used for AG and AGG data, the integration procedure is the same for both. The procedure takes into account that the airborne and ground datasets are measured on different drape surfaces, that long wavelengths are not properly recovered in the airborne datasets, and that noise produces inconsistencies where surveys overlap in horizontal position.

Before combining the two datasets, the input ground and airborne datasets are continued upwards or downwards to the chosen output drape surface using a drape-to-drape continuation procedure. Gaps in the long wavelength information content of the airborne data are filled with long wavelength information from the ground data using a technique termed “crossover” filtering.

A smooth combined output data surface is obtained by jointly inverting the datasets using an equivalent source technique configured with a regular grid of sources. The spatial smoothness of the mass properties for the sources, and hence the smoothness of the fitted potential field surface, is controlled to produce data misfits consistent with the estimates of uncertainty supplied for each data point.

This procedure requires not just the data values and horizontal locations of the observations, but information concerning the vertical position or elevation surface for each dataset, the range of wavelengths present in each dataset and estimates of the uncertainty in the data values. This information is not always readily available, and much effort in the examples was spent on these issues.

The integrated product does not entirely replace the input ground and airborne datasets for interpretation purposes. However, the integrated product adds value because it has a different spectral mix compared with either of the inputs. In the examples that are presented, accurate long wavelength information from the ground data is merged with accurate mid-wavelength information from the airborne data. Additionally, information is carried through to the output from small prospect areas which have detailed and accurate ground data. The combination method described here differs in this respect from the crossover filtering method of combining data which simply replaces the ground data with airborne data within the boundaries of the airborne survey.

Introduction

The present ground gravity coverage of Australia is accurate at the longest wavelengths that are of interest for petroleum and minerals applications (i.e., from tens to hundreds of kilometres). Stations are no more than 11 km apart and observations are tied to the Australian Fundamental Gravity Network. Ground and airborne data acquisition methods are being used by explorers and governments to provide greater detail at short to intermediate wavelengths in specific areas of greater interest. When deciding whether to use ground or airborne methods for this purpose, there is a trade-off between the greater accuracy of ground data and the benefits of decreased acquisition time for large survey areas and avoiding the need for direct land access that are associated with the use of airborne methods.

There are two classes of airborne systems that can provide vertical gravity data; airborne gravity (AG) and airborne gravity gradiometry (AGG) systems.

Airborne gravity (AG) systems measure vertical acceleration using a single sensor. Independent measurement of the motion of the aircraft via GPS navigation information allows inertial acceleration to be calculated and subtracted from the total acceleration, leaving the component of acceleration due to gravity. The uncertainty in GPS produces errors in the inertial acceleration calculation that rise in amplitude as wavelength decreases (see Figure 2.2 of Bruton, 2000). This noise is suppressed by low-pass filtering thus

limiting resolution at short wavelengths. The long wavelength performance is limited by the linearity and rate of drift of the accelerometer output (again, see Figure 2.2 of Bruton, 2000).

The airborne gravity gradiometer (AGG) systems that are presently being operated use complements of four acceleration sensors mounted on rotating disks (Lee, 2001). The inertial acceleration of the disk is common to all sensors, and combinations of the sensor outputs can be used to estimate gradients of the acceleration due to gravity in the plane of the disk. The AGG systems measure two or more components of the gravity gradient tensor depending on the number of disks present and their orientation. The gradients measured at different locations can be transformed to vertical gravity. Residual inertial acceleration effects induced by turbulence limit the performance at short wavelengths. Long wavelength performance is limited principally by the size of the survey and the truncation errors obtained by integration of gradient signals over a finite area to derive vertical gravity.

For an integrated product that combines ground and airborne gravity data to be useful for interpretation purposes, it should cover a larger area than the airborne survey, and thus provide context for the airborne survey data. The integration procedure should not simply involve replacing the ground data with the airborne data within the survey area, but allow detailed and accurate ground data to enhance the airborne data where such data are present within the bounds of the survey area. Since airborne methods are unable to completely capture the longer wavelengths, the final product should include the long wavelength control provided by ground gravity data. A method to integrate ground and airborne gravity data that satisfies these conditions is described in the following section. This method is then demonstrated using field examples of AG and AGG data in combination with ground gravity data.

Method

The ideal method to combine vertical gravity data from ground and airborne observations and output a grid of vertical gravity on a specified drape surface would need to address a number of specific characteristics of the problem. The ground and airborne data relate to locations on different irregular drape surfaces. The chosen output drape surface may or may not correspond to either of these surfaces. Both datasets contain noise which means there will be inconsistencies between the values where the datasets overlap. This noise will introduce instability into any prediction of vertical gravity closer to the source than the original observation (i.e., during downward continuation). The airborne data have been filtered, which modifies the response from the theoretical broadband response and produces correlation between the data errors. The datasets may also be very large, which will introduce computation difficulties.

Schematic sections in Figure 1 illustrate the geometrical aspects of an idealized equivalent source procedure for combining the two datasets. The ground and airborne data would be jointly inverted using a set of equivalent source elements as the model (Figure 1a). The forward modeling algorithm used to generate predicted data for each of the source elements would account for the filtering of airborne observations. Constraints on the spatial variability of the mass properties of the sources would be used to produce a smooth fit to the observations and hence resolve inconsistencies between the datasets. The data misfit calculation would incorporate supplied estimates of the noise for each observation, and allow for any specified correlation between these errors. Having solved the inverse problem, the vertical gravity response on the output drape surface could be predicted by forward modeling (Figure 1b). Either a wideband or filtered response could be generated as required.

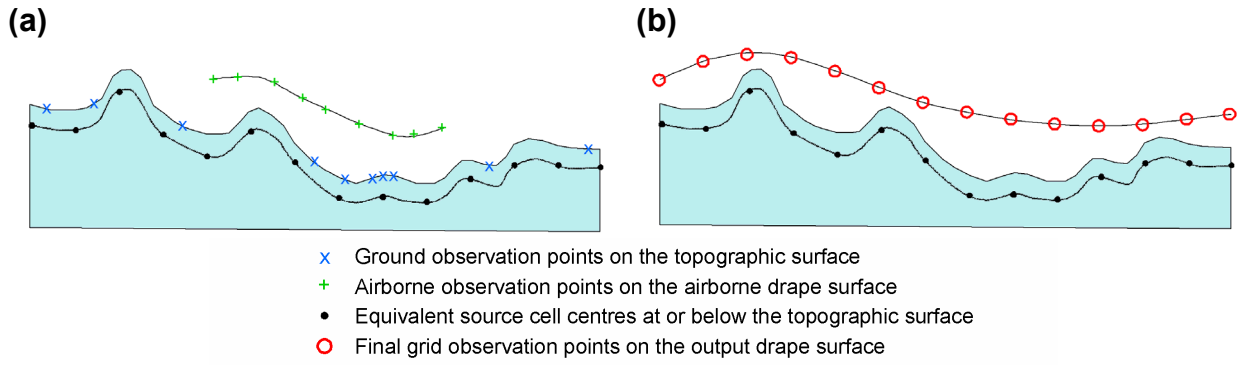

Figure 1. Schematic sections showing an idealised equivalent source procedure. (a) Invert ground and airborne observations for an equivalent source distribution immediately below the ground surface. (b) Forward model the equivalent source distribution at regular locations on the output drape surface. The output drape surface may or may not coincide with either of the topographic or airborne drape surfaces.

Unfortunately, the method described above has not been implemented in any of the readily available geophysical software programs. An alternate procedure was formulated making use of available tools. The geometrical aspects of this procedure are illustrated in Figure 2.

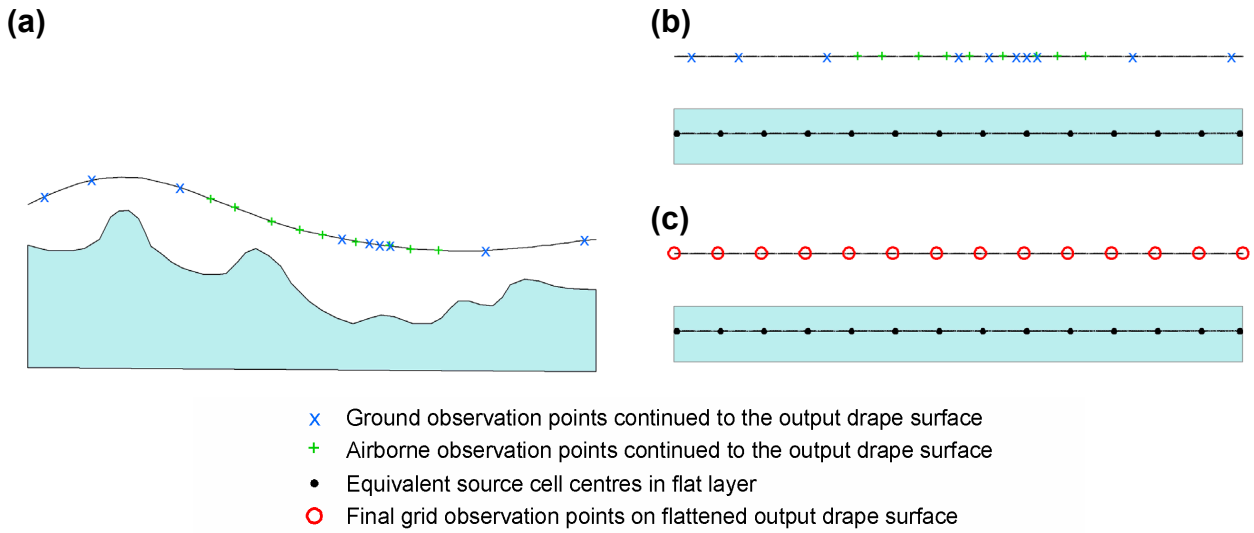

Figure 2. Schematic sections showing the actual method used in the examples. (a) Continue ground and airborne observations as shown in Figure 1(a) onto a smooth output drape surface. Then apply "crossover" filtering to the airborne data (not shown). (b) Assume the observations are now on a flat surface and invert for an equivalent source distribution on a horizontal surface below the flattened output drape surface. (c) Forward model the equivalent source distribution at regular locations on the flattened output drape surface.

Both datasets are first continued onto the output drape surface (Figure 2a) using a drape-to-drape method (Cordell and Grauch, 1985). For this procedure, the datasets are required to be in gridded format. The airborne datasets used in this study were supplied in gridded form, so no further pre-processing of them was required. The ground data were supplied in point located form, so these data were gridded using a minimum curvature method. It is arguable whether to upward continue the ground data to the level of the airborne drape surface or to downward continue the airborne data to the ground surface. The appearance of the short wavelength information in the combined product will be influenced by this choice of output drape surface. Although the short wavelength information will be more prominent in the output if the output surface is close to the ground surface, the actual signal to noise ratio in the short wavelengths will be independent of the choice of elevation surface. Due to the presence of noise, low-pass filtering of the airborne data would be required if the airborne data were required to be downward continued. This would essentially defeat the true purpose of downward continuation. Thus, the output drape surface was always chosen to be at or above the airborne drape surface.

The poorly-resolved longer wavelengths in the airborne data were replaced with more accurate information from ground data using a grid-based "crossover" filtering technique (Hensley, 2003c). For this procedure, a grid-based high-pass filter was first applied to the airborne data, and then the complementary low-pass filter was applied to the ground data. The filtered products were added together to produce a modified airborne dataset which can now be integrated with ground data.

The pre-processing of the data up until this point is designed to minimize the errors associated with simplifying conditions used when jointly fitting a smooth surface to both datasets. The two datasets are assumed to have full spectral content when in actual fact the airborne data have been low-pass filtered, and the datasets are assumed to be observations on a level surface when the observations have actually been continued to the output drape surface that may not be level.

A 3D gravity inversion program described by Li and Oldenburg (1998) was used for the equivalent source inversion. To simplify the geometry of the density layer and reduce the computational requirement, a single layer of close-packed rectangular prisms with square horizontal cross section and vertical extent 10 times their horizontal extent was used. The purpose of the equivalent source inversion was to produce a smooth fit to the two datasets that is consistent with expectations from the supplied noise estimates rather than to faithfully model the actual geometry of the observations. Provided that the output drape surface was sufficiently smooth, the errors introduced by using a flattened approximation of the true geometry as illustrated in Figure 2(b) and (c) would be small. The depth extent of the prisms has an effect on the density values produced by the inversion, but has no real impact on the fit obtained. Prisms with horizontal extent equal to the cell size in the desired combined regional grid were used, with a depth to top equal to the

horizontal extent. These parameters were chosen so that the structure of the model would not contribute to the regularization of the inversion problem, and hence would not impede the desired smooth fit from being obtained. Explicit regularization in the form of lateral "smoothness" and "smallness" constraints on the mass properties of the source elements was used by the inversion program to produce a chi-squared data misfit appropriate to the uncertainty values of the supplied data. To facilitate application of a "smallness" constraint, a first order trend surface was removed from the data prior to inversion. Unfortunately, the basic processing tools available did not allow the missing or aliased short wavelength information of the datasets to be taken into account. These tools also assumed that the errors in the data values were Gaussian and uncorrelated. The latter assumption is false for the airborne data given that spatial filtering has been applied. The shape of the error distribution was not known.

To reduce the size of the inverse problem, unnecessary over-sampling of the airborne datasets is reduced by sub-sampling grids to a larger cell size, but one that was still below the Nyquist sampling rate given the low-pass filtering characteristics of these data. Also, the ground gravity grid previously continued to the output drape surface was re-sampled at the horizontal locations of the original observation to provide data as faithful to the original ground observations as possible.

Following analysis of the inversion results to verify a successful outcome, the response is predicted by forward modeling at regularly spaced locations on the output drape surface (Figure 2c). The first order trend surface removed from the data immediately prior to inversion is restored to produce the final grid of combined ground and airborne vertical gravity.

Application of the method

Example 1: West Arnhem Land Airborne Gravity Survey

Airborne gravity data were acquired with a GT-1A system over a survey area of 6875 km^2 in 2003 (Gabell and Tuckett, 2004). The airborne survey was commissioned after earlier attempts to acquire ground data had to be cancelled due to stalled land access negotiations (Duffett et al., 2004). Lines were flown east-west with 2 km spacing at a constant elevation of 655 m AHD. Tie-lines were flown north-south at 20 km spacing.

Ground measurements

Pre-existing ground gravity data in the vicinity of the survey area consisted of a grid of observations at roughly 11 km spacing and a number of more detailed traverses along roads and tracks (Fraser, Moss and Turpie, 1976). An essential ingredient of the combination method is the assignment of uncertainty to each gravity observation. Uncertainty in the ground vertical gravity Bouguer anomaly values was calculated using estimates of horizontal and vertical positioning accuracy and accuracy of the gravity observations themselves (Equations 1 to 3). Equation 1 is an approximation of the derivative of theoretical gravity with respect to latitude multiplied by the estimate of horizontal position error. Equation 2 is an approximation of the vertical derivative of the combined free-air and Bouguer corrections multiplied by the estimated vertical position error. Equation 3 combines the various error contributions assuming independence between the errors.

$$\varepsilon_{ht} \approx 0.01 \cdot h \cdot \sin 2\varphi \qquad \textit{Equation 1}$$

$$\varepsilon_{v} \approx -2 \cdot v \qquad \textit{Equation 2}$$

$$\varepsilon_{CBA} = \sqrt{\left(\varepsilon_{ht}^{\ 2} + \varepsilon_{v}^{\ 2} + \varepsilon_{obs}^{\ 2} + \varepsilon_{tc}^{\ 2}\right)} \qquad \textit{Equation 3}$$

ε_{ht} is the vertical gravity error in μm/s^2 associated with uncertainty in horizontal positioning, h is the uncertainty in horizontal position in metres, φ is the latitude in degrees north, ε_v is the error in μm/s^2 for simple Bouguer anomaly vertical gravity due to uncertainty in vertical positioning (based on a correction density of 2670 kg/m^3), v is the uncertainty in vertical position in metres, ε_{obs} is the vertical gravity observation error in μm/s^2, ε_{CBA} is the uncertainty in the accuracy of complete Bouguer anomaly values in μm/s^2, and ε_{tc} is the uncertainty in the accuracy of terrain corrections in μm/s^2. The combination with airborne gravity data was based on simple rather than complete Bouguer anomaly values, so the uncertainty in terrain corrections was assumed to be common to both datasets and set to zero. The estimated uncertainty values ranged from 2 μm/s^2 to 10 μm/s^2.

Airborne measurements

The GT-1A airborne gravity system is described by Gabell and Tuckett (2003, 2004). Although complete Bouguer gravity anomaly values were produced from the airborne data, terrain corrections were not available for the ground observations. The two datasets were thus integrated using simple Bouguer anomaly values. For the data used in this study, the most significant filtering was done with a 107 second Kalman filter. At an

average aircraft speed of 69.1 m/s, 107 seconds corresponds to 7.4 km. The filter response is plotted using symbols in Figure 3b, where it is shown that this filter can be approximated by a 7th order Butterworth filter with midpoint wavelength (i.e., the wavelength where the response is reduced by half) of 8.2 km. An average spectrum for the data calculated in the flight line direction (Figure 3a) shows the expected decline in signal amplitude with decreasing wavelength for wavelengths less than 10 km. The marked drop in amplitude for wavelengths shorter than 10 km is consistent with the impact of the Kalman filter shown in Figure 3b.

Results from a number of different investigations were used as inputs to obtain the final estimate of uncertainty in the airborne gravity data of 10 μm/s^2 for wavelengths between 8 and 55 km. Differences in data values where flight lines and tie lines intersect provide an indication of data uncertainty. The mistie values vary depending on the nature of the leveling that has been applied to the data. The standard deviation of the misties was 21.7 μm/s^2 for raw data, 10.3 μm/s^2 after leveling using low order trends, and 3.7 μm/s^2 after final leveling adjustments (Gabell and Tuckett, 2004). A 10 km portion of one of the flight lines was flown 5 times. The precision of the measurements for this repeat line was estimated as 5.2 μm/s^2 using the procedure described by Green and Lane (2003). Differences from one pass along the line to the next that arise from wavelengths longer than the length of the line are excluded from this precision estimate. Thus, the precision estimate is only valid for data that have been high-pass filtered to exclude wavelengths greater than the length of the repeat line (i.e., 10 km in this instance). The uncertainty would be larger if longer wavelength information were also considered. This was the case when the differences between upward continued ground gravity measurements along a 55 km traverse and the final airborne data were examined. The standard deviation of the differences was 10.6 μm/s^2. This was considered the best estimate of the uncertainty in the data, although even this figure must be qualified as referring to data where wavelengths in excess of 55 km have been removed.

Although the airborne data were tied to the Australian Fundamental Gravity Network (Gabell and Tuckett, 2003), there remained long wavelength discrepancies between the existing ground data, upward continued to the height of the airborne survey, and the airborne data. To reduce this discrepancy, a crossover filter was applied to the ground and airborne data. This involves high-pass filtering of the airborne data and replacing the low frequency portion of this dataset with low-pass filtered ground data. The crossover wavelength is chosen based on sample spacing and accuracy considerations.

The complementary high and low-pass filter response functions defined by a cosine roll-off between 35 and 45 km are illustrated in Figure 4. Given a basic sample spacing of 11 km for the ground data, significant aliasing for wavelengths less than 22 km would be expected for these data. The smallest dimension of the survey area, around 60 km, dictates that longest wavelength that will be properly sampled in the airborne data. The crossover wavelength bracket of 35 to 45 km was chosen as midway between these wavelength constraints. An image of the difference between the crossover filtered product and the original airborne data is shown in Figure 4. The image represents the differences for wavelengths greater than 40 km between the ground and airborne data. There is an average offset of around -20 μm/s^2, with indications of a trend from around zero offset in the northwest to around -40 μm/s^2 in the southeast. Having reduced the wavelength range of the AG contribution in the filtered output from 8-60 km to 8-40 km, the noise estimate was revised downward to 8 μm/s^2. This does not imply that the ground gravity data are noise-free for wavelengths greater than 40 km. When it comes to combining the ground data with the output of the crossover filter, these data are identical for wavelengths greater than 40 km, and hence no allowance for inconsistency is required for these wavelengths.

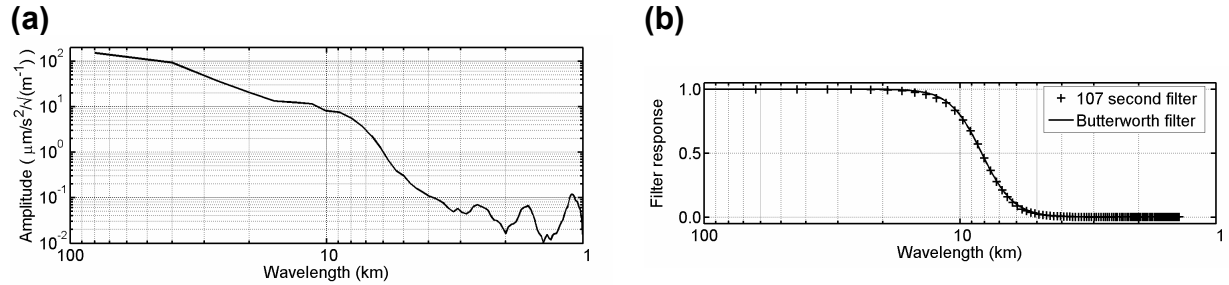

Figure 3. (a) Average amplitude spectrum of West Arnhem Land AG simple Bouguer anomaly data, calculated in the flight line direction (090 or 270 degrees). (b) Filter response for 107 second Kalman filter (symbols) as given by Gabell and Tuckett (2003) and filter response for 7th order Butterworth filter with central wavelength of 8.2 km (solid line).

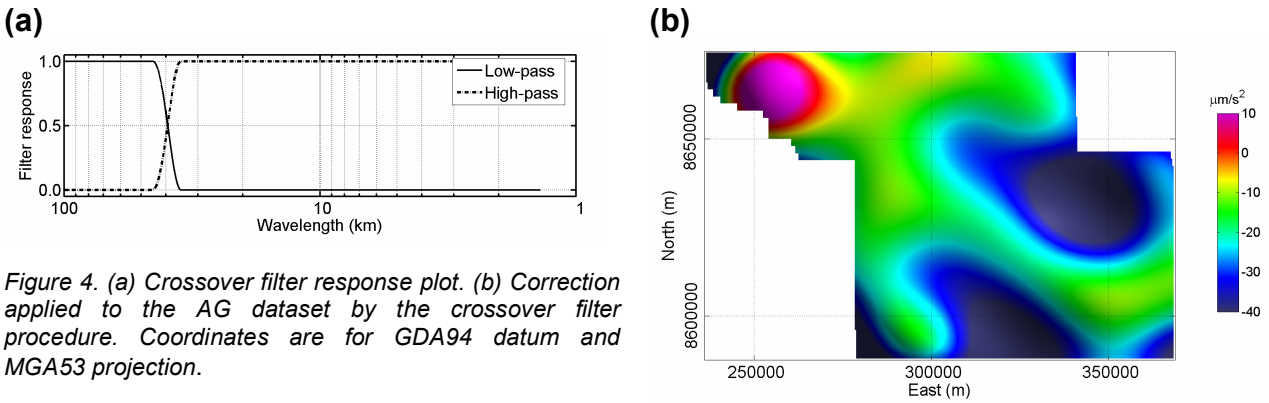

Figure 4. (a) Crossover filter response plot. (b) Correction applied to the AG dataset by the crossover filter procedure. Coordinates are for GDA94 datum and MGA53 projection.

Combined ground and airborne measurements

The airborne data were acquired at a constant height of 655 m AHD (i.e., constant height above the geoid). This flat surface was chosen as the output drape surface to eliminate the need to continue the airborne data to another surface. To reduce the computational load during equivalent layer inversion, the airborne data were up-sampled to 1600 m spacing from the original 400 m grid. This spacing is still well below the 4 km sampling required to capture wavelengths above the 8 km central value of the low-pass filter applied to the airborne data.

The ground data were gridded with 400 m cells then continued from ground level to the output drape surface using a Fourier drape-to-level procedure described by Cordell and Grouch (1985). The data used for the inversion were derived by re-sampling the continued grid at the horizontal locations of the original observations.

The performance of the equivalent source inversion was assessed by reviewing the overall data misfit, histograms of the normalized data misfit, mass properties of the equivalent source layer, the spatial distribution of data misfit values and the vertical gravity predictions on the output drape surface.

The expected value for the chi-squared noise-weighted ("normalized") data misfit is equal to the number of observation points. This assumes that the data errors are approximately normally distributed, the model structure is not an impediment to obtaining a close fit to the data (i.e., that the model layer is not too far below the observations, that the model elements are not too coarse, etc) and the supplied error levels are sufficiently large that any inconsistencies between the ground and airborne data can be resolved without exceeding the expected value of the chi-squared noise-weighted data misfit. The inversion finds a solution that is consistent with the data errors in the sense that the regularization is adjusted to obtain a data misfit with the expected chi-squared value. After each inversion, histograms of normalized data misfit were inspected to see if the distribution of the normalized data misfits approximated a normal distribution. (Figure 5). The number of observations ("N") and the chi-squared normalized data misfit ("chi_sq") is printed in the top right of each of these histograms. Histograms were produced for the combined dataset and for the ground and airborne data separately. This provided a check that the relative errors between the ground and airborne data had been set appropriately. Although the normalized data misfit values did not perfectly match a normal distribution, the observed distributions were considered to be acceptable.

A smooth lateral variation in the mass properties of the equivalent layer was sought to ensure an appropriately smooth fit to the data, particularly in areas with sparse observations. The inversion algorithm automatically adjusts the trade-off parameter between the model objective function and the data misfit so that the desired degree of fit to the data is obtained. The model objective function has two components: lateral smoothness and smallness. The smoothness constraint is the sum of differences between adjacent cells in the east-west and north-south directions, whilst the "smallness" constraint is the sum over all cells of the differences between the density values and the reference density. The latter was everywhere zero in this instance. The variations in the mass properties of the layer can be strongly influenced by factors other than the data and the data errors: the dimensions of the cells, the separation between the top of the cells and the observations, and the relative weighting of smoothness and smallness constraints. In early inversion attempts, the lateral variation in mass properties was not sufficiently smooth (Figure 6). This was rectified by using model elements with smaller horizontal cross-section, greater depth extent and by increasing the smoothness weighting relative to the smallness weighting. Given the geometry of the equivalent layer, there is no direct connection between the mass properties within the layer and the actual subsurface density values in the survey area. The distribution of the properties does however represent a de-convolution of the vertical gravity response into a more focused form. This is evident in a comparison between Figure 6b and Figure 8c.

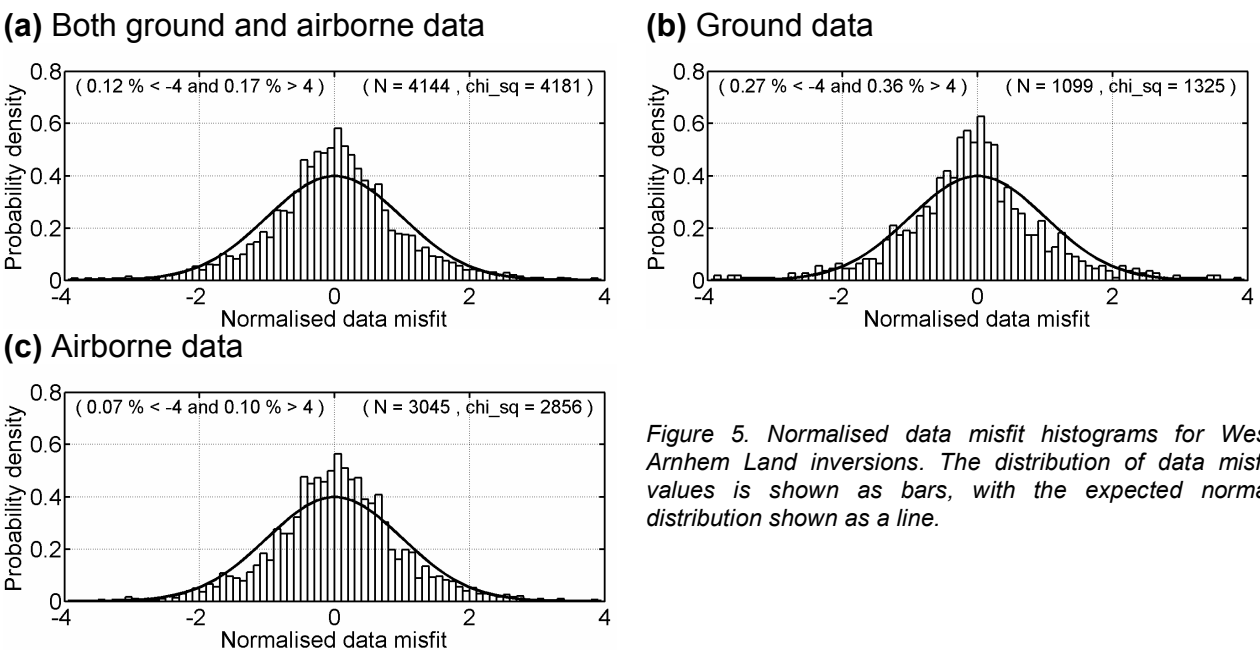

Figure 5. Normalised data misfit histograms for West Arnhem Land inversions. The distribution of data misfit values is shown as bars, with the expected normal distribution shown as a line.

The performance of each inversion was further analyzed by displaying grids of the data misfit for the input ground and airborne datasets (Figure 7). If the correct noise estimates and inversion parameters have been used, there should not be any signal present in these grids. This is more or less the case in the final inversion, though there is a hint of coherent geological structure near the western edge of the survey in the image of airborne data misfit.

Once a satisfactory inversion was obtained, the response was calculated by forward modeling of the equivalent layer mass properties at the desired output spacing of 400 m on the output drape surface (Figure 8). The first order trend surface removed from the data prior to inversion was then restored (not shown). This output represents an optimized combination of the ground and airborne simple Bouguer vertical gravity data.

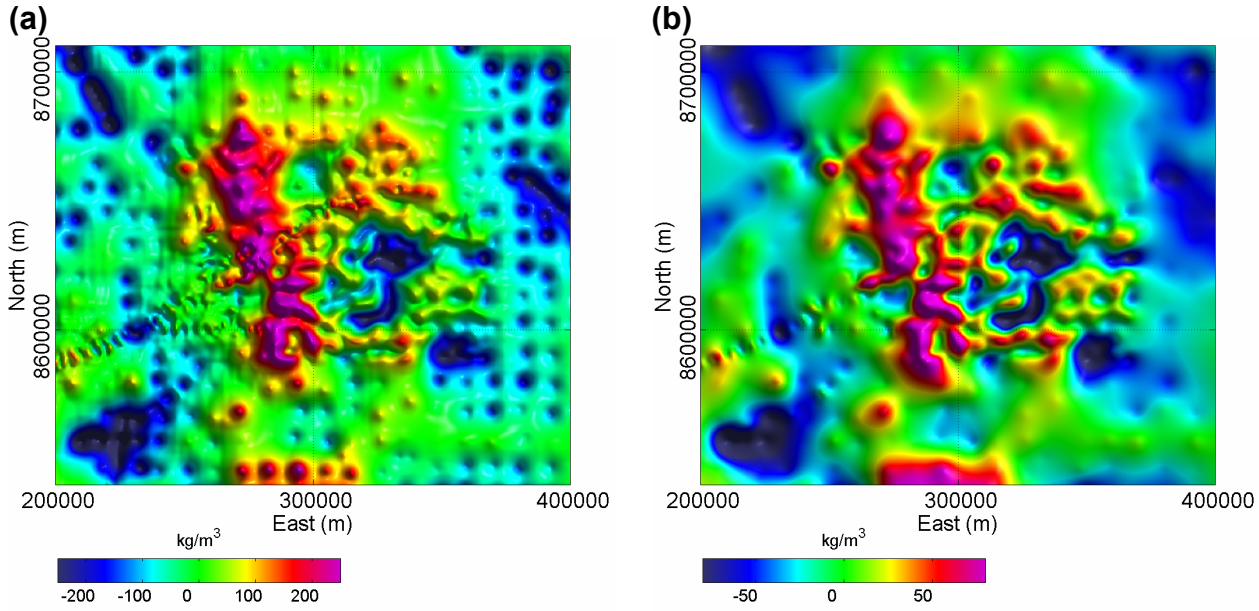

Figure 6. Images of equivalent layer density values. Both inversions fit the observations to the prescribed level of uncertainty. (a) Early inversion result showing inappropriate lateral smoothness in the mass properties of the layer. The model elements were 1600 m below the level of the observations, and had horizontal size 1600 m and vertical extent 2000 m. The weighting of smoothness to smallness model constraints was not high enough for smoothness to dominate. (b) Final inversion result. The model elements were 800 m below the level of the observations, and had horizontal size 800 m and vertical extent 8000 m. The smoothness model constraint was weighted so that it would dominate over the smallness model constraint.

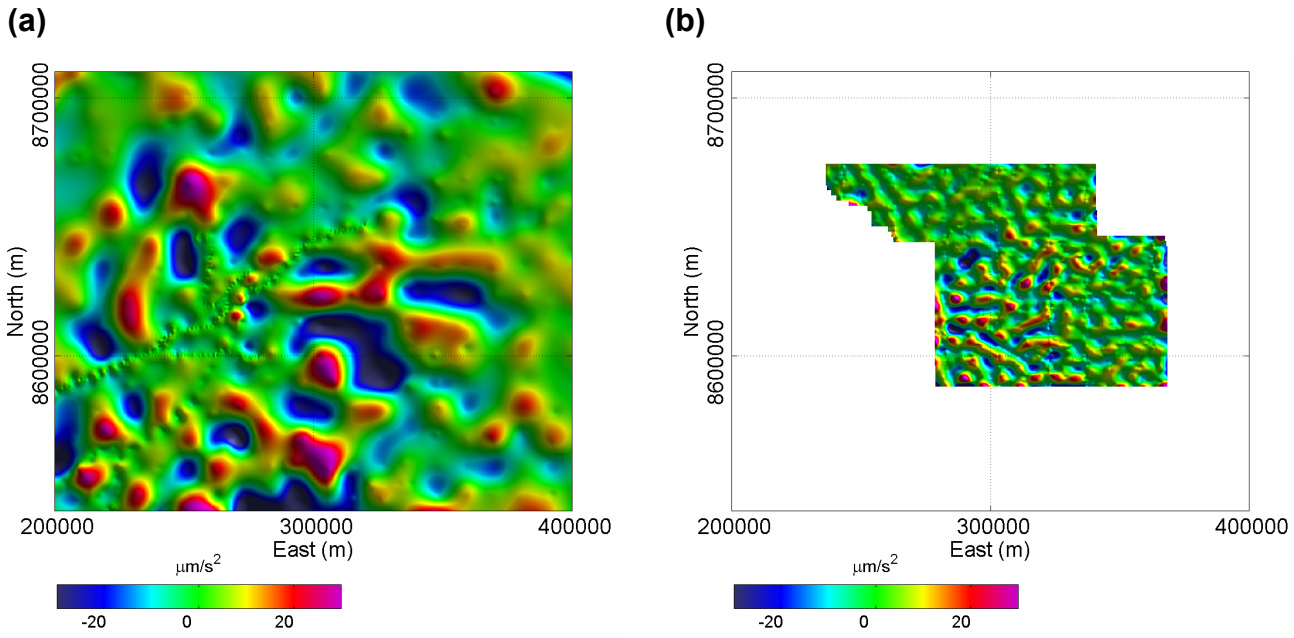

Figure 7. Data misfit images from the final inversion for (a) ground and (b) airborne data.

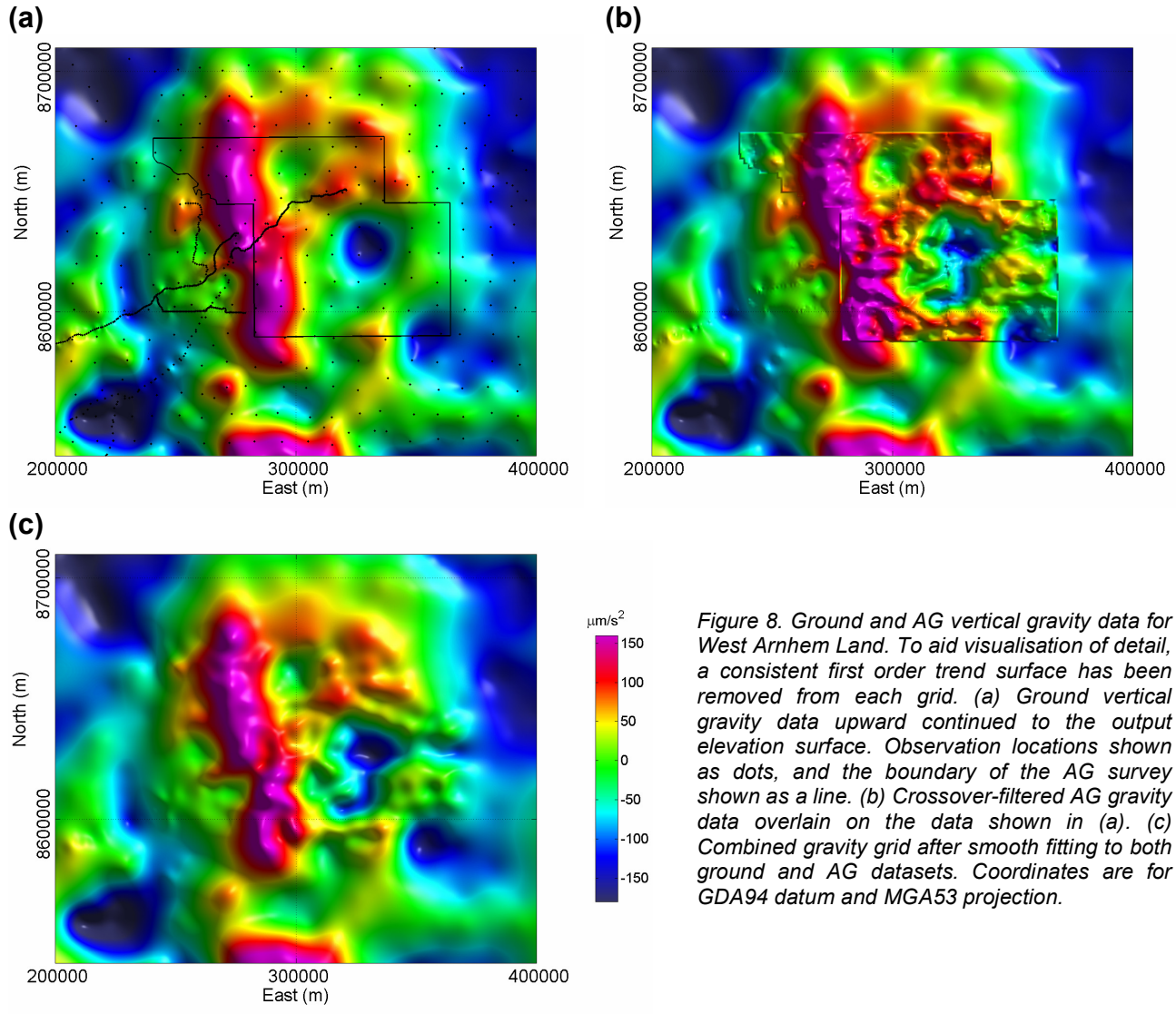

Figure 8. Ground and AG vertical gravity data for West Arnhem Land. To aid visualisation of detail, a consistent first order trend surface has been removed from each grid. (a) Ground vertical gravity data upward continued to the output elevation surface. Observation locations shown as dots, and the boundary of the AG survey shown as a line. (b) Crossover-filtered AG gravity data overlain on the data shown in (a). (c) Combined gravity grid after smooth fitting to both ground and AG datasets. Coordinates are for GDA94 datum and MGA53 projection.

Example 2: Broken Hill Airborne Gravity Gradiometer Survey

A FALCON airborne gravity gradiometer survey was flown in the Broken Hill district early in 2003 to stimulate exploration for base metal, Fe-Cu-Au and Ni-Cu-Pt-Pd deposits (Lane et al., 2003). The survey covered an area of 1186 km^2, with lines flown in 036 and 216 directions at 200 m spacing. The tie lines had 2000 m spacing and the nominal terrain clearance was 80 m (Fugro Airborne Surveys, 2003).

Ground measurements

The pre-existing ground gravity data were acquired over a very large number of acquisition campaigns, with different levels of accuracy and sample spacing. Within the survey area, the maximum sample spacing is 2 km. Some very detailed grids of observations are present, with data acquired at 25 to 50 m spacing on lines 100 to 200 m apart. Using information provided in acquisition and processing reports, estimates of uncertainty in the simple Bouguer gravity values were calculated as per the expressions in Equations 1 to 3. The uncertainty values ranged from 0.5 to 10 μm/s^2, with an RMS value around 1.5 μm/s^2.

Airborne measurements

The FALCON AGG system is described by Lee (2001). Given that two horizontal gradients are measured over the survey area, either or both of the gradients can be transformed to any other gravitational quantity, including vertical gravity. This transformation can be carried out using one of several methods and vertical gravity data were provided from the Broken Hill Survey based on equivalent source and Fourier. These results are not identical because of differences in the assumptions involved and differences in the numerical methods used to treat noise in the gradient data (Hensley, 2003a). In this study, the vertical gravity derived via the Fourier method was used. A low pass filter with a cutoff wavelength of 400 m had been applied to these data. Dransfield et al. (2001) indicate that a 6th order Butterworth filter is used for this filtering. An average amplitude spectrum calculated in the flight line direction from the Fourier method vertical gravity data is shown in Figure 9a. The filter response spectrum for a 6th order Butterworth low-pass filter with a central wavelength of 400 m is shown in Figure 9b for comparison. The rapid attenuation of amplitude for wavelengths less than 500-600 m that is observed in the Broken Hill data is consistent with the given filter response spectrum.

Liu et al. (2001) and Dransfield et al. (2001) indicate that system noise in Falcon AGG data is closely related to the level of turbulence experienced during acquisition. Short duration turbulence events would introduce broadband noise into the measurements. Given decreasing levels of signal with decreasing wavelength, such noise would become a limiting factor at short wavelengths. Accuracy at long wavelengths in vertical gravity data from the system is limited by processing factors. Strictly speaking, transformation of one gravity quantity to another requires knowledge of the response over an infinite extent. Given data from a finite survey area, the maximum wavelength that can be present in the transformed data is related to the dimensions of the survey area. Long wavelength accuracy is further affected because only relative gravity gradients are measured (Dransfield et al., 2001). This means that neither absolute level nor first order trend information in the vertical gravity field will be recovered.

A portion of a flight line was flown on 5 separate occasions in the course of the Broken Hill survey to provide data for an estimate of “repeatability” or precision (Hensley, 2003b). It was not appreciated at the time, however, that a repeat swath rather than a repeat line would be required to meet this objective. Given that spatial transformations are used to produce both gradient and vertical gravity data, the repeat line data were processed using a surrounding set of flight lines that were the same for processing of each separate pass. This violated the assumption required for deriving precision estimates from repeat line data that all of the data involved in processing one pass along the repeat line are independent from the data used for processing any other pass along the line. Consequently, the precision estimates derived from this exercise underestimate the variability in the vertical gravity data. Ground data with sufficient detail and accuracy to be used for estimating the noise level in the AGG data are of limited spatial extent, and hence of limited use for this purpose. Boggs and Dransfield (2003) provide an estimate of the noise in Falcon AGG vertical gravity data. They estimate the noise to have a spectral density of 1 μm/s^2/√(km). Thus, for the Broken Hill survey with wavelengths present up to 20 km, noise levels of around 0.4 μm/s^2 might be anticipated.

To reduce the inconsistency between the ground and airborne data at long wavelengths, a crossover filter procedure was applied. Long wavelength information in the airborne data was replaced with the relevant portion of the ground vertical gravity data spectrum following upward continuation of the ground data to the drape surface for the airborne observations. The maximum spacing between ground gravity observations was 2 km. Thus, wavelengths of 4 km and above are fully sampled. The minimum survey dimension is 20 km, so wavelengths of 10 km or less should be recovered with reasonable accuracy in the AGG data. Various crossover wavelength ranges between 4 and 10 km were trialed before settling on a range of 4-6 km (Figure 10). The image of differences between the airborne data and the crossover filter output shows an

average offset of around 110 μm/s^2 was present between the airborne and ground datasets. An offset of this magnitude was not surprising since the relative gradient measurements do not allow the absolute level of vertical gravity to be recovered. Figure 10b shows that other long wavelength differences of up to 40 μm/s^2 are also present. Based on values extracted at the horizontal position of the original ground observation locations, the standard deviation of the differences between ground data and the airborne data following crossover filtering was 2.1 μm/s^2. This figure is consistent with noise levels that would be predicted for airborne data with wavelength range limited to less than 5 km using the noise spectral density value derived by Boggs and Dransfield (2003) (i.e., 1 μm/s^2/√(km) over a bandwidth of 5 km is approximately 2.2 μm/s^2).

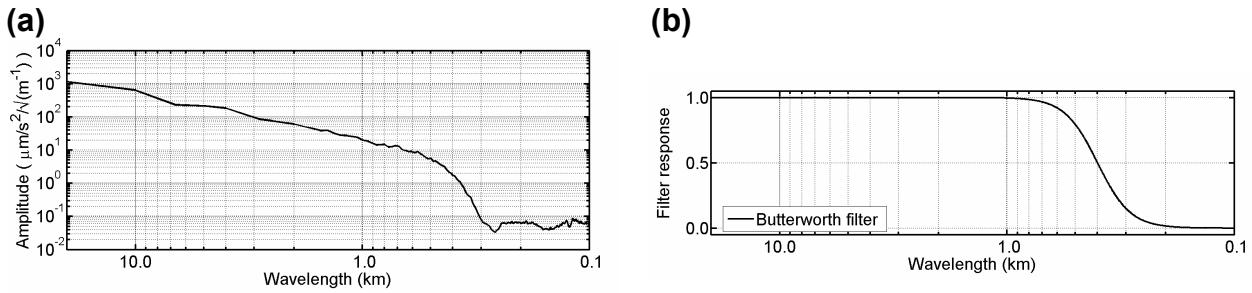

Figure 9. (a) Average amplitude spectrum of Broken Hill AGG vertical gravity data (Fourier method), calculated in the flight line direction (036 or 216 degrees). (b) Filter response for 6th order Butterworth filter with central wavelength of 0.4 km.

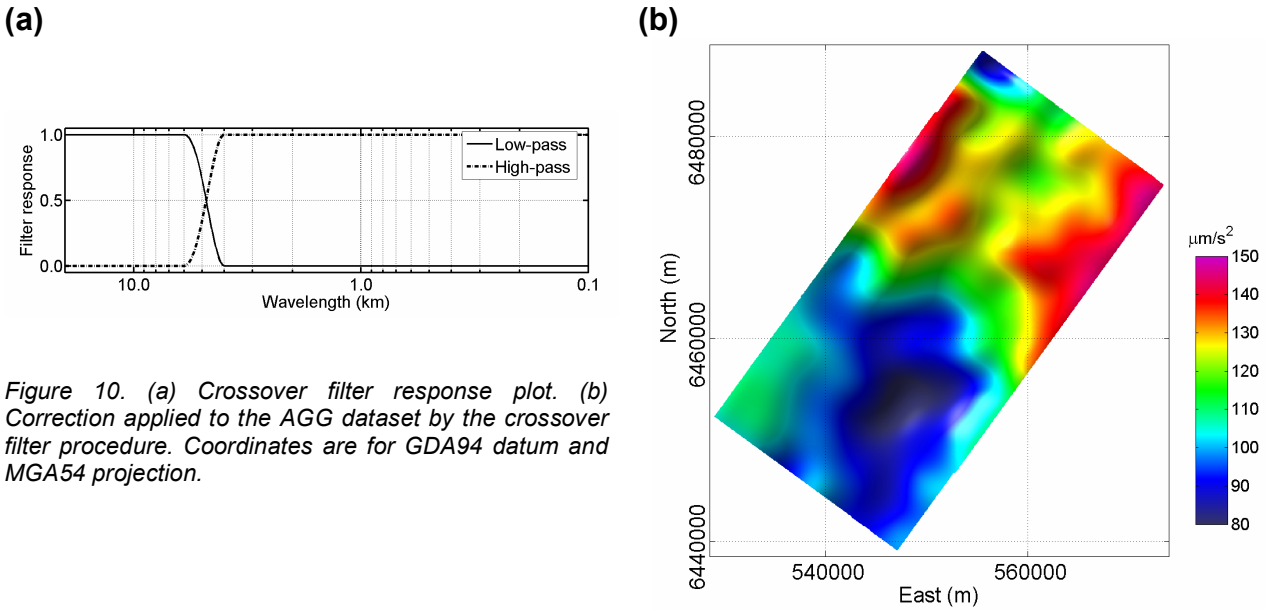

Figure 10. (a) Crossover filter response plot. (b) Correction applied to the AGG dataset by the crossover filter procedure. Coordinates are for GDA94 datum and MGA54 projection.

Combined ground and airborne measurements

The drape surface specified for the Fourier method AGG vertical gravity data was a smoothed version of surface topography offset upwards by 80 m. To avoid having to continue the airborne data, the output drape surface was chosen to coincide with this surface. The ground data were gridded, upward continued to the output drape surface then re-sampled at the horizontal location of the original observations. A first order trend surface was removed from both ground and airborne data prior to equivalent layer inversion so that the average mass property value required to reproduce the residual anomalies would be approximately zero.

Given the use of a 400 m low pass filter, the supplied grids of AGG data with 50 m cell size substantially over-sample the available information. To reduce the computational demands, the crossover-filtered airborne data were up-sampled to the maximum 200 m spacing. This spacing was matched to the horizontal dimensions of the cells in the equivalent source layer and the 200 m vertical separation between the observations and the equivalent source layer. Although it would have been preferable to retain a degree of over-sampling (e.g.,100 m cells, 100 m vertical separation between the observations and the top of the equivalent source layer, and 100 m samples of the airborne data), a substantially more efficient equivalent source inversion algorithm would have been required.

Images of the ground, airborne and combined data are shown in Figure 11. Owing to the large number and close spacing of the observations in this example, results of a vertical derivative applied to each of these grids are also given (Figure 12). These images of the vertical gravity gradient clearly illustrate the relatively seamless integration of ground and airborne data through the method outlined in this paper, as well as the resultant loss of short wavelength resolution that necessarily accompanies the procedure.

Figure 11. Ground and AGG vertical gravity data for Broken Hill. (a) Ground vertical gravity data upward continued to the output elevation surface. Observation locations shown as dots. (b) Crossover-filtered AGG gravity data (Fourier method) overlain on the data shown in (a). (c) Combined gravity grid after smooth fitting to both ground and AGG datasets. Coordinates are for GDA94 datum and MGA54 projection.

Figure 11(a) Ground vertical gravity data upward continued to the output elevation surface. Observation locations shown as dots.

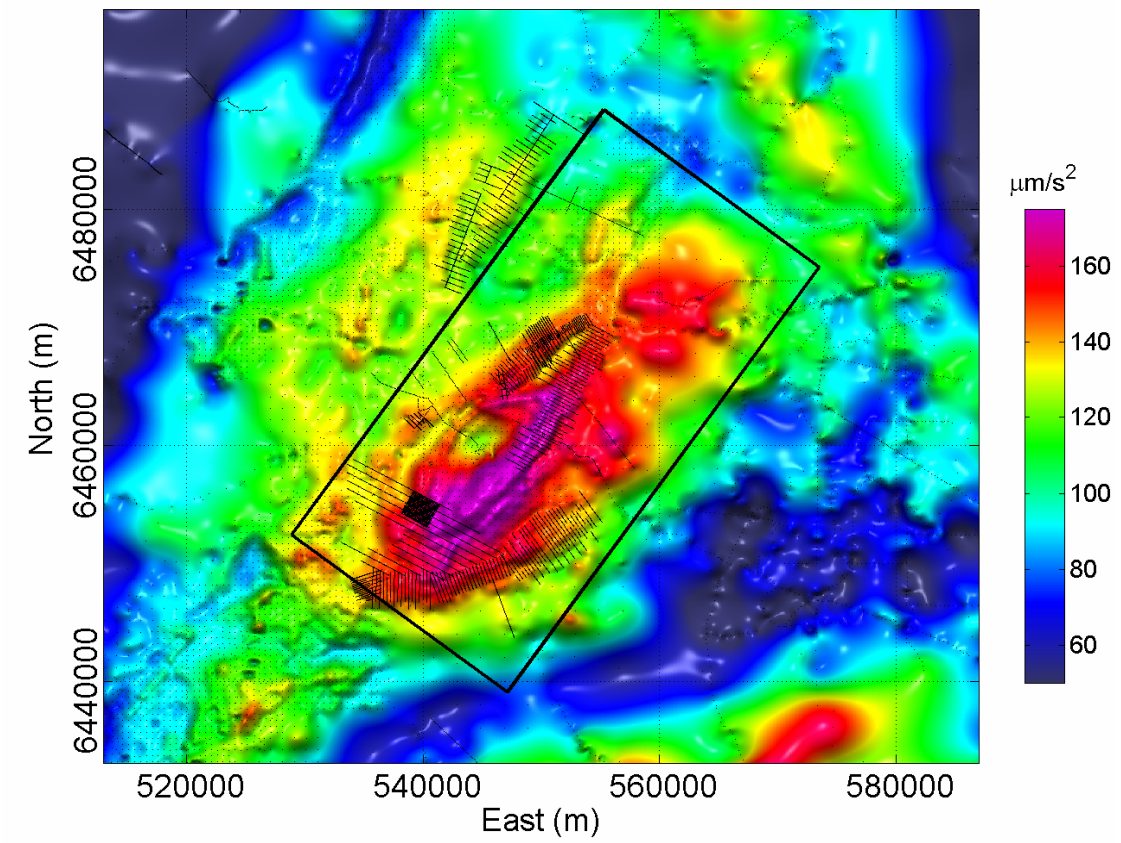

Figure 11(b) Crossover-filtered AGG gravity data (Fourier method) overlain on the data shown in (a).

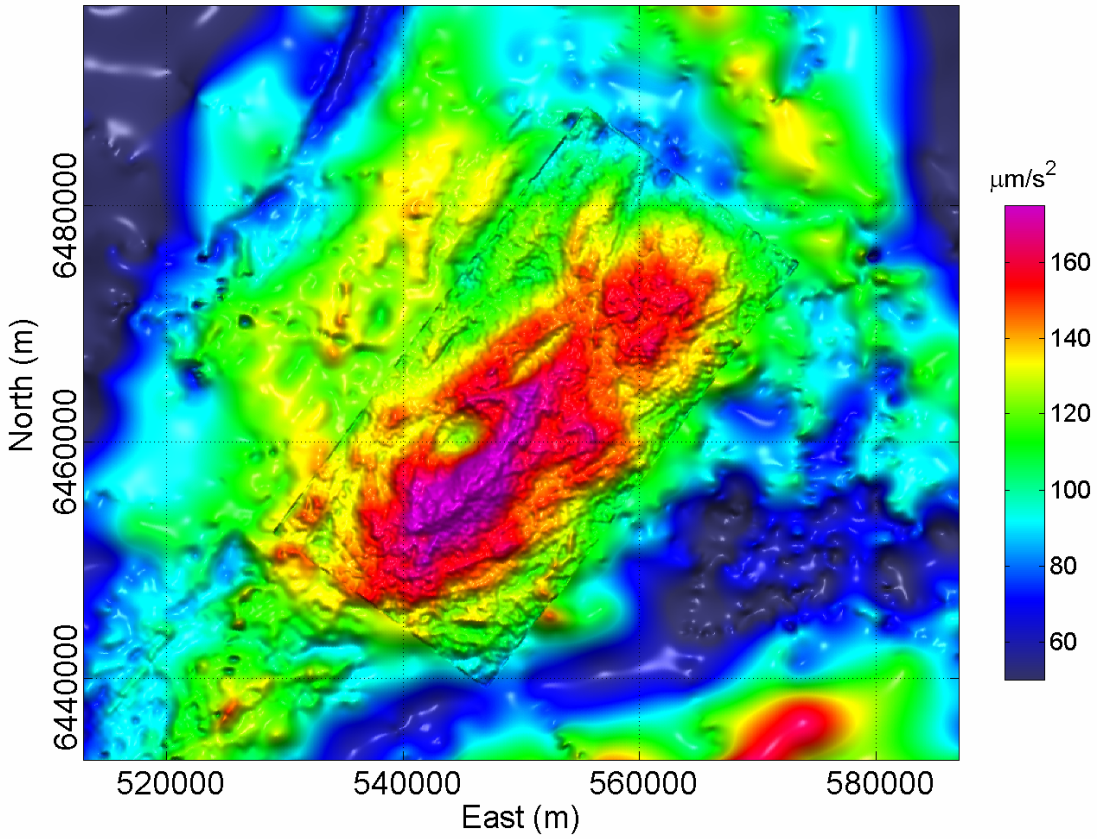

Figure 11(c) Combined gravity grid after smooth fitting to both ground and AGG datasets. Coordinates are for GDA94 datum and MGA54 projection.

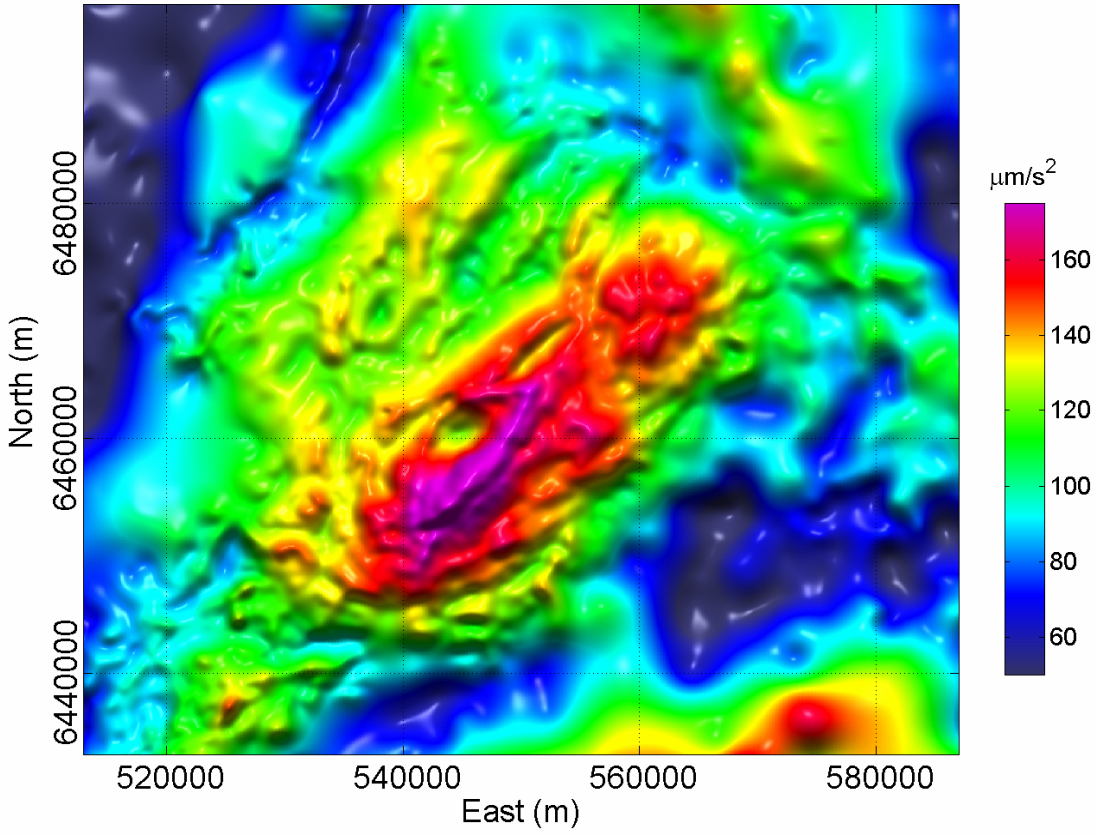

It is standard practice to use an exact fitting procedure such as minimum curvature gridding to grid potential field data. Short wavelength artifacts will be produced when noise-contaminated observations with variable spacing are present (Figure 11a). These short wavelength artifacts are given additional emphasis when a vertical derivative is applied to the grid of vertical gravity to produce a grid of the vertical gravity gradient (Figure 12a). The reduction in impact of these artifacts in the smooth-fitting grid (Figure 11c and Figure 12c) provides some justification for producing such a grid to complement the exact-fit grid. Although the benefit of a smooth-fitting procedure is a reduction in the level of short wavelength artifacts, the downside is a blurring of signal.

Figure 12. Ground and AGG vertical gravity gradient data for Broken Hill. (a) Ground vertical gravity gradient data upward continued to the output elevation surface. (b) Crossover-filtered AGG vertical gravity gradient data (Fourier method) overlain on the data shown in (a). (c) Combined vertical gravity gradient grid after smooth fitting to both ground and AGG datasets.

Figure 12(a) Ground vertical gravity gradient data upward continued to the output elevation surface.

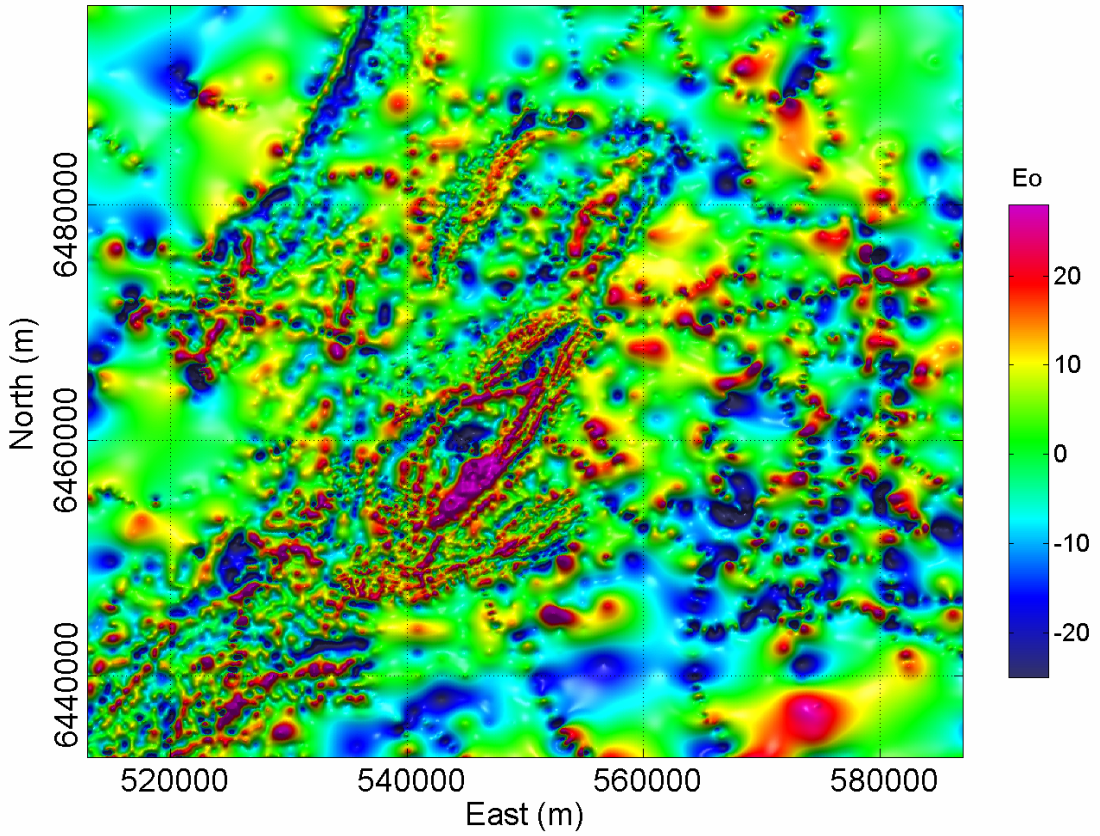

Figure 12(b) Crossover-filtered AGG vertical gravity gradient data (Fourier method) overlain on the data shown in (a).

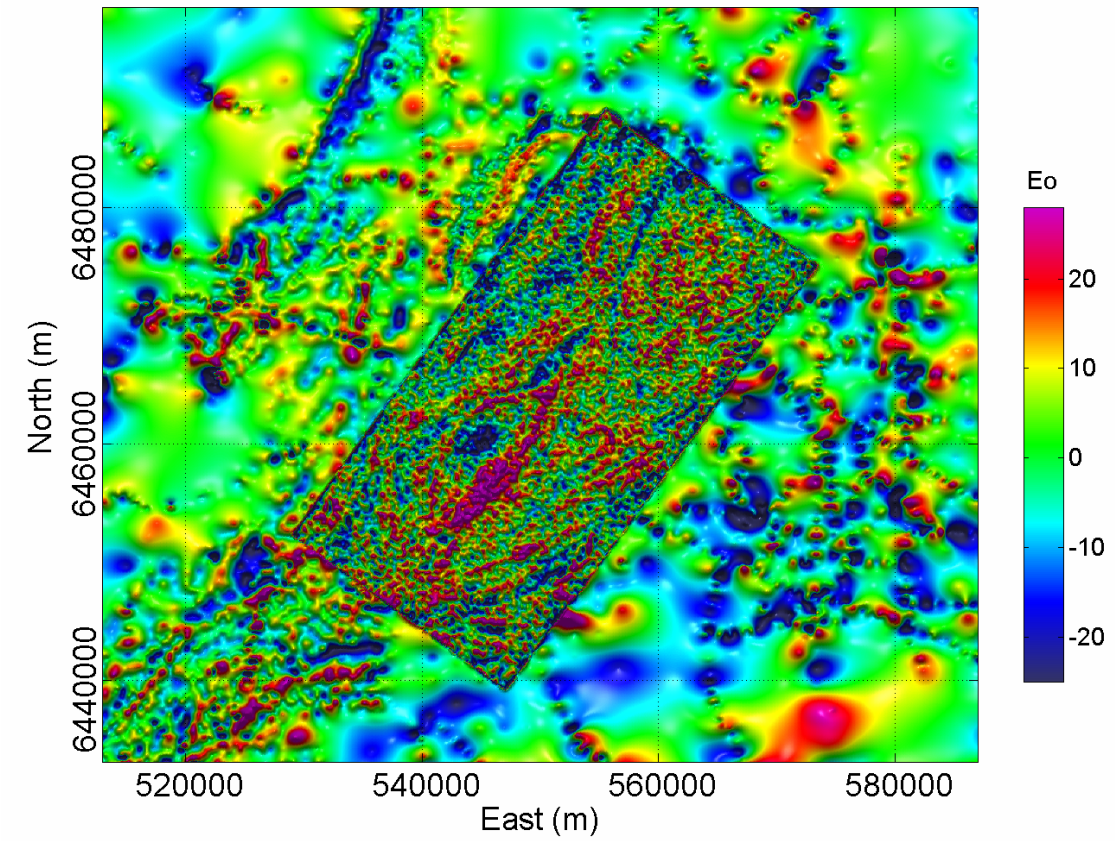

Figure 12(c) Combined vertical gravity gradient grid after smooth fitting to both ground and AGG datasets.

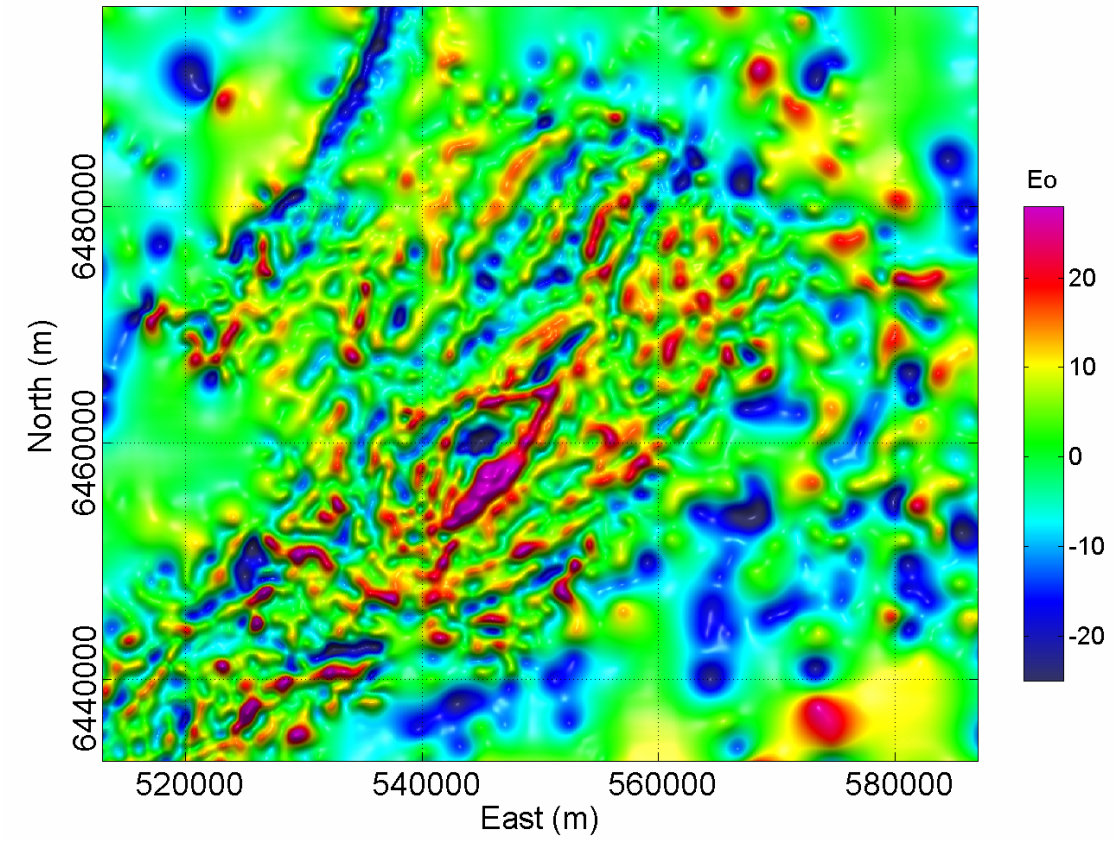

Discussion

The range of wavelengths present in each of the datasets examined is summarised in Figure 13. Limitations in the signals at either short or long wavelengths (or both) were observed in each of them. Ideally, the datasets used to produce a compilation would span the entire wavelength range with sufficient overlap to allow inconsistencies between the datasets to be resolved. It is more important to have adequate signal at mid to long wavelengths since most of the power in the vertical gravity signal is present in these wavelengths. Fortunately, the existing ground gravity coverage provides this for all onshore locations in Australia. There are deficiencies in the signal at short wavelengths in each of the datasets used in the examples, and hence in the combined products, but this does not preclude coherent regional appreciation of the mid to long wavelengths that are available.

The size of an airborne survey places restrictions on the wavelengths that can be recovered using either of the systems discussed in this study. Drift in the system response and the need to level the data plays a part in the processing of the AG data. Integration of a gradient response over a finite survey area is a restriction in the case of the AGG system. The deficiencies are not restricted to the absolute level or to the longest wavelength, but impact a number of the longer wavelength terms that are obtained by 2D Fourier decomposition. Longer wavelengths in the airborne data were replaced with more accurate and complete information from the existing ground gravity data. In both examples, there was sufficient overlap in wavelengths to allow this to be done. For an overlap to exist, the maximum spacing of the ground gravity observations within the airborne survey area must be less than half of the smallest dimension of the survey area. The maximum spacing of the ground gravity observations would preferably be less than a quarter of the smallest dimension of the survey area to allow for diminished accuracy at the shorter wavelengths in the ground data and the longer wavelengths in the airborne data. The maximum ground gravity station spacing anywhere in Australia is 11 km, so this condition will be met for surveys that are at least 22 km in size, and preferably at least 44 km in size across the smallest dimension.

Turbulence is noted as a major source of noise for both AG and AGG methods. At the time scales relevant to the resolution of the systems, turbulence would give rise to a random series of impulsive noise events with constant amplitude over all wavelengths. Given that the vertical gravity signal diminishes in amplitude with decreasing wavelength, the signal to noise will thus be smaller at short wavelengths. Low-pass filtering had been applied to both the AG and AGG datasets to restrict the visual impact of noise at short wavelengths, and the cut-off wavelength of this filter defined the short wavelength resolution of the data.

The wavelength chart in Figure 13 shows that acquisition of AG data in the Broken Hill area would not have produced new information. The existing ground data already provide information over the 8 to 80 km wavelength range of the AG data. Acquisition of AGG data in the West Arnhem Land area would also have been problematic, since this would have left only partial coverage of wavelengths between 10 and 44 km. It can thus be seen that consideration of the wavelength range that can be obtained from AG and AGG systems provides one criterion for deciding on the suitability of these methods for improving the gravity coverage in a given region.

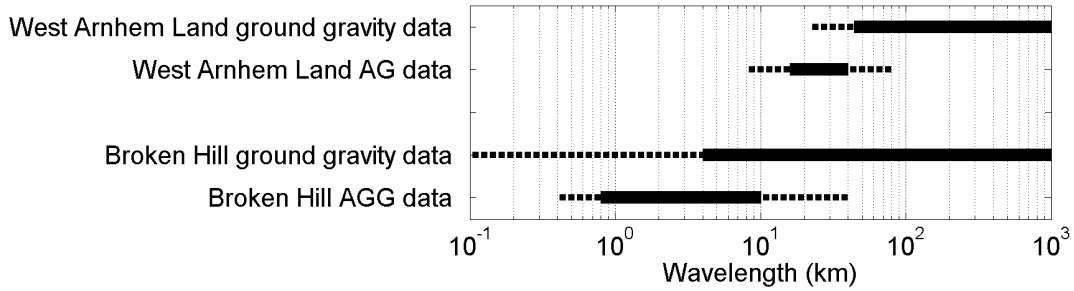

Figure 13. Chart of data source and estimated wavelength range. Solid lines indicate accurate data whilst dashed lines indicate either partial spatial coverage or reduced accuracy.

An equivalent source method was used to produce a smooth fit to the two input datasets. As noted by Billings et al. (2002a,b), this is one of a group of methods which can be described as radial basis functions. Other methods from this group, such as splines, kriging or collocation, could have been used in the fitting procedure. The equivalent source method was chosen in this instance because it directly models the gravity signal being considered. Although not unique amongst smoothing functions, the specific implementation of the equivalent source method used in this study had the desirable characteristic of producing a smooth fit that was adaptive to the spatial distribution of observations and to their individual noise estimates.

Conclusions

A multi-stage procedure for combining ground and airborne vertical gravity data was described and successfully applied to field examples involving data sourced from AG and AGG surveys. Although acquisition methods, output bandwidth and noise levels were very different for the two airborne datasets, the same procedure was found to be suitable when combining data from either of these systems with ground gravity data.

Since the ground and airborne data are associated with different elevation drape surfaces, there must be a conscious selection of an output drape surface. A drape-to-drape method was used to continue both datasets onto this surface.

Deficiencies were recognized in the long wavelength accuracy of both of the airborne datasets, brought about by the finite size of the survey areas and instrument drift. A crossover filtering method was used to replace the longer wavelengths in the airborne datasets with information from ground data.

The presence of noise means that there are inconsistencies between the data values where the datasets overlap, and hence it is not possible to exactly fit a surface to both datasets. An equivalent source method was used to construct a density model that produced a smooth vertical gravity response that approximately fitted both datasets. Smoothness constraints on the lateral variability in the mass properties of the sources allowed a smooth rather than exact surface to be fit to the data. The misfit between the input and fitted data was dependent on the noise levels assigned to each individual observation. A regular grid of output data values was generated by forward modeling the equivalent source distribution at specified locations on the output drape surface.

It was noted that a smooth-fitting method can complement the usual exact-fitting method used for gridding ground gravity data, regardless of whether these data are gridded alone or combined with airborne data. The uncertainty in ground data is sufficient to produce large artifacts at short wavelengths in grids produced using exact-fitting methods. These artifacts are suppressed in the smooth fitting grids. This benefit must be balanced against the attenuation of short wavelength signal.

A number of separate stages in the procedure could be eliminated and larger datasets could be combined if a more efficient equivalent source fitting program specifically designed for this task was available.

Acknowledgments

The West Arnhem Land Airborne Gravity Survey was a joint project between the Northern Territory Geological Survey (NTGS), Geoscience Australia, Cameco Australia Pty Ltd and Rio Tinto Exploration Pty Ltd. The Broken Hill Airborne Gravity Gradiometry Survey was a joint project between the NSW Department of Mineral Resources, pmd*CRC, Geoscience Australia, Gravity Capital and BHP Billiton. Thoughtful comments on drafts of this paper from Peter Milligan and Ian Hone were greatly appreciated. This paper is published with the permission of the Chief Executive Officer, Geoscience Australia.

References

Billings, S.D., Beatson R.K., and Newsam, G.N., 2002a, Interpolation of geophysical data using continuous global surfaces: Geophysics, 67, 1810-1822.

Billings, S.D., Newsam, G.N., and Beatson R.K., 2002b, Smooth fitting of geophysical data using continuous global surfaces: Geophysics, 67, 1823-1834.

Boggs, D.B., and Dransfield, M.H., 2003, Analysis of errors in gravity derived from the FALCON Airborne Gravity Gradiometer: Submitted for inclusion in M. Talwani and E. Biegert (eds), Gravity Gradiometry – Instrumentation, Processing and Case Studies, Society of Exploration Geophysicists. (Reproduced as a paper in this volume).

Bruton, A.M., 2000, Improving the Accuracy and Resolution of SINS/DGPS Airborne Gravimetry: Ph.D Thesis, The Department of Geomatics Engineering, University of Calgary, UCGE Report No. 20145. (http://www.geomatics.ucalgary.ca/Papers/Thesis/KPS/00.20145.AMBruton.pdf)

Cordell, L, and Grauch, V.J.S., 1985, Mapping basement magnetization zones from aeromagnetic data in the San Juan Basin, New Mexico: in Hinze, W.J., (ed.), The Utility of Regional Gravity and Magnetic Anomaly Maps, Tulsa, Society of Exploration Geophysicists, 181-197.

Dransfield, M., Christensen, A., Rose, M., Stone, P., and Diorio, P., 2001, FALCON test results from the Bathurst Mining camp: Exploration Geophysics, 32, 243-246.

Duffett, M., Bacchin, M., and Lane R., 2004, West Arnhem Land Airborne Gravity Survey: In Record of Abstracts, Annual Geoscience Exploration Seminar (AGES) 2004, Northern Territory Geological Survey Record 2004-001.

Fraser, A.R., Moss, F.J., and Turpie, A, 1976, Reconnaissance gravity survey of Australia: Geophysics, 41, 1337-1345.

Fugro Airborne Surveys, 2003, Acquisition and Processing Report, Job 1572, Broken Hill, NSW, Airborne Gravity Gradiometer and Magnetic Geophysical Survey for BHPBilliton.

Gabell, A.R., and Tuckett, H., 2003, Final Report for GT1-A Demonstration Project: Zuisin Technology and Canadian Micro Gravity Pty Ltd.

Gabell, A.R., and Tuckett, H., 2004, Acquisition and processing report for Project 200380 West Arnhem Land, Northern Territory, GT-1A Airborne Gravity Survey: Fugro Airborne Surveys Pty Ltd (FAS Job No. 1608) and Canadian Micro Gravity Pty Ltd (CMG Job No. 2003-2).

Green, A., and Lane, R., 2003, Estimating Noise Levels in AEM Data: Extended Abstract, ASEG 16th Geophysical Conference and Exhibition, February 2003, Adelaide.

Hensley, C., 2003a, Data Processing Report, Airborne Gravity Gradiometer Survey, Broken Hill, NSW, Australia: BHPBilliton Falcon Operations Report CR 10657 for Survey USN 142911122002.

Hensley, C., 2003b, Repeat Line Data for the Broken Hill FALCON™ Survey: BHPBilliton Falcon Operations Memorandum CM10047.

Hensley, C., 2003c, Merging of Ground Gravity and Falcon™ Airborne Gravity Gradiometry to constrain long wavelengths at Broken Hill: BHPBilliton Falcon Operations Memorandum CM10052.

Lane, R., Milligan, P., and Robson, D., 2003, An airborne gravity gradiometer survey of Broken Hill: In Peljo M., (compiler), 2003, Broken Hill Exploration Initiative: Abstracts from the July 2003 Conference: Geoscience Australia Record 2003/13, 89-92.

Lee, J.B., 2001, FALCON gravity gradiometer technology: Exploration Geophysics, 32, 247-250.

Li, Y., and Oldenburg, D.W., 1998, 3-D inversion of gravity data: Geophysics, 63, 109-119.

Liu, G., Diorio, P., Stone, P., Lockhart, G., Christensen, A., Fitton N., and Dransfield, M., 2001, Detecting kimberlite pipes at Ekati with airborne gravity gradiometry: Extended Abstract, ASEG 15th Geophysical Conference and Exhibition, Brisbane, August 2001.

Airborne gravity data acquisition and processing: A case study in the Prince Charles Mountains, East Antarctica

Mark McLean
University of Melbourne, Australia
m.mclean@pgrad.unimelb.edu.au

Detlef Damaske, Volkmar Damm and Gernot Reitmayr
Bundesanstalt für Geowissenschaften und Rohstoffe, Hannover

Introduction

The Lambert Glacier/Amery Ice Shelf in East Antarctica is a north-northeast trending graben which extends inland for at least 700 km (Figure 1) (Wellman and Tingey, 1976; Kurinin and Grikurov, 1982; Stagg, 1985). This graben is inferred to represent a failed rift emanating from a triple point or four armed junction between India and Antarctica (Stagg, 1985) either before (Lisker et al., in press) or during the break-up of Gondwana (Boger and Wilson, 2003). While the present configuration of this structure suggests a failed rift, recently proposed models suggest that the Lambert region also preserves evidence of an earlier Cambrian suture between at least two Pre-Cambrian blocks that collided during the assembly of Gondwana (Boger et al., 2001). Although sporadic outcrops in the north yield some geological information, large areas to the south are covered with ice rendering it inaccessible to geological sampling (Figure 1).

This paper describes the acquisition and preliminary processing phases of an airborne gravity, magnetic and ice-penetrating radar survey undertaken during the Prince Charles Mountains Expedition of Germany and Australia 2002/03 (PCMEGA). PCMEGA was Australia's first airborne geophysical investigation in the Antarctic continent. This expedition consisted of a field leader, five members of a traverse team, five geophysicists, thirteen geologists, three surveyors, one glaciologist, three field training officers, one doctor, and six members in a helicopter and twin otter crew. From a geophysical perspective, the objective of this investigation was to further our understanding of the Lambert / Amery Rift system and its possible extension underneath the polar ice cap.

Acquisition and Processing

The study area covered part of the southern Prince Charles Mountains, from approximately 72º 45' S to 77º 30' S and 62º E to 72º E (Figure 1). A total of 29 844 km of survey data at 5 km line spacing and 25 km tie-line spacing was acquired over an area of approximately 81 000 km². The tie-line spacing of 25 km (i.e., 1:5 ratio of flight line to tie-line spacing) was chosen to combat the unusually high magnetic diurnal effects at high latitudes. The main grid extended over 350 km, from Wilson's Bluff to 78º S. More lines were flown over an area 150 km by 60 km to the west of the main grid (Figure 1).

The gravity, magnetic and ice-penetrating radar equipment were installed in a De Havilland DHC-6-300 Twin Otter aircraft (Figure 2).

The ice radar was capable of detecting the bedrock to a maximum depth of 3600 metres below the ice surface. To enable the thickest parts of the ice sheet to be accurately surveyed, it is desirable to acquire ice radar data using a drape surface with minimum constant terrain clearance. The ice radar yields an acceptable performance within a terrain clearance range of 200 m and 800 m above ground level.

In contrast to the requirements imposed by the ice radar equipment, the gravity system used for this survey needed to be flown at a constant elevation. Since the ice sheet increases in thickness towards the south, there are conflicting requirements in terms of an optimum drape surface when collecting gravity and ice radar data simultaneously. This conflict was resolved by dividing the survey into three blocks. Each block was flown with a constant flight elevation: 2160 m in the northern block, 2760 m in the central block and 3360 m in the southern block (Figure 3) (all heights referenced to the WGS84 ellipsoid). As the aircraft approached terrain clearance limits of 200 m or 800 m above the ice surface, depending on whether a line was being flown north to south or south to north, the aircraft elevation was increased or decreased by 600 m to the elevation required for the next block. The gravity meter was clamped during each change in elevation. It took several minutes for the gravity meter to settle after this change, so there was a data gap of 10 to 15 km for each a step in elevation. The gaps in the gravity images are a reflection of these data gaps.

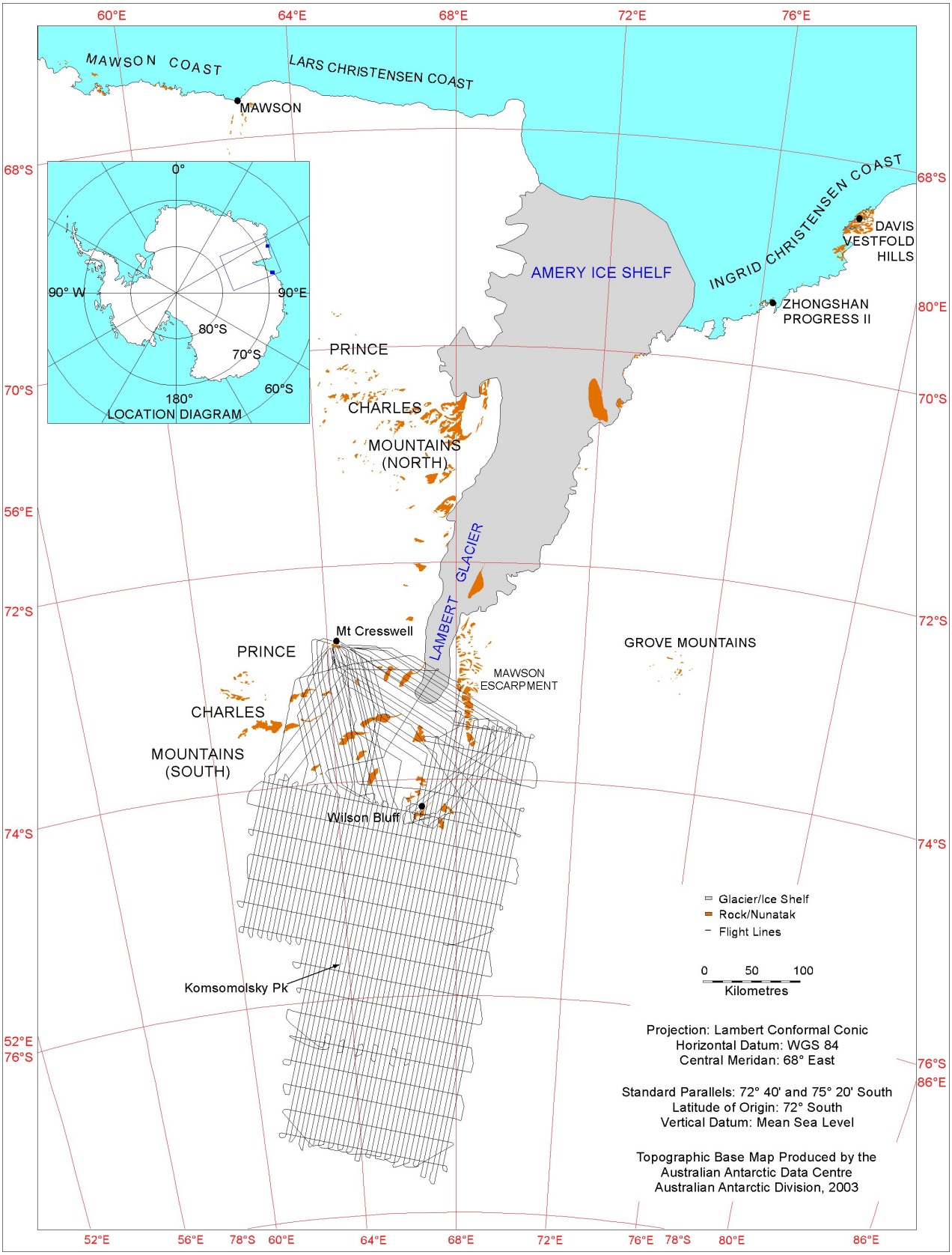

Figure 1. Location map for the PCMEGA survey in the Prince Charles Mountains. The locations of flight lines are shown as black lines.

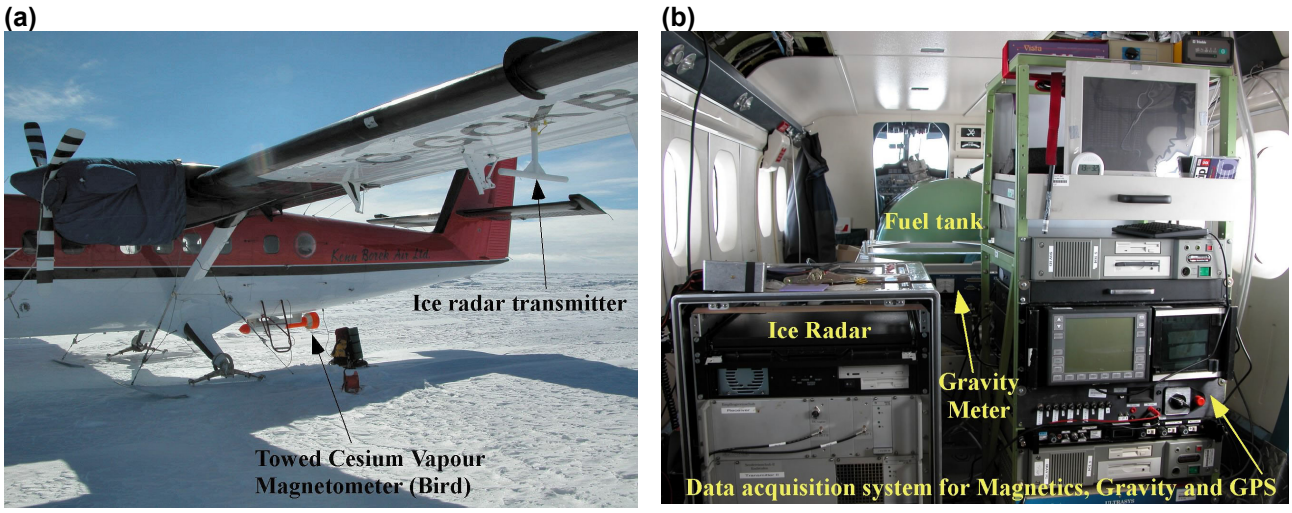

Figure 2. (a) External view of the De Havilland DHC-6-300 Twin Otter data acquisition aircraft at Mt Cresswell base. The bird is housed underneath the aircraft and the ice radar transmitter is fixed to the underside of the wing. (b) Arrangement of equipment inside the aircraft.

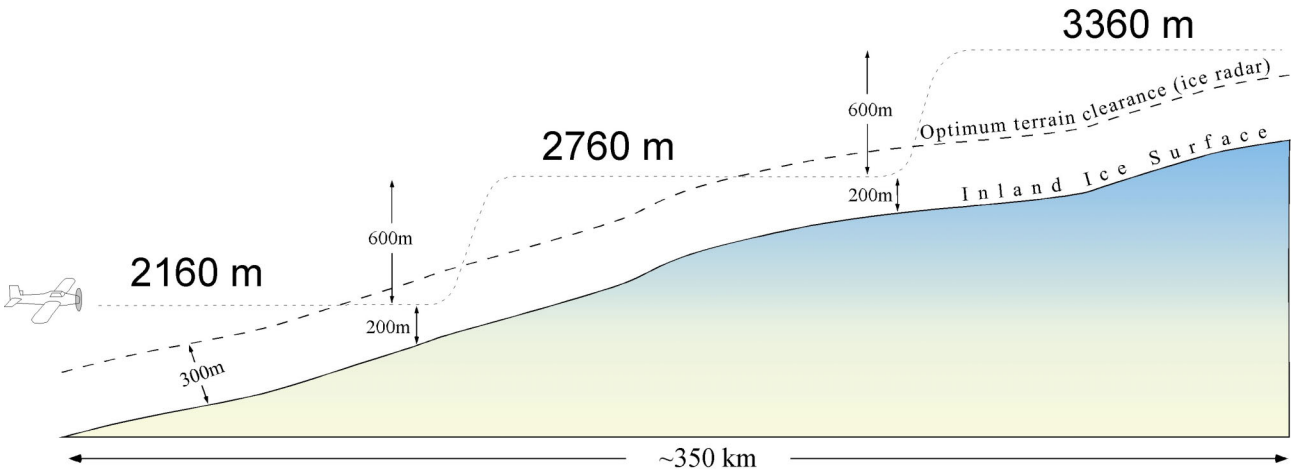

Figure 3. Schematic diagram of drape surface whereby data were collected at three elevation levels: 2160 m, 2760 m, and 3360 m above the WGS84 ellipsoid. The gravity system used for this survey required acquisition at constant elevation whilst the ice radar required a terrain clearance of 200 to 800 m.

A cesium vapour magnetometer in a towed bird (Figure 2a) was used to acquire magnetic data. These data were subject to de-spiking, followed by the application of diurnal, IGRF, levelling and micro-levelling corrections. A low-pass filter of length 50 s was then applied. An image of total magnetic intensity is shown in Figure 4. The filtering was far more severe than would normally be applied due to the elevated level of diurnal activity that occurs at high latitudes. The impact of the filtering was, however, diminished by the anticipated minimum depth to magnetic source (i.e., the minimum depth to bedrock) of at least 1000 m.

The airborne gravity system consisted of a ZLS Ultra-Sys Air/Marine upgrade LaCoste and Romberg 'S' Meter mounted on a vibration isolation platform (Williams and MacQueen, 2001). The gravity sensor was located on the aircraft centreline, just aft of the auxiliary fuel tank (Figure 2b). This position was chosen because it is close to the aircraft's centre of gravity. The gravity meter has a working range of 0 - 20,000 mGal, a sensitivity of 0.1 mGal and an operating temperature range of -20 to +45 ºC. Gravity measurements were made at a frequency of 1 Hz (approximately 70 m).

Two LaCoste and Romberg G-type meters were used to take base station and calibration readings prior to commencement and at the end of the survey at the Mt Cresswell base. These calibration procedures were used to determine the gravity meter drift over the survey time period and to ensure that the system was functioning properly.

Initial processing of the gravity data to the stage of free-air anomaly values was carried out by the equipment supplier (Baron-Hay et al., 2003). In calculating the free-air gravity anomaly values, a number of corrections were applied to the measured gravity values. These included a drift correction, the theoretical gravity correction based on the IGSN71 gravity datum and 1967 International Gravity Formula, the airborne Eötvös correction, and the free-air anomaly correction. A tidal correction was considered unnecessary since the survey area was so close to the pole. Several other corrections such as for vertical accelerations calculated from GPS measurements were applied, but the details of these corrections were considered proprietary by the contractor. Details of the low-pass filter applied to the data are yet to be received. After these processes were carried out, the data were levelled and gridded with a 1000 m cell size.

Bouguer corrections

Taking the contractor-supplied free-air anomaly values and deriving a meaningful Bouguer anomaly map in an ice covered terrain is complicated by the need to take the ice thickness and density into account as well as the surface topography and the density of the bedrock. The simple Bouguer correction needs to be calculated in two stages; first applying a standard Bouguer slab correction based on the surface elevation and a density value chosen for bedrock, then an adjustment to this correction to account for the thickness and density of the ice layer (Torge, 1989; Reitmayr, 2003).

Simple Bouguer anomaly values are derived by calculated the effect of an infinite horizontal slab extending between the elevation datum and the ground surface vertically below each measurement point:

$$g_{SBA} = 0.04192 \rho_b \cdot h \qquad \textit{(Equation 1)}$$

where g_{SBA} is the simple Bouguer correction (mGal), ρ_b is the mean density of the slab (in g/cm^3, with a value of 2.67 g/cm^3 typically used) and h is the surface elevation in metres above the geoid (Torge, 1989; Reitmayr, 2003). Once the simple Bouguer correction has been calculated for each geographic locality, it is subtracted from the free-air gravity value.

A correction can then be applied to account for the density of ice relative to the density assigned to the slab:

$$g_{ice} = -0.04192(\rho_b - \rho_{ice}) \cdot t_{ice} \qquad \textit{(Equation 2)}$$

where g_{ice} is the correction for the presence of ice (mGal), ρ_b is the density used in the simple Bouguer correction (2.67 g/cm^3 in this instance), ρ_{ice} is the density of ice (0.87 g/cm^3 was used in this case) and t_{ice} is the thickness of ice in metres. Subtracting this ice correction from the simple Bouguer anomaly yields simple Bouguer anomaly values corrected for the presence of ice.

As part of the next phase of this investigation, a 2D surface and sub-ice terrain correction will be calculated using Fourier domain terrain modelling techniques described by Parker (1973) and applied by Studinger et al. (2004).

Preliminary observations from the survey

As expected, there is a strong correlation between the free-air gravity (Figure 5) and the sub-ice elevation data derived from the ice radar (Figure 6). A north-east-trending sub-ice valley that enters from the south-west corner of the grid has been interpreted as the extension of the Lambert Rift. In the northern region of the grid, another sub-ice valley underlies the upper Lambert Glacier and extends towards the south-east. We suggest that this valley is the third arm of a triple point proposed by Stagg (1985).

Given the smoothness of the surface topography (Figure 7), it is not surprising that the simple Bouguer anomaly map without ice correction (Figure 8) is similar to the free-air anomaly map (Figure 5). The simple Bouguer anomaly image with ice correction (Figure 9) is quite different to either of these previous gravity images. There is a strong south to north gradient which is likely to reflect deep crust or mantle density variations. The high observed in the free-air gravity associated with the Gamburtsev Mountains is a low in the ice-corrected simple Bouguer anomaly map. Although less obvious, there is a positive Bouguer anomaly that coincides with the rift observed in the ice radar dataset. The appearance of relatively short wavelength features such as this is enhanced by removing a first order trend surface from the ice-corrected simple Bouguer data (Figure 10).

It should be noted that the Bouguer anomaly map is limited by the accuracy of the sub-ice and surface elevation data (Figures 6 and 7, respectively). Since there are discrepancies in both of these datasets, some caution should be exercised when interpreting the Bouguer anomaly data. In a similar airborne geophysical

survey, Studinger et al. (2004) estimated the standard deviation of the errors in the surface elevation values to be 2.7 m and the standard deviation of the errors in the sub-ice elevation values to be 81 m.

Acknowledgments

The PCMEGA project was jointly funded by the Australian Antarctic Division and the Bundesanstalt für Geowissenschaften und Rohstoffe (BGR). The gravity and magnetic equipment was supplied and operated by Fugro Airborne Surveys. Ice penetrating radar equipment was supplied and operated by Dr. Volkmar Damm from the BGR. The Twin Otter aircraft used for the geophysical surveys was owned and operated by Kenn Borek Air, on contract to the Australian Antarctic Division.

References

Baron-Hay, S., Parsons, M. and Stenning, L. 2003, Antarctic Magnetic and Gravity Geophysical Survey: Acquisition and Processing Report for PCMEGA, Prince Charles Mountains Expedition Germany and Australia: Fugro Airborne Surveys (Unpublished).

Boger, S.D. and Wilson, C.J.L., 2003, Brittle faulting in the Prince Charles Mountains, East Antarctica: Cretaceous transtensional tectonics related to the break-up of Gondwana: Tectonophysics, 367, 173-186.

Boger, S.D., Wilson, C.J.L. and Fanning, C.M., 2001, Early Paleozoic tectonism within the East Antarctic craton: The final suture between east and west Gondwana?: Geology, 29, 463-466.

Kurinin, R.G., and Grikurov, G.E., 1982, Crustal structure of part of East Antarctica from geophysical data: in Craddock, C. (Ed.), Antarctic Geoscience, University of Wisconsin Press, Dadison, 895-901.

Lisker, L., Brown, R. and Fabel, D., In Press, Denudational and thermal history along a transect across the Lambert Graben, Northern Prince Charles Mountains, Antarctica: Tectonics.

Parker, R.L., 1973, Rapid calculation of potential anomalies: Geophysics J. R. Astron. Soc., 31 447-455.

Reitmayr, G. 2003, Continuation of Gravity Measurements in Victoria Land and at the Oates Coast, Antarctica, during GANOVEX VII: Ber. Arch. BGR – Hannover.

Stagg, H. M. J., 1985, The structure and origin of Prydz Bay and MacRobertson Shelf, East Antarctica: Tectonophysics, 114, 315-340.

Studinger, M., Bell, B.E., Buck, R.W., Karner, G.D. and Blankenship, D.D., 2004, Sub-ice geology inland of the Transantarctic Mountains in light of new aerogeophysical data: Earth and Planetary Science Letters, 220, 391-408.

Torge, W., 1989, Gravity: Berlin, New York (W. de Gruyter).

Wellman, P. and Tingey, R.J., 1976, Gravity evidence for a major crustal fracture in east Antarctica: BMR Journal of Australian Geology and Geophysics, 1, 105-108.

Williams, S., and MacQueen, J.D., 2001, Development of a versatile, commercially proven, and cost-effective airborne gravity system: The Leading Edge, 20, 651-654.

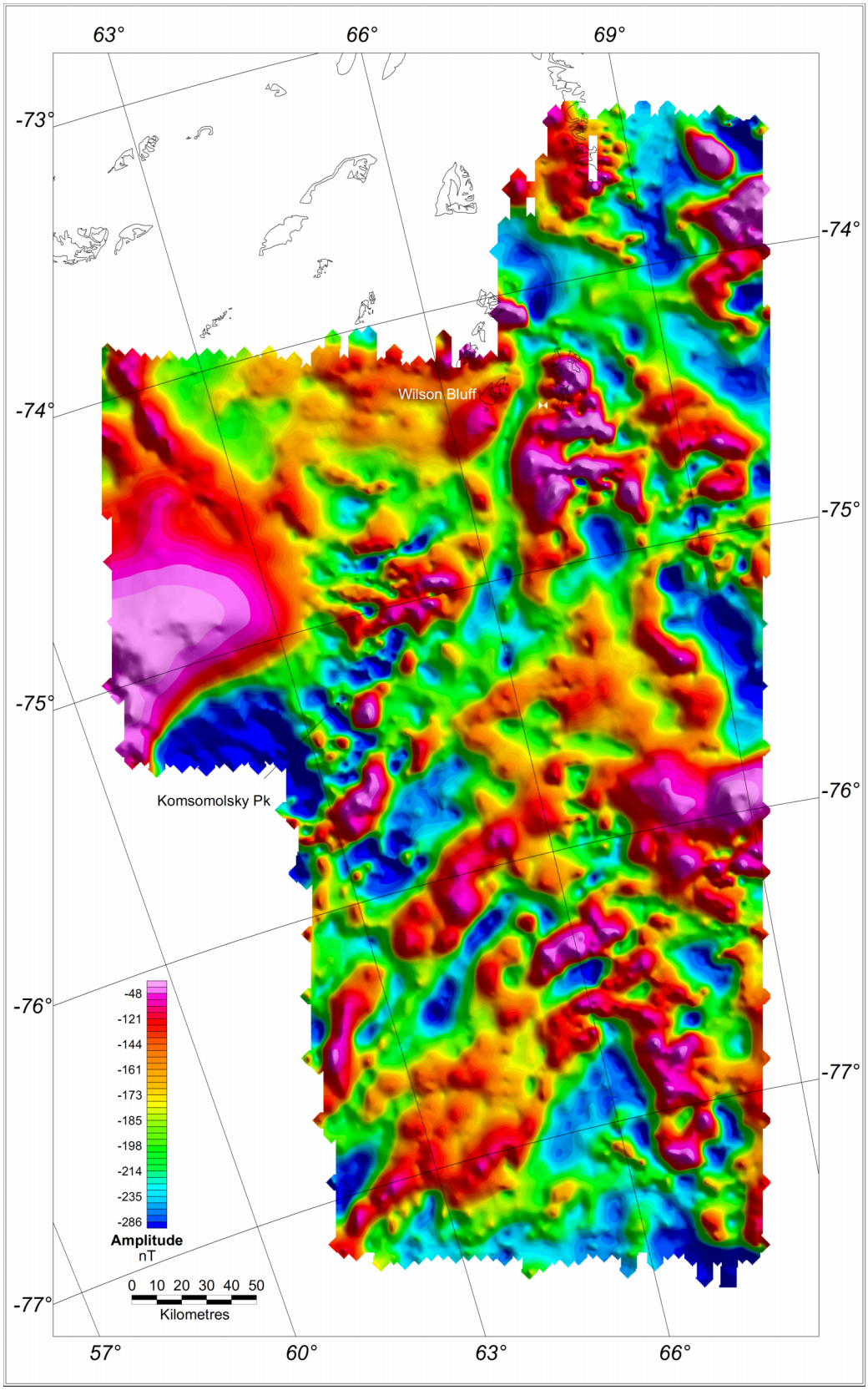

Figure 4. Total magnetic intensity image for the Southern Prince Charles Mountains.

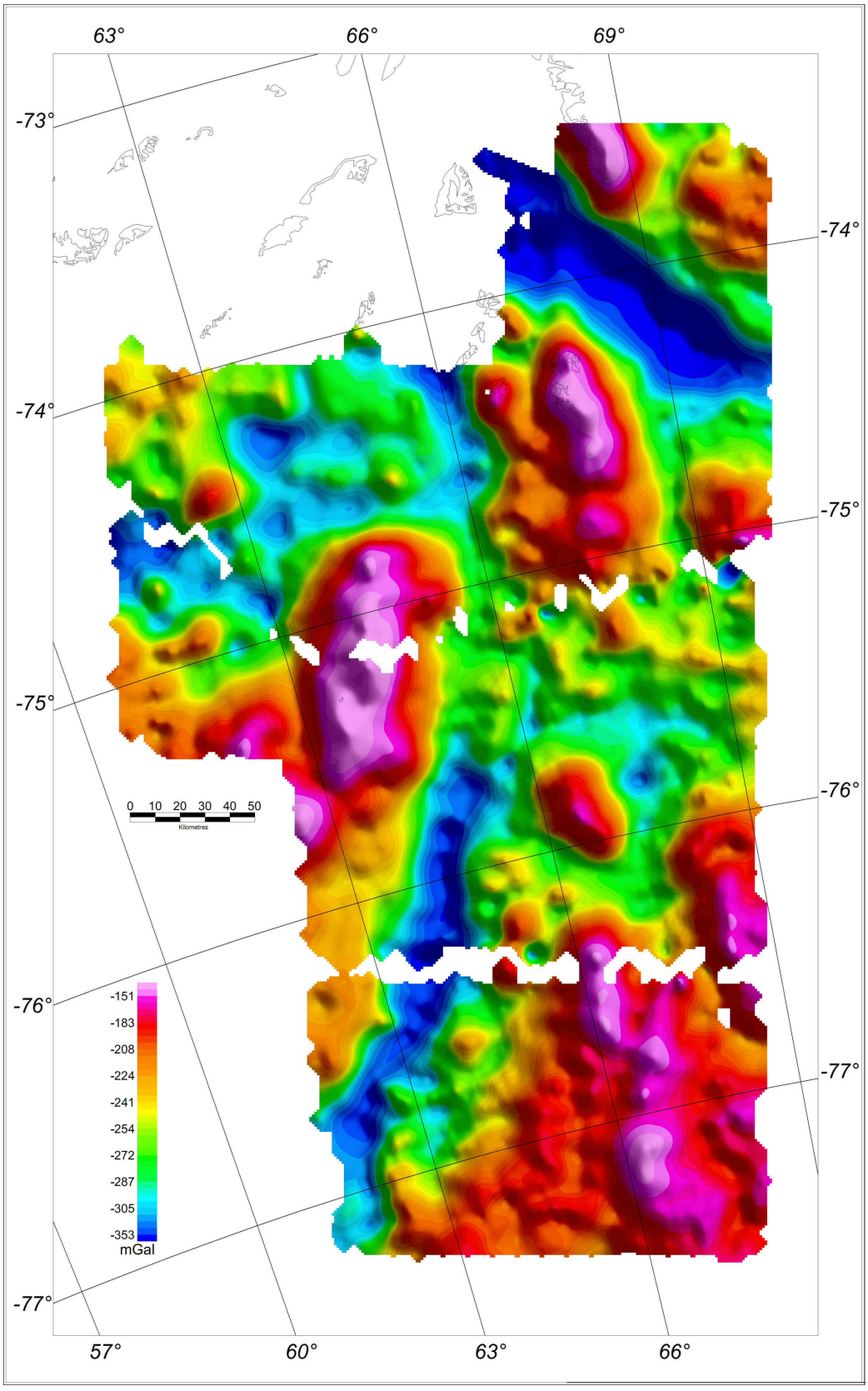

Figure 5. Free-air gravity map for the Southern Prince Charles Mountains.

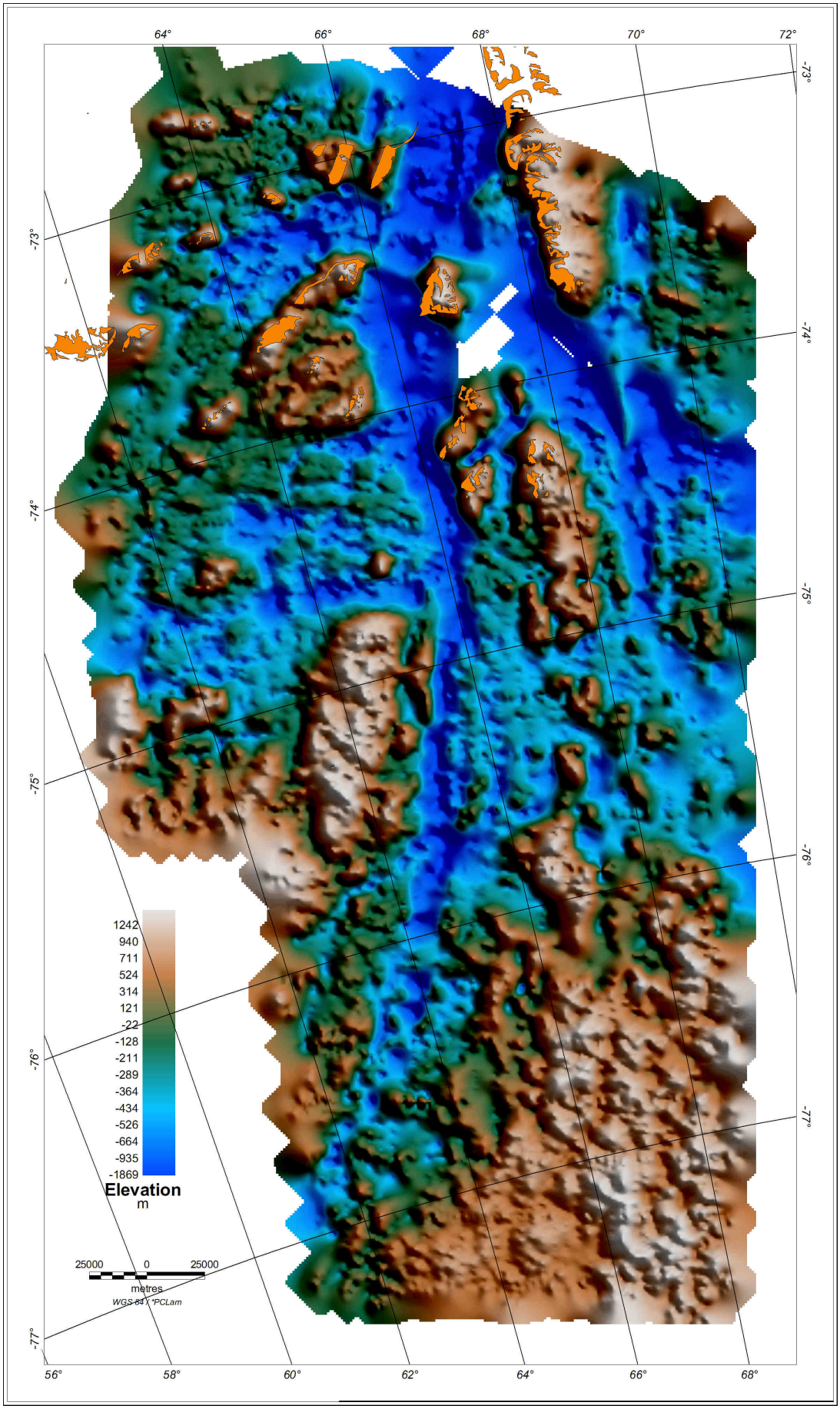

Figure 6. Sub-ice elevation map for the Southern Prince Charles Mountains. Maximum ice thickness is approximately 3776 m and mean ice thickness is approximately 1720 m.

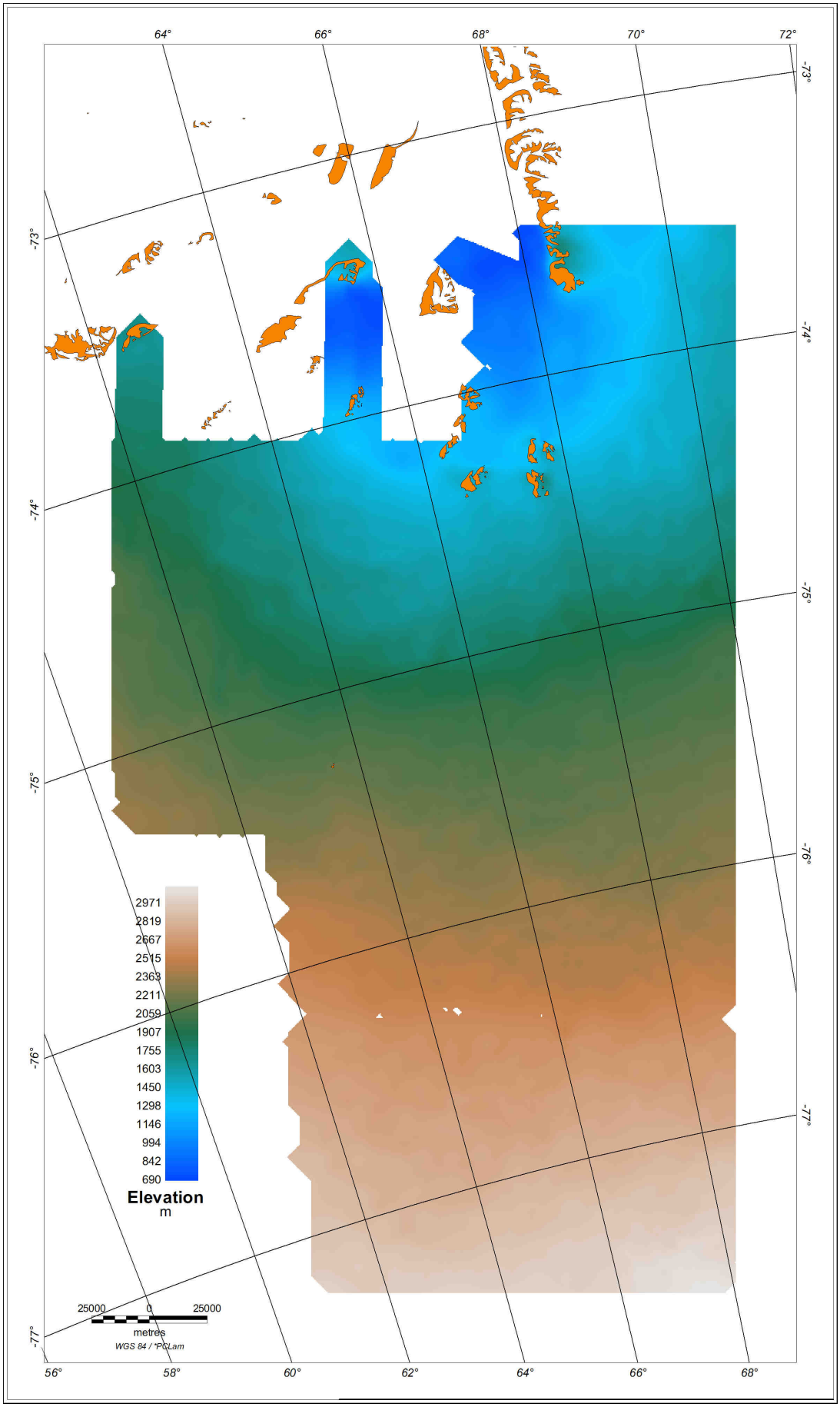

Figure 7. Surface elevation map for the Southern Prince Charles Mountains.

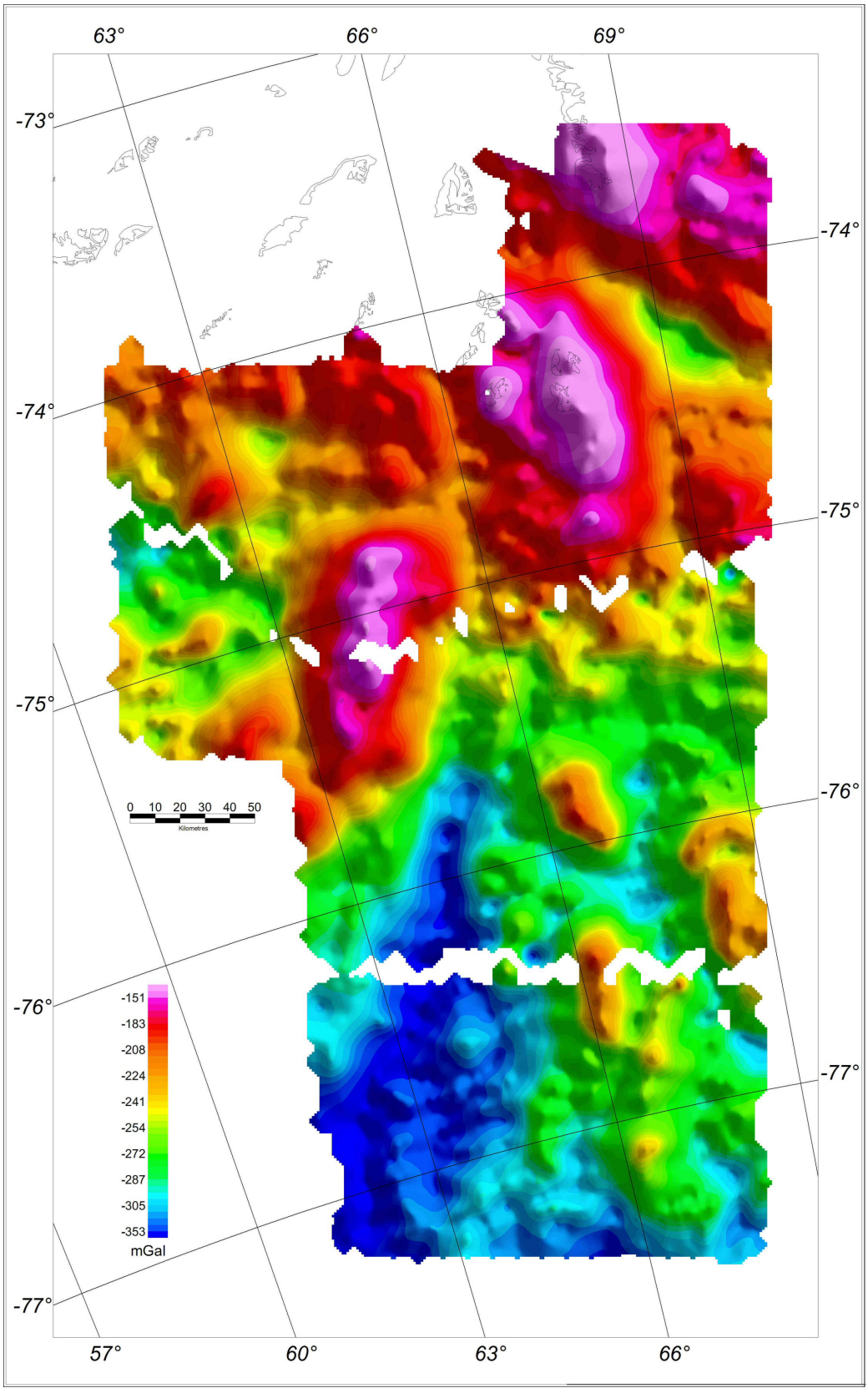

Figure 8. Simple Bouguer anomaly map (without ice correction) for the Southern Prince Charles Mountains

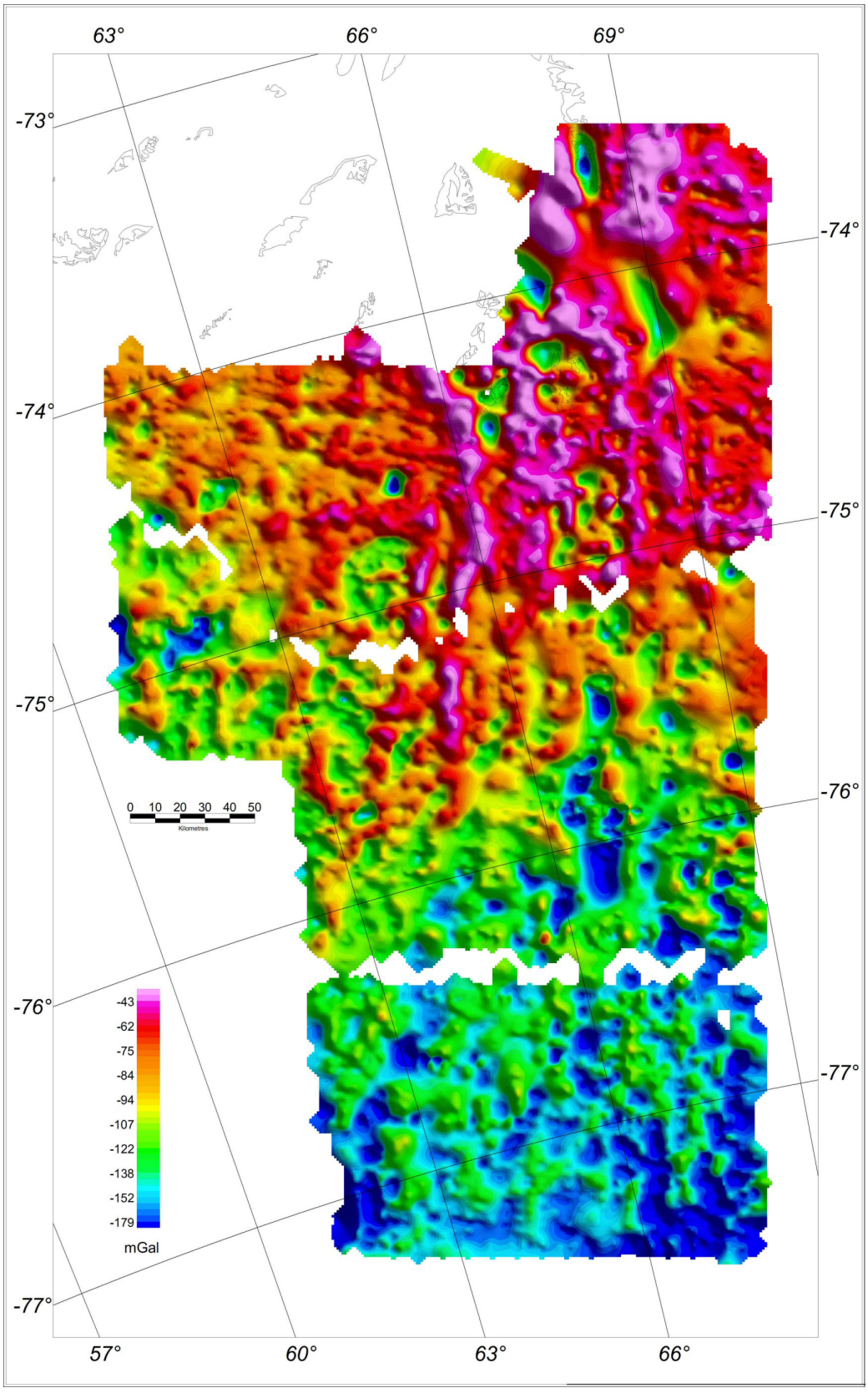

Figure 9. Simple Bouguer anomaly map (with ice correction) for the Southern Prince Charles Mountains.

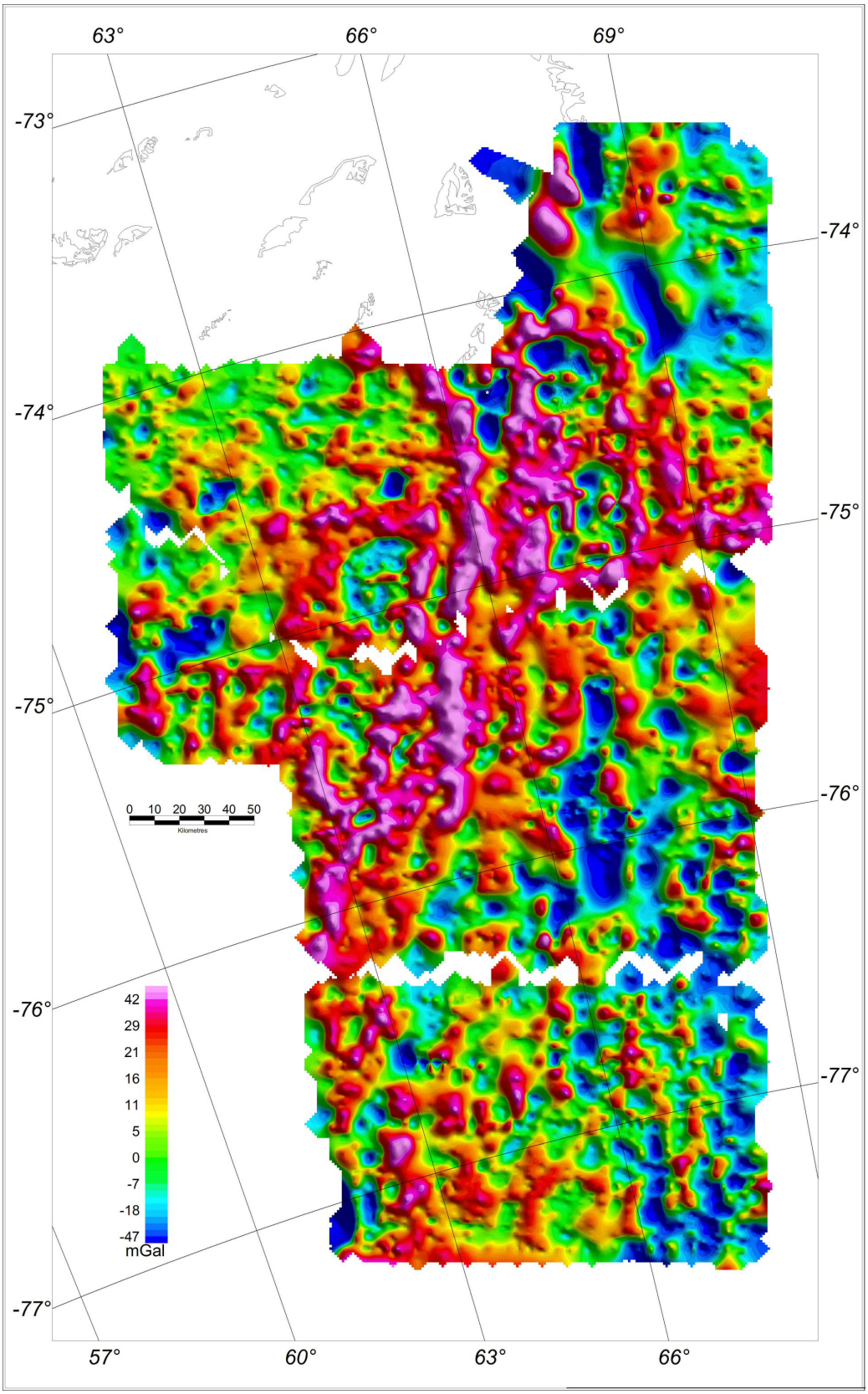

Figure 10. Residual simple Bouguer anomaly map (with ice correction) for the Southern Prince Charles Mountains after removing a first order trend surface.

AIRGrav airborne gravity survey in Timmins, Ontario

Stefan Elieff
Sander Geophysics Ltd.
s_elieff@sgl.com

Stephan Sander
Sander Geophysics Ltd.
stephans@sgl.com

Abstract

Results are presented from an AIRGrav airborne gravity survey flown near Timmins, Ontario, Canada. The survey demonstrates the application of airborne gravity to mineral exploration; the system was able to accurately reproduce existing ground data, with the advantages of rapid data acquisition and uniform sampling of an area that was difficult or impossible to access on the ground.

Introduction

An airborne gravity evaluation survey was flown immediately north of Timmins, Ontario, using the AIRGrav (Airborne Inertially Referenced Gravimeter) system (Elieff, 2003). Four production flights totalling 1836 line kilometres were performed in a four day period to complete the survey.

The survey block comprises an area of 810 km^2 just north of Timmins, Ontario. Survey operations were based out of Timmins Airport, which lies within the survey area. A Cessna Grand Caravan 208B aircraft was used to fly the survey. The coordinates for the survey boundary are given in Table 1. Terrain elevations within the survey block vary between approximately 250 m and 400 m above mean sea level, with the largest relief in the south west portion of the area. The Mattagami River crosses the survey block from south to north, west of the block centre.

Table 1. Coordinates for the boundary of the Timmins Survey (WGS84 datum, UTM zone 17 N projection).

Corner	UTM east (m)	UTM north (m)
1	452000	5373000
2	452000	5395500
3	488000	5395500
4	488000	5373000

Flight specifications

Primary flight lines were flown north-south and spaced 500 m. East-west tie lines were spaced 5000 m apart. All flight lines were extended beyond the survey boundary to ensure that the gravimetric system had time to settle following turns and was on-line before entering the survey area. The survey was flown at a constant ellipsoid height of 468 m, which is approximately 500 m above mean sea level. This height was chosen to provide safe clearance of the highest terrain features in the survey area. The average terrain clearance was approximately 200 m.

The AIRGrav system

The AIRGrav system is described in detail in Sander et al. (2004) and will be only briefly summarised here. An inertial platform supports three orthogonal accelerometers, which remain fixed in inertial space, independent of the manoeuvres of the aircraft. The acceleration due to the motion of the aircraft is modelled using GPS measurements and subtracted from the measured acceleration values to leave the acceleration due to gravity.

System tests

Gravimeter calibration

The accelerometers within the gravimeter were calibrated before the beginning of the survey. Prior to each flight, the AIRGrav system automatically aligns and calibrates its gyros. Before and after each flight, the consistency of the measured gravity was confirmed by recording data at a fixed location on the ground. The results, presented in Table 2, are given as deviations in these reference measurements from a local gravity value of 9.8082771 m/s^2 (Canadian Gravity Standardization Network station 9201-1975 – Timmins Airport

Terminal). The values in Table 2 are all within 1 mGal of the local gravity reading, demonstrating the stability and low drift rate of the AIRGrav system.

Table 2. Pre- and Post-flight AIRGrav static readings in mGal relative to a local gravity value of 9.8082771 m/s^2 (Canadian Gravity Standardization Network station 9201-1975 – Timmins Airport Terminal).

Flight number	Pre-Flight	Post-Flight
1	0.58	0.43
2	0.75	0.13
3	-0.96	0.63
4	-0.02	0.46

Radar and laser altimeter calibration

A test flight to calibrate the radar and laser altimeters was flown. Five passes were flown over a runway at heights from 80 m to 350 m above ground. A ground pass taxiing along the runway was carried out to establish the runway height. The radar and laser altimeter values were compared to the post-flight differentially corrected GPS altitude information to calibrate the altimeters (Figure 1). Ideal altimeters would yield a slope of 1, and an intercept of 0. For the laser altimeter test, the calculated slope was 1.007, and the intercept 0.37 m, while for the radar altimeter the slope was 1.01 and the intercept 1.49 m. These results are well within the expected accuracy of the altimeters.

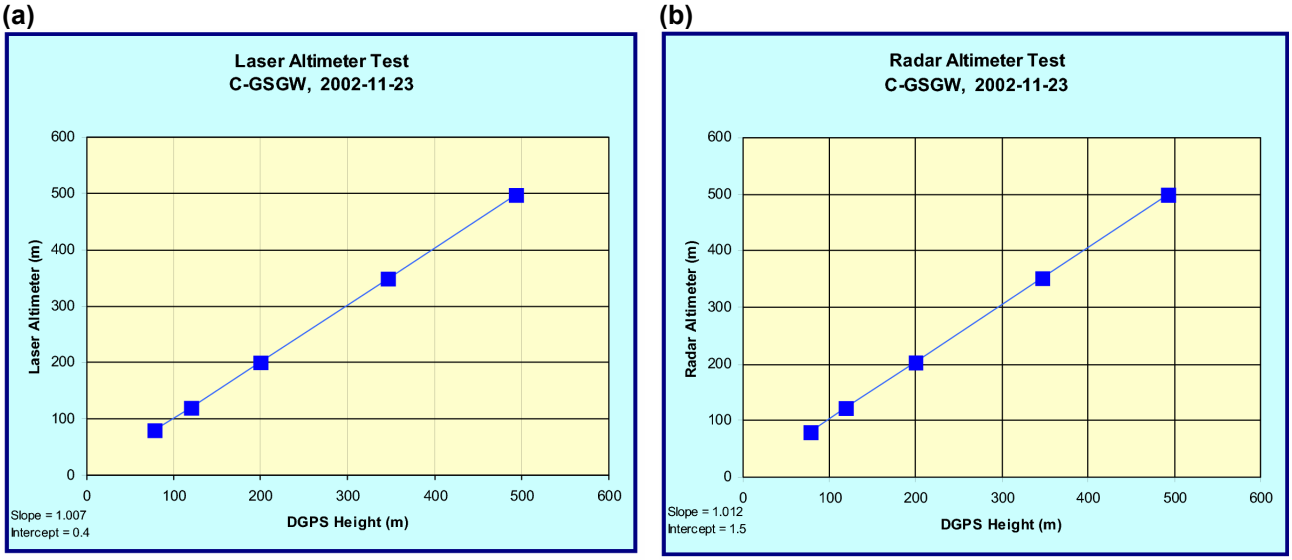

Figure 1. (a) Laser altimeter calibration results. (b) Radar altimeter calibration results.

Digital data compilation

Preliminary processing for on-site quality control was performed in the field as each flight was completed. This included routine printing of data profiles as a hard copy reference, verification of data on the computer screen, and plotting of the DGPS flight path data. Final data processing and map production were performed at Sander Geophysics' head office in Ottawa.

Gravity data

The gravity data processing sequence is described in Sander et al. (2004). Once isolated from the acceleration measurements, the gravity data are corrected for the Eötvös effect and normal gravity. Bouguer anomaly data are derived by applying free-air, Bouguer slab, Earth curvature, terrain and levelling corrections.

Grids of the free air and Bouguer anomaly were generated by filtering the line data to remove high frequency noise and then averaging the filtered line data within the grid using a Fourier domain filter with a

wavenumber mid point equivalent to 2.85 km (0% pass at 2.1 km, 100% pass at 4.3 km), full sine wave, or 1.42 km half sine wave. Note that the filter midpoint is not (2.1 km + 4.3 km)/2 because these are wavenumber domain filters. The midpoint is instead (1/2.1km + 1/4.3 km)/2, or about 1/2.85 km.

Positional data

A GPS data processing package, GPSoft, was used to calculate DGPS positions from raw 10 z range data obtained from the moving (airborne) and stationary (ground) receivers. Accurate locations of the GPS antennae were determined by differentially correcting the ground station position data using a permanent GPS reference station. This technique provides a final receiver location with an accuracy of better than 5 cm. The entire airborne data set was processed differentially using the calculated ground station location.

System resolution and accuracy

After the standard processing was completed, the results were evaluated using tests of internal consistency and a comparison with existing ground gravity measurements.

Internal consistency – crossover errors

Internal consistency was measured first by determining crossover errors. The crossover error is the difference between control and traverse line data at each intersection. An 85 s filter (approximately 4 km full sine wave at 50 m/s aircraft speed) was applied to all survey lines for this test. Figure 2 shows a histogram of the errors. The standard deviation of the crossover errors was 0.64 mGal, which indicates an accuracy of $1/(\sqrt{2})$ * 0.64 mGal or 0.45 mGal for the line data.

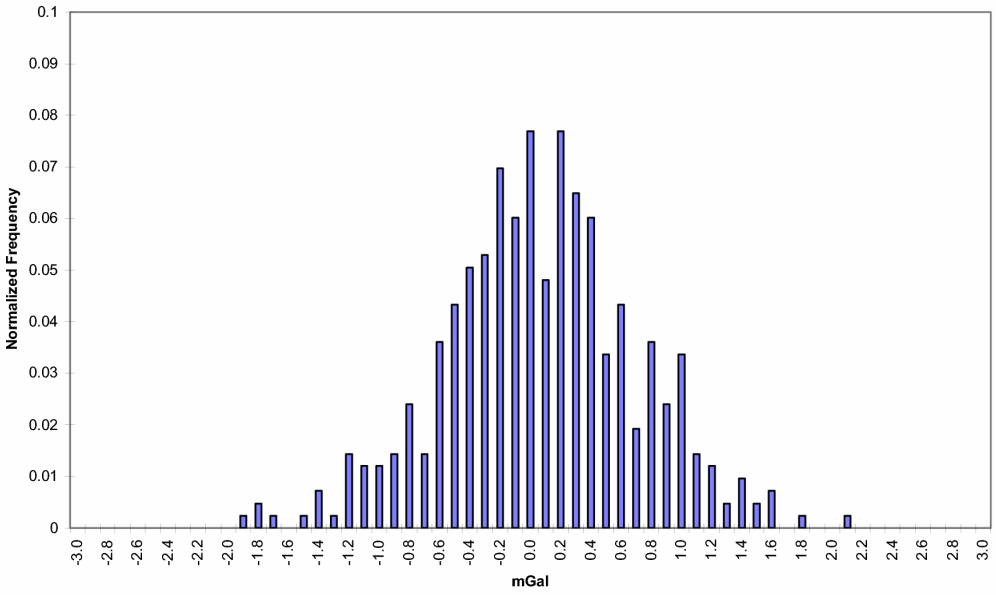

Figure 2. Histogram of flight line and tie line crossover errors. The standard deviation of the errors was 0.64 mGal.

A second test of internal consistency was provided by measuring the difference between two grids, one made from the odd and the second from the even numbered lines (Sander et al., 2002). These grids are two independent data sets of 1 km spaced lines. The 2.85 km spatial filter described earlier was applied to each grid. The standard deviation of the differences between these two grids was 0.29 mGal. This represents a noise level of 0.5 * 0.29 mGal or 0.15 mGal on the full data set of 500 m spaced lines.

External consistency – ground data comparison

Further evaluation of the data was made through comparisons of the airborne data to ground Bouguer gravity data acquired in previous years. The ground data consists of several distinct sets of data points. The largest and most recent survey was performed in 2001 and has 573 stations within the AIRGrav survey area. A further 213 ground readings taken between 1949 and 1970 supplement the 2001 survey, for a total of 780 ground readings. A map showing the relative location of the airborne survey flight lines and all ground data points is given in Figure 3.

A grid was created from the ground data points using a minimum curvature gridding algorithm and 250 m grid cell size, matching the AIRGrav data grid. This may appear to be a relatively coarse grid cell size given 500 m line spacing, but this spacing was considered adequate given the filters used on the airborne data and the spacing of ground points. Areas that were more than three grid cells away (750 m) from a ground data point were left as nulls in the grid, indicating places where ground coverage is incomplete. The AIRGrav grid and the ground grid are given as Figures 4 and 5, respectively.

As these figures show, the AIRGrav and ground data match very well. They are displayed in Figures 4 and 5 with identical contours, colour levels, and grid cell sizes. After tying AIRGrav ground readings at the airport to the known gravity value at the airport (see Table 2), a small constant offset was found to be present between the airborne and ground data in the survey block. This offset results from a combination of errors in the ground data set, errors and noise in the airborne data, differences in terrain heights used for Bouguer corrections in each data set, and other systematic data reduction differences. The offset was easily removed by applying a single shift to the entire airborne data set. The average difference between the airborne and ground data points, 1.4 mGal, was added to the AIRGrav grid. This is the simplest and most reliable way of tying the airborne data to existing ground surveys. No other adjustments, such as stretching or tilting, are necessary.

A more direct comparison of the ground and airborne data is provided in Figure 6. The ground data were first upward continued by 200 m, the average aircraft height above the ground. These data were then subtracted from the AIRGrav data to produce the difference grid shown in this figure.

The best way to quantitatively compare the ground data set with the AIRGrav data is on a point-by-point basis. A simple grid comparison is less valid because there are many cells within the grid that do not contain an observation. The values in these cells are entirely dependent on the grid interpolation method. For each ground reading, the east and north UTM coordinates were used to select a value from the AIRGrav grid. The ground readings were upward continued by 200 m, the average aircraft height above the ground. For the 780 ground readings that fall within the AIRGrav survey boundary, the standard deviation of the differences between the air and ground readings was 0.62 mGal. It should be noted that this statistic of the differences between ground and airborne data includes the errors present in the ground data, and hence represents an upper limit on the noise in the airborne data.

Another AIRGrav survey with very similar specifications was recently flown over a petroleum basin. The internal consistency as measured by crossover errors was the same as that obtained for the Timmins survey, but the agreement with ground gravity data was better than that obtained for the Timmins Surveys (0.35 mGal in the petroleum basin compared with 0.62 mGal in Timmins). There are a number of potential reasons for the difference. We believe two factors are the most significant in this instance. First, the geological signal in the Timmins area has shorter wavelengths and larger amplitudes. The attenuation of these geological signals with flying height would be greater than over a petroleum basin where sources may be several kilometres deep, and consequently have long wavelengths and small amplitudes. A low-pass filter applied to the airborne data is also more likely to alter the geological signal in Timmins than in a petroleum basin where longer frequencies are dominant. Second, the quality and sampling of ground data points is variable in ground surveys. The standard deviation of differences includes any errors in the ground data. Where ground data are higher quality, the standard deviation of the differences between airborne and ground data sets will be smaller since errors in each data set should not be correlated.

Details in the Bouguer gravity grids can be enhanced by calculating the first vertical derivative (FVD). Figures 7 and 8 show the FVD of the AIRGrav Bouguer gravity and the upward continued ground gravity data grids, respectively. Again, all the significant features in the ground data are clearly captured by the AIRGrav system.

There is good correspondence between the AIRGrav gravity data and features shown on geological maps of the area. Figure 9 shows the first vertical derivative of the AIRGrav grid with a geological overlay. As expected, gravity highs tend to be associated with higher density rock types.

Discussion

The survey results show that the AIRGrav system can be used to quickly acquire gravity data. Only four flights over four days were needed to complete the survey covering 810 km^2. The data were evenly sampled and hence the final data represent a consistent grid dataset. The survey was flown at a relatively low altitude (200 m average terrain clearance) and in normal daytime conditions.

Laser altimeter data were combined with the post-flight differentially corrected GPS data to create a digital terrain model. High resolution magnetic data can be acquired concurrently with gravity data during a survey, although they were not required in this instance because of existing coverage in the area.

The accuracy and resolution of airborne gravity data depend in part on aircraft speed and survey line spacing. The results obtained on this survey could be enhanced by flying closer line spacing or by flying the survey at a slower ground speed using a helicopter. Doubling the line spacing to 250 m or using a helicopter to fly at approximately 50 knots (25 m/s) would have the effect of reducing errors (if the filter length is unchanged) or increasing resolution (by producing the same error level with a shorter filter).

In this example, the survey was flown with 500 m line spacing. The data were low-pass filtered to a wavelength of 2.85 km. An analysis of flight line and tie line crossover errors indicated a standard deviation of 0.64 mGal, suggesting a noise level of 0.45 mGal for the data. The method of odd and even line number grids revealed differences with a standard deviation of 0.29 mGal, suggesting a noise level of 0.15 mGal for the data. A comparison with upward continued ground gravity data produced a standard deviation of 0.62 mGal, which represents an upper limit on the accuracy of the airborne data.

Following on from this evaluation survey, three larger survey areas in the Timmins region were flown at 500 m and 1 km line spacing with the AIRGrav system to upgrade the present ground gravity coverage (see announcements on the Discover Abitibi website; www.discoverabitibi.com). These data are expected to assist regional mapping for mineral exploration purposes.

Acknowledgements

The Timmins Survey was carried out by Sander Geophysics Ltd. for the Timmins Economic Development Corporation's "Discover Abitibi Project". We wish to acknowledge the efforts of the Timmins field crew in acquiring the data used for this paper.

References

Elieff, S., 2003, Project report for an airborne gravity evaluation survey, Timmins, Ontario: Report produced for the Timmins Economic Development Corporation on behalf of the Discover Abitibi Initiative. (http://www.discoverabitibi.com/technical-projects.htm)

Sander, S., Argyle, M., Elieff, S., Ferguson, S., Lavoie, V., and Sander, L., 2004, The AIRGrav airborne gravity system: This volume.

Sander, S., Ferguson, S., Sander, L., Lavoie, V., and Charters, R.A., 2002, Measurement of noise on airborne gravity data using even and odd grids: First Break, 20.8, 524-527.

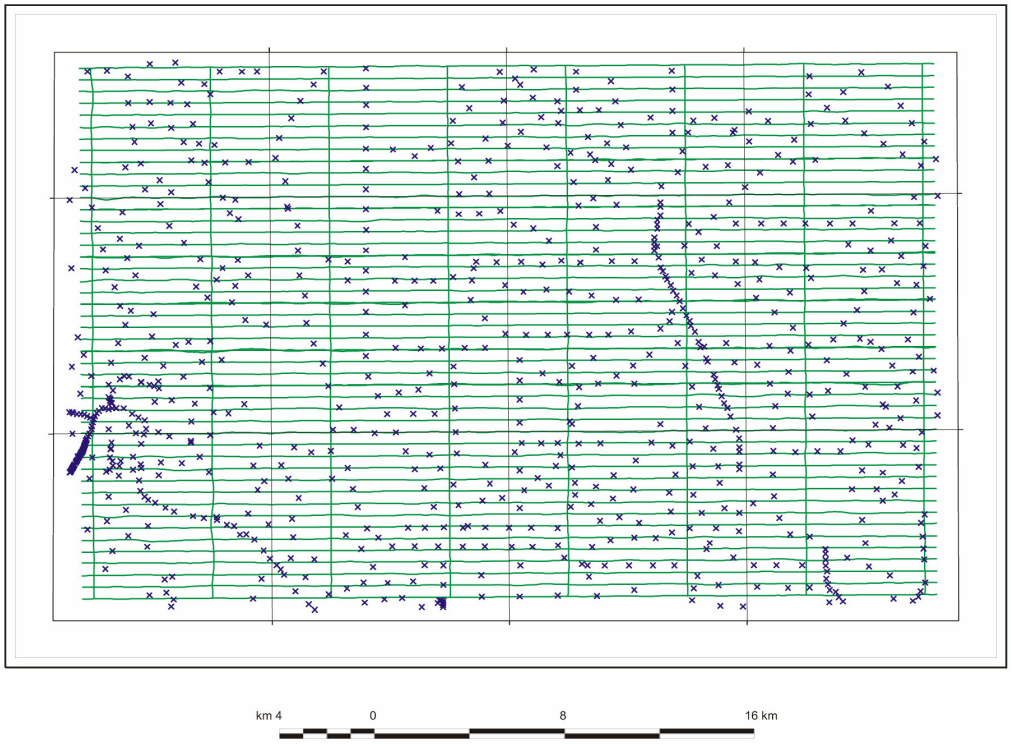

Figure 3. Map of gravity data coverage. AIRGrav flight lines are shown as green lines, and ground data points as blue crosses.

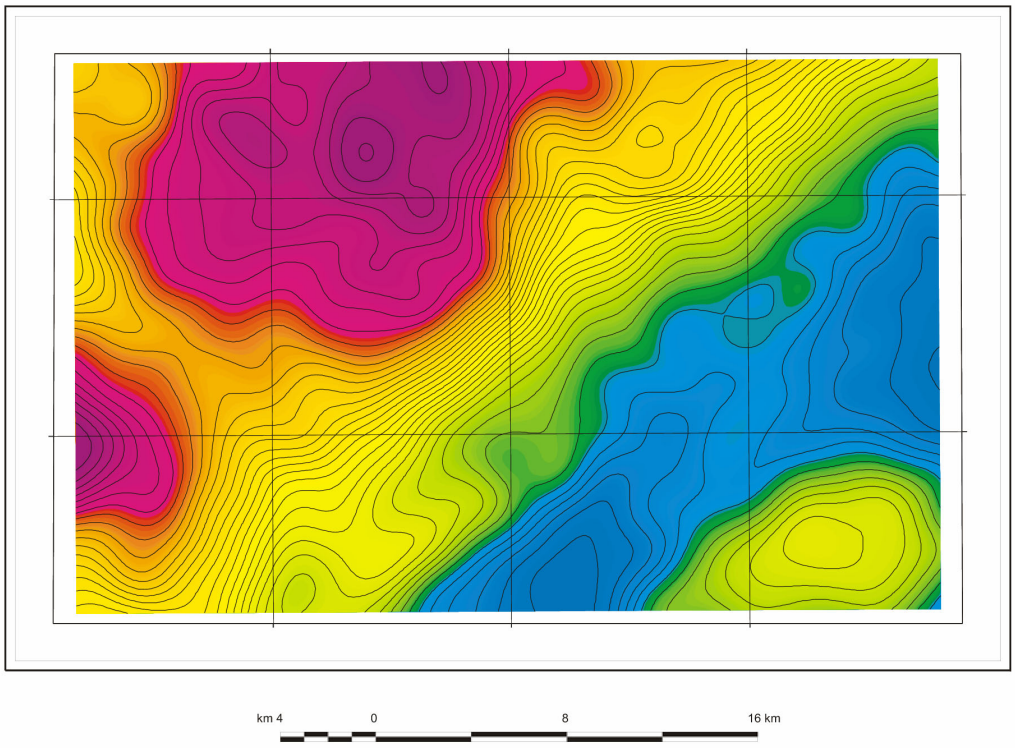

Figure 4. AIRGrav Bouguer data grid with 1 mGal contour levels and 10 km UTM graticule. Note that all subsequent figures are shown with the same 10 km UTM graticule.

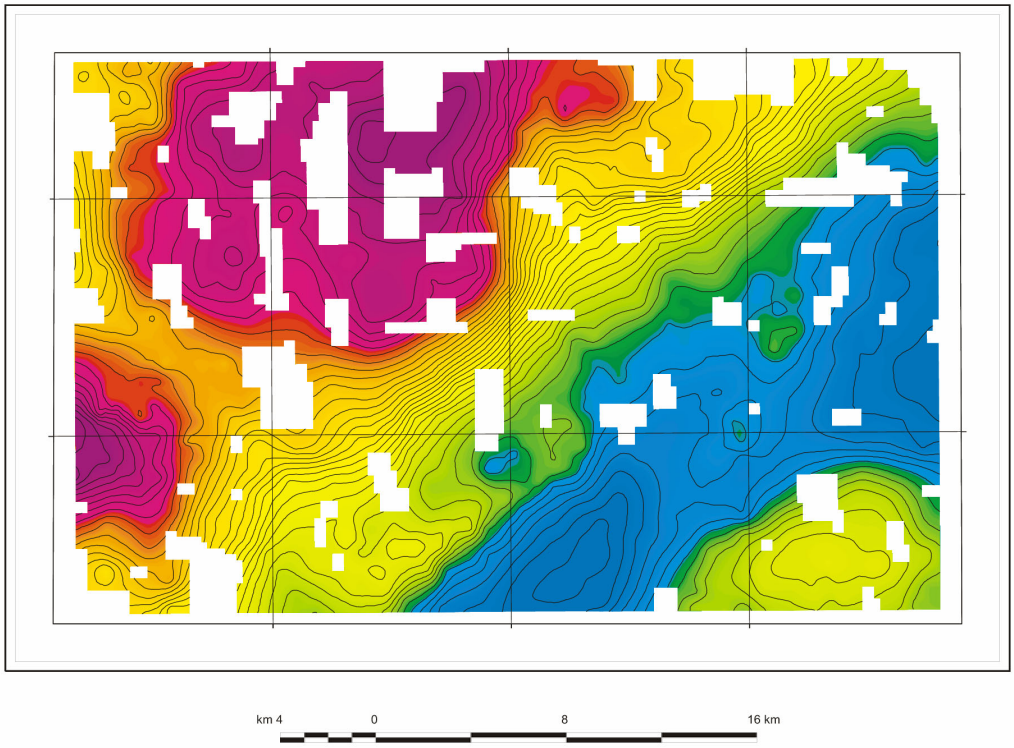

Figure 5. Ground Bouguer data grid with 1 mGal contour levels.

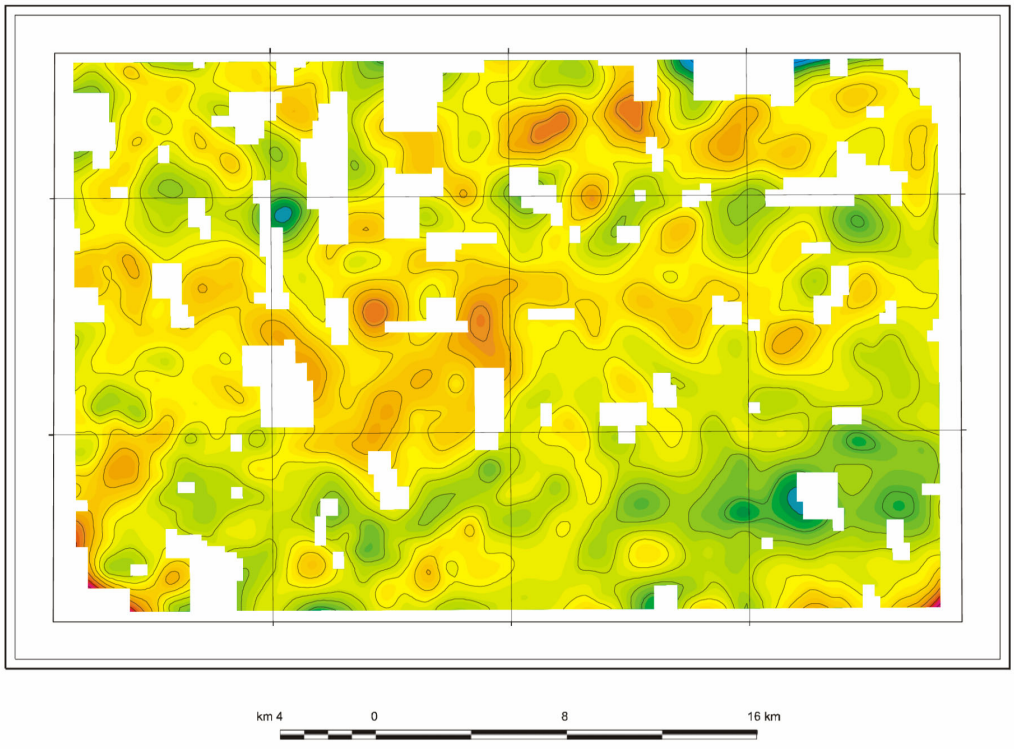

Figure 6. Image of the difference between Bouguer gravity values from AIRGrav and upward continued ground data. The contour interval is 0.5 mGal.

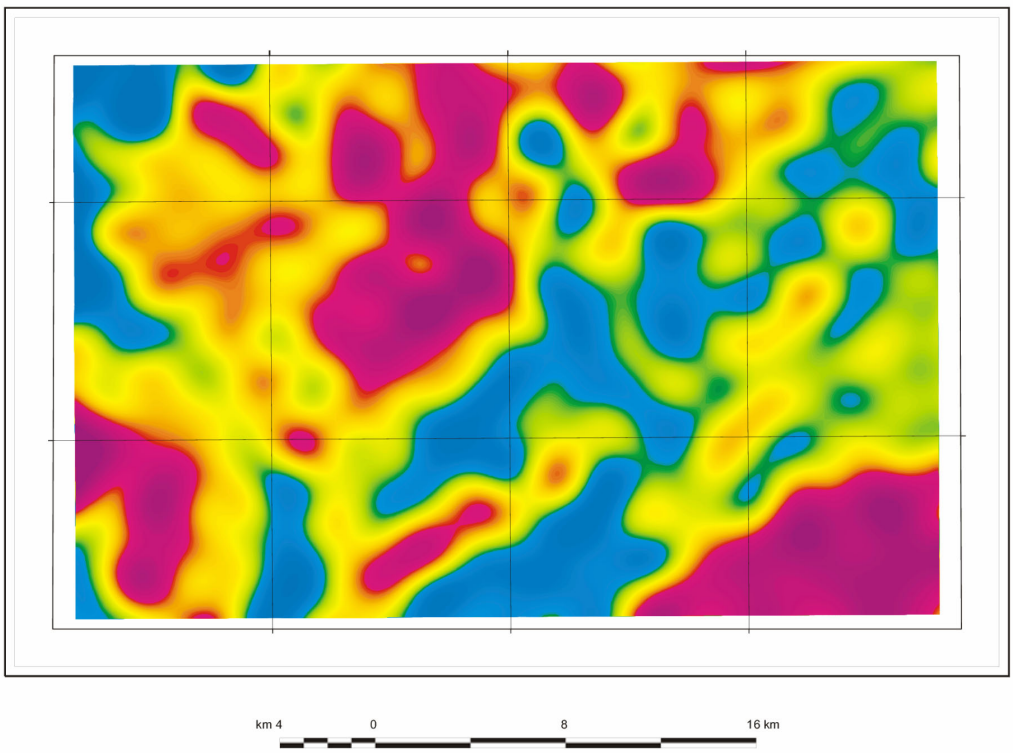

Figure 7. First vertical derivative of the AIRGrav Bouguer gravity grid.

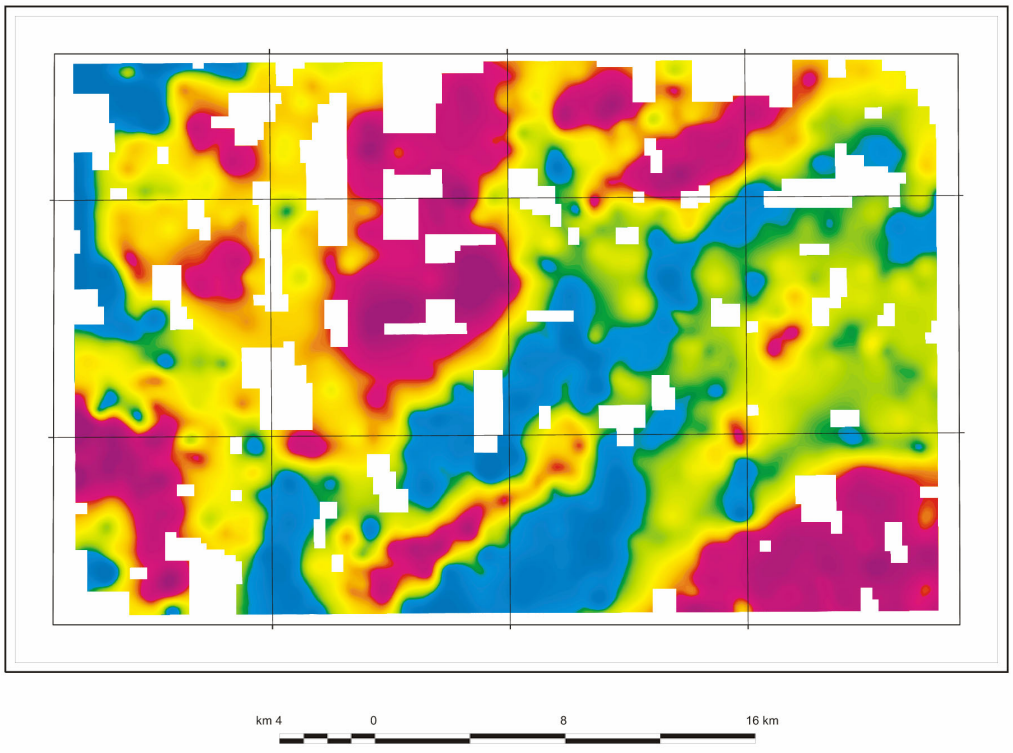

Figure 8. First vertical derivative of the ground Bouguer gravity grid after upward continuation by 200 m.

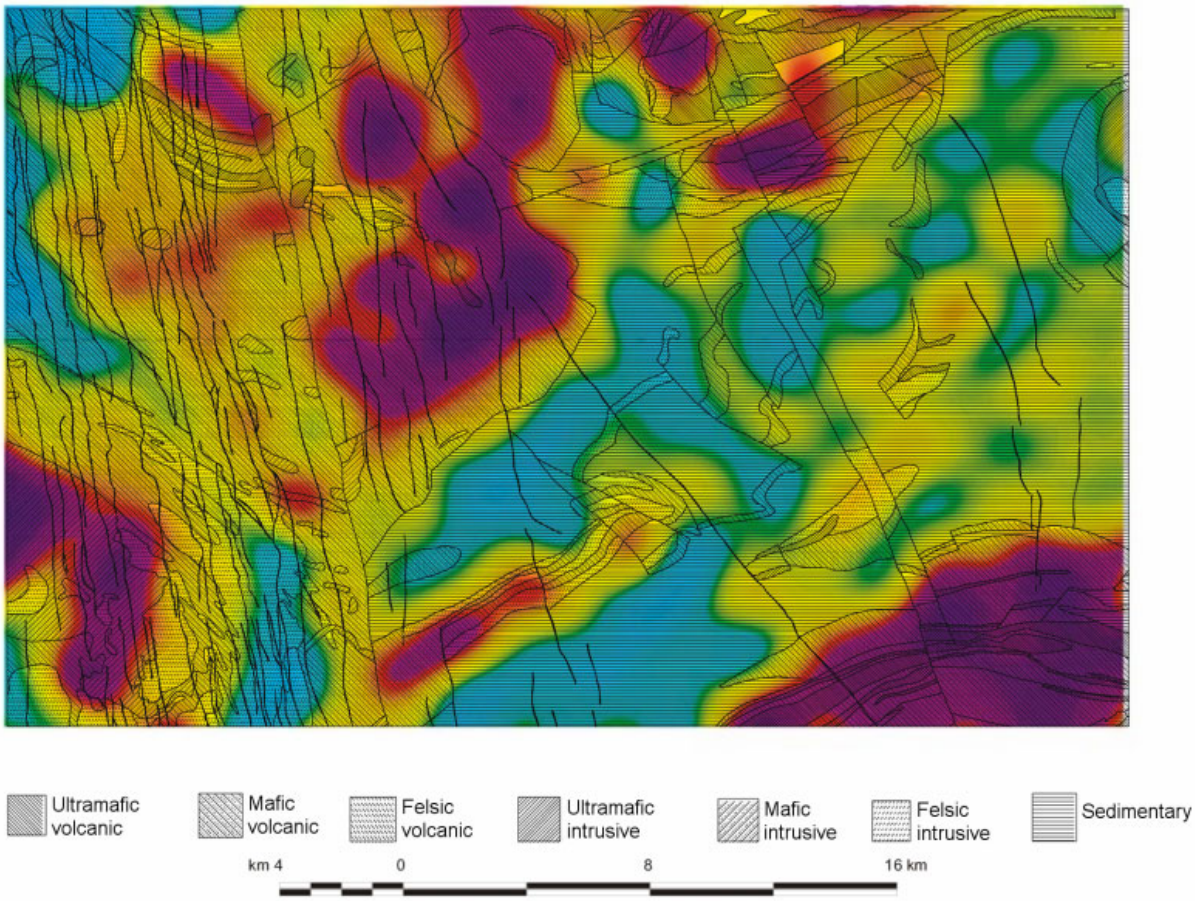

Figure 9. First vertical derivative of the AIRGrav Bouguer gravity grid with geology overlay.

Examples of Falcon™ data from diamond exploration projects in Northern Australia

David Isles
Gravity Capital Limited
david.isles@gcap.com.au

Ian Moody
Gravity Capital Limited
ian.moody@gcap.com.au

Introduction

Detailed Falcon™ airborne gravity gradiometer (AGG) data have been acquired as the essential element of Gravity Capital's diamond exploration programs in Northern Australia. Surveys are located in the Ellendale, King George North and Phillips Range districts within the Kimberley Region of WA, and in the Victoria River Basin, the Hodgson Basin, the McArthur Basin and in Arnhem Land in the Northern Australian Craton, NT (Figures 1 and 2). All surveys were flown in 'mature' project areas where prior exploration had returned significant encouragement, particularly in the form of kimberlitic indicator minerals.

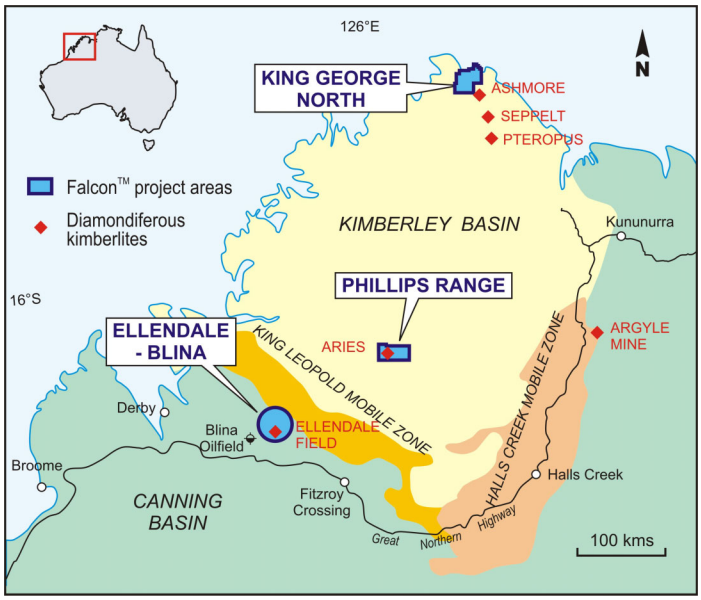

Figure 1. Locations for surveys in the Kimberley Region, Western Australia

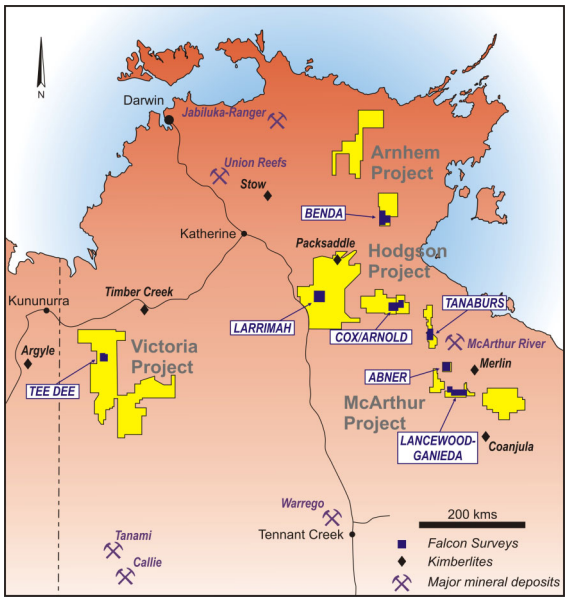

Figure 2. Locations for surveys in Northern Territory.

In general terms the Falcon™ AGG data, combined with magnetics and high resolution digital elevation data acquired simultaneously with the AGG data, have shown a remarkable ability to map fine scale geological variations and identify potential kimberlite pipes and palaeochannels.

This paper presents a selection of data, including data acquired over known pipes and palaeochannels. The survey areas represent a wide range of geological environments and illustrate a number of the interpretation and targeting issues associated with airborne gravity gradiometry. All surveys were flown with 100 m line spacing at 80 m mean terrain clearance.

Phillips Range

The Aries kimberlite 'cluster' lies in the Phillips Range district in the south central Kimberley region 150 km northeast of the Ellendale lamproite field. The main Aries pipe is one of the largest in Australia and comprises a weathered near surface zone above a core zone of competent kimberlite rock containing numerous mafic and sedimentary derived xenoliths (Towie et al., 1991; Edwards et al., 1992). The pipe intrudes relatively flay lying, mid Proterozoic sandstone and mafic lavas and produces a sizeable magnetic anomaly (+50 nT at 80 m terrain clearance).

The main pipe yields a clearly discernable vertical gravity gradient (Gdd) low, thought to be due to the near-surface weathered zone. The Aries North pipe also exhibits a recognisable Gdd low coincident with the known pipe boundaries. The southern 'lobes' at Aries, Athena and Helena, together yield a stronger Gdd low than the main pipe, but there is insufficient deep drilling data on these 'lobes' to explain the magnitude of this low. Significantly, to the south of Athena and Helena, two much smaller kimberlite bodies have been

discovered as a result of the Falcon™ survey data. In the case of Persephone, the veracity of the gravity low evident from the Falcon™ survey data was first confirmed by a local ground gravity survey before drilling established the low to be associated with a kimberlite. Subsequently, a lesser Gdd low, essentially along trend from Persephone was also drilled, resulting in the discovery of the Niobe kimberlite.

Detailed ground gravity and rock density measurements could be used at Aries to elucidate the exact causes of the Gdd anomalies. However, from an explorer's viewpoint, the Gdd responses constitute valid targets and drill testing is for the most part the cost-effective means of follow-up.

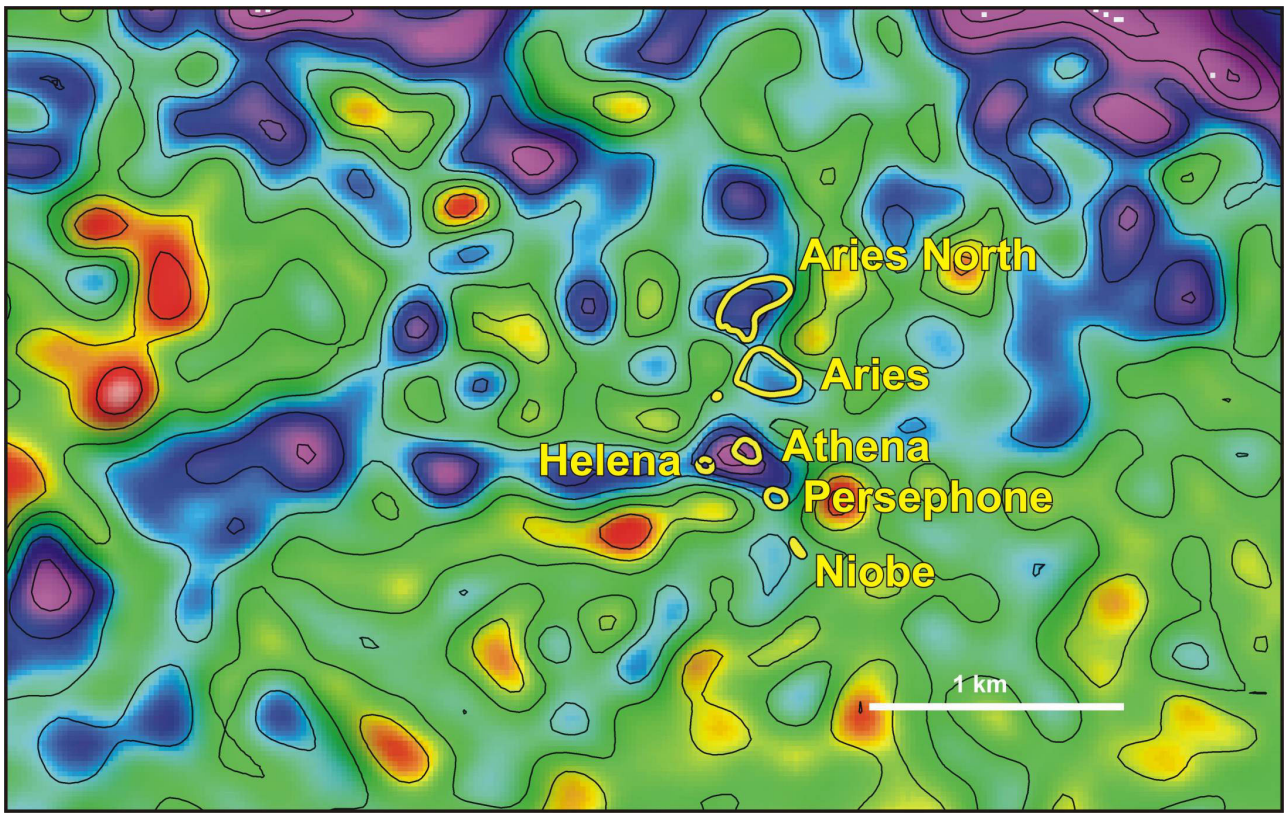

Figure 3. Vertical gravity gradient (Gdd) image over the Aries kimberlite district. The contour interval is 10 Eo.

Ellendale

The Falcon™ survey at Ellendale covered the north eastern part of the lamproite field and included ten pipes which had been previously delineated from detailed aeromagnetic data (Jenke and Cowan, 1994). The survey aimed to detect pipes dominated by crater facies material which might consequently be expected to be non-magnetic. Crater facies material frequently carries the better diamond grades in the district. The portion of the AGG survey presented in Figure 4 illustrates the characteristics of the known pipes.

The three largest pipes, Mt North (16 Ha), E16 (17 Ha) and E21 (19 Ha) all have associated Gdd highs, suggesting that they have a significant component of magmatic lamproitic material. Mt North, however, is also associated with a strongly developed Gdd low peripheral to the central high. This is almost certainly associated with the tuffaceous zone reported to fringe the magmatic lamproite. Mt North is a prominent hill and is largely coincident with the magnetic anomaly. The central vertical gravity gradient high is regarded as a true reflection of subsurface density contrasts, rather than a terrain effect since similar topographic features in other areas do not yield Gdd anomalies. E16 and E21 appear as isolated highs without peripheral lows, suggesting that only minor amounts of tuffaceous crater facies material are present.

Sizeable pipes E19 (11 Ha) and E27 (7 Ha) show no distinctive Gdd 'signatures' but local minor Gdd variations could be construed as being associated with them. We interpret this as an indication that there is insufficient density contrast with respect to the local host geology to generate an anomalous gravity response. The other pipes are generally very small in area (0.5 to 1 Ha or less) and as anticipated, show no discernable Gdd response.

Of particular interest are the strongly developed sinuous Gdd lows associated with palaeochannels. These are very coherent features of 15-40 Eo and initial drilling suggests that they may be as thin as 20 m in average depth extent. The palaeochannels are highly prospective for alluvial diamonds.

At the time of writing, the main phase of drill testing of newly-defined Falcon™ targets had not begun.

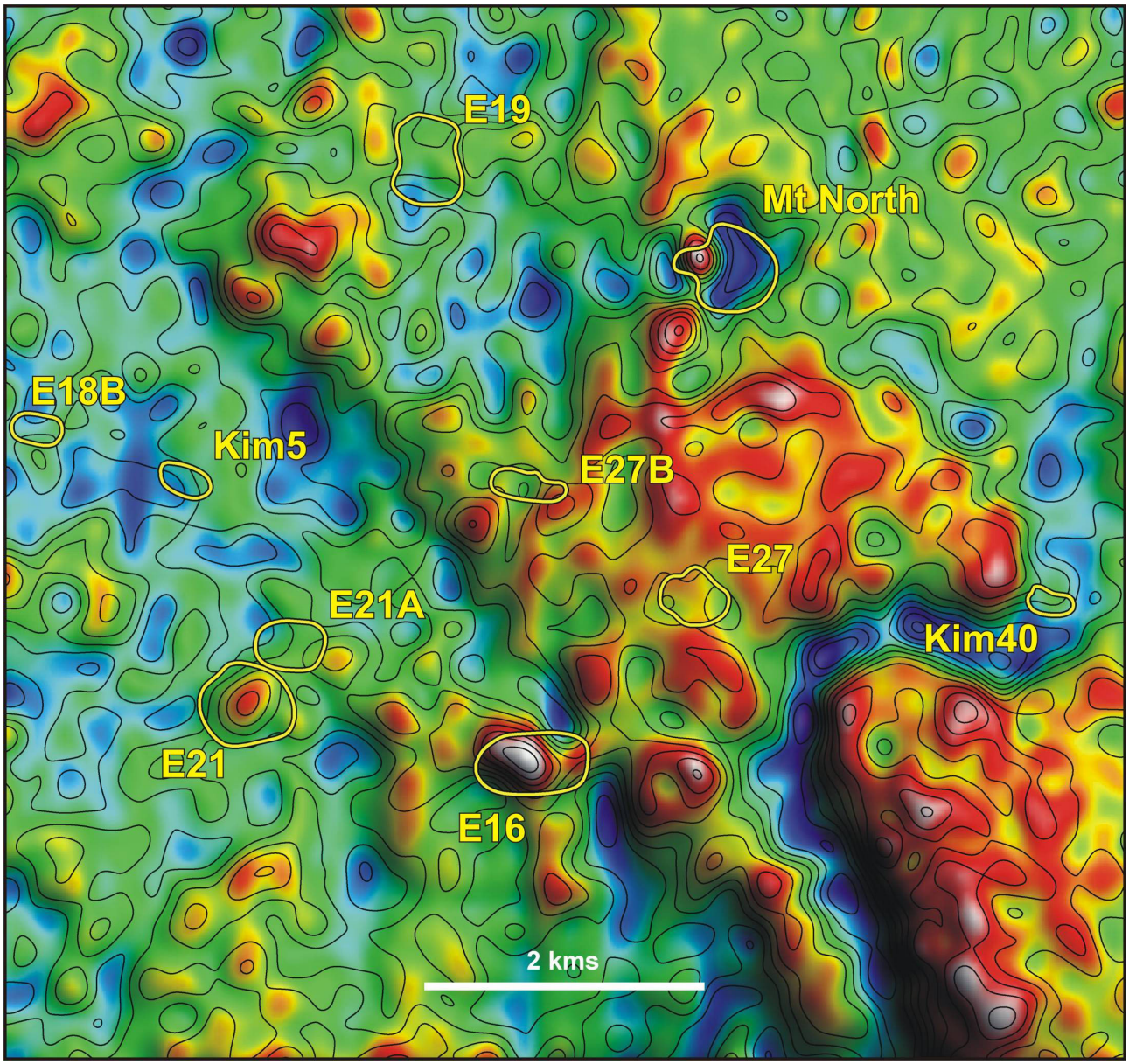

Figure 4. Vertical gravity gradient (Gdd) data for a portion of the Ellendale Survey. The contour interval is 5 Eo.

King George North [1]

No kimberlite pipes of significant size have been discovered in the King George North area and, as with Ellendale, field testing of major targets was not at an advanced stage at the time of writing. Earlier exploration has made fairly extensive use of ground gravity, mainly in the form of single profiles. One area of abundant indicator minerals had received a detailed ground survey (observations on a 100 m by 100 m grid) and it is instructive to compare the ground (residual Bouguer) to the airborne (Gdd) data.

The principal feature of the ground gravity grid is a 0.35 mGal low recognisable over an area of 10 Ha. In general terms the match between the ground and airborne data is quite good and in the particular case of the main gravity low, the match is exceptional. On this basis, and supported by other comparative examples,

[1] It is unfortunately not possible at this time to show data from the King George North or Northern Territory surveys.

we are sufficiently confident in the nature and location of Gdd anomalies to drill them directly without needing to first confirm their veracity through acquisition of ground gravity data.

Northern Territory Areas A and B

Area A is an area of little or no outcrop where magnetic data indicates the presence of near surface, flat lying basalts. Fault structures evident in the magnetics are also clearly evident in the Gdd. The Gdd, however, has patterns that appear to reflect geological features beneath the basalt and when considered in the context of the magnetics, leads to the inference that the basalt layer is quite thin (<50 m). Tightly defined magnetic lows are seen to coincide with Gdd lows and these constitute excellent kimberlite targets. There is no discernible correlation between Gdd variations and topography, suggesting that the terrain corrections have been effective.

Area B has quite substantial topographic variations, particularly in the form of folded quartzite ridges. Although initial inspection suggests that the Gdd variations follow topography, detailed comparison shows that the response follows geological units, rather than topography. In particular, the Gdd resolves density variations within sedimentary sections sufficiently well as to provide a basis for tracking particular units.

Summary

In a short time frame, Falcon™ has established its credentials as a front-line diamond exploration tool in Australia. The principal conclusions drawn from work carried out by Gravity Capital to date are:

- Falcon™ senses the density variations associated with kimberlite pipes in a range of geological environments.
- Under suitable conditions Falcon™ can detect quite small pipes (< 150 m diameter).
- Falcon™ Gdd data matches ground data with similar sampling specifications.
- The Falcon™ terrain corrections based on laser scanner and GPS data largely eliminate topographic correlations from the Gdd data.

References

Edwards, J.D., Rock, N.M.S., Taylor, W.R., Griffin, B.J., and Ramsay, R.R., 1992, Mineralogy and petrology of the Aries diamondiferous kimberlite pipe, Central Kimberley Block, Western Australia: J. Petrology, 33, 1157-1191.

Jenke, G., and Cowan, D.R., 1994, Geophysical signature of the Ellendale Lamproite Pipes, Western Australia: In “Geophysical Signatures of Western Australian Mineral Deposits”, Geology and Geophysics Department (Key Centre) & UWA Extension, The University of Western Australia, Publication No. 26, 1994, 403-414.

Towie, N.J., Bush, M.D., Manning, E.R., Marx, M.R., and Ramsay, R.R., 1991, The Aries diamondiferous kimberlite pipe, Central Kimberley Block, Western Australia: Exploration, setting and evaluation: Proceedings of the Fifth International Kimberlite Conference, Volume 2: Diamonds: Characterization, genesis and exploration: CPRM special publication IBJAN94, 319-328.

A comparison of the Falcon® and Air-FTG™ airborne gravity gradiometer systems at the Kokong Test Block, Botswana

Donald Hinks
Kennecott Exploration Company
donald.hinks@riotinto.com

Steve McIntosh
Rio Tinto M E Ltd
smcintosh@mweb.co.za

Richard Lane
Geoscience Australia
richard.lane@ga.gov.au

Abstract

A field comparison of the Falcon® and Air-FTG™ airborne gravity gradiometer systems has been carried out to establish performance levels for these systems when used in diamond exploration. The test site is the Kokong Test Block, a 40 km^2 block in the Kalahari Desert, southern Botswana. Seven kimberlites of varying sizes are known within the survey area and detailed ground gravity data are available for a 3 by 5 km portion of the survey area. Each airborne survey contractor processed the data twice and there are significant differences between the first and second versions. Upper bounds on the noise levels of the airborne systems are established by comparing the airborne datasets with upward continued and low-pass filtered ground data. The Falcon data, low-pass filtered at 400 m, has a standard deviation of vertical gravity gradient noise of less than 8.1 Eo. The Air-FTG system, low-pass filtered at 700 m, has a standard deviation of vertical gravity gradient noise of less than 7.1 Eo. After removing a first order trend surface from both ground and airborne datasets, the differences between ground and airborne vertical gravity data have a standard deviation of 0.22 mGal for both systems. This amounts to a noise spectral density of 0.1 mGal/√km. Not all of the kimberlites in the test block have a recognisable gravity response, even with accurate ground data. Both systems clearly show the response of the largest pipe, but anomalies for the smaller pipes are at or below the limits of reliable detection when this limit is defined as a peak-to-peak anomaly three times the standard deviation of the noise. Random noise with amplitude and bandwidth the same as that observed in the trials has been added to the modelled vertical gravity gradient response for a set of kimberlite bodies to show how the results of the field comparison can be used for an assessment of kimberlite detection. We conclude that the two systems have very similar performance levels, and that only a subset of economic kimberlites has an airborne gravity gradient response that will be detectable with these systems.

Introduction

The Falcon and Air-FTG airborne gravity gradiometer (AGG) systems have prompted a re-think of the role of gravity data in regional diamond exploration. Although modelling studies can provide insight into the signal levels to be expected over different kimberlite targets, field tests are required to derive complementary information about noise levels. With both signal and noise levels characterised, the limits for detection of various targets can be realistically predicted and used to guide decisions on future exploration. When there is more than one acquisition system available, it is natural to ask how the systems compare in terms of technical performance. This can be gauged by acquiring data with both systems over the same test site. Independent knowledge of the gravity variations and geology of the survey area enhances the comparison. On this basis, the Kokong Test Block, a 4 by 10 km area within the Kalahari Desert of southern Botswana (Figure 1), is considered an ideal test site.

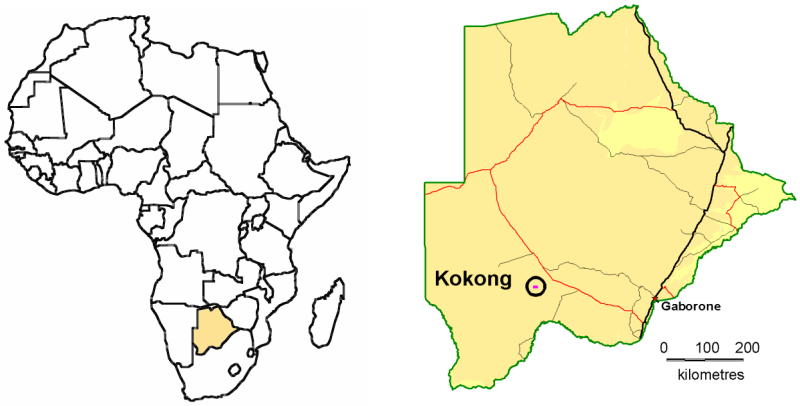

Figure 1. Location of the Kokong Test Block, southern Botswana.

The area was explored between 1979 and 1985 by Falconbridge, who discovered a total of seven kimberlite pipes using airborne magnetics, ground gravity and indicator sampling. The locations of the kimberlites discovered during this period are shown superimposed on a Total Magnetic Intensity image in Figure 2. The pipes are buried beneath 70 to 120 m of Kalahari Sand and the present ground surface is flat. Detailed ground gravity data are available for a portion of the survey area. The pipes have a variety of gravity responses, reflecting differences in diameter, density contrast and surrounding host lithology. Table 1 summarises basic information for these kimberlites. The diameter values were estimated from magnetic and gravity data as there is insufficient drilling of these sub-economic pipes to determine their size directly.

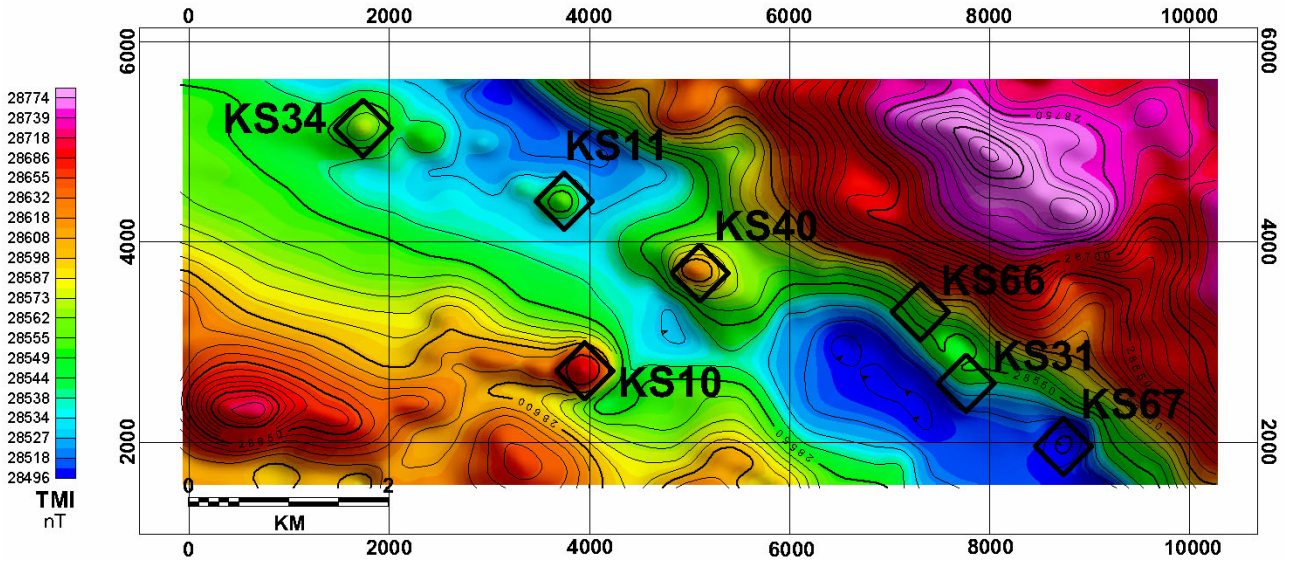

Figure 2. Airborne Total Magnetic Intensity data for the Kokong Test Block, showing the locations of kimberlites known prior to the airborne gravity gradiometer surveys.

The magnetic and gravity responses of these pipes do not always coincide; KS40 has an offset magnetic high and gravity low, and the drill hole which intersected KS31 was drilled between a magnetic low and gravity low. KS66 does not have a magnetic anomaly at all and KS67 is associated with a magnetic low. The ground gravity anomalies for all these pipes are either lows or below the detection level of 0.1 mGal. The gravity features vary in amplitude from less than -0.1 mGal to more than -1.2 mGal in the case of the largest body, KS40. The pipe diameters were estimated from ground geophysical data, and range from 300 m (KS31) to 1000 m (KS40).

Table 1. Diameter, thickness of cover and gravity anomaly characteristics of the kimberlites in the Kokong Test Block.

Kimberlite	Diameter (m)	Thickness of Kalahari Sand cover (m)	Amplitude of associated ground gravity anomaly (mGal)
KS40	1000	120	-1.20
KS67	400	77	-0.40
KS66	600	105	-0.30
KS31	300	80	-0.25
KS34	500	70	-0.15
KS11	600	90	<0.10
KS10	600	99	<0.10

Airborne gravity gradiometer surveys

The Falcon and Air-FTG systems are described in greater detail elsewhere in this volume and will only be briefly summarised here. The systems both use Lockheed-Martin AGG technology to measure acceleration. The Falcon system measures two horizontal gravity gradients which can be spatially transformed to produce vertical gravity (gZ) and vertical gravity gradient (Gzz) data. The Air-FTG system is a full tensor gravity gradient system which can measure the five independent gravity gradient tensor components. Transformation to vertical gravity again requires spatial transformation.

A direct comparison of system performance levels based on surveys over the same area under the same conditions provides the evidence required to judge the relative technical merits of the systems involved. Although the two surveys were flown a year apart (the Falcon survey in January 2002 and the Air-FTG survey in January 2003), similar elevated levels of turbulence were encountered during both surveys. January is not the ideal month to acquire airborne gravity gradiometer data as air turbulence from the summer heat is at a maximum at this time of year.

Both contractors processed their data twice, and in each case, there are significant differences between the first and second versions. This is likely to be due to a combination of factors, including the low level of geological signal in the test area, the amount of noise present in the airborne datasets, the small signal from the buried kimberlite pipes, and the relative immaturity of the data processing techniques. Only the final results are presented here.

Falcon Survey

The Falcon data were acquired over two flights, with 100 m line spacing, terrain clearance of 80 m, and east-west line direction. North-south tie lines were spaced at 2500 m intervals. An initial gZ and Gzz dataset was provided and later, a second dataset was provided which was produced with new processing routines. Although terrain corrections were produced, they were not applied as the maximum terrain correction value of less than 0.7 Eo was considered unimportant. During assessment of the data, amplitude spectra have been calculated for each row in the final Gzz grid and then averaged (Figure 3). The rapid drop in amplitude for wavelengths less than 400 m indicates that a high order (i.e., steep) low-pass filter with a 400 m cut-off was applied to these data.

Air FTG Survey

This was the second survey flown with the Air-FTG system in Africa, and it would be natural to expect that improvements to acquisition and processing methods would be made as greater experience was gained. The Kokong survey involved eight flights, with 100 m line spacing, terrain clearance of 90 m, and east-west line direction. Due to turbulence and concerns over data quality, the spacing of north-south tie lines was reduced to 250 m and a number of the flight lines were re-flown. Two versions of the gZ and Gzz data were supplied. The dynamic range of the data in the first set of products is much higher than in the second version, which is interpreted as an indication that considerably more noise is present in the first set of products or that more filtering was applied the second time around. The first version of the Gzz grid has a standard deviation of 17 Eo, whilst the final version has a standard deviation of 7.1 Eo. For comparison, the standard deviation of the Falcon final Gzz grid is 8.7 Eo.

As far as we are aware, the complete Air-FTG dataset including original and re-flown lines was used for the preliminary processing. It is unclear whether noisy flight lines were excluded when compiling the final products. No terrain corrections were calculated for the Air-FTG data. The experience from the Falcon survey suggests that the effect of this omission is not significant. Whilst analysing the data, an average amplitude spectrum from the rows of the final Gzz grid has been derived (Figure 3). The drop in amplitude at the short wavelength end of the spectrum is less dramatic for the Air-FTG Gzz data. It was inferred through comparison with the spectrum for the Falcon Gzz data that a gradational, low order low-pass filter was applied to wavelengths less than 700 m.

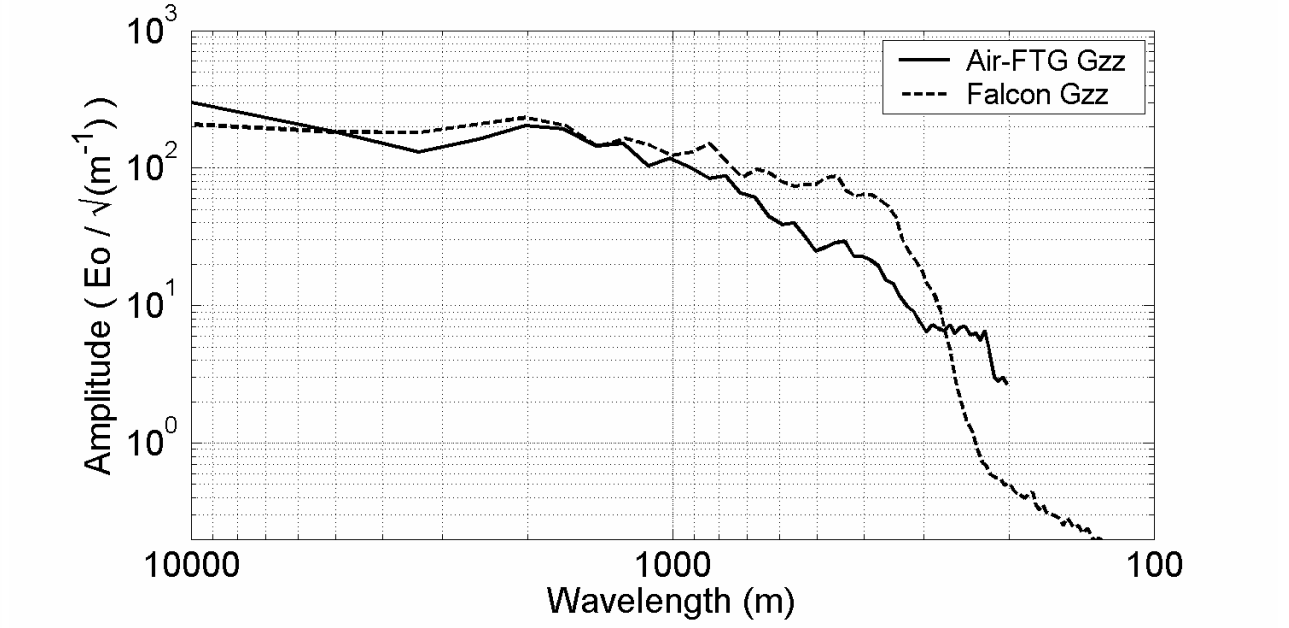

Figure 3. Average east-west spectral response of Falcon and Air-FTG Gzz data. The drop in amplitude at shorter wavelengths is due to a combination of the terrain clearance of the measurements, the depth to the sources below surface and low-pass filtering of the data.

Acquisition of ground gravity data

Rio Tinto acquired ground gravity data on a 100 by 100 m grid over part of the test area as a check of the Falconbridge ground gravity data and to confirm magnitudes of the gravity responses associated with the kimberlites,. The station locations are shown in Figures 4 and 5. These data were acquired with a Scintrex CG3 gravity meter, with location control provided by real time differential GPS measurements. The errors in the GPS locations were thought to be to less than 10 cm. The errors in the ground Bouguer data were estimated to be less than 0.04 mGal.

Qualitative assessment of survey results

Falcon

The final Falcon Gzz data are shown in Figure 4. The large negative gravity response associated with KS40 is clearly seen in the centre of the test block. A further four pipes (KS34, KS66, KS67 and KS10) are associated with Gzz lows, although it is unlikely that KS10 and KS34 would be picked as anomalies from this dataset alone. There are many other Gzz lows with similar character to the lows associated with KS10 and KS34 (e.g., 350E 3400N, 2000E 3450N, 8900 E 3550N, 3800E 3300N, etc), suggesting that these features may be due to system noise or to a very common set of geological conditions.

There is an anomaly in the vertical gradient data at 550E 2300N, near the south-west corner of the grid. This was drilled as a result of this survey and found to be a new kimberlite (K075).

Air-FTG

The final Air-FTG Gzz data are shown in Figure 5. Once again, the anomaly associated with KS40 is clear. There are also vertical gravity gradient lows coincident with the KS66, KS67 and KS10 pipes: however, there are other Gzz lows with similar amplitude to the known pipes at 3600E 3400N, 6750E 3650N, 4800E 2000N. Although there is a low at K075, the feature has lower amplitude than in the Falcon data and it is unlikely that this feature would have been picked for follow-up from the Air-FTG dataset.

Although the Air-FTG system measures all five independent components of the gradient tensor, the other components are not discussed in this paper. As part of the processing carried out on the full tensor data, features in one component that are inconsistent with the response observed in the other components are rejected as noise. This creates a dependency between the data for the various components, and hence there is less new information than might be expected in the other components.

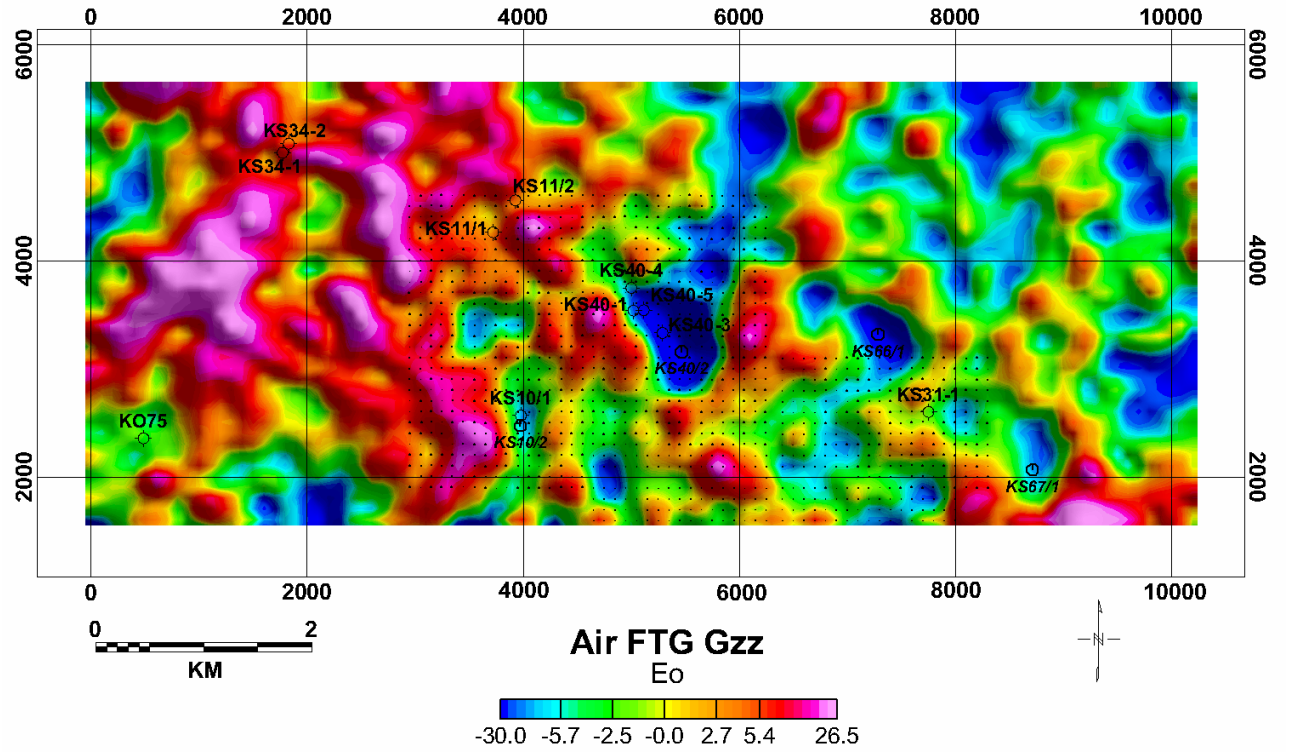

Figure 5. Image of final Air-FTG Gzz data with an overlay showing the boreholes that intersected kimberlite and the locations of the Rio Tinto ground gravity stations.

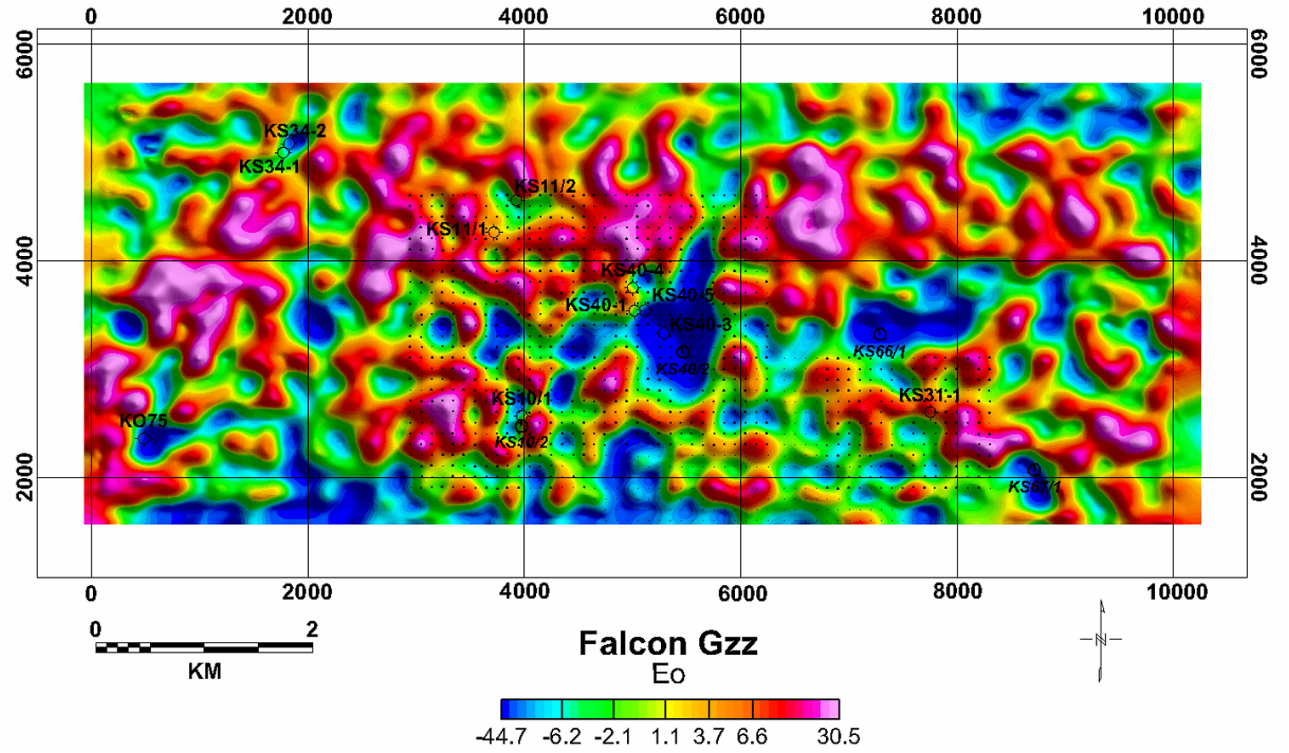

Figure 4. Image of final Falcon Gzz data with an overlay showing the boreholes that intersected kimberlite and the locations of the Rio Tinto ground gravity stations.

Quantitative comparison of ground and airborne data

Identical subsets of the airborne Gzz grids are presented with the first vertical derivative of the ground Bouguer gravity data in Figure 6. The ground data were upward continued and low pass filtered so that they could be considered to be equivalent to the airborne data. In all three images, the response associated with the KS40 pipe appears as a north-west orientated Gzz low. A secondary low trending north-north-east has been confirmed through TEM soundings and drilling to be due to a channel at the base of the Kalahari Sand.

Differences between the airborne and ground data reflect the noise in the two inputs. Given the accuracy and sample spacing of the ground data, it is expected in this instance that the differences are dominated by noise from the airborne data. The standard deviation of the difference grid thus provides an estimate of the noise level for each airborne system. The standard deviation of the Air-FTG Gzz difference grid is 7.1 Eo and the Falcon Gzz difference grid is 8.1 Eo.

Figure 7 shows Bouguer ground gravity data and subsets of the airborne gZ data. The images have the same colour scaling, and the differences in colour indicate that both airborne datasets have significantly different long wavelength signals than those of the ground data. This is not an unexpected result. The airborne gZ data are derived by spatial integration of the gradient information. The finite extent of the survey area limits the wavelengths of gZ information that can be recovered through this integration. This is an important source of error in the derivation of vertical gravity data from AGG surveys (Brzezowski and Heller, 1988). This factor significantly contributed to the differences observed between ground and airborne data. To more equitably compare these datasets, the airborne datasets were masked to the extent of the ground gravity data and a first order trend surface was removed from each of the ground and airborne datasets. This effectively removed wavelengths longer than the dimensions of the ground dataset from consideration. The residuals are shown as images in Figure 8. It could be argued that the Air-FTG data reproduce the ground gZ data more closely than is the case with the Falcon data. However, this is not supported by quantitative analysis. The residual ground vertical gravity data were subtracted from the airborne gZ data to produce residual gZ difference grids. Both difference grids have a standard deviation of 0.22 mGal. Given a wavelength range of 500 to 4000 m for these datasets, this result is approximately equivalent to a noise spectral density of 0.1 mGal/√km. This is the same figure derived by Boggs and Dransfield (2003) in their analysis of Falcon vertical gravity data.

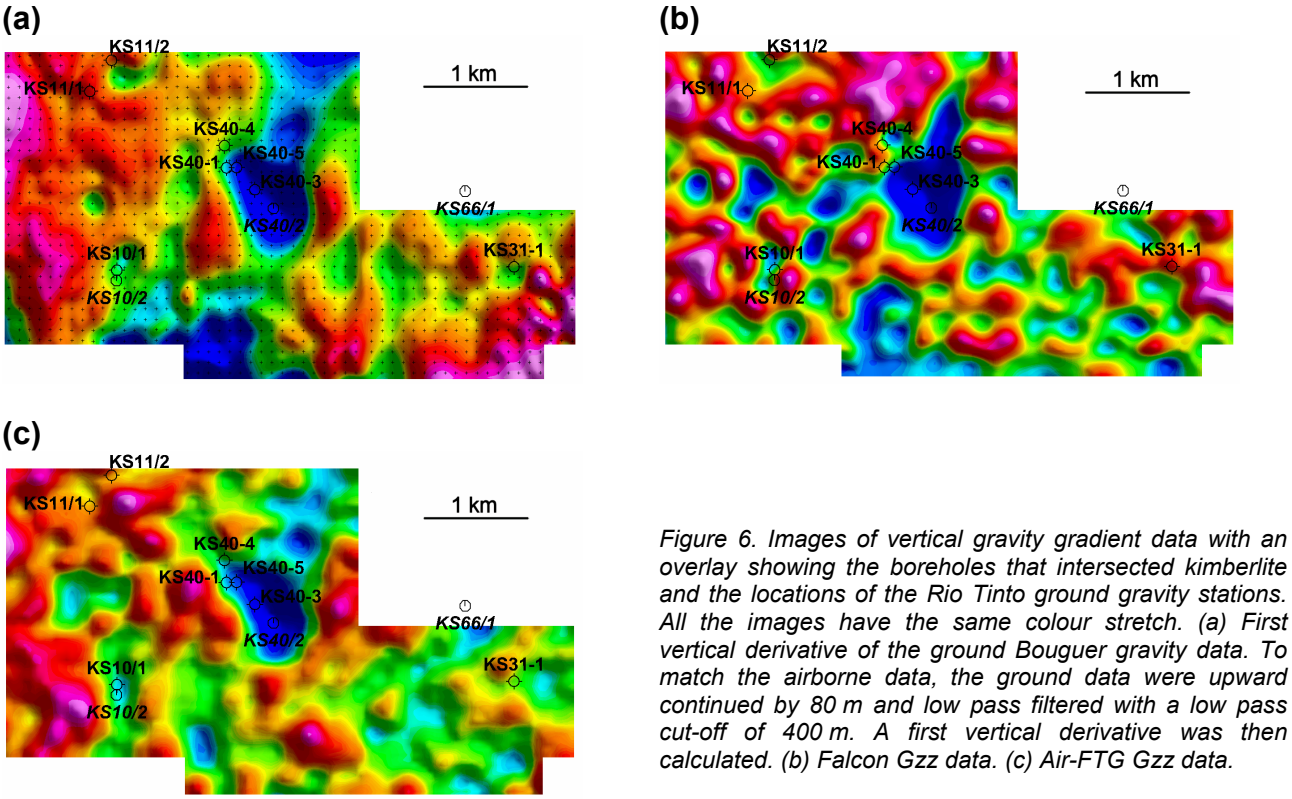

Figure 6. Images of vertical gravity gradient data with an overlay showing the boreholes that intersected kimberlite and the locations of the Rio Tinto ground gravity stations. All the images have the same colour stretch. (a) First vertical derivative of the ground Bouguer gravity data. To match the airborne data, the ground data were upward continued by 80 m and low pass filtered with a low pass cut-off of 400 m. A first vertical derivative was then calculated. (b) Falcon Gzz data. (c) Air-FTG Gzz data.

Figure 7(a)

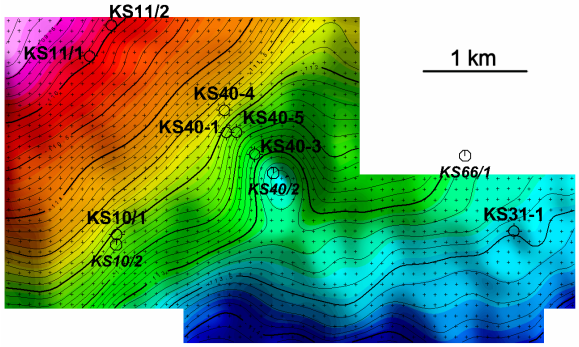

Figure 7(b)

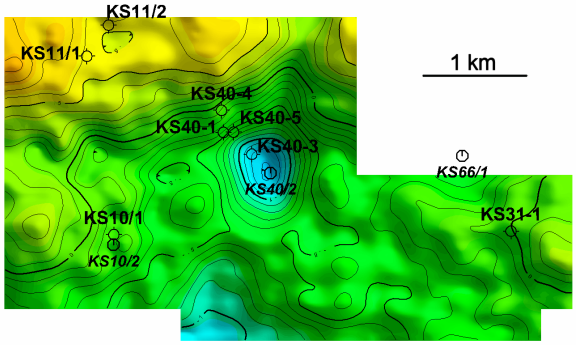

Figure 7(c)

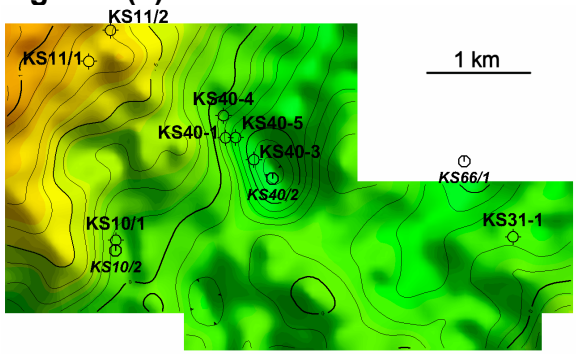

Figure 7. Images of vertical gravity data with an overlay showing the boreholes that intersected kimberlite and the locations of the Rio Tinto ground gravity stations. All the images have the same linear colour stretch, and the contour interval is 0.1 mGal. (a) Ground Bouguer gravity data. To match the airborne data, the ground data were upward continued by 80 m and low pass filtered with a low pass cut-off of 400 m. (b) Falcon gZ data. (c) Air-FTG gZ data.

Figure 8(a)

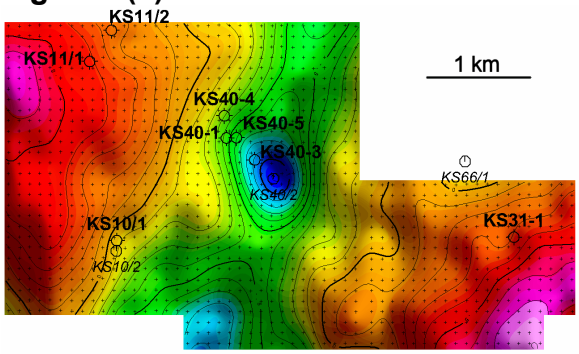

Figure 8(b)

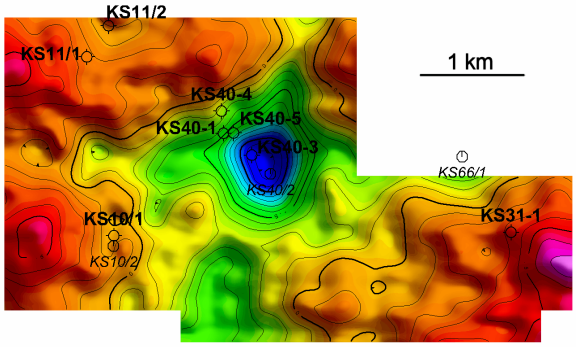

Figure 8(c)

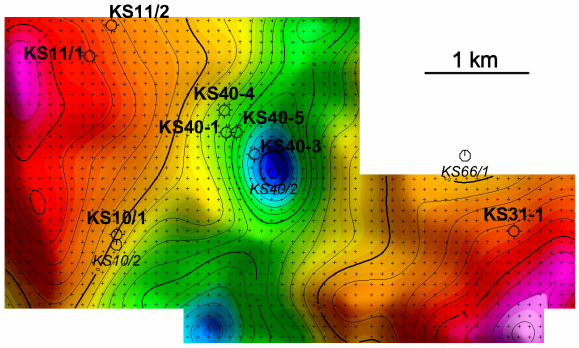

Figure 8(d)

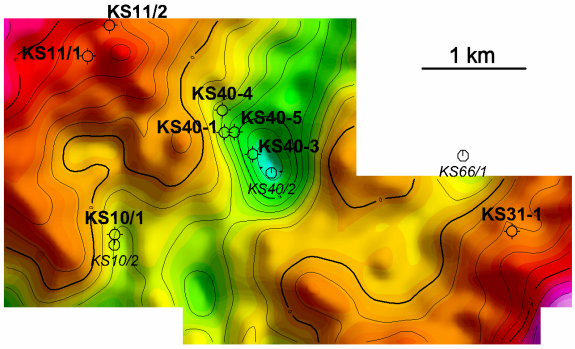

Figure 8. Images of residual vertical gravity data with an overlay showing the boreholes that intersected kimberlite and the locations of the Rio Tinto ground gravity stations. A first order trend surface was removed from each grid. All the images have the same linear colour stretch, and the contour interval is 0.1 mGal. To match the airborne data, the ground data were upward continued by 80 m before being low-pass filtered. (a) Ground Bouguer gravity data, low-pass filtered with a cut-off of 400 m. (b) Falcon gZ data. (c) Ground Bouguer gravity data, low-pass filtered with a cut-off of 700 m. (d) Air-FTG gZ data.

Profiles of Gzz and gZ data for an east-west line across the KS40 pipe are shown in Figure 9. Both airborne systems map the amplitude of the KS40 anomaly in both Gzz and gZ form. It appears that the amplitude of the Gzz response associated with the KS40 pipe is slightly larger in the Falcon data than in the Air-FTG data, but the difference is not significant given that the standard deviation of the noise is 7 to 8 Eo. Additional short wavelength variations are evident at both ends of the profile in the Falcon Gzz data in comparison with the Air-FTG Gzz data. This observation is consistent with the spectral comparison shown in Figure 3. The improvement in correlation between ground and airborne gZ data following removal of a first order trend is evident when the profiles of Figure 9b and 9c are compared.

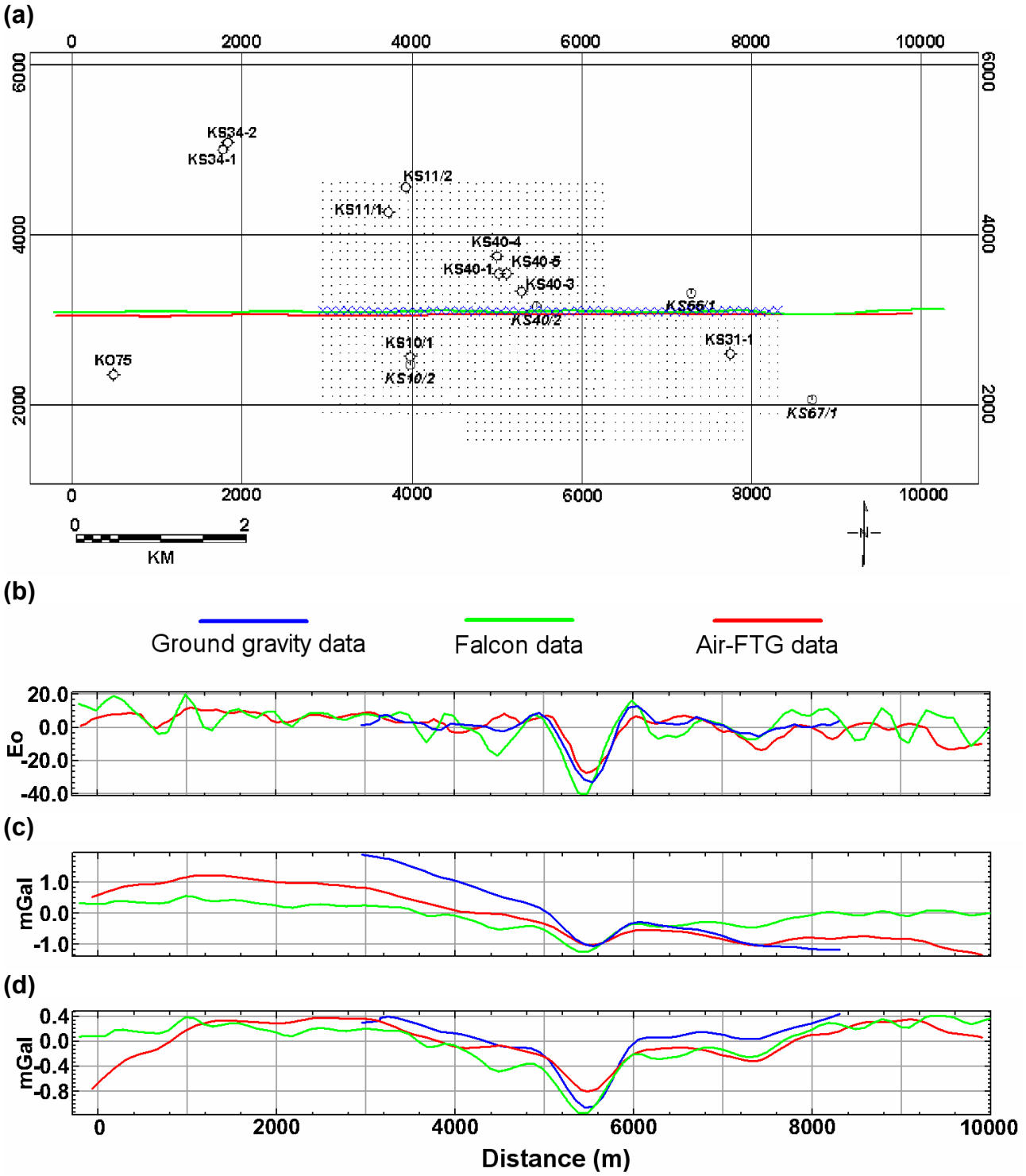

Figure 9. Profiles for an east-west line across the KS40 gravity anomaly. (a) Location of the flight lines and ground observations used in the profiles. (b) Comparison of airborne Gzz data with the first vertical derivative of upward continued ground Bouguer gravity data. (c) Comparison of airborne gZ data with upward continued ground Bouguer gravity data. (d) Comparison as per (b) following removal of a first order trend from each dataset.

Modelling studies

The response for a "kimberlite plantation" of 16 pipes ranging in surface area from 6 Ha to 50 Ha at various depths from surface to 150 m below surface was forward modelled for a Gzz sensor at 80 m elevation (Figure 10) (P. Diorio, personal communication, 2001). The basic kimberlite model used was that proposed by Anglo American for a CAMIRO modelling study (MIRA Geoscience, 2001). It consists of a 200 m thick crater facies with a density of 2.25 g/cm^3 density, above a 200 m thick diatreme with density 2.5 g/cm^3, embedded within a host of density 2.6 g/cm^3. The crater edges dip inwards at 65º. The anomaly amplitudes for these pipes range from 10 to 70 Eo.

Random noise similar in amplitude and low-pass filter characteristics to the noise estimated from the airborne surveys was then added to the synthetic kimberlite model response (Figure 11). This result was used to asses the detection levels of the airborne systems. A figure of 3 times the noise standard deviation is commonly used as a definition for detection of an anomaly. It would be unlikely that the anomalies for a 6 Ha kimberlite at 50 m depth and that for a 25 Ha kimberlite at 150 m depth (with the density contrasts specified) would be identified as anomalous. Kimberlite pipes which are larger, at a shallower depth, or had larger density contrasts might be expected to be detected.

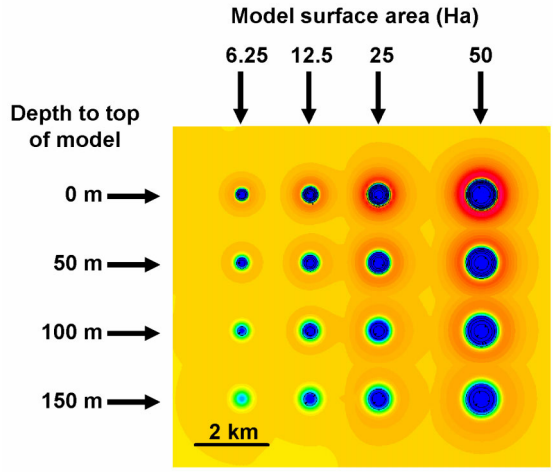

Figure 10. Gzz response of the kimberlite plantation model. Contour interval is 10 Eo.

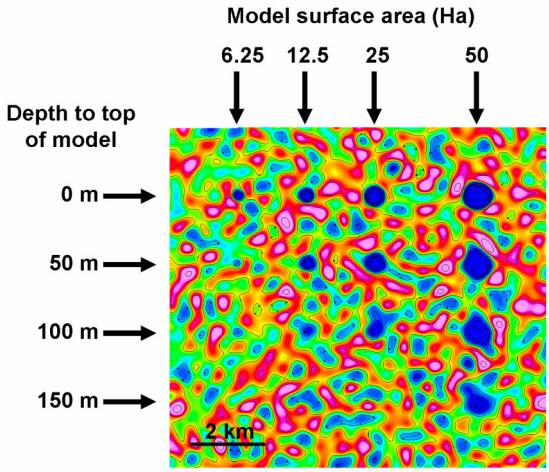

Figure 11. Gzz response of the kimberlite plantation model with added artificial noise. The noise grid has been low-pass filtered with a 550 m cut-off and has a standard deviation of 7.6 Eo. This is representative of the noise levels observed in the Kokong data. Contour interval is 10 Eo.

Conclusions

Two airborne gravity gradiometer systems, Falcon and Air-FTG, have been flown over the same test block to evalute their capacity to map anomalies associated with known kimberlite pipes of different sizes in an area.

Both contractors provided two different versions of the gZ and Gzz data, and there are significant differences between each version and between the results from the two systems. This is primarily an indication of the relatively low signal to noise for the response measured by the systems in the survey area. The test area is extremely flat so terrain corrections were not required and these corrections did not play a role in the comparison of the systems.

Although, the response of the largest pipe is clearly seen in all datasets, the anomalies associated with the majority of the smaller pipes are of similar amplitude to the noise floor of both systems and as such would be difficult to pick from the airborne gravity gradient data alone. There are low amplitude, local anomalies in the Falcon data over the KS34 and K075 pipes. These are marginally clearer than the equivalent features in the Air-FTG data. The response over KS34 is small, and it could be argued that it is a 'lucky' coincidence of a noise feature above the known kimberlite. The K075 pipe was discovered as a direct result of the follow-up to the Falcon survey, and must hence be considered to be an anomaly of exploration significance.

Difference grids were calculated by subtracting ground data from the airborne data. The standard deviation values of these grids are interpreted as an estimate of the noise levels in the airborne data. The values for the two systems are similar; for vertical gravity gradient data, 7.1 Eo with a 700 m low pass cut-off for the Air-FTG system, and 8.1 Eo with a 400 m cut-off for the Falcon system; for vertical gravity data, 0.22 mGal for

both systems. The additional short wavelength content of the Falcon data is clearly evident in comparisons carried out in profile and spectral form. Since AGG systems cannot recover long wavelengths in gZ data, it is necessary to remove these wavelengths from each of the datasets before any meaningful comparison can be made between ground and airborne gZ data. Both visually and numerically, the two airborne systems are able to reproduce the known vertical gravity field to the same degree. It is worth noting that gZ grids are derived from other measurements, and hence the noise estimates for gZ data are of secondary importance in making an assessment of the technical performance of the two systems.

A random noise grid, which was based on the the noise estimates from difference grids, was added to the response calculated for a collection of kimberlite models to assess the range of pipe sizes and burial depths that would allow the pipes to be detected by these AGG systems. The results depend on a range of factors, most notably the density contrast with the surrounding host, but it is clear that not all of the pipes of potential economic size and burial depth would be located from the airborne gravity gradiometer data alone. This result supports the evidence from the field trial.

Acknowledgments

We would like to thank Rio Tinto, BHPBilliton and Bell Geospace for allowing us to present this data, and Peter Milligan for critically reviewing the paper. This paper draws most of its information from an internal Rio Tinto report (McIntosh and Hinks, 2003). One of the authors (Lane) publishes with the permission of the CEO, Geoscience Australia.

References

Boggs, D.B., and Dransfield, M.H., 2003, Analysis of errors in gravity derived from the FALCON Airborne Gravity Gradiometer: Submitted for inclusion in M. Talwani and E. Biegert (eds), Gravity Gradiometry – Instrumentation, Processing and Case Studies, Society of Exploration Geophysicists. (Reproduced as a paper in this volume).

Brzezowski, S.J. and Heller, W.G., 1988, Gravity gradiometer survey errors: Geophysics, 53, 1355-1361.

Mira Geoscience, 2001, Project Report – CAMIRO Project 2001E01: Detectability of mineral deposits with airborne gravity gradiometry: Released as Miscellaneous Release - Data 134 by the Ontario Geological Survey.

McIntosh, S., and Hinks, J.D., 2003, A review of the performance of the BHP-Billiton Falcon and the Bell Geospace full tensor gravity gradiometers in comparison to ground gravity data at Kokong, Botswana: Rio Tinto Report (Unpublished).

Analysis of errors in gravity derived from the Falcon® airborne gravity gradiometer*

David B. Boggs
BHP Billiton
David.B.Boggs@BHPBilliton.com

Mark H. Dransfield
BHP Billiton
Mark.H.Dransfield@BHPBilliton.com

Abstract

Falcon® airborne gravity gradient data can be converted to vertical gravity via direct integration techniques (Gunn, 1975) or equivalent source methods (Dampney, 1969), and hence compared with conventional gravimetry data. Either conversion process amplifies long wavelength features from the gravity gradient data and therefore reconstructs regional scale features poorly.

Recent Falcon surveys over a number of areas with pre-existing ground gravity have allowed proper assessment of the extent of this problem. Comparison of Falcon and ground data from three different areas indicated that derived vertical gravity is very good at wavelengths less than the minimum survey dimension, spectral analysis showing errors are typically 0.1 mGal / $\sqrt{\text{km}}$ for wavelengths below this limit.

A similar analysis by Bruton et al., (2001), of profile gravity data from three airborne gravimetry systems, showed error of different spectral character to that achievable via Falcon, with steadily decreasing contribution to the total error from longer wavelengths. The independent analysis of the airborne gravity systems indicated that the limiting wavelength, beyond which airborne gravimetry profiles becomes more accurate than a detailed Falcon gradiometry survey data, is approximately 10-20 km.

Here we show that this shortcoming of Falcon gravity data can be rectified with the use of regional-scale gravity databases, sparse marine track data, or satellite-derived gravity, to conform the Falcon gravity to the regional data beyond a certain wavelength. Given typical survey dimensions of 10-100 km, and provided that the reliable range of wavelengths in the Falcon and regional data overlap sufficiently, it is possible to derive gravity data having errors of approximately 0.1 mGal / $\sqrt{\text{km}}$ and sampling all features with wavelengths greater than 300 m.

Introduction

The Falcon airborne gravity gradiometer (AGG) measures the two horizontal differential curvature gradients (Lee, 2001), quantities also measured by the original Eötvös torsion balances (Heiland, 1968; Telford, 1990). Within a north, east, down coordinate system and using subscripts for derivatives, these quantities are second derivatives of the gravitation potential referred to as G_{NE} and $G_{UV} = ((G_{NN} - G_{EE})/2)$. Differential curvature gradients measure the degree of distortion of the gravitational equipotential surface from a spherical shape. Traditional gravimeters, on the other hand, measure the vertical acceleration due to gravity (G_D), arguably a less abstract quantity.

Gravimeters and gravity gradiometers both measure derivatives of the gravitational potential. Well known algorithms allow conversion between these various derivatives to produce theoretically equivalent quantities. Such conversions, based on integration of the gravity gradients and equivalent source techniques, are applied routinely to Falcon gravity gradient data to derive the more familiar vertical gravity. A limitation of these processes is that accurate recovery of long wavelength information in the Falcon G_D product is not possible, particularly at wavelengths greater than the survey dimensions.

Although this limitation was expected, until recently it was of no concern, direct detection of mineral deposits being the sole aim of Falcon surveys. In these situations, important information is contained almost exclusively in relatively short wavelengths. Extension of the use of the system to contract services in oil and gas exploration, where target signals are at relatively longer wavelengths, has led to requirements both to quantify noise and improve representation of regional gravity features in the Falcon gravity, G_D.

---

* This paper, which is cited by several authors in this volume, has been submitted for inclusion in M. Talwani and E. Biegert (eds), Gravity Gradiometry – Instrumentation, Processing and Case Studies, Society of Exploration Geophysicists. This is yet to be published, so the paper is reproduced as a service to the readers.

Previous estimations of error in the Falcon G_D have used various forward projections and approximations based on the known noise character of the gravitational gradient measurements. Recent surveys flown over areas covered by pre-existing surface gravity have permitted more rigorous analysis of the error characteristics of the Falcon gravity by comparing results with a known reference field.

A key result stemming from the analysis comprised improvements to the processing software allowing use of regional ground, marine track or satellite gravity in conjunction with the Falcon gravity gradients, to ensure that the final Falcon gravity product can represent accurately the gravitational field at all scales.

Analysis of Falcon® gravity using reference data

Analysing accuracy of derived Falcon gravity requires availability of a known reference gravity field, located on the same flight surface and with equivalent compensations applied. An obvious complication with surface gravity is that it is generally measured 100 metres lower than the equivalent Falcon products. Other differences are that surface gravity data usually have free-air and Bouguer slab corrections applied. By contrast, Falcon gravity gradient data does not require a free-air correction, and a full terrain correction is normally applied because of the higher sensitivity of gravity gradients to irregular terrain.

Despite these differences, Bouguer corrected surface gravity data are nearly equivalent to terrain corrected Falcon data. Additionally, free-air corrected surface gravity data are nearly equivalent to Falcon data with no terrain correction, especially when topographic undulations are mild. Upward continuation of surface gravity can compensate for differences in measurement surfaces; however, little difference to the end results occurs except in wavelengths less than 1 km. Such relatively small features are often inadequately sampled by the surface gravity in any case, and this can lead to more serious errors in the reference data due to aliasing.

Numerous Falcon surveys have been conducted in regions previously covered by conventional surface gravity surveys. Density of the existing data is generally variable from site to site, and in some cases the data have been of sufficient quality to allow derivation of a detailed reference gravity field. Three such sites, covering a broad range of wavelengths, have been selected for the purposes of this analysis.

To analyse the Falcon G_D performance in comparison to the available reference data, we used a procedure similar to that described by Bruton et al., (2001). Reference fields were prepared by gridding available surface data and applying upward continuation to adjust for the mean altitude difference. The Falcon gravity data were then subtracted from the reference field to derive “error” grids. Any residual first-order (linear) trend was removed from the grids and amplitude spectra of the residuals were then computed, characterising the error in the respective Falcon gravity data.

Amplitude spectral analyses were performed by standard Fourier methods (as described in appendix A) as well as low-pass filtering at preset wavelengths followed by computation of the variances of the residual grids. Bruton et al., (2001) also used this latter method to analyse performance of some airborne gravimeter systems. It can be used to derive power spectral density estimates by noting the reduction in variance relative to the increase in filter wavelength at each step. This alternate PSD computation method is an application of Parseval’s theorem (Champeney, 1973, p.58) and was confirmed to produce results identical to the standard methods. Results from the analysis of Bruton et al., (2001) have also been converted in this manner to allow comparison of the Falcon AGG system with a high-quality airborne gravimetry system.

In each test area, the analysis was performed on two separate Falcon gravity products. The first product involved use of only the Falcon gravity gradients by themselves to derive vertical gravity, hereafter referred to as the “raw” or “un-conformed” Falcon gravity. The second preparation also used third party regional gravity data for the purpose of conforming the Falcon product to a regional surface. Conforming data involved summation of the appropriately filtered data: a high-pass filter to remove erroneous long-wavelength features from the Falcon data and a low-pass filter to remove overlapping spectral regions from the regional data. The resulting product is hereafter called the “conformed” Falcon gravity.

In practice, surface gravity sampled at a regional scale with a Nyquist wavelength of approximately 10 to 20 km is often available, allowing conformed Falcon gravity to be produced for many Falcon surveys. The most visible effects of conforming the Falcon gravity are often at wavelengths much greater than the survey dimensions, appearing as almost linear trends at the scale of the Falcon survey.

As well as spectral analysis of errors in both the raw and conformed Falcon gravity, we provide images of the conformed Falcon and reference gravity at each test area for direct visual comparison.

Test surveys

Location 1 – Mount Woods, South Australia

The first area comprised a Falcon survey of 15 km x 45 km with 200 meter line spacing, also covered by variable density ground gravity (mostly 800 m north-south lines x 400 m stations), making it suitable for analysis of Falcon performance in the 1km - 10km wavelength band. Approximately one-half of the survey is restricted from publication due to confidentiality agreements, so we use just the unrestricted (12 km x 24 km) portion in this analysis. Ground gravity data was accrued sporadically over a ten-year period and several levelling problems are apparent in the resulting data set. The levelling problems are less evident in the reference field prepared from the data (Figure 1) due to the 100 m upward continuation operation.

To derive the conformed Falcon gravity product, a simulated regional survey was contrived from the available ground gravity by decimating stations to a grid spacing of approximately 4 km, with regional conformance of the Falcon gravity at all wavelengths beyond 12 km. By not compensating for the levelling problems in the ground gravity, we simulated errors likely to occur in a regional gravity data set. The resultant conformed gravity is shown in Figure 2, actual station positions selected for the simulated regional survey being shown as black dots in Figure 1. The unconformed gravity derived for this area (not shown) was similar to the conformed gravity product if just the North-South linear trend were removed.

Qualitatively, the conformed Falcon gravity appears very similar to the reference data, the RMS difference between the two being just 0.8 mGal. A visual inspection of the error grid also showed some features trending North-South, obviously indicative of the residual levelling errors in the reference data.

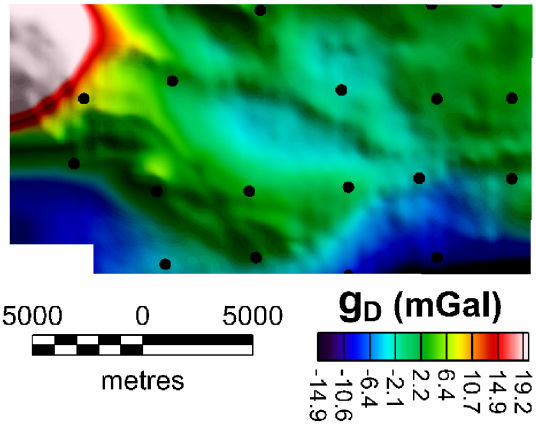

Figure 1. Reference gravity for location 1. Positions of the simulated regional data are shown as dots.

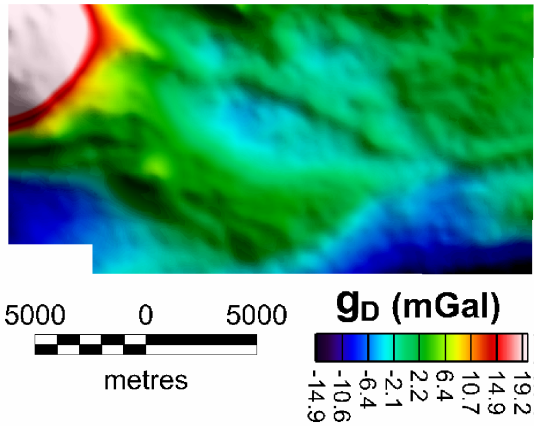

Figure 2. The conformed Falcon gravity product for location 1.

Location 2 – Wilgunya, Queensland

The second test area was a significantly larger survey, comprising an irregular shaped block of around 120 km x 70 km with 200 m spaced lines, located in central Queensland, Australia. Available reference data sources comprised sparse ground gravity from Geoscience Australia's (GA) Australian National Gravity Database, as well as a more detailed survey having 4 km station coverage over 90% of the area. The lack of high-resolution ground gravity in this area meant that no assessment of Falcon's performance below wavelengths of around 8 km was justified, although the large survey footprint allowed assessment of performance in the 8 km – 80 km wavelength region.

The reference grid was derived by merging all the available ground gravity, followed by minimum curvature gridding and upward continuation by 100 m. A simulated regional gravity data set, for use in conforming the Falcon gravity, was again created by decimating the available ground gravity to approximately 10 km station spacing. The reference gravity as well as positions of the simulated regional gravity survey are plotted in Figure 3. It is worth pointing out that the GA database has such regional data for most of the Australian continent, similar databases being available for other continental regions.

Conformed and unconformed Falcon gravity products were created, the crossover to regional being defined as wavelengths beyond 30 km. Both products appeared very similar, although closer inspection revealed that peak-to-peak amplitude of the regional gravity anomaly in the unconformed result was approximately 10% less than in the reference grid. Similarity of the conformed data (Figure 4) to the reference grid was significantly better, the RMS difference between the two being only 1.8 mGal. Visual inspection of this error

grid revealed that most of the contribution to this difference occurred near the positions of the sharp high and low gravity anomalies and therefore could, at least in part, be due to aliasing of these features within the sparsely sampled reference data.

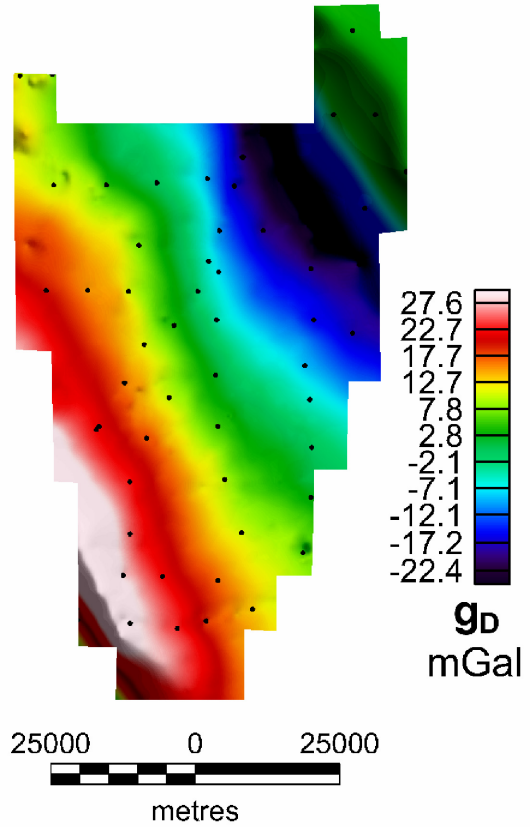

Figure 3. Reference gravity for location 2. Positions of the simulated regional survey are shown as dots.

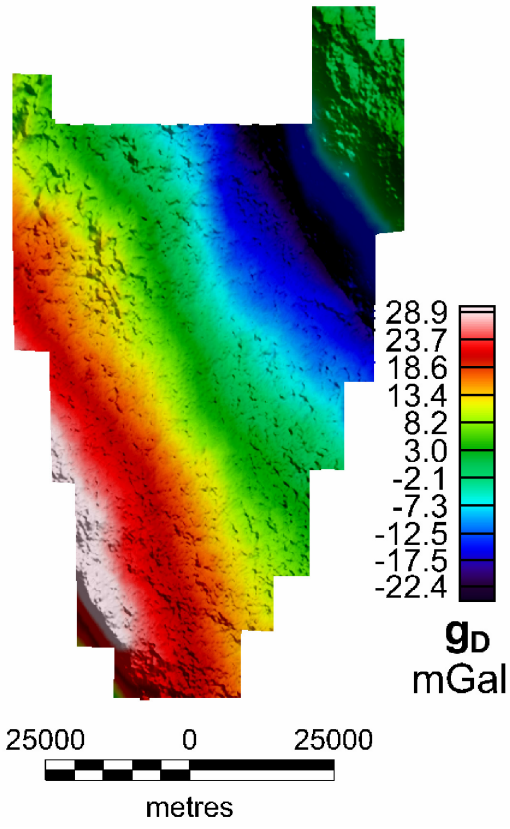

Figure 4. The conformed Falcon gravity product for location 2.

Location 3 – Bass Strait, Victoria

The third data set comes from an offshore Falcon survey of 30 km x 40 km, having 300 m line spacing and being located in water 70 m deep within Bass Strait, between the mainland and Tasmania. A detailed marine gravity survey (360 m lines, 98.4% of data smoothed to an effective cut wavelength of 562 m) was used as the reference gravity for this test. Spectral analysis of the error grid for wavelengths between 1 km and 30 km therefore was expected to indicate error in the Falcon gravity data for this area.

Additional regional data sources available consisted of sparse GSA marine track data and satellite derived gravity. These independent regional data sources let us properly assess the accuracy of the conformed Falcon gravity product. The satellite gravity data were selected for the regional data source in this case, its global coverage making it the obvious choice for offshore regions.

Unfortunately, the satellite-derived gravity used is limited to wavelengths beyond 10 – 25 km, with relatively large errors at the shortest wavelengths (Anderson and Knudsen, 2000). Therefore we decided to limit introduction of regional data in the conformed Falcon product to wavelengths beyond 60 km, the estimated accuracy of satellite data at these wavelengths being around 1 mGal according to relations provided by Fairhead and Green (2001). Considering the dimensions of the Falcon survey (30 km), we expected some contribution to the overall error due to insufficient overlap of reliably sampled wavelengths from the two sources.

Despite these expected shortcomings, the conformed gravity product (Figure 6) compared favourably with the reference gravity grid (Figure 5). RMS difference between the two grids was 1.6 mGal, significantly less than for the unconformed Falcon data, which had RMS difference of 3.1 mGal.

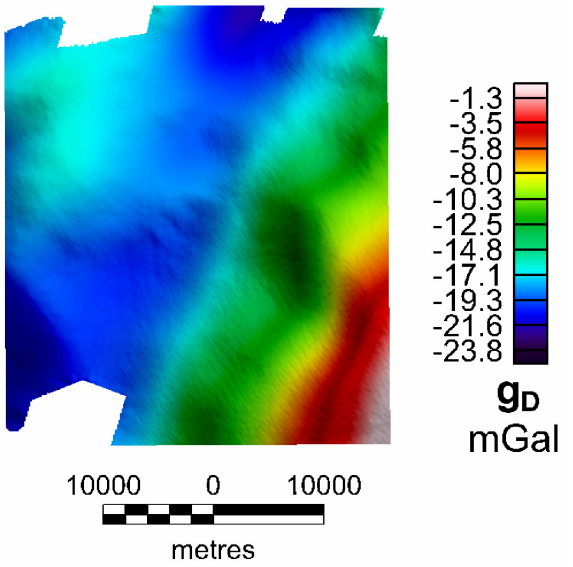

Figure 5. Reference gravity for location 3, derived from a detailed marine gravity survey.

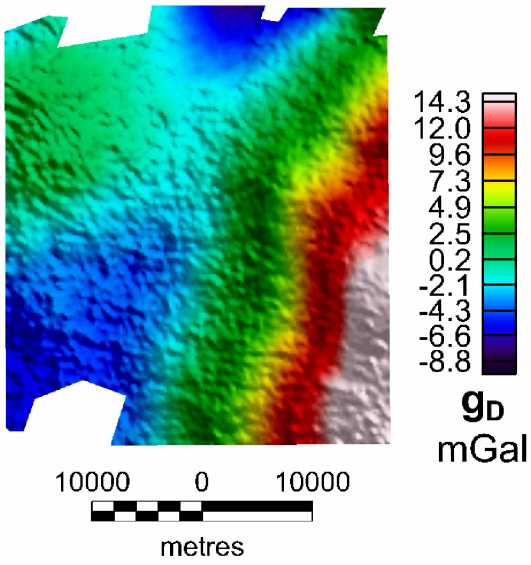

Figure 6. Conformed Falcon gravity data for location 3, satellite data being the regional gravity data source.

Spectral analysis results

For each test location, we computed power spectra of the differences between the reference gravity field and both the conformed Falcon gravity and the raw Falcon gravity. The resultant 2-D power spectral densities were integrated and translated into a single dimension, to indicate contribution to variance of the error grids as a function of wavelength only (see Appendix A). Results for all test surveys and both the conformed and unconformed Falcon gravity are shown in Figure 7 and Figure 8. Note that the error spectra suggest little improvement between unconformed and conformed Bass Strait data, and this is not surprising given the 60 km wavelength used for transition to the satellite data. Despite the apparent lack of improvement indicated by Figure 7 and Figure 8, introduction of features beyond 60 km wavelengths did reduce the RMS error from 3.1 to 1.6 mGal via restoration of the almost linear regional trend apparent in the data of Figure 6.

A significant feature of the unconformed Falcon error spectra are that error levels appear roughly constant at 0.1 mGal/$\sqrt{\text{km}}$ until wavelengths approach the minimum bounding dimension of the survey. Conforming the Falcon gravity to a regional was able to reduce error beyond these wavelengths, and limited the total RMS error to 1-2 mGal in all cases. Assuming these observations are representative of Falcon gravity capabilities, we can make some statements about reliability.

Firstly, at wavelengths approaching and beyond the minimum bounding dimension of the survey, raw Falcon gravity becomes less reliable. Below this wavelength, RMS error should be approximately $0.1\sqrt{\lambda}$ mGal or less, where λ represents a high-pass cut-off wavelength (in km). Secondly, provided regional data exist that adequately sample wavelengths beyond λ, a conformed Falcon gravity product typically can be derived with RMS error of 1-2 mGal or less. Note that the reference fields used in previous analyses were not perfect and probably have contributed to the RMS errors estimated from the previous results, particularly at Test Location 2.

Finally, for comparison with the Falcon gravity capability, Figure 7 and Figure 8 show an amplitude spectral density of the noise in profile data from the best of the airborne gravimeters analysed by Bruton et al., (2001). Although the data analysis methods of each technique were not strictly the same (1-D spectral analysis of profile data was performed by Bruton et al., whereas we have performed a spectral analysis of 2-D Falcon data), the curve provides the first quantitative measure of the relative performance of airborne gravimetry and airborne gradiometry. It indicates that a Falcon AGG survey generally can outperform current airborne gravimeters when measuring features with wavelengths of less than 10 - 20km.

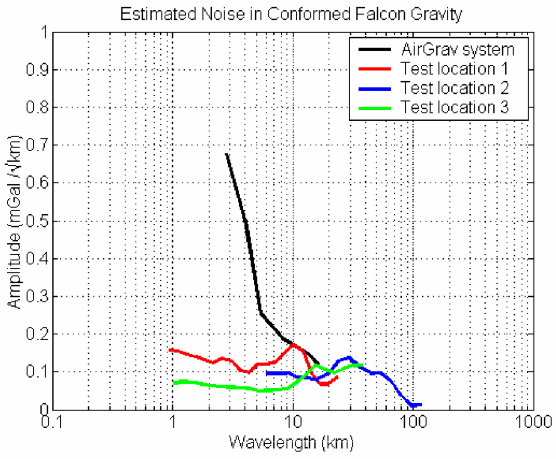

Figure 7

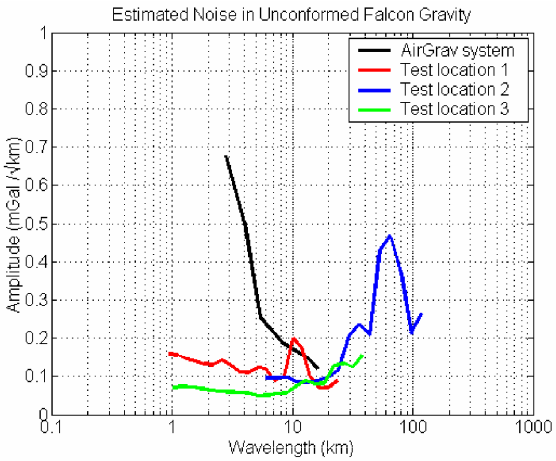

Figure 8

Amplitude spectra of errors in conformed (Figure 7) and unconformed (Figure 8) Falcon data. Errors were determined by differencing Falcon gravity from the reference data at each test location. Spectra have been clipped to wavelengths corresponding to content of the reference data at each site. Error spectral density for an airborne gravimeter is also plotted for reference.

Conclusions

The detailed spectral analysis of data from the three Falcon surveys presented has pointed to an attainable noise of approximately 0.1 mGal/$\sqrt{\text{km}}$. This figure implies that the RMS error in Falcon survey data is roughly 0.3 mGal for wavelengths below 10 km, which is satisfactory for mineral exploration purposes. Accuracy at wavelengths longer than the survey's bounding dimensions appears to diminish, this being attributable to the integration step required to convert gravitational gradients to vertical gravity measurements.

The method of conforming the Falcon data to a regional gravity data source can correct this shortcoming, achieving RMS differences to the reference data of 0.8, 1.8 and 1.5 mGal for data from each of the test locations. A proportion of these residual differences are attributable to signal improperly sampled within the reference data. Some proportion of differences may also be attributed to differences in method of terrain correction, approximations in upward continuations and also errors in the reference data measurements.

Comparison with a similar analysis of some airborne gravimeters (Bruton et al., 2001) showed that accuracy of a Falcon survey can exceed airborne gravimetry for wavelengths shorter than 10 – 20 km, provided the Falcon survey is big enough. Given that peak contributions to the total energy from a monopole gravity source occur at wavelengths of approximately 2 to 8 times depth to target (Appendix A), this would imply Falcon is more suited to detecting such sources if they are located within approximately 2 – 4 km of the ground surface. This result accords with previous analysis by Dransfield (1994) and Li (2001).

Finally, the analysis has demonstrated that hybridisation of regional gravity and gradiometry data can produce a result superior to either method in isolation. Thus, results acceptable for mineral, oil and gas exploration purposes can be derived in most situations from a Falcon survey combined with a pre-existing regional gravity data source, such as satellite or sparse continental gravity databases.

References

Anderson, O.B. and Knudsen, P., 2000, The role of satellite altimetry in gravity field modelling in coastal areas: Phys. Chem. Earth (A), 25, 17-24.

Bruton, A.M., Hammada, Y., Ferguson, S., Schwarz, K.P., Wei, M. and Halpenny, J., 2001, A comparison of inertial platform, damped 2-axis platform and strapdown airborne gravimetry: in Proceedings of the International Symposium on Kinematic systems in Geodesy, Geomatics and Navigation, The Banff Centre, Banff Canada, June 5-8 2001, 542–550.

Champeney, D.C., 1973, Fourier transforms and their physical applications: Academic Press.

Dampney, C. N. G., 1969, The equivalent source technique: Geophysics, 34, 39-53.

Dransfield, M.H., 1994, Airborne Gravity Gradiometry: unpublished PhD. thesis, University of Western Australia.

Fairhead, J. D., Green, C. M. and Odegard, M. E., 2001, Satellite-derived gravity having an impact on marine exploration: The Leading Edge, 20, no. 8, 873-876.

Gunn, P. J., 1975, Linear transformations of gravity and magnetic-fields: Geophys. Prosp., 23, 300-312.

Heiland, C.A., 1968, Geophysical Exploration: Hafner Publishing Co.

Lee, J.B, 2001, FALCON gravity gradiometer technology: Exploration Geophysics, 32, 247-250.
Li, X., 2001, Vertical resolution: gravity versus vertical gravity gradient: The Leading Edge, 20, no.8, 901-904.
Telford, W.M., Geldart, L.P., Sherriff, R.E., 1990, Applied Geophysics Second Edition: Cambridge University Press.

Appendix A – notes on the use of power spectral density

Champeney (1973) defines the power spectrum density (PSD) of a function, $f(\mathbf{r})$, in N dimensions as:

$$P_f(\mathbf{k}) = \lim_{V \to \infty} \frac{1}{V} \left| \int_{\varsigma} f(\mathbf{r}) \cdot \right|^2$$

For spatial functions, the power spectrum indicates contributions to the variance (i.e., 'power') in $f(\mathbf{r})$ as a function of wave-number. The quantity $(2\pi)^{-N} P_f(\mathbf{k}) \cdot \mathbf{dk}$ represents the contribution to the variance from the signal with wave-numbers in the hypercube having corners **k** and **k**+**dk**.

Translation of wave-numbers to wavelength $\lambda = 2\pi/|\mathbf{k}|$ is straightforward and is often used to present power spectra in terms of the latter. However, re-scaling of the data to units of "power/unit of wavelength" (from original "power/units of wave-number") is usually neglected and the authors believe that the PSD loses some of it's original meaning under this partial translation, as the integrated area under the PSD curve no longer represents contribution to the variance of the original function. Rescaling appropriately requires the original units be multiplied by a factor of $(|\mathbf{k}|^2/2\pi)^N$ and, if the original power spectrum was in more than one dimension, gathering power from all equivalent wavelengths via an integration process. It is worth pointing out here that this integration step is not equivalent to the more commonly used radial averaging scheme.

Under such a translation, the relative importance of wavelengths that contribute to a simple gravity anomaly can also easily be seen (Figure 9). Selection of an instrument best suited to detect such an anomaly (be it airborne gravimeter or airborne gravity gradiometer) follows if the noise power spectra of both systems are also known.

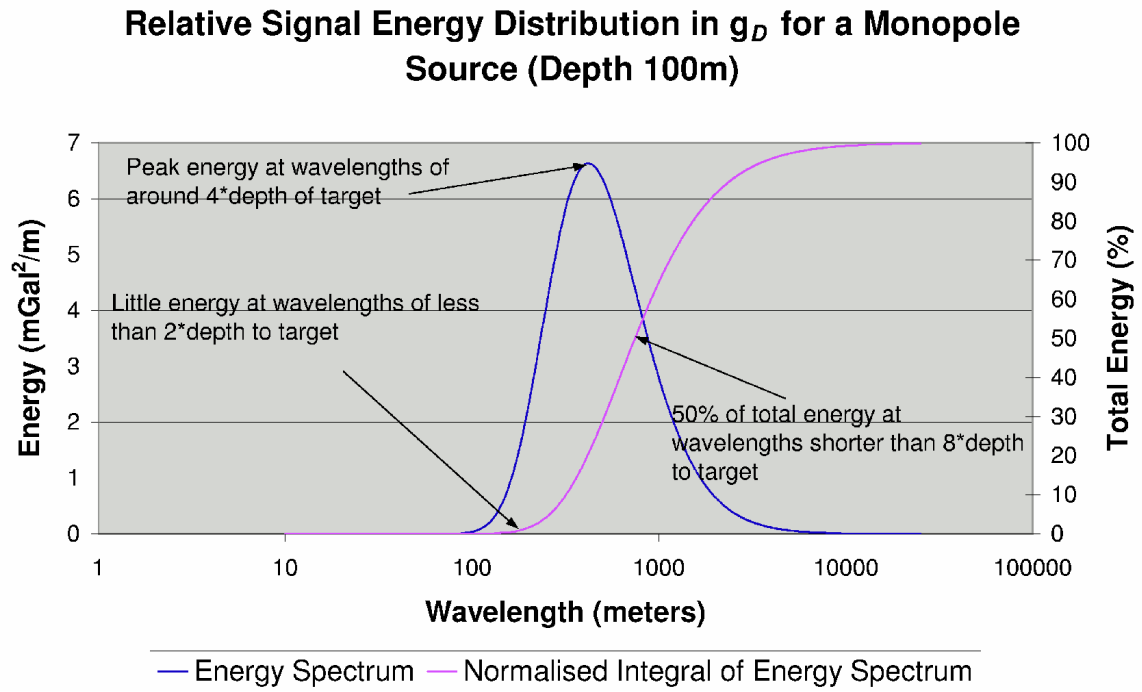

Figure 9. Analytical result for the energy spectrum of gravity from a monopole source at a depth of 100m, presented as a function of wavelength. The energy spectrum is derived via the same method as power spectral density, with the exception that it is not normalised for total area (the 1/V factor).